FERROELECTRIC AND ANTIFERROELECTRIC PROPERTIES OF HfO_2-BASED THIN FILMS

By

PATRICK DOMINIC LOMENZO

A DISSERTATION PRESENTED TO THE GRADUATE SCHOOL
OF THE UNIVERSITY OF FLORIDA IN PARTIAL FULFILLMENT
OF THE REQUIREMENTS FOR THE DEGREE OF
DOCTOR OF PHILOSOPHY

UNIVERSITY OF FLORIDA

2016

© 2016 Patrick D. Lomenzo

ACKNOWLEDGMENTS

I would like to acknowledge Dr. Nishida, my PhD advisor, for his encouragement, openness to new ideas, and his constant support throughout my time as a PhD student at the University of Florida. Under Dr. Nishida's guidance, I learned an immense amount of technical and non-technical skills which will continue to aid me in the future. I thank all of my PhD committee members for their interest and support: Dr. Y.K. Yoon, Dr. Jing Guo, and Dr. Brent Gila.

I would like to acknowledge the Nanoscale Research Facility (NRF) staff for all of their help throughout my program. Discussions with David Hays and Bill Lewis always made me walk away with a greater understanding of the fabrication equipment I was using. Andres Trucco was invaluable in helping me run the ALD tool and solving problems we encountered along the way. I would especially like to thank Brent Gila who kept the Nanoscale Research Facility running efficiently and in a user-friendly manner. Dr. Gila's help in developing ALD recipes and his willingness to expand the capabilities of various tools helped make my project a success.

I would also like to thank Qanit Takmeel for his help in fabrication as well as Dr. Saeed Moghaddam. Dr. Jacob Jones is acknowledged for helping us analyze and better understand the material properties of the HfO_2 thin films which led to many productive collaborations. I would like to thank Sean McLaughlin for his support of the HfO_2 project, I had many good discussions with Sean and his team at Northrop Grumman. I would also like to thank all of my colleagues at IMG, it has been a rewarding experience working with such a great group of people. I would also like to thank the Semiconductor Research Corporation (SRC) for awarding me a fellowship that supported me during my time as a PhD student.

TABLE OF CONTENTS

page

ACKNOWLEDGMENTS ... 3

LIST OF TABLES ... 7

LIST OF FIGURES ... 8

LIST OF ABBREVIATIONS ... 14

ABSTRACT ... 15

CHAPTER

1 INTRODUCTION ... 17

1.1 Properties of Ferroelectrics ... 17
1.2 Dissertation Organization ... 25

2 HAFNIUM OXIDE: BULK AND THIN FILM PROPERTIES ... 29

2.1 Background ... 29
2.2 Properties of Bulk HfO_2 ... 30
2.3 HfO_2 Thin Film Properties ... 33
2.3.1 HfO_2 as a High-K Gate Material ... 33
2.3.2 Enhancing the Dielectric Constant of HfO_2 ... 36
2.4 Ferroelectricity in HfO_2-Based Thin Films ... 39
2.5 Applications for Ferroelectric and Antiferroelectric HfO_2 ... 47

3 MEASUREMENT METHODS AND TECHNIQUES ... 56

3.1 Background ... 56
3.2 Electrical Measurements and Techniques ... 57
3.2.1 Hysteresis Loops ... 57
3.2.2 Dynamic Hysteresis Currents ... 61
3.2.3 Positive-Up-Negative-Down (PUND) ... 64
3.2.4 Capacitance-Voltage (CV) ... 67
3.2.5 Endurance Cycling ... 69
3.2.6 Retention Tests ... 73
3.2.7 Impedance Spectroscopy ... 75
3.3 Materials Characterization Techniques ... 78
3.3.1 X-ray Photoelectron Spectroscopy (XPS) ... 78
3.3.2 Time-of-Flight Secondary Ion Mass Spectrometry (TOF-SIMS) ... 80
3.3.3 Grazing Incidence X-ray Diffraction (GI-XRD) ... 82
3.3.4 Transmission Electron Microscopy (TEM) ... 83

4 FERROELECTRIC PHENOMENA IN Si-DOPED HfO_2 THIN FILMS WITH TiN AND Ir ELECTRODES 84

4.1 Background 84
4.2 Experiment 87
4.3 Results and Discussion 89
4.4 Conclusion 102

5 THE EFFECTS OF LAYERING IN FERROELECTRIC Si-DOPED HfO_2 THIN FILMS 104

5.1 Background 104
5.2 Experiment 106
5.3 Results 108
5.4 Conclusion 114

6 TaN INTERFACE PROPERTIES AND ELECTRIC FIELD CYCLING EFFECTS IN Si-DOPED HfO_2 THIN FILMS 116

6.1 Background 116
6.2 Experiment 119
6.3 Results and Discussion 122
6.4 Conclusion 138

7 FERROELECTRIC Si-DOPED DEVICES PROPERTIES ON HIGHLY DOPED GERMANIUM 141

7.1 Background 141
7.2 Experiment 142
7.3 Results and Discussion 143
7.4 Conclusion 146

8 MIXED Al AND Si DOPING IN FERROELECTRIC HfO_2 THIN FILMS 148

8.1 Background 148
8.2 Experiment 149
8.3 Results and Discussion 151
8.4 Conclusion 157

9 ANNEALING BEHAVIOR OF FERROELECTRIC Si-DOPED HfO_2 THIN FILMS. 158

9.1 Background 158
9.2 Experiment 160
9.3 Results and Discussion 161
9.4 Conclusion 171

10 STUDIES ON FERROELECTRIC AND ANTIFERROELECTRIC HAFNIUM-ZIRCONIUM OXIDE-BASED THIN FILMS 173

10.1 Background ... 173
10.2 Experiment ... 175
10.3 Influence of Doping $Hf_{0.5}Zr_{0.5}O_2$ with Al or Si ... 176
10.4 Thickness Dependence of Ferroelectric $Hf_{0.5}Zr_{0.5}O_2$ ... 182
10.5 Compositionally Graded $Hf_xZr_{1-x}O_2$ Thin Films ... 187
10.6 Conclusion ... 192

11 SUMMARY AND FUTURE WORK ... 194

APPENDIX

A: PROCESS FLOW FOR FERROELECTRIC HfO_2 CAPACITORS ... 196

B: DESCRIPTION OF ATOMIC LAYER DEPOSITION PROCESS ... 197

LIST OF REFERENCES ... 200

BIOGRAPHICAL SKETCH ... 209

LIST OF TABLES

Table page

2-1 Conventional nonvolatile memory technologies compared with FRAM. 49

2-2 Comparison of emerging alternative nonvolatile memory technologies. 52

6-1 Acceleration factors for the Si-doped HfO_2 thin films. 125

B-1 List of ALD precursors and the materials grown. 198

B-2 ALD recipe specifications. 199

LIST OF FIGURES

Figure page

1-1 In a linear dielectric or cubic crystal, an electric field is required to induce a dipole moment in which the distortion of the electron cloud around the nuclei of the atoms produces polarization. 19

1-2 For ferroelectric lead titanate, the tetragonal lattice cell is noncentrosymmetric and the displacement of the central Ti cation with respect to the oxygen anions dictates the polarization direction. 20

1-3 A single crystal ferroelectric has a square polarization vs. electric field profile, whereas the polycrystalline ferroelectric is slanted. 22

1-4 While as-grown ferroelectrics have a random alignment of ferroelectric domain orientations, electrically poling ferroelectrics can induce a preferred polarization direction in both single crystals and polycrystalline materials. 22

1-5 Ferroelastic switching occurs when a-domains 90 ° switch to c-domains, whereas 180 ° switching occurs during conventional polarization reversal with the application of an electric field. 23

1-6 Aberration corrected STEM is used to map out the dipole orientations and domain walls in PTO. 24

2-1 Phase diagram of the $Hf_xZr_{1-x}O_2$ solid solution system. 31

2-2 Phase diagram of HfO_2 with temperature and pressure. 32

2-3 Unit lattice cells of some crystal phases of HfO_2 and ZrO_2. Large atoms are the metal cations and small atoms are the oxygen anions. 32

2-4 Breakdown field and bandgap of various high-k materials plotted against the dielectric constant. 34

2-5 Direct and indirect scavenging techniques. 35

2-6 PMOS and NMOS transistor structures for Intel's 22 nm node. 36

2-7 The measured dielectric constant of $Hf_{1-x}Si_xO_2$ as a function of Si concentration. 38

2-8 Atomic force microscopy scans of HfO_2 thin films annealed at 1000 °C with and without a TiN electrode. 39

2-9 The Si-doped HfO_2 thin film which is capped with a TiN electrode during a crystallization anneal led to a strong orthorhombic or tetragonal diffraction signal. 40

2-10 Hysteresis and piezoelectric displacement curves illustrate how Si doping can lead to ferroelectric and antiferroelectric-like characteristics........ 41

2-11 The hysteresis and relative permittivity indicates a paraelectric to ferroelectric phase transition as the composition of HfO_2 is modified with Zr until a $Hf_{0.5}Zr_{0.5}O_2$ film composition is reached........ 42

2-12 The $2P_r$ and relative phase fraction of $Hf_{0.5}Zr_{0.5}O_2$ films from 5.5 nm to 25 nm thick as a function of anneal temperature. 44

2-13 Different crystal phases of hafnium oxide. 46

2-14 STEM is used to identify the polar orthorhombic phase. 47

2-15 Two different forms of the FRAM memory cell........ 49

2-16 Process flow and cross-sectional image of 3D trench capacitors incorporating Al-doped HfO_2 are shown along with the equivalent planar area hysteresis measurement........ 51

3-1 An implementation of the Sawyer-Tower used to extract the hysteresis plots of ferroelectric capacitors. 57

3-2 A hysteresis plot allows the extraction of several important ferroelectric parameters. 59

3-3 The energy storage density and loss of an antiferroelectric capacitor can be determined by integrating regions within the hysteresis plot. 61

3-4 Modified Sawyer-Tower circuit for dynamic hysteresis current measurements. . 62

3-5 Dynamic hysteresis current measurements........ 63

3-6 PUND waveform and measurement circuit........ 64

3-7 The PUND waveform is applied to a ferroelectric thin film........ 66

3-8 C-V characteristics of ferroelectric thin films. 68

3-9 Bipolar square waves are used to cycle ferroelectric capacitors. 70

3-10 Fatigue occurs in these ferroelectric Al/Si-doped HfO_2 thin films from 10^4 to 10^8 cycles. 72

3-11 Retention tests are performed by baking ferroelectric capacitors in a polarization state and delivering pulse trains to measure data retention. 74

3-12 The Ti 2p binding energy spectra show that Ti is chemically bonded in the forms of TiO_2, Ti_2O_3, TiN, and TiC on the surface of an ALD TiN film. 79

3-13 Depth profile obtained with XPS of ALD grown TiN electrodes. 80

3-14 TOF-SIMS profile of a TaN/Si-doped HfO_2/TaN capacitor where the Si concentration has been quantified and relative count yields for the other elements are given. 82

3-15 TEM is used to confirm the thickness and crystallinity of $Hf_{0.5}Zr_{0.5}O_2$ after ALD growth at 400 °C... 83

4-1 Growth of the HfO_2/SiO_2 interfacial layer and the expansion of the TiN electrode can be seen when compared to the as-deposited film. 89

4-2 Electrical and ferroelectric characterization of TiN MFIS devices after different annealing conditions. 91

4-3 Electrical and ferroelectric characterization of Ir MFIS devices after different annealing conditions. 92

4-4 Comparison of HF surface treatment vs. native SiO_2. 94

4-5 HAADF STEM images of Ir and TiN MFIS stacks... 95

4-6 Hysteresis of TiN and Ir capped MFIS devices different anneals. 96

4-7 Hysteresis of MFIS HfO_2 capacitors with varying Si-doping concentrations. 98

4-8 GIXRD of the Ir and TiN capped HfO_2 films with different doping concentrations are shown with the theoretical peak positions of the orthorhombic, tetragonal, and monoclinic phases of HfO_2. 99

4-9 Ferroelectric and capacitance characteristics of MFM device with Ir electrodes annealed at 1000 °C for 1 s. 101

5-1 Hysteresis dependence on Si layering. 110

5-2 Changing the Si concentration and the ALD cycle ratio both show changes in the hysteresis characteristics.. 111

5-3 Cross-sectional HAADF STEM images of the Ir/HfO_2:SiO_2/Si-stacked samples. 112

5-4 Cycling characteristics of layered Si-doped HfO_2 thin films.. 113

6-1 Hysteresis of the 1.2 mol. % Si films with sputtered TaN electrodes. 124

6-2 The change in the remanent polarization with cycling. 125

6-3 GIXRD of the Si-doped HfO2 thin films shows the crystal structure to be consistent with the tetragonal or orthorhombic phase for both compositions. .. 126

6-4 XPS analysis of the TE interface. 128

6-5 As-grown ferroelectric domains are preferentially polarized upward toward the top electrode in the Si-doped HfO_2 thin films. 130

6-6 TEM confirms the presence of a ~ 1 nm Ta_xO_y layer at the TaN BE interface.. 131

6-7 Switching properties of the Si-doped HfO_2 thin films with TaN electrodes........ 133

6-8 Switching kinetics and switching current of 1.6 mol. % Si doped HfO_2 thin film with a lower anneal temperature.. 137

7-1 HRTEM cross-sectional images of different device stacks. 144

7-2 Ferroelectric characteristics of Si-doped HfO_2 on Ge. 144

7-3 Grazing incidence x-ray diffraction shows that the Si-doped HfO2 thin films are consistent with the tetragonal or $Pca2_1$ orthorhombic phase...................... 145

7-4 Switching characteristics of ferroelectric SI-doped HfO_2 on Ge....................... 146

8-1 Hysteresis characteristics of the mixed Al and Si doped HfO_2 thin films........... 152

8-2 GIXRD confirms the possible existence of the orthorhombic $Pca2_1$ phase in all three of the Al and Si doped HfO_2 thin films annealed at 800 °C. 154

8-3 TOF-SIMS depth profiles of the mixed Al and Si-doped HfO_2 thin films. 155

8-4 HR-TEM image of the Si-Al-Al-Si doped HfO_2 thin film after annealing at 850 °C. Lattice fringes can be seen in the polycrystalline TiN electrodes................ 155

8-5 Anneal temperature dependence of the mixed Al and Si-doped HfO_2 thin films. 156

9-1 The virgin hysteresis characteristics of the 24:1 and 16:1 HfO_2:SiO_2 thin films show an antiferroelectric-like to ferroelectric transition for increasing anneal temperature. 162

9-2 The relative permittivity of the virgin 24:1 HfO_2:SiO_2 captures the antiferroelectric-like to ferroelectric transition which occurs with increasing anneal temperature. 163

9-3 Electrical and ferroelectric parameters of Si-doped HfO_2 with anneal temperature. 164

9-4 Ferroelectric and electrical properties of Si-doped HfO2 with anneal time. 167

9-5 Three unique cases demonstrating the effects of electric field cycling in the Si-doped HfO_2 thin films. 169

10-1 Hysteresis and dynamic hysteresis currents with cycling for HZO films 177

10-2 Energy storage density and efficiency of Al or Si-doped $Hf_{0.5}Zr_{0.5}O_2$ thin films with anneal temperature. 180

10-3 Energy storage density and efficiency of Al or Si-doped $Hf_{0.5}Zr_{0.5}O_2$ thin films with cycling. 181

10-4 Reliability of Si-doped $Hf_{0.5}Zr_{0.5}O_2$ with cycling at elevated temperature. 182

10-5 Reliability of Al-doped $Hf_{0.5}Zr_{0.5}O_2$ with cycling at elevated temperature. 182

10-6 Hysteresis characteristics of $Hf_{0.5}Zr_{0.5}O_2$ thin films from 15 nm – 6 nm in thickness with different anneal temperatures. 183

10-7 The remanent polarization of the $Hf_{0.5}Zr_{0.5}O_2$ films with thickness and anneal temperature, before and after cycling at 1 kHz. 184

10-8 The relative permittivity vs. electric field curves show that most of the films have secondary high-field shoulders which disappear after cycling, except in the case of the 6 nm thick $Hf_{0.5}Zr_{0.5}O_2$ films. 185

10-9 Retention characteristics of 10 nm $Hf_{0.5}Zr_{0.5}O_2$ films before and after cycling at 1 kHz. 185

10-10 Retention tests carried out on 15, 10, and 6 nm thick $Hf_{0.5}Zr_{0.5}O_2$ films after cycling at 1 kHz. 186

10-11 Imprint shifts are shown in red and blue for positive and negative state bakes respectively. 187

10-12 Hysteresis characteristics of $Hf_{0.5}Zr_{0.5}O_2$ thin films with a Hf-rich center at different thicknesses and anneal temperatures. 188

10-13 Hysteresis characteristics of $Hf_xZr_{1-x}O_2$ thin films with a Hf-rich center and Zr-rich ends at different thicknesses and anneal temperatures. 189

10-14 The retention characteristics of the HRC films at 6 nm shows an increase in the polarization margin with higher electric fields. 190

10-15 Inverse capacitance with film thickness for binary $Hf_{0.5}Zr_{0.5}O_2$, HRC, and ZRE films. 191

B-1 Flow diagram of an ALD recipe. 198

LIST OF ABBREVIATIONS

CMOS	Complementary Metal Oxide Semiconductor
DRAM	Dynamic Random Access Memory
E_c	Coercive Field
E_{IB}	Internal Bias Field
ESD	Energy Storage Density
FeFET	Ferroelectric Field Effect Transistor
FRAM	Ferroelectric Random Access Memory
FTJ	Ferroelectric Tunnel Junction
HZO	$Hf_xZr_{1-x}O_2$
MFIS	Metal Ferroelectric Insulator Semiconductor
MFM	Metal Ferroelectric Metal
MFS	Metal Ferroelectric Semiconductor
NVM	Nonvolatile Memory
P	Polarization
P_r	Remanent Polarization
P_s	Spontaneous Polarization
P_{sw}	Switched Polarization
RTA	Rapid Thermal Anneal
V_c	Coercive Voltage

Abstract of Dissertation Presented to the Graduate School
of the University of Florida in Partial Fulfillment of the
Requirements for the Degree of Doctor of Philosophy

FERROELECTRIC AND ANTIFERROELECTRIC PROPERTIES OF HfO_2-BASED THIN FILMS

By

Patrick D. Lomenzo

May 2016

Chair: Toshikazu Nishida
Major: Electrical and Computer Engineering

Ferroelectric HfO_2-based thin films are attractive candidates for nonvolatile memories technologies such as ferroelectric random access memory (FRAM) and ferroelectric field effect transistors (FeFETs). Conventional perovskite ferroelectric memories have been unable to scale to high densities and are not CMOS compatible, which has prevented ferroelectric-based memory technologies from being widely adopted despite their low read/write power, high read/write speeds, and impressive cycling properties. Ferroelectric HfO_2 thin films can overcome the integration hurdles associated with perovskite ferroelectrics because HfO_2 can be deposited through conformal atomic layer deposition (ALD), exhibit ferroelectric properties down to 5nm thicknesses, and are CMOS compatible.

A variety of processing techniques and devices were investigated to study the ferroelectric behavior of HfO_2 based thin films under different conditions. When dopants such as Si and Al were incorporated into HfO_2, mutually competing phase transitions produced paraelectric, ferroelectric, or antiferroelectric characteristics. The overall concentration of such dopants and the spatial distribution of the dopant layers was shown to substantially impact ferroelectricity in HfO_2. The fully miscible $Hf_xZr_{1-x}O_2$

composition was adjusted to produce a range of ferroelectric and antiferroelectric properties. Layered concentration gradients of Hf and Zr within $Hf_xZr_{1-x}O_2$ thin films were demonstrated to add further capabilities in the ability to engineer the electrical and ferroelectric properties of HfO_2-based thin films.

Extrinsic effects such as the device structure, the substrate and capping electrode material, and defects, such as oxygen vacancies, were observed to influence the overall behavior of ferroelectric HfO_2-based thin films. Due to the ultra-thin dimensions of HfO_2-based ferroelectrics, interactions between the electrode and ferroelectric interface were found to induce space charge effects and depolarization fields. The overall reliability of HfO_2-based ferroelectrics was heavily influenced by the choice of electrode material, anneal temperature, and applied electric field.

$Hf_{0.5}Zr_{0.5}O_2$ thin films doped with Al or Si exhibited antiferroelectric characteristics in which reversible field-induced phase transitions took place. The large energy storage density and high efficiency of antiferroelectric thin films make them exceptional candidates for on-chip energy storage. Reliability tests at elevated temperature were carried out to demonstrate the cycling characteristics of doped $Hf_{0.5}Zr_{0.5}O_2$ antiferroelectrics and the data retention of HfO_2-based ferroelectrics.

CHAPTER 1
INTRODUCTION

1.1 Properties of Ferroelectrics

The ability to retain a remanent polarization (P_r) in the absence of an electric field gives a ferroelectric material the unique capability of harnessing its polarization state as the basis for electronic memories. Ferroelectricity occurs in crystalline or polycrystalline materials which have a polar, noncentrosymmetric crystal structure. Ferroelectrics can be further defined as a pyroelectric material in which there are at least two thermodynamically stable polarization states.[1] Unlike linear dielectrics where a net polarization produced by the distortion of the electron cloud and the nuclei of the atoms vanishes when an applied electric field is removed, a relative displacement of anions and cations within the unit lattice cell of a ferroelectric persists even without an electric field. Due to the noncentrosymmetric lattice cell, the center of positive and negative charge do not coincide and a spontaneous polarization (P_s) is produced as a result of the ionic displacement within the unit cell. The remanent polarization remains stable when the applied electric field is removed and can be reversed when the opposite polarity of the electric field is applied.

In general, polarization (P) may be defined as the net dipole moment per unit volume. The net dipole moment can be defined as[2]

$$P = \sum q_n r_n \tag{1-1}$$

where q_n is the charge and r_n is the position vector of the charge. In the absence of an external electric field, the net dipole moment of nonpolar systems is zero whereas polar molecules and materials, H_2O and ferroelectrics for example, will yield a finite net dipole moment. The electric displacement field in free space is given by[3]

$$D = \varepsilon_0 E \quad (1\text{-}2)$$

where ε_0 is the permittivity of free space and E is the electric field. For linear isotropic dielectrics or cubic crystals, the polarization produced from the net dipole moment of the electron cloud and atomic nuclei of the material must be added to Eq. 1-2

$$D = \varepsilon_0 E + P \,. \quad (1\text{-}3)$$

The polarization can be further defined as

$$P = \varepsilon_0 \chi_e E \quad (1\text{-}4)$$

where χ_e is the electric susceptibility of the material. The electric displacement field from Eq. 1-3 can now be expressed as

$$D = \varepsilon_0 E + \varepsilon_0 \chi_e E = \varepsilon_0 (1 + \chi_e) E = \varepsilon E \quad (1\text{-}5)$$

where ε is the material permittivity. From Eq. 1-5, the relative permittivity is

$$\varepsilon_r = \frac{\varepsilon}{\varepsilon_0} = 1 + \chi_e \,. \quad (1\text{-}6)$$

For anisotropic materials or non-cubic crystals, Eq. 1-5 and Eq. 1-6 must be rewritten with the electric susceptibility and dielectric constant tensors[4]

$$D_i = \varepsilon_{ij} E_j \quad (1\text{-}7)$$

$$\varepsilon_{r,ij} = 1 + \chi_{e,ij} \,. \quad (1\text{-}8)$$

Figure 1-1 shows an illustration of the net dipole moment of a dielectric with and without an applied electric field. The relative permittivity of a dielectric is important because it determines the capacitance as shown by

$$C = \frac{\varepsilon_r \varepsilon_0 A}{d} \quad (1\text{-}9)$$

where A is the electrode area and d is the dielectric film thickness.

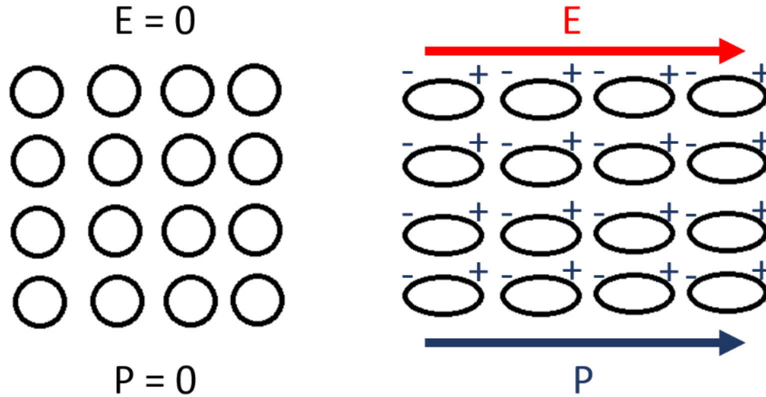

Figure 1-1. In a linear dielectric or cubic crystal, an electric field is required to induce a dipole moment in which the distortion of the electron cloud around the nuclei of the atoms produces polarization.

In a ferroelectric, the application of an electric field displaces ions within the noncentrosymmetric lattice cell and produces a dipole moment called the spontaneous polarization. The spontaneous polarization term must now be included in Eq. 1-5

$$D = \varepsilon_0 E + \varepsilon_0 \chi_e E + P_s = \varepsilon E + P_s \,. \qquad (1\text{-}10)$$

The electric displacement field for ferroelectrics includes both the non-switching dielectric term and the ferroelectric dipole switching term from the spontaneous polarization.[5]

Figure 1-2 illustrates the polarization produced by the tetragonal lattice cell of a common perovskite ferroelectric material, $PbTiO_3$, known as lead titanate (PTO) which is similar to $Pb(Zr_xTi_{1-x})O_3$ (PZT). In PTO, the displacement of the central cation with respect to the oxygen anions shifts the positive and negative center of charge, thus creating a dipole moment. If the oxygen anions shift more strongly in the same direction as the central cation, then the polarization direction would be reversed in Figure 1-2 since the polarization vector begins at net negative charge and ends at net positive charge.[6] The change in direction of polarization, either up or down along the long c-axis

of the PZT tetragonal lattice cell, can be achieved by applying an electric field. Polarization reversal is typically referred to as ferroelectric switching or simply as switching.

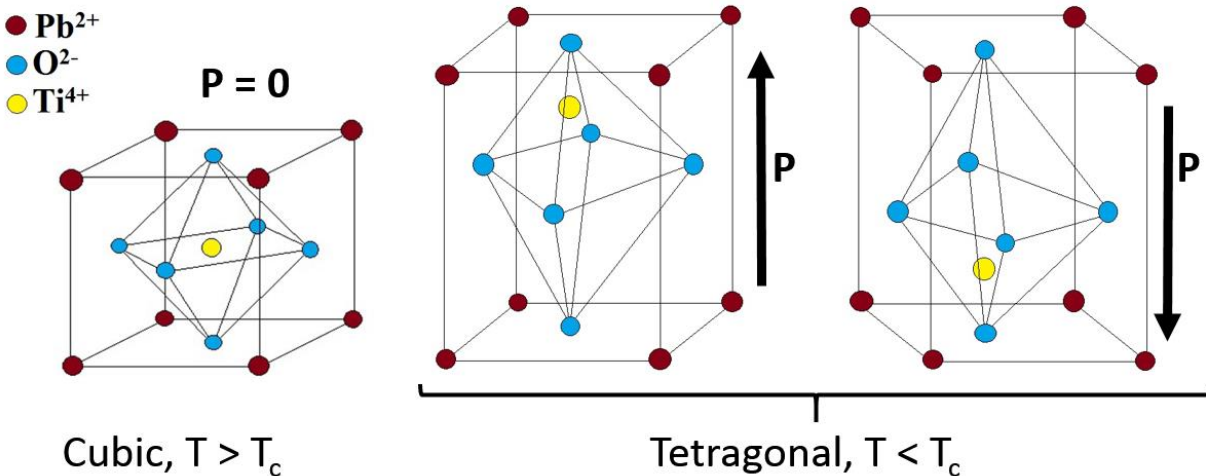

Figure 1-2. For ferroelectric lead titanate, the tetragonal lattice cell is noncentrosymmetric and the displacement of the central Ti cation with respect to the oxygen anions dictates the polarization direction. These diagrams assume only the cation shifts during polarization reversal.

Since ferroelectricity is intricately tied to the crystal structure of a material, crystal phase diagrams related to composition, stress, and temperature provide insight into what crystal structure changes may occur under a variety of conditions. The crystal phase transition temperatures are particularly important when considering ferroelectric materials for specific applications. For instance, ferroelectric memories must remain below the Curie temperature in order to retain the polarization state. The Curie temperature (T_c) is the temperature above which the spontaneous polarization disappears.[7] In the case of PTO, the tetragonal lattice cell undergoes a transition to the cubic phase when the Curie temperature is exceeded and becomes paraelectric, i.e. a linear dielectric. Above the Curie temperature, the relative permittivity of a ferroelectric exhibits the following temperature dependence[7]

$$\varepsilon_r = \frac{C}{T - T_0} \tag{1-11}$$

where C is the Curie constant, T is the temperature, and T_0 is extracted from an extrapolation of when the inverse relative permittivity intersects the temperature axis.

Ferroelectric materials may be single crystal or polycrystalline. Bulk ferroelectrics may be single crystal depending on the growth conditions while thin film ferroelectrics are typically polycrystalline. The switching properties of ferroelectrics can be strongly influenced on whether the material is single crystal or polycrystalline. For instance, in a single crystal, all of the ferroelectric dipoles switch uniformly and are aligned in the same direction. However, for a polycrystalline ferroelectric, the dipoles are aggregated into contiguous clusters called ferroelectric domains. Ferroelectric domains may have different polarization orientations and switching characteristics; however, contiguous lattice cells within a ferroelectric domain generally share the same polarization orientation up to a domain wall boundary. Ferroelectric single crystals have a single domain while polycrystalline ferroelectrics may have many domains. Figure 1-3 illustrates the typical differences in the polarization vs. electric field response between a single crystal and a polycrystalline material.

Figure 1-4 illustrates a conceptual sketch of how domains may behave in polycrystalline materials and single crystals. Barring extrinsic effects which can produce internal electric fields, when ferroelectrics are grown, all of the domains have a random polarization orientation and will yield a net zero polarization. Poling of a ferroelectric encourages the ferroelectric domains to align in a direction parallel to the applied electric field. A ferroelectric exposed to a DC electric field for a given period of time is said to be poled.[8] In single crystals, one domain will be oriented to the direction of the

electric field, while polycrystalline ferroelectrics will have some domains which align with the electric field but will also have domains which have an in-plane polarization. Ferroelectric dipoles which are polarized in the plane of the film do not participate in the ferroelectric switching process that occurs with a transverse electric field.

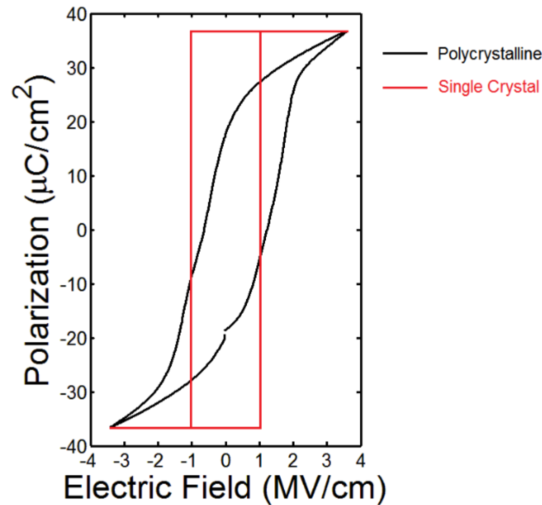

Figure 1-3. A single crystal ferroelectric has a square polarization vs. electric field profile, whereas the polycrystalline ferroelectric is slanted.

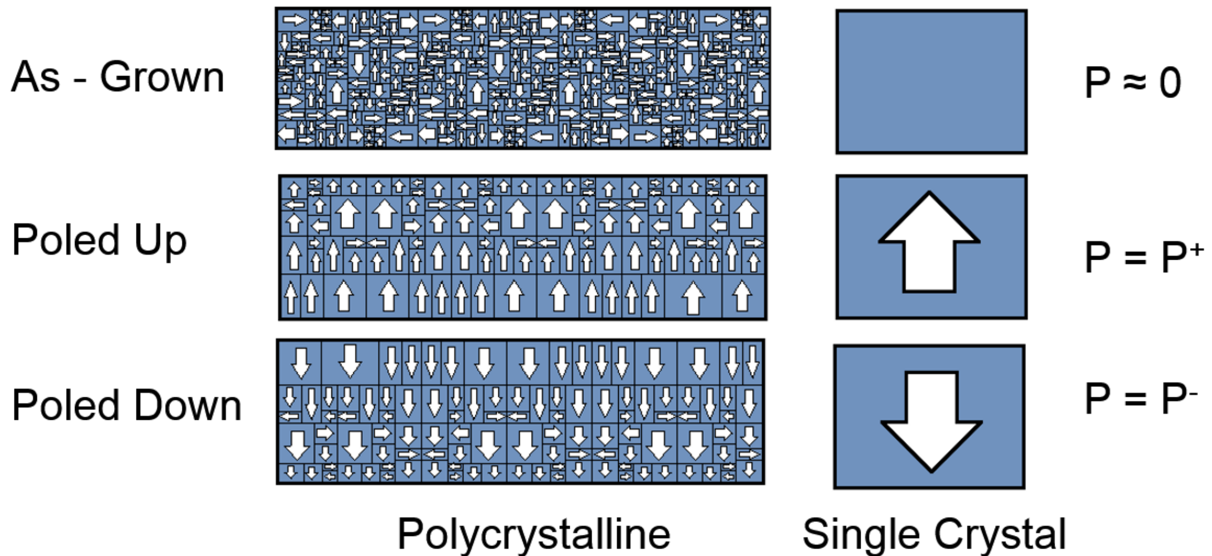

Figure 1-4. While as-grown ferroelectrics have a random alignment of ferroelectric domain orientations, electrically poling ferroelectrics can induce a preferred polarization direction in both single crystals and polycrystalline materials.

For tetragonal ferroelectric perovskites such as PZT, out-of-plane and in-plane domains are called c-domains and a-domains respectively. The c-domains and a-domains are named in reference to the long c-axis and shorter a-axis of the tetragonal lattice cell (the spontaneous polarization vector is always aligned along the tetragonal c-axis). Thus, a-domains have ferroelectric dipoles which are oriented in the plane of the film and their c-axis is parallel to the film plane. While a transverse electric field is unable to switch in-plane domains, under energetically favorable conditions, an a-domain may be converted to a c-domain in what is called ferroelastic switching or 90 ° domain switching.[8–11] Ferroelastic switching can occur with applied stress and/or an electric field. Figure 1-5 provides an illustration of 90 ° and 180 ° domain switching.

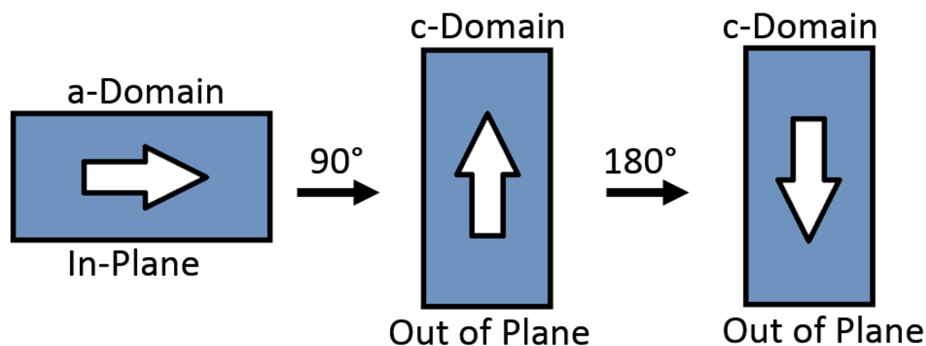

Figure 1-5. Ferroelastic switching occurs when a-domains 90 ° switch to c-domains, whereas 180 ° switching occurs during conventional polarization reversal with the application of an electric field.

Modern atomic-scale imaging techniques such as aberration-corrected scanning transmission electron microscopy (STEM) can allow a precise determination of domain wall boundaries and dipole orientations.[6] As will be discussed in Chapter 2, STEM can also allow a determination of the crystal structure of a ferroelectric material to confirm the origin of ferroelectricity. Figure 1-6 shows how modern computing and atomic imaging can be used to map out dipole orientations and domain wall boundaries in lead

titanate. Interesting and unexpected physical insights are being generated from these powerful imaging techniques.

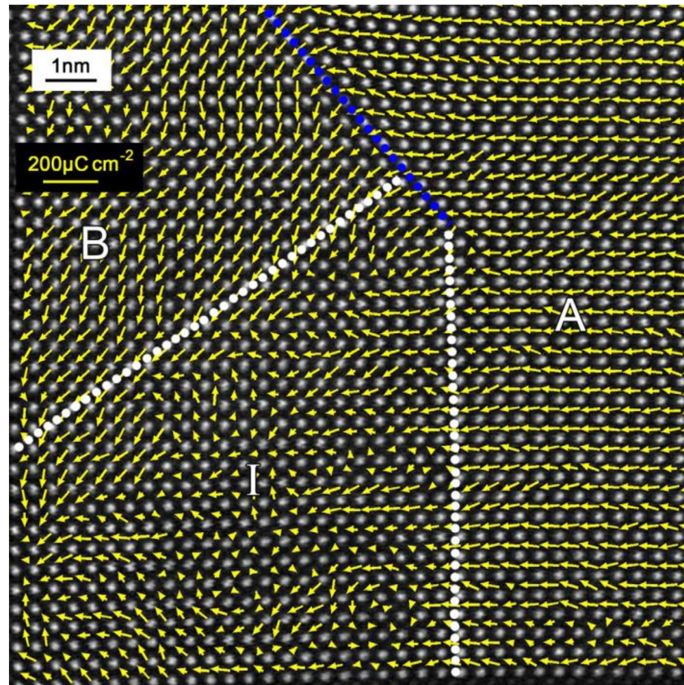

Figure 1-6. Aberration corrected STEM is used to map out the dipole orientations and domain walls in PTO. [Reprinted with permission from Y.L. Tang, Y.L. Zhu, Y.J. Wang, W.Y. Wang, Y.B. Xu, W.J. Ren, Z.D. Zhang, and X.L. Ma, "Atomic-Scale Mapping of Dipole Frustration at 90 ° Charged Domain Walls in Ferroelectric $PbTiO_3$", Sci. Rep. 4, 4115 DOI:10.1038/srep04115 (2014). CC Attribution 3.0 Unported license. http://creativecommons.org/licenses/by/3.0/]

Ferroelectric materials also exhibit piezoelectric and pyroelectric properties which make them valuable as actuators and sensors. The piezoelectric effect occurs when applying a voltage across a ferroelectric produces a strain in the material and causes an out-of-plane deflection. Similarly, the inverse piezoelectric effect occurs when a strained ferroelectric generates a voltage across the film. The relaxation of dipole moments and/or crystal phase transitions can occur when ferroelectric films are heated, thus, an electric current is generated in what is known as the pyroelectric effect.

Ferroelectrics are an intriguing class of materials with a wide array of applications, yet there remains a growing need for new ferroelectric materials in

microelectronic applications due to a variety of limitations with conventional perovskite ferroelectrics. As will be shown in this dissertation, the uncovered ferroelectric and antiferroelectric properties of HfO_2 thin films are particularly suited for microelectronics and are a viable alternative to perovskite ferroelectrics.

1.2 Dissertation Organization

The organization of the dissertation begins with the general description of ferroelectrics as described in Chapter 1. Chapter 1 covers the basic principles of dielectrics and the resulting polarization which occurs with the application of an electric field. The concept of ferroelectricity is then introduced and several differences are drawn which distinguish a ferroelectric from a dielectric material. The switching properties of conventional ferroelectrics are discussed and specific examples are taken from the literature.

The subject of Chapter 2 is on hafnium oxide (HfO_2). The properties of bulk HfO_2 is first discussed to introduce the different crystal phases and the effects of doping on the hafnia material system, many of which are applicable to thin film HfO_2. This leads into HfO_2 thin film dielectrics and the efforts at enhancing the dielectric constant of HfO_2 for microelectronics applications. Finally, the current state of knowledge on ferroelectric HfO_2 is overviewed along with its applications.

Chapter 3 contains a description of the various methods and techniques to characterize ferroelectric HfO_2 thin films. Chapter 3 is broadly divided into electrical and materials characterization techniques which provide complementary data used to understand the physics of ferroelectric thin films. While many of the electrical measurements are specific to ferroelectric thin films, a few of the electrical tests are more general and can be used to evaluate dielectrics and gate oxides.

Chapter 4 investigates the role of Si-doping in ferroelectric HfO_2 thin films with TiN and Ir capping electrodes. The Si-doped HfO_2 thin films are characterized in a metal-ferroelectric-insulator-semiconductor (MFIS) stack structure on a p+ Si substrate. MFIS capacitors can be useful to study because they form the gate stack structure for many ferroelectric field effect devices. A discussion of the effects of annealing, Si-doping, the capping electrodes, and the scavenging effect on ferroelectric HfO_2 are presented in Chapter 4.

The impact of the spatial distribution of Si-dopants on the ferroelectric properties of HfO_2 is the topic of Chapter 5. Adjusting the spacing between an equal number of Si dopant layers is shown to influence the ferroelectric properties of HfO_2. Furthermore, both the spatial distribution of Si-dopants and the overall Si doping concentration leads to changes in the ferroelectric characteristics of HfO_2. The results are particularly relevant for FeFETs since lowering the remanent polarization can reduce the depolarization field.

Chapter 6 presents the effects sputtered TaN electrodes had on Si-doped HfO_2 thin films. A significant internal electric field was found to be present in the ferroelectric capacitors and the cause of the imprint was investigated. Electric field cycling was performed to investigate various aspects of the wake-up effect. Changes in the internal electric field, relative permittivity, and remanent polarization were analyzed as a function of cycling. X-ray photoelectron spectroscopy and high resolution transmission electron microcopy was used to develop a model to understand the ferroelectric behavior of the Si-doped HfO_2 thin films with sputtered TaN electrodes.

The ferroelectric characteristics of Si-doped HfO_2 thin films grown on a highly doped p+ Ge substrate is the subject of Chapter 7. Si-doped HfO_2 is incorporated into three different devices stacks with a TaN, Ge, or SiO_2/Si bottom electrode. A comparison is drawn between the ferroelectric device performances for the different device structures. The absence of an interfacial layer between the Si-doped HfO_2 ferroelectric and Ge substrate enabled a lower operating voltage for polarization reversal compared to the HfO_2 film grown on a Si substrate. Ferroelectric HfO_2 on Ge is highlighted as an attractive prospect for future ferroelectric field effect transistors.

Chapter 8 is an investigation of the effects of co-doping HfO_2 with Al and Si. By using ALD, it was possible to manipulate the arrangement of the Al and Si dopant monolayers within the HfO_2 thin films. Three specific doping arrangements were incorporated into the film with two sandwich doping arrangements and an alternating dopant layering. The ferroelectric properties of the co-doped HfO_2 thin films were dependent on the dopant layering arrangement. The effects of annealing and cycling are discussed in the context of the mixed Al and Si doped HfO_2 thin films.

A study of the rapid thermal annealing dependence of Si-doped HfO_2 thin films is presented in Chapter 9. Three differently doped Si:HfO_2 thin films are annealed at various temperatures between 700 °C and 900 °C. Both isochronal and isothermal annealing is employed to understand the effects of annealing on the properties of Si-doped HfO_2 thin films. Device characteristics such as the remanent polarization, the leakage current, relative permittivity, cycling effects, and the breakdown field are presented as a function of anneal time and temperature.

Chapter 10 is a study composed of several experiments on $Hf_xZr_{1-x}O_2$ thin films. Al and Si incorporated into $Hf_{0.5}Zr_{0.5}O_2$ which causes the undoped ferroelectric capacitors to exhibit antiferroelectric behavior. The antiferroelectric behavior of both Al and Si doped $Hf_{0.5}Zr_{0.5}O_2$ thin films is characterized in terms of energy storage density and efficiency. The thickness dependence and data retention of $Hf_{0.5}Zr_{0.5}O_2$ thin films is also investigated. Chapter 10 concludes with an investigation of compositionally graded $Hf_xZr_{1-x}O_2$ thin films of different thicknesses.

CHAPTER 2
HAFNIUM OXIDE: BULK AND THIN FILM PROPERTIES

2.1 Background

Hafnium oxide, also referred to as hafnium dioxide or hafnia, has historically been used in the nuclear industry due to its large neutron absorption coefficient.[12] In addition, HfO_2 has a large bulk modulus, robust chemical stability, and a high melting point which are attractive for structural applications.[13] Hafnium was not discovered until 1922 due to the very similar chemical properties it shares with zirconium.[14] In nature, hafnium and zirconium are found alloyed, with zirconium being the more abundant element. The structural and chemical properties of hafnia (HfO_2) and zirconia (ZrO_2) are remarkably similar, yet important differences exist such as the crystal phase transition temperatures.

In recent years, the microelectronics industry has brought HfO_2 into its foundries as a high-k gate dielectric to overcome the excessive tunneling leakage currents in ultra-thin SiO_2 gates due to shrinking device dimensions.[15,16] State-of-the-art CMOS devices now regularly employ nanometer-scale high-k HfO_2 gate dielectrics in advanced technology nodes. HfO_2 gate dielectrics are amorphous which improves gate leakage currents while Si doping can be used to improve thermal stability and prevent crystallization.[15] Various efforts have been undertaken to increase the dielectric constant by doping polycrystalline HfO_2 thin films so that a higher permittivity crystal phase could be stabilized.[17–19] Despite years of intense study on thin film HfO_2 and no observations of ferroelectricity, the emergence of ferroelectric behavior was finally uncovered using a suitable combination of doping and annealing conditions in 2011.[20]

2.2 Properties of Bulk HfO_2

While traditional use of bulk HfO_2 has been important in nuclear applications due to its high neutron cross-section absorption coefficient, transformation toughening in ceramics for structural applications has been an area of great interest.[12] Transformation toughening refers to the improvement in mechanical properties of a ceramic material during a crystal phase transition, such as the tetragonal → monoclinic phase transition in zirconia and hafnia, which can be brought about by stress or external forces. ZrO_2 and ZrO_2 toughened ceramics have demonstrated an exceptionally large fracture toughness and fracture strength, but their utility in applications is limited to temperatures less than 1000 °C due to the stabilization of the tetragonal phase above that temperature.[12] The higher tetragonal → monoclinic phase transformation in HfO_2 which occurs at approximately 1700 °C could potentially be used for higher temperature applications, although it has not demonstrated the superior mechanical properties seen in ZrO_2.[12]

Nonetheless, HfO_2 and ZrO_2 form a completely miscible solid solution system which can be expressed as $Hf_xZr_{1-x}O_2$. Phase transition temperatures and the melting point of $Hf_xZr_{1-x}O_2$ increases as the Hf content increases.[21] Figure 2-1 illustrates the phase diagram of the $Hf_xZr_{1-x}O_2$ solid solution system. There is a notable hysteresis in the monoclinic and tetragonal phase transition temperatures when heating and cooling which is more prominent in ZrO_2 than HfO_2.

Although under ambient pressure HfO_2 undergoes a monoclinic → tetragonal → cubic → liquid phase transition with increasing temperature, high pressures can lead to the formation of an orthorhombic phase.[12,22,23] Figure 2-2 shows the bulk HfO_2 phase diagram as a function of pressure and temperature. There has been a wide variation in

the reported pressures that led to the observation of the orthorhombic phase in bulk HfO_2.[12] Figure 2-3 illustrates some of the unit lattice cells of the monoclinic ($P2_1/c$) and orthorhombic ($Pbc2_1$, *Pbca*, and *Pnma*) crystal structures that have been reported in ZrO_2 or HfO_2.[23]

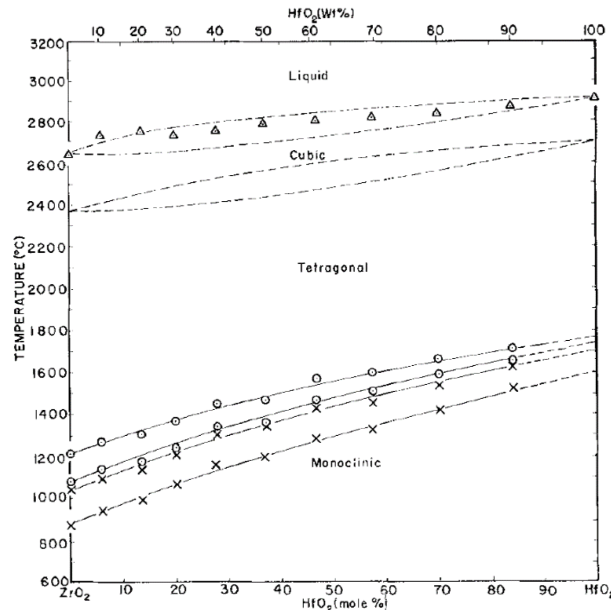

Figure 2-1. Phase diagram of the $Hf_xZr_{1-x}O_2$ solid solution system. [Reprinted with permission from R. Ruh, H.J. Garrett, R.F. Domagala, and N.M. Tallan, J., "The System Zirconia-Hafnia", Am. Ceram. Soc. 51, 23 (1968). Copyright 2006, John Wiley and Sons]

It has been been noted that doping HfO_2 with a variety of compounds, such as MgO, Y_2O_3, and Yb_2O_3, can influence the stabilization of the tetragonal and cubic phases, whereby the dopant typically lowers the phase transition temperatures.[12] While studying the crystal structure of partially stabilized Mg-doped zirconia at low temperatures and under hydrostatic pressure, Kisi was the first to conjecture the existence of an orthorhombic $Pbc2_1$ crystal phase which originated from a tetragonal→orthorhombic phase transformation.[24] The orthorhombic $Pbc2_1$ phase (which is more appropriately written as the $Pca2_1$ space group)[25] would later be called upon to explain the origin of ferroelectricity in HfO_2.[20]

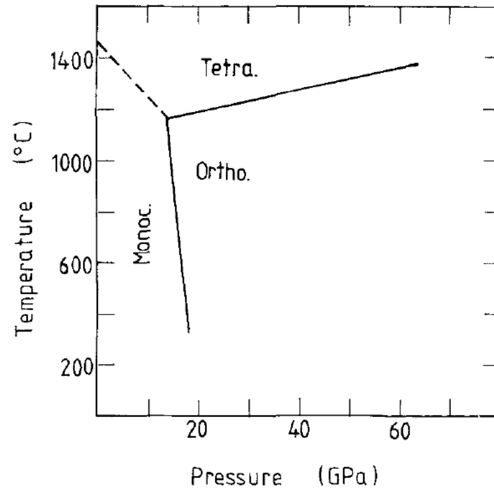

Figure 2-2. Phase diagram of HfO_2 with temperature and pressure. [Reprinted with permission from J. Wang, H.P. Li, and R. Stevens, “Hafnia and Hafnia Toughened Ceramics”, J. Mater. Sci. 27, 5397 (1992). Copyright 1992, Springer]

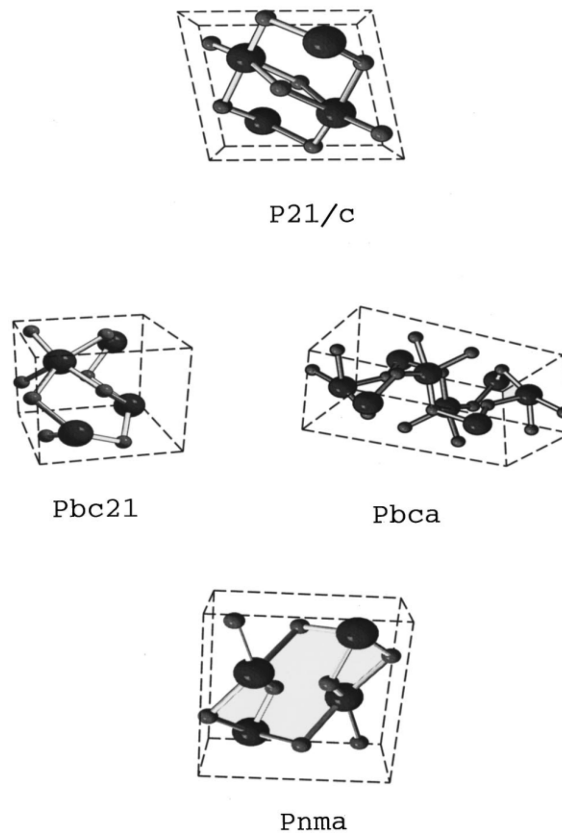

Figure 2-3. Unit lattice cells of some crystal phases of HfO_2 and ZrO_2. Large atoms are the metal cations and small atoms are the oxygen anions. [Reprinted with permission from J.E. Lowther and J.K. Dewhurst, “Relative Stability of ZrO_2 and HfO_2 Structural Phases”, Phys. Rev. B 60, 485 (1999). 1999 Copyright by the American Physical Society]

2.3 HfO_2 Thin Film Properties

2.3.1 HfO_2 as a High-K Gate Material

A surge of research into HfO_2 thin films took place in early 2000 as various high-k gate materials were being investigated to replace SiO_2 as the gate oxide for CMOS transistors.[15,16,26,27] The replacement of SiO_2 in CMOS devices became necessary due to the excessive tunneling currents which occurred in SiO_2 film with thicknesses on the order of 1.2 nm and below.[28] For continuing the scaling of device geometries, high-k gate dielectrics were sought after since their higher permittivity could enable thicker films which prevented tunneling currents while maintaining the equivalent oxide thickness (EOT). The equivalent oxide thickness (t_{eq}) can be calculated by

$$t_{eq} = \varepsilon_{SiO2} \frac{t_{high-k}}{\varepsilon_{high-k}} \quad (2\text{-}1)$$

where ε_{SiO2} is the silicon dioxide relative permittivity (3.9), $t_{high\text{-}k}$ is the thickness of the high-k dielectric, and $\varepsilon_{high\text{-}k}$ is the relative permittivity of the high-k material.

Several high-k candidates arose as potential replacements for the traditional SiO_2 gate oxide including Al_2O_3, Si_3N_4, ZrO_2, HfO_2, Ta_2O_5, TiO_2, and $SrTiO_3$. The polarizability of a material tends to increase as the size of its atoms increases because the outer electrons are more loosely bound to the nuclei. For this reason, transition metal oxides became prime candidates due to their high dielectric constants.[28] While a high permittivity material was required to replace SiO_2, it was observed that higher dielectric constants could only be obtained at the cost of smaller bandgaps (E_G) and lower breakdown fields (E_{BD}), as shown in Figure 2-4. Band offsets and interfacial reactions with the Si substrate were also important factors in evaluating the suitability of high-k dielectrics as replacements for SiO_2.[15,28]

High-k gate materials such as Al_2O_2 and Si_3N_4 did not improve upon the dielectric constant of SiO_2 enough to satisfactorily replace it, despite having a high breakdown field and large bandgap. On the other end of the spectrum, $SrTiO_3$ and TiO_2 exhibited very large dielectric constants (> 75) but have small bandgaps and poor thermal stability on the Si substrate. Ta_2O_5 was also a promising high-k gate dielectric candidate because of its high relative permittivity and moderate ~4eV bandgap, but its poor interfacial stability with the Si substrate ultimately proved prohibitive for incorporation into CMOS transistors.

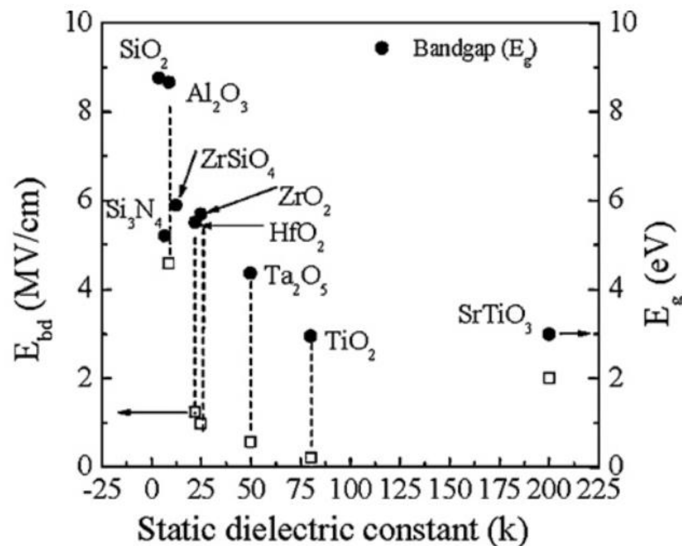

Figure 2-4. Breakdown field and bandgap of various high-k materials plotted against the dielectric constant. [Adapted with permission from Mater. Sci. Eng. R Reports, R 72/6, J.H. Choi, Y. Mao, and J.P. Chang, “Development of Hanfnium Based High-k Material – A Review”, 97-136, Copyright (2011), with permission from Elsevier]

The high dielectric constant of HfO_2 and ZrO_2 (k ~ 20-25) is balanced by a reasonably large breakdown field and bandgap. Thus, both Zr-based and Hf-based transition metal oxides became viable high-k dielectric candidates to replace SiO_2. However, ZrO_2 is not as thermally robust as HfO_2 since it exhibits a lower crystallization temperature and a silicide ($ZrSi_2$) may form at the Si surface.[28] In contrast, HfO_2 exhibits

excellent thermal stability on the Si substrate where the formation of a hafnium silicate interface can improve the interface trap density.[27]

The interface between HfO_2 and the Si channel in CMOS transistors often benefits from the growth of a sub-nanometer layer of SiO_2.[29] Once the HfO_2-based gate oxide has been deposited, a variety of subsequent thermal steps may lead to an increase in the interfacial layer thickness and a concomitant increase in the equivalent oxide thickness. In order to mitigate interfacial layer growth in HfO_2 gate dielectrics with subsequent annealing steps, scavenging techniques were developed to improve the HfO_2/Si interface.[30–32]

There are two different scavenging techniques that can be used to reduce the interfacial layer. In direct scavenging, the HfO_2 thin film incorporates a dopant which will getter oxygen during annealing. Indirect scavenging occurs when oxygen from the interfacial layer is scavenged by the gate electrode material. TiN and TaN are common gate scavenging electrode materials.[30] Figure 2-5 illustrates the different cases for direct and indirect scavenging. Note that in direct scavenging, the HfO_2 thin film can be doped during deposition or dopant diffusion from the metal gate into HfO_2 can occur during annealing. In both direct scavenging cases, the scavenging element is incorporated into the HfO_2 thin film.

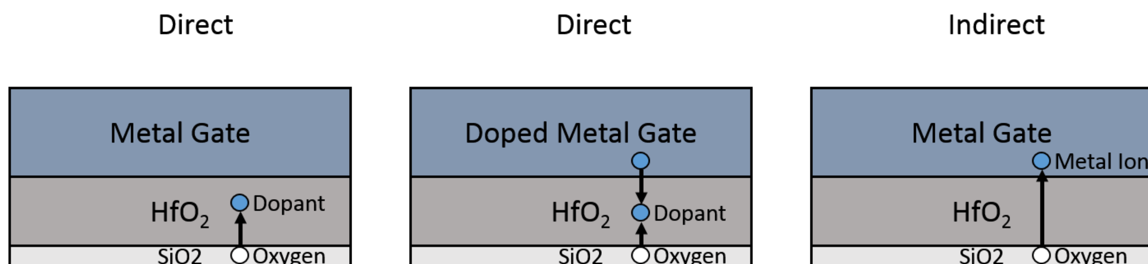

Figure 2-5. Direct and indirect scavenging techniques.

Ever since it was first incorporated into commercial production when Intel announced ALD HfO_2 gate oxides at the 45 nm node in 2007, HfO_2-based high-k dielectrics have endured as the most attractive high-k metal gate material.[28] The advancements in processing technology and the competitive nature of the semiconductor industry has driven transistors from conventional planar devices to intricately engineered 3D geometries, as shown in Figure 2-6. Despite the myriad changes that have occurred to transistor structures since 2007, Hf-based gate dielectrics have remained unchallenged in advanced CMOS technology nodes.

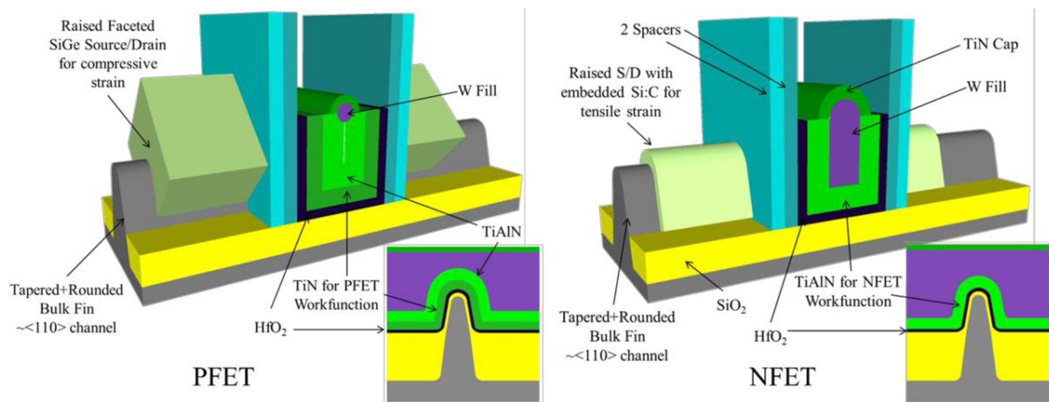

Figure 2-6. PMOS and NMOS transistor structures for Intel's 22 nm node. [Reprinted with permission from R.D. Clark, "Emerging Applications for High K Materials in VLSI Technology", Materials (Basel). **7**, 2913 (2014) DOI: 10.3390/ma7042913, CC Attribution 3.0 Unported license, http://creativecommons.org/licenses/by/3.0/]

2.3.2 Enhancing the Dielectric Constant of HfO_2

Due to HfO_2's use as both a dielectric material in transistors and metal-insulator-metal (MIM) capacitors for DRAM applications, there has been interest in enhancing its dielectric constant to improve device performance. Amorphous HfO_2 has a dielectric constant of about 20 while the monoclinic crystal phase most commonly observed at room temperature in HfO_2 has a lower dielectric constant of approximately 16.[13,17] Hence, not only are amorphous HfO_2 films preferred for gate transistors due to their

lower leakage currents, but the relative permittivity of amorphous films is also higher than monoclinic HfO_2. Nonetheless, achieving a higher dielectric constant in polycrystalline HfO_2 thin films may have advantages if a higher permittivity crystal phase could be stabilized.

The three most commonly observed crystal phases in HfO_2 are the monoclinic, tetragonal, and the cubic phases. The dielectric constant of the tetragonal and cubic phases of HfO_2 is 70 and 29 respectively, marking a significant improvement in the relative permittivity compared to amorphous HfO_2 films.[13] While monoclinic HfO_2 is typically seen at room temperature, higher temperatures can lead to phase transitions toward the tetragonal and then to the cubic crystal phases.[12] Chemically doping bulk HfO_2 or ZrO_2 can lower the crystal phase transition temperatures and may lead to the partial stabilization of the tetragonal or cubic phase.[12]

Doping polycrystalline HfO_2 thin films with Si was found to stabilize the tetragonal phase and increased the dielectric constant for doping concentrations less than 10 atomic %.[17] Ab initio simulations have shown that Si-doping makes the monoclinic phase less energetically stable than the tetragonal phase due to the shorter Si-O bond length stretching in the tetragonal phase compared to the monoclinic phase in HfO_2.[33] Figure 2-7 illustrates the measured dielectric constant in $Hf_{1-x}Si_xO_2$ films for the amorphous, monoclinic, and tetragonal phases. For low Si doping concentrations (< 10 atomic %), an annealing temperature of 800 °C is sufficient to crystallize the HfO_2 thin films. Higher Si doping concentrations increases the crystallization temperature of HfO_2, leading to amorphous films for both 400 °C and 800 °C anneal temperatures as shown

in Figure 2-7. A decrease in the dielectric constant of amorphous HfO_2 occurs at very high Si-doping concentrations because of the lower polarizability of Si compared to Hf.[33]

La and Y doping of HfO_2 thin films were found to stabilize the cubic phase and resulted in an increase in the relative permittivity.[18,34] La doping also increases the crystallization temperature of HfO_2 but Y doping has little influence on it.[19] Zr-rich $Hf_{1-x}Zr_xO_2$ polycrystalline thin films exhibited an improved dielectric constant of about 35 due to the favorable formation of the tetragonal phase.[35]

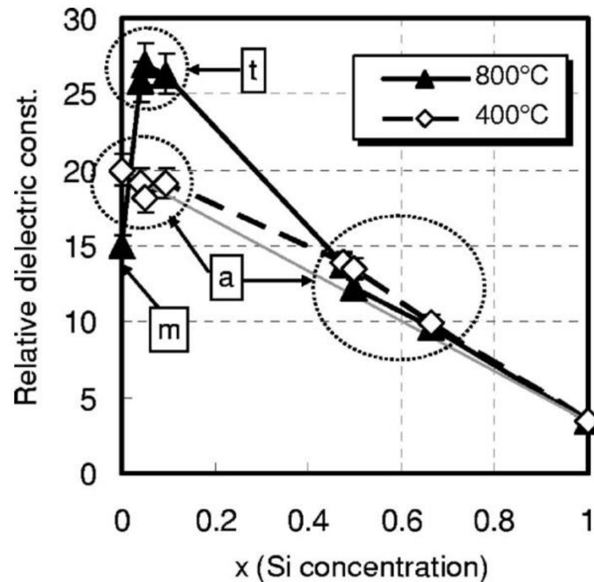

Figure 2-7. The measured dielectric constant of $Hf_{1-x}Si_xO_2$ as a function of Si concentration. The dielectric constant is greatly impacted by the structure of the film as indicated by a, m, and t which stand for amorphous, monoclinic, and tetragonal respectively. [Reprinted with permission from K. Tomida, K. Kita, and A. Toriumi, "Dielectric Constant Enhancement Due to Si Incorporation into HfO_2", Appl. Phys. Lett. 89, 142902 (2006). Copyright 2006, AIP Publishing LLC.]

In contrast to traditional doping, using a discrete ZrO_2 capping layer on HfO_2 was found to induce the tetragonal phase in HfO_2 thin films which was conjectured to be because the discrete layers of ZrO_2 and HfO_2 crystallized separately, thus enabling the tetragonal ZrO_2 capping layer to serve as a template for the HfO_2 layer by making the

monoclinic phase less favorable.[36] TiN, a traditional capping gate electrode material, was also found to encourage the tetragonal phase in HfO_2 thin films after post-metallization anneals by preventing the volume expansion associated with the tetragonal to monoclinic phase transition through the mechanically constraining effect of the electrode.[37] As shown in Figure 2-8, post metallization anneals with a TiN capping electrode reduced the surface roughness of the HfO_2 thin films after annealing which resulted in improved leakage current characteristics.

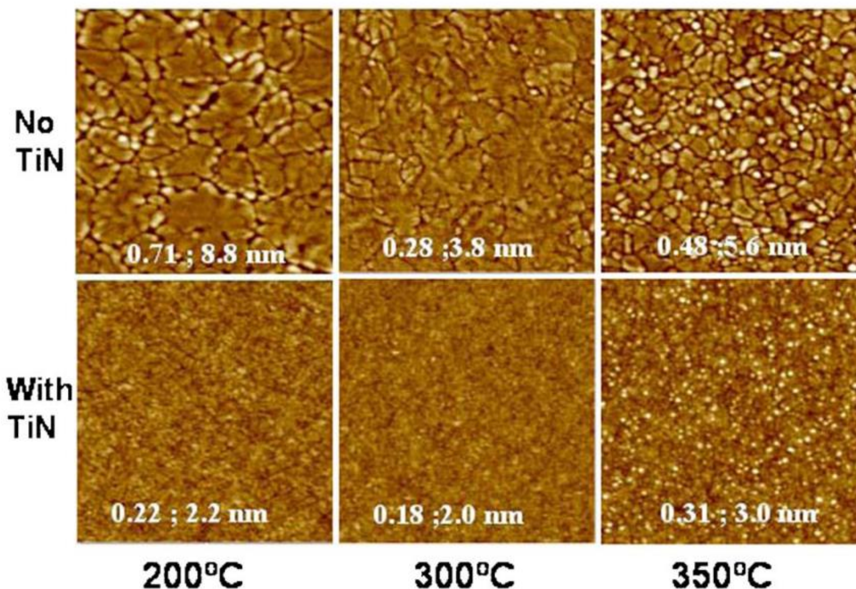

Figure 2-8. Atomic force microscopy scans of HfO_2 thin films annealed at 1000 °C with and without a TiN electrode. The temperatures listed are deposition temperatures. The surface roughness and maximum Z value of the films are shown in the figure. [Reprinted with permission from D.H. Triyoso, P.J. Tobin, B.E. White, R. Gregory, and X.D. Wang, "Impact of Film Properties of Atomic Layer Deposited HfO_2 Resulting from Annealing with a TiN Capping Layer", Appl. Phys. Lett. 89, 132903 (2006). Copyright 2006, AIP Publishing LLC.]

2.4 Ferroelectricity in HfO_2-Based Thin Films

In 2011, the first observations of ferroelectric behavior in 10 nm thick Si-doped HfO_2 thin films was reported by Böscke *et al.*[20] Böscke first encountered ferroelectric properties in HfO_2 thin films at Qimonda in 2007 while investigating enhanced dielectrics

for DRAM capacitors.[25] Improvements in DRAM dielectrics could be achieved by doping HfO_2 with Si or using a capping TiN electrode during annealing.[17,37] It is no surprise that the search for enhanced DRAM dielectrics led to the discovery of ferroelectricity in HfO_2 since the first report combined Si-doping and a post-metallization anneal (PMA) with a capping TiN electrode to stabilize a noncentrosymmetric, orthorhombic $Pca2_1$ space group.[20] As shown in Figure 2-9, a capping electrode was required to increase the fraction of the orthorhombic phase whereas the monoclinic phase was predominant in the uncapped Si-doped HfO_2 thin films.

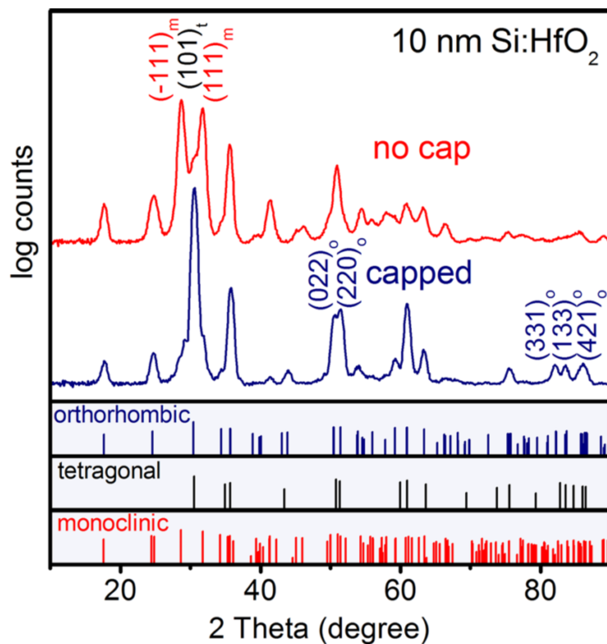

Figure 2-9. The Si-doped HfO_2 thin film which is capped with a TiN electrode during a crystallization anneal led to a strong orthorhombic or tetragonal diffraction signal. [Reprinted with permission from T.S. Böscke, J. Müller, D. Bräuhaus, U. Schröder, and U. Böttger, "Ferroelectricity in Hafnium Oxide Thin Films", Appl. Phys. Lett. 99, 102903 (2011). Copyright 2011, AIP Publishing LLC.]

Adjusting the Si-doping concentration from approximately 2 – 6 mol. % Si produced ferroelectric and antiferroelectric-like properties.[20] Low-to-moderate doping stabilized ferroelectricity while higher amounts of Si incorporation produced

antiferroelectric-like behavior.[20] Figure 2-10 shows the hysteresis characteristics and piezoelectric displacement of the HfO_2 thin films doped with 3.8 mol. % Si and 5.6 mol. % Si which exhibited ferroelectric and antiferroelectric-like properties respectively. The ability to change the behavior of HfO_2 thin films with Si doping concentration can be useful to tailor the capacitor properties for specific applications such as memory or energy storage.

Soon after the first report of ferroelectricity in Si-doped HfO_2, binary $Hf_{0.5}Zr_{0.5}O_2$ thin films from 7.5 nm to 9.5 nm thick were also shown to exhibit ferroelectricity.[38] In contrast to Si-doped HfO_2 thin films which were annealed at 1000 °C and had a crystallization temperature above 500 °C, the $Hf_{0.5}Zr_{0.5}O_2$ thin films were crystallized during the top TiN electrode deposition at 450 °C.[20,38]

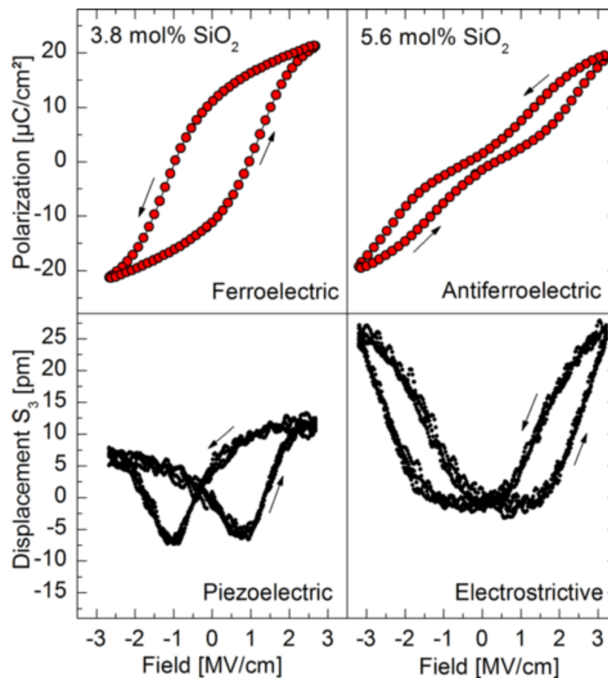

Figure 2-10. Hysteresis and piezoelectric displacement curves illustrate how Si doping can lead to ferroelectric and antiferroelectric-like characteristics. [Reprinted with permission from T.S. Böscke, J. Müller, D. Bräuhaus, U. Schröder, and U. Böttger, “Ferroelectricity in Hafnium Oxide Thin Films”, Appl. Phys. Lett. 99, 102903 (2011). Copyright 2011, AIP Publishing LLC.]

The low thermal budget and the excellent polarization retention at room temperature make $Hf_{0.5}Zr_{0.5}O_2$ particularly suitable for FRAM applications where back end CMOS processing requires low anneal temperatures.[38] Approximately 10 nm thick films of ZrO_2 and $Hf_{0.3}Zr_{0.7}O_2$ exhibited antiferroelectric properties where the critical field associated with a field-induced phase transition decreased with a decrease in temperature.[39] Figure 2-11 shows the $Hf_xZr_{1-x}O_2$ solid soluble thin film system in which ferroelectric and antiferroelectric characteristics are determined by the relative concentration of Hf to Zr.

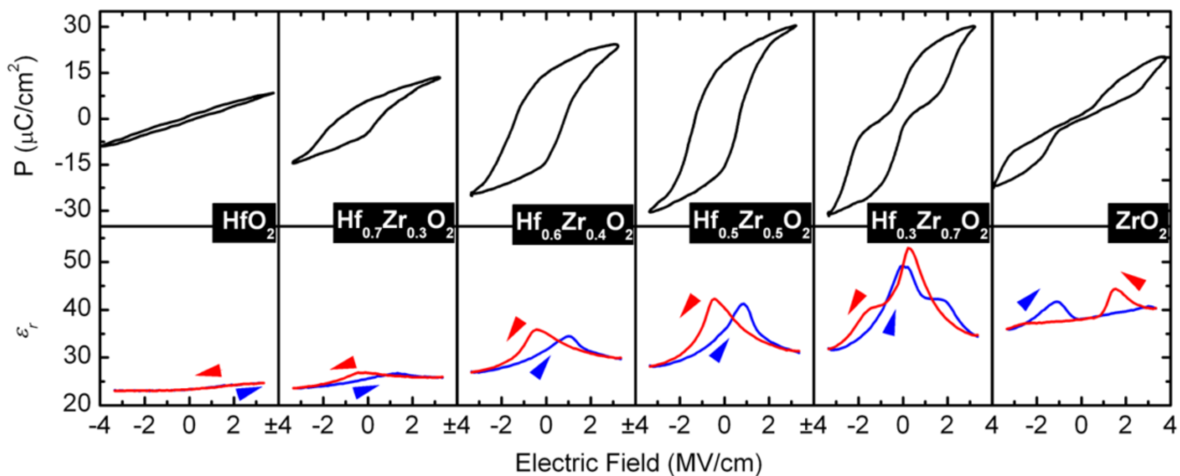

Figure 2-11. The hysteresis and relative permittivity indicates a paraelectric to ferroelectric phase transition as the composition of HfO_2 is modified with Zr until a $Hf_{0.5}Zr_{0.5}O_2$ film composition is reached. Further increasing the Zr content yields antiferroelectric behavior all the way to pure ZrO_2 thin films. [Adapted with permission from J. Müller, T.S. Böscke, U. Schröder, S. Mueller, D. Bräuhaus, U. Böttger, L. Frey, and T. Mikolajick, “Ferroelectricity in Simple Binary ZrO_2 and HfO_2”, Nano Lett. 12, 4318 (2012). Copyright 2012 American Chemical Society.]

The behavior of polycrystalline undoped HfO_2 thin films tend to form the monoclinic phase while pure ZrO_2 has a predominately tetragonal polycrystalline structure.[39] This can be understood to arise from the smaller critical grain size of the tetragonal phase in HfO_2 (~7 nm – 10 nm) compared to ZrO_2 (~ 30 nm) – since grain sizes smaller than 30 nm are readily achieved in polycrystalline ZrO_2, the tetragonal

phase is favored.[40] Simulations have shown that ZrO_2 can exhibit antiferroelectricity through a reversible field-induced tetragonal → orthorhombic phase transition.[41] Further theoretical simulations carried out by Materlik *et al.* found that the ferroelectric orthorhombic phase was unstable in bulk $Hf_{0.5}Zr_{0.5}O_2$ but could be stabilized by introducing a phenomenological surface energy term into the Helmholtz free energy, thus accounting for ferroelectricity being observed in nanoscale $Hf_{0.5}Zr_{0.5}O_2$ thin films to 5 nm.[42]

Due to the critical grain size of the tetragonal phase and surface energy effects in thin film $Hf_{0.5}Zr_{0.5}O_2$, the formation of the polar orthorhombic ferroelectric phase can be influenced by the film thickness. Park *et al.* studied the effect of the anneal temperature and film thickness on the ferroelectric characteristics and polycrystalline structure of $Hf_{0.5}Zr_{0.5}O_2$ thin films.[40] As shown in figure 2-12, $Hf_{0.5}Zr_{0.5}O_2$ films thicker than 10 nm showed an increase in the fraction of the monoclinic phase and were accompanied by a lower remanent polarization and relative permittivity. The degradation of the ferroelectric properties with increasing film thickness can be prevented by inserting a dielectric insulator layer within $Hf_{0.5}Zr_{0.5}O_2$ to engineer smaller grain sizes and make the formation of the ferroelectric orthorhombic phase more favorable.[43]

HfO_2 thin films doped with Yttrium in the range of 2 – 5 mol. % exhibited ferroelectricity after either a post-deposition or a post-metallization anneal.[44] Ferroelectricity was enhanced when Y-doped HfO_2 was annealed with a capping electrode as has been observed for Al-doped HfO_2 as well as $Hf_{0.5}Zr_{0.5}O_2$.[44–46] Ferroelectric Y-doped HfO_2 thin films have been fabricated with a variety of deposition techniques including ALD, sputtering, and chemical solution deposition.[44,47,48] The

remanent polarization of Y-doped HfO_2 was largest in films that were deposited by atomic layer deposition, indicating that ALD produces the highest quality ferroelectric HfO_2-based thin films.[44]

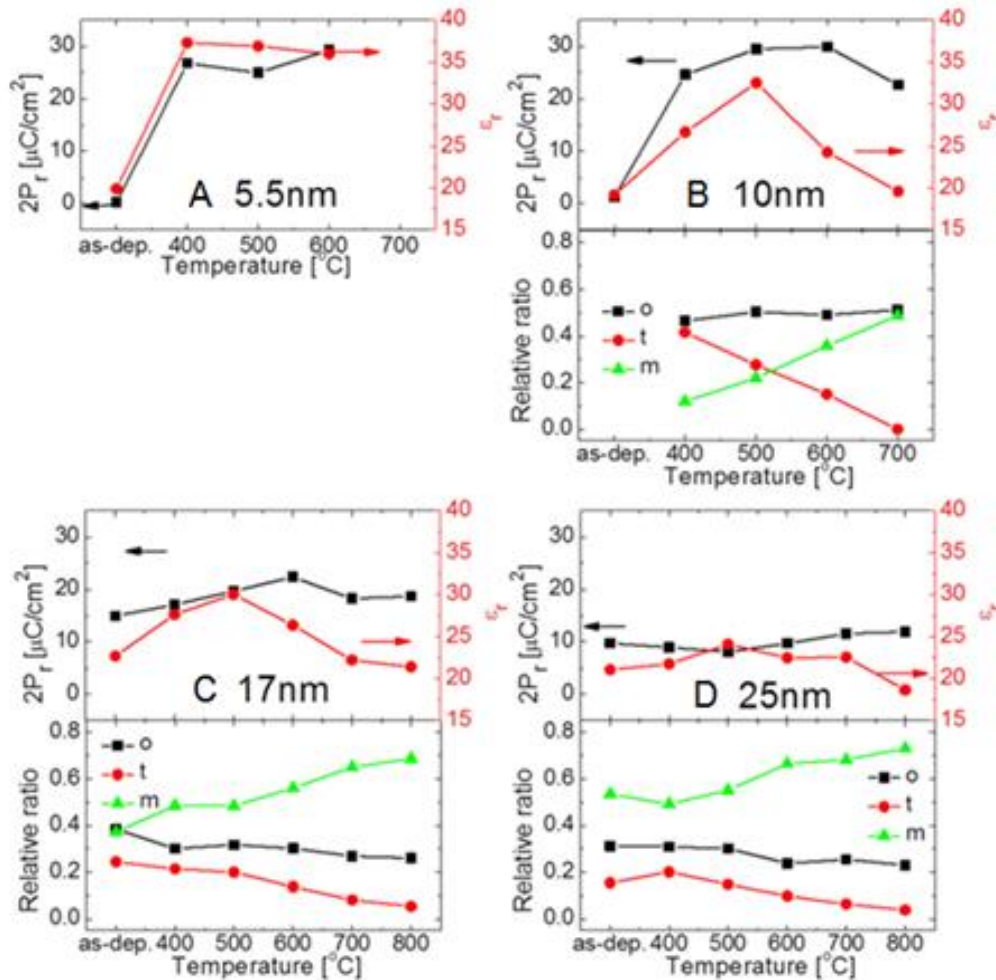

Figure 2-12. The $2P_r$ and relative phase fraction of $Hf_{0.5}Zr_{0.5}O_2$ films from 5.5 nm to 25 nm thick as a function of anneal temperature. [Reprinted with permission from M. Hyuk Park, H. Joon Kim, Y. Jin Kim, W. Lee, T. Moon, and C. Seong Hwang, "Evolution of Phases and Ferroelectric Properties of Thin $Hf_{0.5}Zr_{0.5}O_2$ Films According to the Thickness and Annealing Temperature", Appl. Phys. Lett. 102, 242905 (2013). Copyright 2011, AIP Publishing LLC.]

Other dopants which have been incorporated in HfO_2 thin films to encourage the formation of the ferroelectric orthorhombic phase include Sr, Gd, and La.[49] A wide compositional doping range from approximately 3 – 22 mol. % of Sr was found to

stabilize ferroelectricity in Sr-doped HfO_2 and is the largest doping range reported to date for the trace dopants.[50] At the time of writing, the highest P_r found in HfO_2-based ferroelectrics is 40 μC/cm^2 in La-doped HfO_2, although more reports are needed to confirm the reproducibility of this result.[25,49] The first direct confirmation of the presence of the polar *Pca*2$_1$ orthorhombic phase was measured by aberration corrected high-angle annular dark-field (HAADF) scanning electron microscopy (STEM) in Gd-doped HfO_2 and unambiguously proved the origins of ferroelectricity predicted by simulations.[51] Figure 2-13 illustrates the crystal structures and space groups of the monoclinic, tetragonal, and orthorhombic phases projected along the major axes. The coordination of the Hf-atoms in all of the orthorhombic space groups are the same, but the arrangement of the oxygen atoms are different.[51] Figure 2-14 confirms the presence of the orthorhombic phase in the Gd-doped HfO_2 thin films. Since all of the Hf atomic positions are the same in all three orthorhombic space groups, position averaged convergent beam electron diffraction (PACBED) was used to determine the symmetry and polarity of the orthorhombic phase and distinguished between the space groups.[51] PACBED confirmed the presence of the polar, noncentrosymmetric *Pca*2$_1$ orthorhombic space group responsible for the ferroelectric behavior in HfO_2-based thin films.[51]

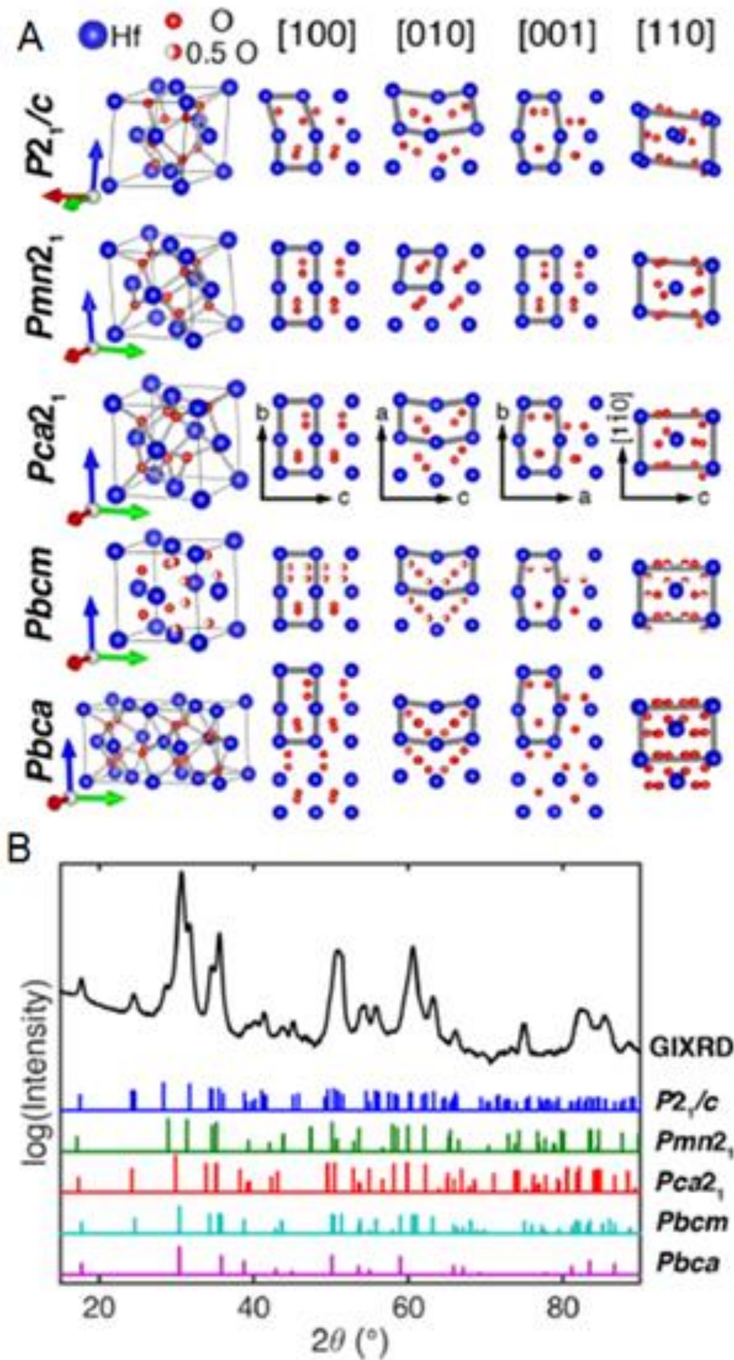

Figure 2-13. Different crystal phases of hafnium oxide. A) The crystal structures of HfO_2 for the tetragonal (*P*2₁/*c*), monoclinic (*Pmn*2₁), and orthorhombic (*Pca*2₁, *Pbcm*, and *Pbca*) crystal phases projected along the major axes. B) Measured GIXRD pattern of Gd-doped HfO_2 and reference GIXRD patterns from powder-diffraction phases of HfO_2. [Reprinted with permission from X. Sang, E.D. Grimley, T. Schenk, U. Schroeder, and J.M. LeBeau, "On the Structural Origins of Ferroelectricity in HfO_2 Thin Films", Appl. Phys. Lett. 106, 162905 (2015). Copyright 2015, AIP Publishing LLC.]

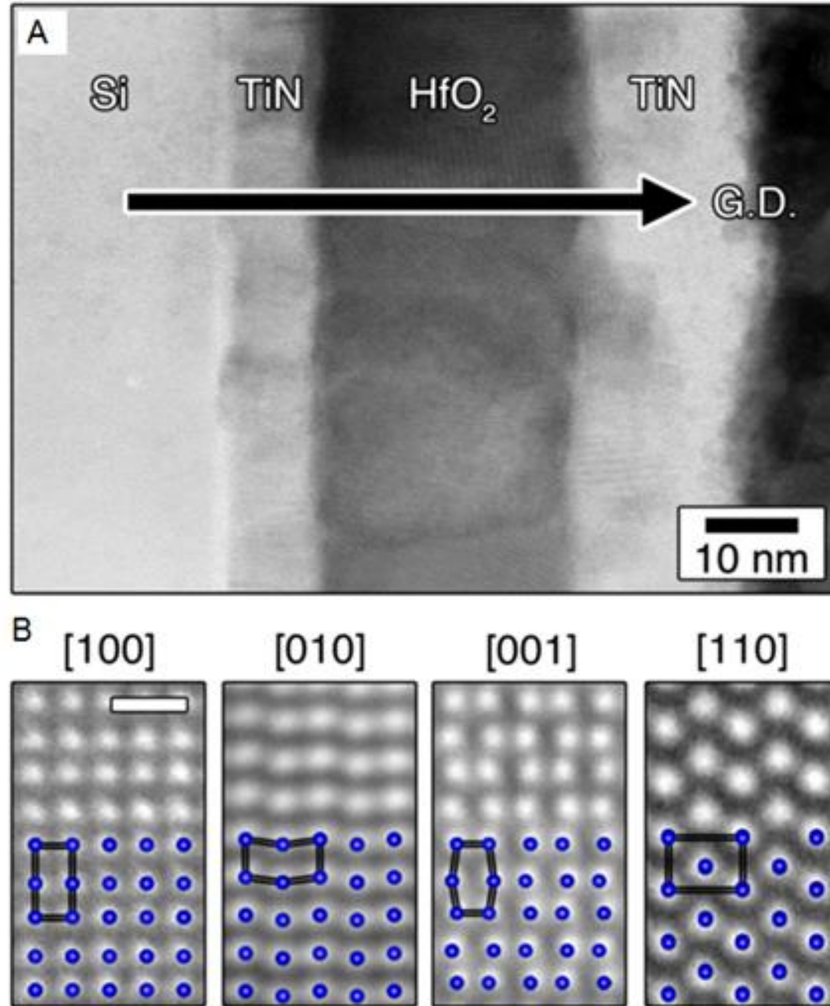

Figure 2-14. STEM is used to identify the polar orthorhombic phase. A) STEM of Gd-doped HfO_2. B) The HAADF-STEM images provide direct confirmation of the orthorhombic crystal structure in Gd-doped HfO_2. [Reprinted with permission from X. Sang, E.D. Grimley, T. Schenk, U. Schroeder, and J.M. LeBeau, "On the Structural Origins of Ferroelectricity in HfO_2 Thin Films", Appl. Phys. Lett. 106, 162905 (2015). Copyright 2015, AIP Publishing LLC.]

2.5 Applications for Ferroelectric and Antiferroelectric HfO_2

Ferroelectric HfO_2-based thin films have great potential for microelectronics nonvolatile memory technologies. In one type of nonvolatile memory technology called ferroelectric random access memory (FRAM), HfO_2 can serve as the ferroelectric in the conventional metal-ferroelectric-metal (MFM) capacitor geometry. In FRAM, the polarization state of the ferroelectric capacitor is directly interrogated by pulsing the

ferroelectric and comparing it to a reference capacitor. The polarization difference is detected by a sense amplifier in a destructive read operation.[1] Due to the destructive read, FRAM capacitors must be rewritten which requires the ferroelectric material to have a high cycling endurance. Because the negative and positive polarization states are probed during read operations, ferroelectrics with a large remanent polarization are desirable for FRAM. As shown in Figure 2-15, FRAM is typically employed in one of two memory array structures as either a 1 transistor/1-capacitor (1T/1C) cell or a 2 transistor/2-capacitor (2T/2C) cell. While an FRAM array consisting of 1T/1C memory cells take up less real estate on a wafer and could be used to achieve higher memory densities, only 1 reference capacitor is used in the 1T/1C implementation and faster degradation of the reference capacitor can lead to memory failure.[1] However, a 2T/2C memory cell has a reference capacitor for every ferroelectric capacitor, thus providing a more reliable memory circuit for commercial applications at the cost of reducing memory density.

Current FRAM commercial products include embedded FRAM in the MSP430 Wolverine microprocessors distributed by Texas Instruments which has maximum density of 128 kb and standalone FRAM memory chips which have up to 4 Mb made by Fujitsu. Both companies use lead zirconate titanate (PZT) thin films on the order of 70 - 150 nm thick as the ferroelectric material at the 130 nm and 180 nm CMOS process technology nodes respectively.[52,53] Conventional perovskites such as PZT have failed to

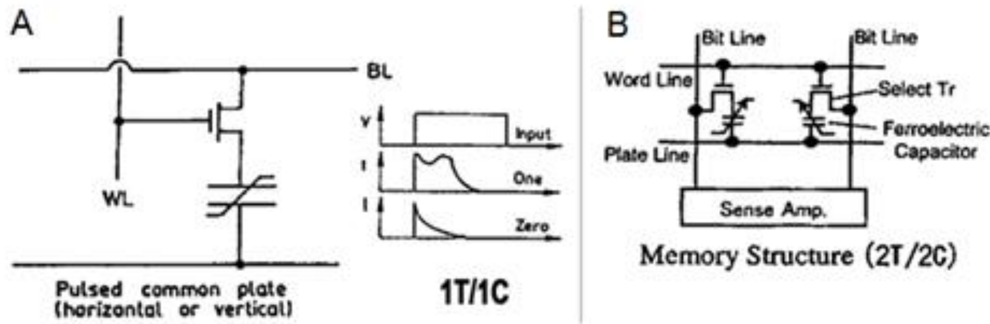

Figure 2-15. Two different forms of the FRAM memory cell. A) 1T/1C and B) 2T/2C memory architectures for FRAM applications. [Reprinted figure with permission from M. Dawber, K.M. Rabe, and J.F. Scott, "Physics of Thin Film Ferroelectric Oxides", Rev. Mod. Phys. 77, 1083 (2005). Copyright 2005 by the American Physical Society.]

garner widespread industry adoption of FRAM due to the potential for Pb contamination in CMOS foundries, poor scaling properties, limited memory array densities, and reliability concerns such as imprint and data retention. Table 2-1 shows a comparison of FRAM with commonly used nonvolatile memory technologies, electrically erasable programmable read only memory (EEPROM) and FLASH. While technology improvements since the year 2000 would require some modifications to the performance specifications in Table 2-1, the overall comparison trends highlight the relevant differences in the nonvolatile memory technologies.

Table 2-1. Conventional nonvolatile memory technologies compared with FRAM.

Nonvolatile Memory	Area/Cell (Normalized)	Read Access Time	Write Access Time	Energy per 32b Write	Energy per 32b Read
EEPROM	2	50ns	10µs	1µj	150pJ
FLASH	1	50ns	100ns	2µj	150pJ
FRAM	5	100ns	100ns	1nj	1nJ

© 2000 IEEE [Reprinted, with permission, from A. Sheikholeslami and P.G. Gulak, "A Survey of Circuit Innovations in Ferroelectric Random-Access Memories", Proc. IEEE 88, 667 (2000).]

The cell size of FLASH is much smaller than current FRAM technologies which enables far higher memory array densities than FRAM due to scaling limitations of

conventional ferroelectric perovskites. Ferroelectric HfO_2-based thin films are well-suited to surpass the material issues associated with limited FRAM scaling because HfO_2-based thin films possess ferroelectricity down to 5 nm in thickness.[54] 3-dimensional trench capacitors using ferroelectric Al-doped HfO_2 have demonstrated the intriguing scaling potential of HfO_2-based ferroelectrics for FRAM applications,[55] as illustrated in Figure 2-16. The conformal ALD growth of HfO_2 and the feasibility of obtaining ferroelectricity in ultra-thin HfO_2 films make integration of 3D structures a practical solution to obtain higher density FRAM arrays. While the polar orthorhombic crystal phase in HfO_2-based thin films benefits from film thicknesses on the order of 10 nm,[40] PZT capacitors degrade when scaled to the same thicknesses with a large increase in the coercive field and a decline in the remanent polarization.[56,57] PZT is also known to be very sensitive to hydrogen and requires a barrier layer to prevent its ferroelectric properties from degrading[58] whereas HfO_2-based thin films are resilient against hydrogen contamination.[59] Forming gas anneals containing hydrogen are routinely employed to achieve optimal transistor performance on Si wafers.[59]

Another advantage FRAM has over conventional FLASH and EEPROM technologies is the much lower energy needed to perform a write operation. The energy required to write to FRAM is 1000x smaller than either FLASH or EEPROM, making it very attractive for low-power, mobile devices. Though HfO_2-based ferroelectrics may be in a position to pivot FRAM technologies toward higher densities and expand FRAM's presence in mobile devices, it must compete with other emerging nonvolatile memories such as resistive random access memory (RRAM), magnetic random access memory

(MRAM), phase change memory (PCM), and spin transfer torque random access memory (STT-RAM).

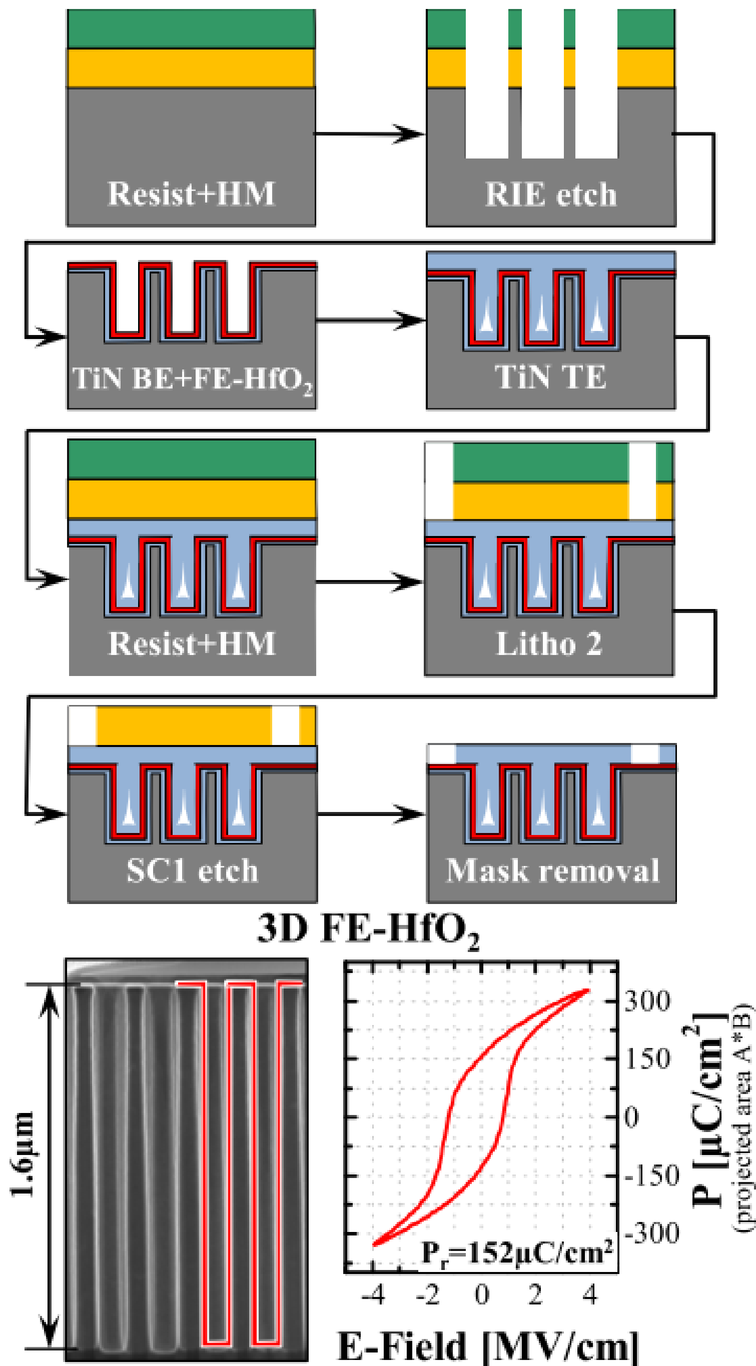

Figure 2-16. Process flow and cross-sectional image of 3D trench capacitors incorporating Al-doped HfO_2 are shown along with the equivalent planar area hysteresis measurement. © 2000 IEEE [Reprinted with permission from P. Polakowski, S. Riedel, W. Weinreich, M. Rudolf, J. Sundqvist, K. Seidel, and J. Muller, “Ferroelectric deep trench capacitors based on Al:HfO_2 for 3D

nonvolatile memory applications", in *2014 IEEE 6th Int. Mem. Work.* (IEEE, 2014), pp. 1–4.]

Table 2-2. Comparison of emerging alternative nonvolatile memory technologies.

Features	FRAM	MRAM	STT-RAM	PCM
Cell size (F^2)	Large, ~40 – 20	Large, ~25	Small, ~6 – 20	Small, ~8
Storage Mechanism	Polarization of a ferroelectric	Magnetization of a ferromagnet in a MTJ	Spin polarized current applies torque on magnetic moment	Amorphous/polycrystalline phase change
Read Time (ns)	20 – 80	3 – 20	2 – 20	20 – 50
Write/Erase Time (ns)	50/50	3 – 20	2 – 20	20/30
Endurance	$>10^{12}$	$>10^{15}$	$>10^{16}$	$>10^{12}$
Write Power	Mid	Mid to high	Low	Low
Nonvolatility	Yes	Yes	Yes	Yes
Maturity	Limited production	Test chips	Test chips	Test chips
Applications	Low density	Low density	High density	High density

© 2014 Nanoscale Research Letters [Adapted with permission from J. Meena, S. Sze, U. Chand, and T.-Y. Tseng, Nanoscale Res. Lett. 9, 526 (2014). CC Attribution 4.0 license, http://creativecommons.org/licenses/by/4.0/]

RRAM is considered to be one of the most promising alternative candidates due to its small cell structure compared to MRAM and STT-RAM while also operating faster than PCM. Table 2-2 gives a comparison of FRAM, MRAM, STT-RAM, and PCM. The performance specifications for FRAM assume PZT or SBT is the ferroelectric material, but table 2-2 does not take into account what cell size may be achievable with ferroelectric HfO_2-based thin films.[60]

While FRAM is a memory technology under development, there remains other ferroelectric-based nonvolatile memories which are emerging and still in the research phase. One emerging nonvolatile memory device is the ferroelectric field effect transistor (FeFET) which has a simple 1 transistor (1T) memory cell. FeFETs incorporate a ferroelectric material as the gate. By switching the polarization state of the ferroelectric, the threshold voltage can be shifted. A memory window is established by

the difference in the threshold voltages for the two polarization states in a FeFET.[61] One major hindrance to the successful demonstration of FeFETs has been the poor data retention when perovskite materials are used as the gate material.[1] The poor data retention in FeFETs is primarily due to a depolarization field generated from the lack of compensating charge carriers at the ferroelectric-semiconductor interface in the MFS stack.[62] Perovskite ferroelectrics tend to exhibit poor interfacial stability on Si, but when an insulating buffer layer is sandwiched between the ferroelectric and the Si channel, the resulting MFIS device structure exacerbates the depolarization field.[62] The depolarization field in a FeFET can be expressed as[62]

$$E_{Dep} = \frac{P_r}{\varepsilon_r\left(\frac{C_{IS}}{C_F}+1\right)} \tag{2-1}$$

where P_r is the remanent polarization, ε_r is the relative permittivity of the ferroelectric, C_{IS} is the interfacial layer capacitance, and C_F is the ferroelectric capacitance. Eq. 2-1 shows that if the thickness of the interfacial layer could be reduced to zero (i.e. C_{IS} goes to infinity), then the depolarization field could effectively be neutralized. Due to the addition of a buffer layer or the growth of interfacial layers, thick perovskite ferroelectric films must be employed to mitigate depolarization fields in ferroelectric field effect transistors which make perovskites unsuitable for advanced CMOS technology nodes.[25]

Ferroelectric HfO_2-based thin films are excellent candidates for FeFET technologies because HfO_2 is already being used as a gate dielectric materials in advanced CMOS technologies.[28] Ferroelectric Si-doped HfO_2 thin films incorporated into FeFETs have demonstrated an extrapolated 10 year memory window of 650 mV which surpasses the best performing FeFETs based on strontium barium titanate and

PZT.[61] Furthermore, FeFETs fabricated at the 28 nm technology node have shown the scaling potential for ferroelectric Si-doped HfO_2 thin films.[63] Several challenges must be overcome to make HfO_2-based FeFETs a viable memory technology such as cycling degradation and poor data retention at elevated temperatures, both of which are associated with charge trapping and the interfacial SiON layer typically employed in the MFIS stack.[63,64] As will be discussed in Chapter 7, an interfacial layer between the semiconductor and ferroelectric HfO_2 may be avoided by using a different substrate material as the basis for a ferroelectric field effect transistor and ultimately improve the device characteristics.

In addition to FeFETs being used as a nonvolatile memory storage element, a capacitor-less DRAM cell can be constructed in a volatile memory scheme.[65] The advantages of using a FeFET in place of a conventional DRAM capacitor include a much smaller cell size, a longer refresh rate due to the better data retention in FeFETs, and lower power consumption.[65] $Hf_{0.5}Zr_{0.5}O_2$ thin films integrated into FeFET device structures have shown that the capacitor-less DRAM cell can exhibit superior leakage current properties, a smaller cell size, and the potential for sub-ns switching operation which would not be feasible in conventional 1T/1C DRAM capacitors.[66] In addition to using ferroelectric HfO_2-based thin films for their memory capability in transistors, transistor performance can be enhanced through a reduction of the subthreshold slope.[67] Antiferroelectric HfO_2-based thin films may result in sub-threshold slopes down to 33 mV/decade due to the negative capacitance effect.[68]

Antiferroelectric HfO_2-based thin films are believed to exhibit a reversible field induced phase transition between the polar orthorhombic phase and the tetragonal

phase.[41] The reversible phase transition can be utilized in energy storage capacitors because much of the electrical energy involved in the field-induced phase transition is returned when the phase transition is reversed as the applied electric field is removed. Park *et al.* quantified the energy storage density in $Hf_xZr_{1-x}O_2$ thin films which yielded an impressive 28 J/cm^3 with a 50% efficiency over a 25 °C – 175 °C temperature range.[69] Furthermore, the electrocaloric effect was exhibited in antiferroelectric $Hf_xZr_{1-x}O_2$ which could be useful for refrigeration applications.[70] Practical applications for infrared detectors based on the pyroelectric effect has been shown to be possible for antiferroelectric Si-doped HfO_2 thin films.[71]

CHAPTER 3
MEASUREMENT METHODS AND TECHNIQUES

3.1 Background

There are various electrical and materials characterization techniques that can be used to probe the properties of ferroelectric thin films. Electrical measurements specific to ferroelectric capacitors include hysteresis, dynamic hysteresis current measurements, Positive-Up-Negative-Down (PUND), pulsed transient current measurements, capacitance-voltage (CV) sweeps, endurance cycling, and retention tests. Another electrical technique which can be used to determine specific film properties and gain additional insight about the quality of the films is impedance spectroscopy. While a single electrical measurement cannot provide the necessary information to understand all of the physics in ferroelectric films, taken together, they offer a powerful tool to evaluate a ferroelectric's potential for many applications and provide a canvas from which important physical insights may be drawn.

Materials characterization techniques aid in providing a more in-depth look at both the structure and composition of ferroelectric thin film devices. While there is an immense array of materials techniques to choose from in studying ferroelectric films, some of the more important techniques include x-ray photoelectron spectroscopy (XPS), time-of-flight secondary ion mass spectrometry (TOF-SIMS), grazing incidence x-ray diffraction (GI-XRD), and transmission electron microscopy (TEM). The use of both electrical and materials characterization techniques is complementary since practical use of ferroelectric thin films draws almost entirely on the electrical tests while materials techniques can unveil physical details that may not be possible through electrical measurements.

3.2 Electrical Measurements and Techniques

3.2.1 Hysteresis Loops

The most frequently used technique to evaluate the ferroelectric behavior of a material is by looking at its hysteresis characteristics. A hysteresis graph is generated by plotting the ferroelectric's polarization as a function of voltage or electric field (commonly denoted as a P-V or P-E plot respectively). The Sawyer-Tower circuit is commonly used to take hysteresis measurements.[72] Figure 3-1 shows an implementation of the Sawyer-Tower circuit which is used in extracting the P-V or P-E curves of ferroelectric thin films. In the Sawyer-Tower circuit, a triangle wave is applied across a ferroelectric capacitor (C_F) and a series linear sense capacitor (C_S) where the linear capacitor is grounded. The sense voltage (V_S) is measured at the terminal between the ferroelectric capacitor and linear capacitor.

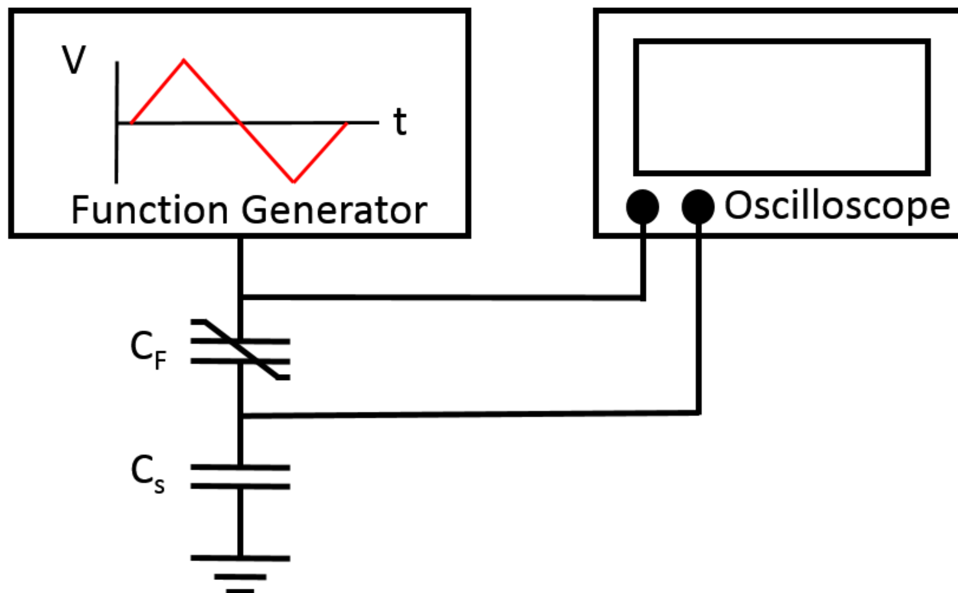

Figure 3-1. An implementation of the Sawyer-Tower used to extract the hysteresis plots of ferroelectric capacitors.

The ferroelectric charge (Q_F) generated from applying a voltage across the capacitors can be calculated by[73]

$$Q_F = \frac{V_s}{C_s} \tag{3-1}$$

where V_s is the sense voltage. Because the sense voltage must be small enough such that it does not reduce the applied voltage below the switching voltage, the following constraint should be met to ensure an accurate hysteresis measurement,

$$C_s >> C_F \,. \tag{3-2}$$

The electric field displacement can be calculated from the ferroelectric charge by

$$D = \frac{Q_F}{A} = \varepsilon_0 E + P \tag{3-3}$$

where A is the area of capacitor, E is the electric field, ε_0 is the permittivity of free space, and P is the polarization. The polarization is calculated from Eq. 3-3,

$$P = D - \varepsilon_0 E \,. \tag{3-4}$$

The subtractive second term in Eq. 3-4 makes it the most accurate way to plot P-E or P-V loops. Nonetheless, the difference between D and P tends to be very small and the extraction of the remanent polarization (P_r) remains the same.[74]

There are several important parameters of a ferroelectric that can be extracted from hysteresis loops, as shown in Figure 3-2. The remanent polarization is the most frequently cited parameter because it serves as a figure of merit for ferroelectrics used in nonvolatile memory applications such as FRAM. The remanent polarization is the total amount of switched charge within the ferroelectric film which remains stable when the electric field is removed. The remanent polarization (P_r) from the hysteresis loop is determined by

$$P_r = \frac{\left|P_r^+\right| + \left|P_r^-\right|}{2} \tag{3-5}$$

where P_r^+ is the positive remanent polarization and P_r^- is the negative remanent polarization.

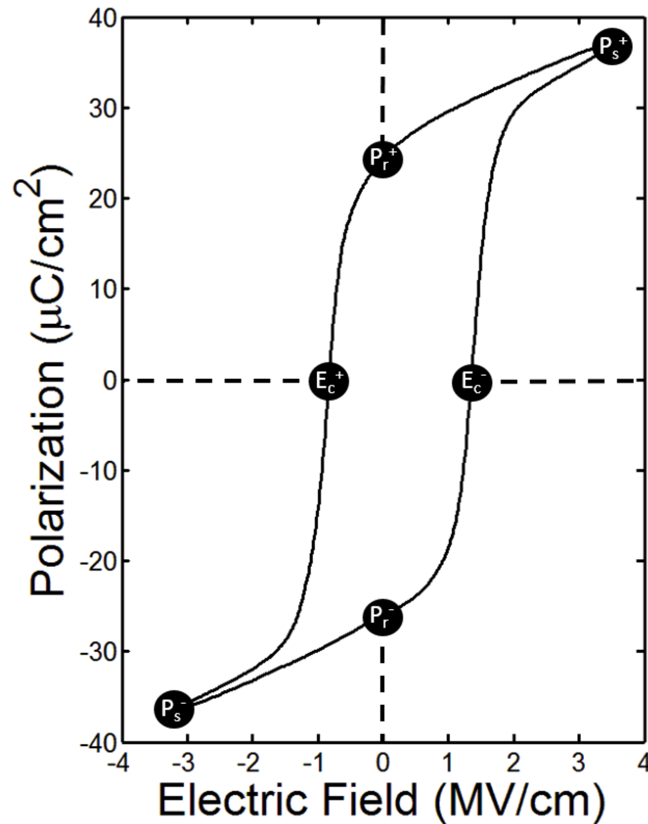

Figure 3-2. A hysteresis plot allows the extraction of several important ferroelectric parameters.

The coercive field, E_c, is another key characteristic of a ferroelectric because it is the electric field required to switch ferroelectric dipoles within the material. When P-V plots are being discussed, the term coercive field can be substituted by the coercive voltage (V_c) and is the voltage required to switch the ferroelectric. The coercive field is calculated by

$$E_c = \frac{V_c}{d} = \frac{|V_c^+| + |V_c^-|}{2d} = \frac{|E_c^+| + |E_c^-|}{2} \tag{3-6}$$

where d is the ferroelectric film thickness, V_c^+ is the positive coercive voltage, V_c^- is the negative coercive field, E_c^+ is the positive coercive field, and E_c^- is the negative coercive

field. The spontaneous polarization (P_s) is the total amount of switched charge at the maximum applied electric field and due to relaxation effects in polycrystalline ferroelectric thin films, is always larger than the remanent polarization.

Hysteresis plots can also be used to evaluate an antiferroelectric film's energy storage properties. Figure 3-3 illustrates the integrated (colored) regions which can be used to determine the energy storage density (*ESD*) and loss. The energy storage density for both positive and negative fields can be determined by the following equation

$$ESD = \frac{|ESD^+| + |ESD^-|}{2} = \frac{\left|\left(\int_0^{E_{MAX}} P_s^+ dE - (\lambda^+ - I_1)\right)\right| + \left|\left(\int_0^{E_{MIN}} P_s^- dE - (\lambda^- - I_2)\right)\right|}{2}$$

$$= \frac{\left|\left(\int_0^{E_{MAX}} P_s^+ dE - \int_{E_{MAX}}^{0} P(E)dE\right)\right| + \left|\left(\int_0^{E_{MIN}} P_s^- dE - \int_{E_{MIN}}^{0} P(E)dE\right)\right|}{2} \quad (3\text{-}7)$$

where ESD^+ is the positive energy storage density, ESD^- is the negative energy storage density, λ^+ is the loss in the positive portion of the loop, λ^- is the loss in the negative portion of the loop, E_{MAX} is the maximum applied electric field, E_{MIN} is the minimum applied electric field, I_1 and I_2 are integration regions, and $P(E)$ is the polarization as a function of the electric field. The loss (λ) can be determined by

$$\lambda = \frac{|\lambda^+| + |\lambda^-|}{2} = \frac{\left|\int_0^{E_{MAX}} P_{Top}^+(E)dE - \int_0^{E_{MAX}} P_{Bottom}^+(E)dE\right| + \left|\int_0^{E_{MIN}} P_{Bottom}^-(E)dE - \int_0^{E_{MIN}} P_{Bottom}^-(E)dE\right|}{2} \quad (3\text{-}8)$$

Where P^+_{Top} and P^-_{Top} is the top of the polarization curve on the positive and negative E-axis respectively and P^+_{Bottom} and P^-_{Bottom} is the bottom of the polarization curve on the

positive and negative E-axis respectively. The energy storage efficiency (*Eff*) of an antiferroelectric capacitor can be determined from Eq. 3-7 and Eq. 3-8,

$$Eff = \frac{ESD}{ESD + \lambda} \tag{3-9}$$

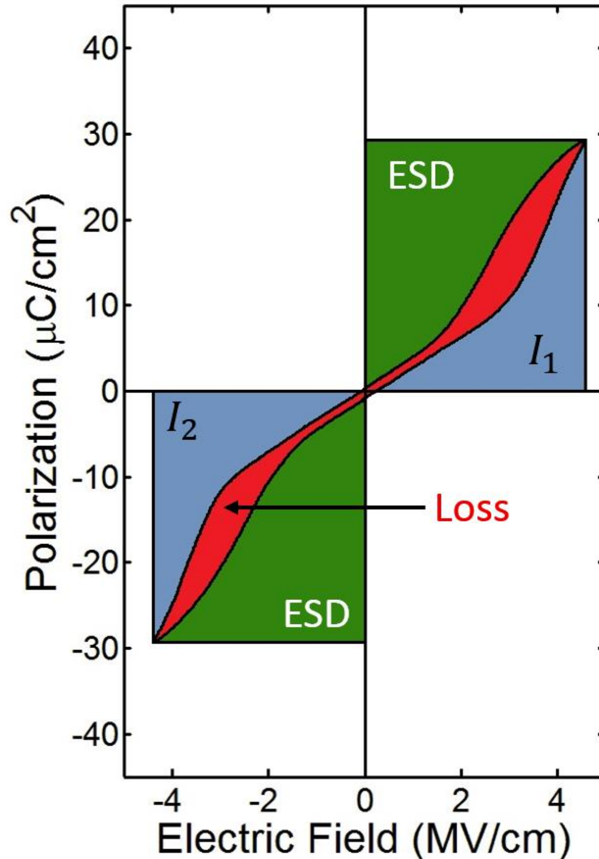

Figure 3-3. The energy storage density and loss of an antiferroelectric capacitor can be determined by integrating regions within the hysteresis plot.

3.2.2 Dynamic Hysteresis Currents

A variation of the Sawyer-Tower circuit can be made by replacing the sense capacitor with a series resistor which enables the dynamic hysteresis current measurement (Figure 3-4). The dynamic hysteresis current density (J_F) can be determined from the sense voltage across the resistor and calculated from

$$J_F = \frac{I_F}{A} = \frac{V_s}{R_s A} \tag{3-10}$$

where I_F is the measured hysteresis current and R_s is the sense resistor.

Distorted hysteresis loops which deviate from typical ferroelectric or antiferroelectric shapes can sometimes be observed, and in other cases, conventional P-V plots may obscure distortions in the shape of the hysteresis loop near the coercive voltage. Dynamic hysteresis currents give direct access to the switching currents that ferroelectric films produce when excited by a triangle wave.

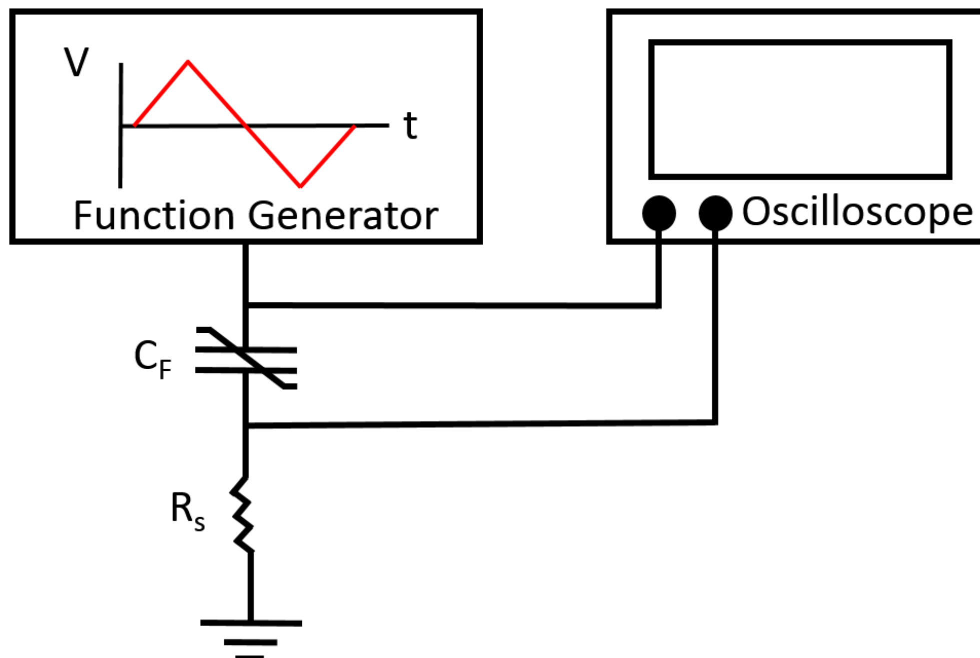

Figure 3-4. Modified Sawyer-Tower circuit for dynamic hysteresis current measurements.

While dynamic hysteresis currents generally produce a more qualitative understanding of the behavior of a ferroelectric than P-V plots since fewer quantitative parameters are extracted, it can corroborate aspects of conventional hysteresis loops and provide additional insights into the switching characteristics of a ferroelectric film. Moreover, the critical forward phase field (E_F) and the critical backward phase field (E_A) of an antiferroelectric film are easier to extract in a dynamic hysteresis current plot from the switching current peaks as shown in Figure 3-5 (right column). The critical forward

phase field is associated with an antiferroelectric to ferroelectric phase transition (AFE→FE) as an electric field is applied, while the critical backward phase field is associated with a ferroelectric to antiferroelectric (FE→AFE) when the electric field is removed.[75] Electric field cycling can also lead to changes in the P-V characteristics of a ferroelectric, and dynamic hysteresis current measurements can provide a more detailed view of the switching current properties as illustrated in Figure 3-5 (left column). The coercive field can also be extracted from the dynamic hysteresis current plot from the switching current peaks. A review on the insights dynamic hysteresis current measurements can provide was written by Schenk *et al.*[74]

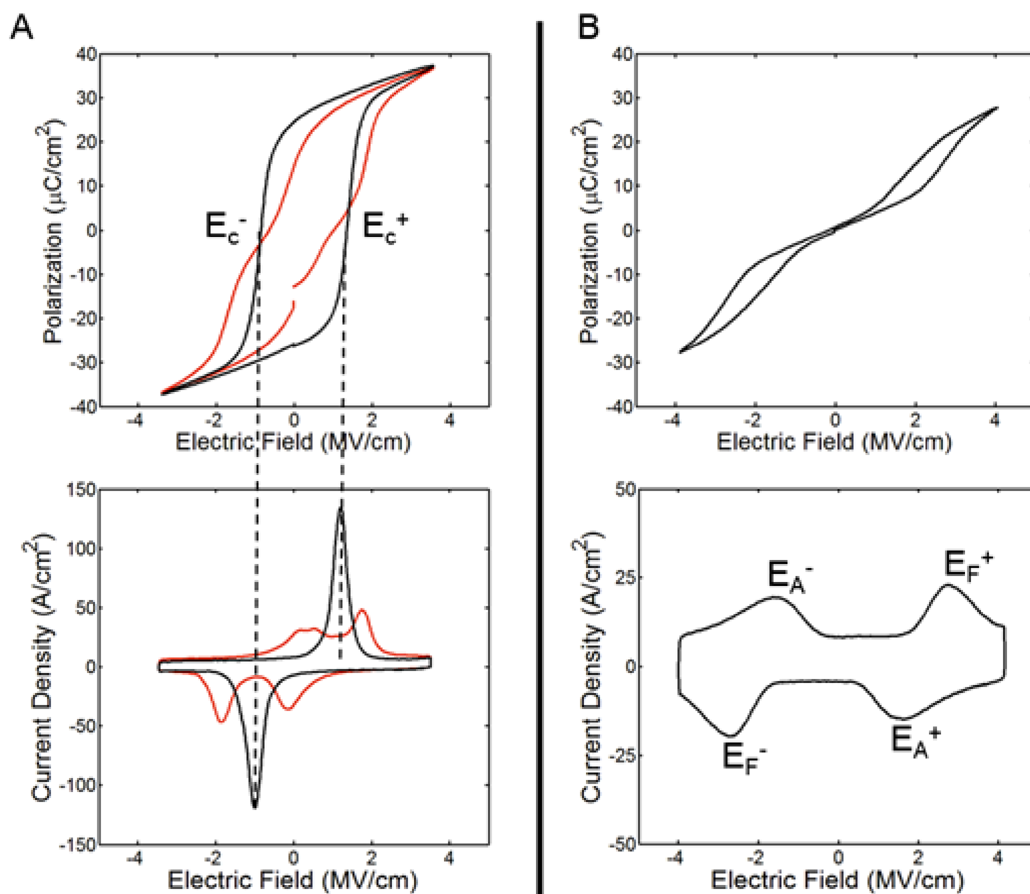

Figure 3-5. Dynamic hysteresis current measurements. A) Dynamic hysteresis loops can shed more light about the switching currents before (red) and after cycling (black). B) Four distinct switching peaks in four quadrants are a signature of an antiferroelectric film.

3.2.3 Positive-Up-Negative-Down (PUND)

Hysteresis plots have remained one of the most common methods to probe the ferroelectric characteristics of thin films. However, hysteresis measurements are carried out with a relatively low frequency, typically 1 kHz, and a triangle wave which does not accurately capture how the ferroelectric would behave in a memory circuit. To emulate how a ferroelectric would behave in a high speed FRAM memory circuit, the Positive-Up-Negative-Down (PUND) measurement was developed.[76] The name PUND is descriptive of the actual waveform that is sent to the ferroelectric thin film which consists of two positive voltage pulses followed by two negative voltage pulses. A virgin film is usually set with a negative voltage pulse before the PUND pulse train begins, as shown in Figure 3-6.

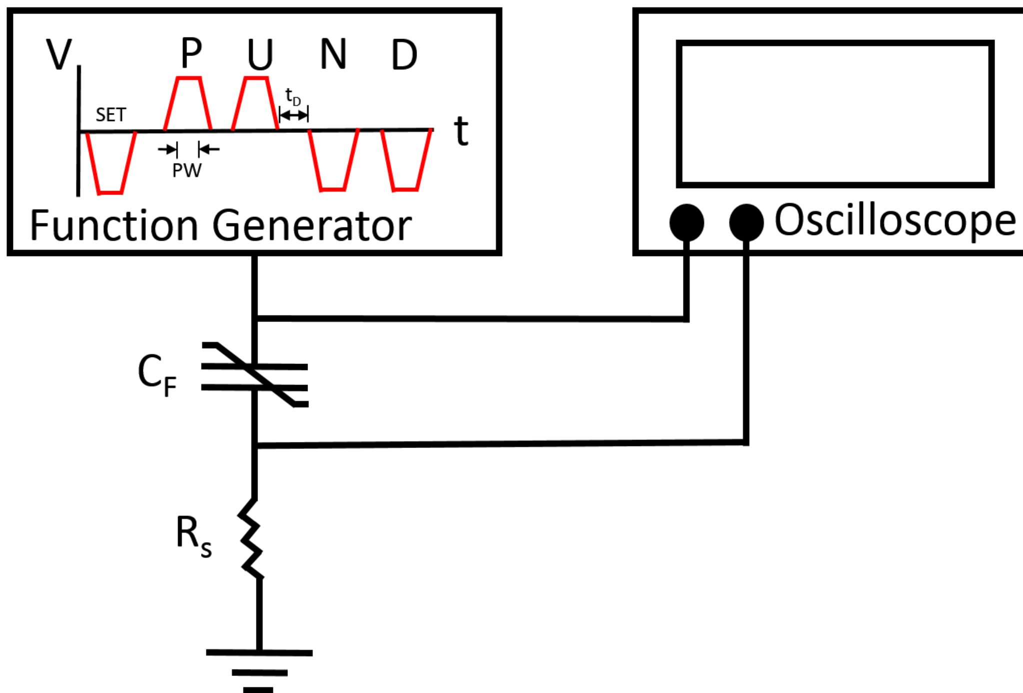

Figure 3-6. PUND waveform and measurement circuit.

The pulse width and the pulse delay time are very important aspects of the PUND waveform that can influence the measurement. Smaller pulse widths tend to

decrease the amount of switched charge in the ferroelectric and may accurately reproduce the switching properties in a higher frequency memory circuit. Since FRAM is a nonvolatile memory and data retention is expected to last for up to 10 years, relaxation effects in a ferroelectric must be accurately taken into account. For this reason, 1 s pulse delays should be used when taking PUND measurements because almost all of the polarization relaxation occurs within 1 s.[76] If shorter pulse delays are used, then the switched polarization charge will be overestimated compared to long data retention times because of the larger contribution of the transient polarization.

Each of the terms in the PUND waveform have important physical significance. The P term contains the total amount of positive switched charge, permanent and transient, and the dielectric response of the ferroelectric material. The U term contains the positive transient polarization and the dielectric response. The P and U terms are measured by integrating the current density in Eq. 3-10

$$P = \int J_P dt \tag{3-11}$$

$$U = \int J_U dt \tag{3-12}$$

where J_P is the measured current density from the P pulse and J_U is the measured current density from the U pulse. The N term contains the total amount of negative switched charge, permanent and transient, and the dielectric response of the ferroelectric material. The D term contains the negative transient polarization and the dielectric response. The N and D terms can be calculated by

$$N = \int J_N dt \tag{3-13}$$

$$D = \int J_D dt \tag{3-14}$$

where J_N is the measured current density from the N pulse and J_D is the measured current density from the D pulse. The total amount of switched ferroelectric polarization charge that can be used in memory circuit can be calculated as

$$P_{SW}^{+} = P - U \tag{3-15}$$

$$P_{SW}^{-} = N - D \tag{3-16}$$

$$P_{SW} = \frac{P_{SW}^{+} + P_{SW}^{-}}{2} \tag{3-17}$$

where P_{SW^+} is the positive switched polarization and P_{SW^-} is the negative switched polarization. Figure 3-7 shows an example of the PUND waveform applied to a ferroelectric Si-doped HfO_2 thin films.

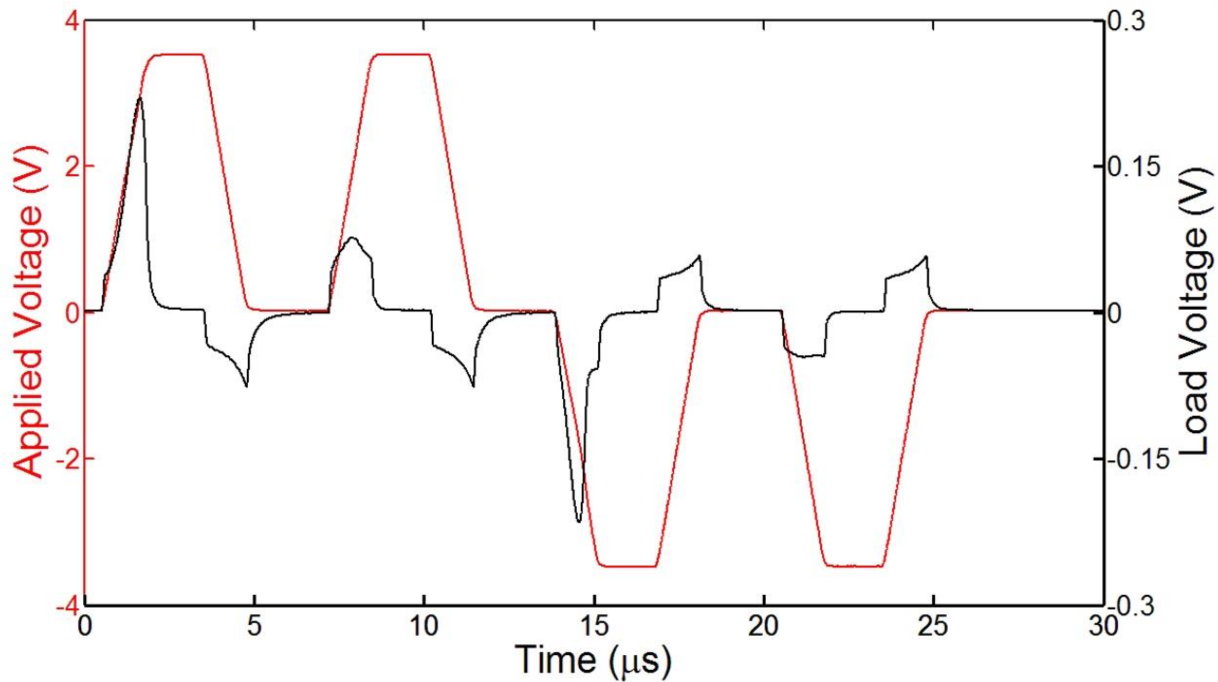

Figure 3-7. The PUND waveform is applied to a ferroelectric thin film. The switching current is extracted from the load voltage for each of the pulses and integrated to measure the amount of switched charge.

3.2.4 Capacitance-Voltage (CV)

Ferroelectric materials exhibit nonlinear capacitance-voltage characteristics due to dipole or domain switching. When the thickness of the ferroelectric material is known, it is common to extract the relative permittivity (Eq. 1-9) to generate ε_r as a function of voltage. The relative permittivity can give indirect evidence about the electrical quality of the ferroelectric while yielding potential insights about the crystal structure or growth of interfacial layers within the films.[77] Thus, the extraction of ε_r can aid in better understanding the physical properties of the ferroelectric whereas the capacitance may be more pertinent for specific electrical applications.

The CV characteristics of a ferroelectric are measured by applying a sweeping DC voltage with a small AC signal superimposed. The AC signal must be small enough to ensure linearity for an accurate impedance measurement while also providing a strong enough signal. AC signals between 15 mV – 75 mV are sufficient to ensure linearity and signal strength in solid state ferroelectric capacitors. The AC signal frequency can be chosen based upon the application of interest, but generally 1 kHz to 100 kHz is acceptable unless the radio frequency (RF) behavior is being investigated. The DC voltage may be swept in either a clockwise or anticlockwise direction and always terminates at the voltage polarity from whence it commenced.

The distinctive butterfly loop of a ferroelectric material is demonstrated in Figure 3-8. The two switching peaks in the relative permittivity are associated with the switching of domains within the ferroelectric film. The peaks occur near the coercive voltage of a ferroelectric and can provide corroborating evidence of the switching behavior within the thin film. The relative permittivity maxima occurs near the coercive field because when the sweeping DC voltage approaches near the coercive field, only a

small AC voltage is required to switch ferroelectric domains.[78] The double butterfly loop of an antiferroelectric is also shown in Figure 3-8. Like the dynamic hysteresis current measurements, CV sweeps can permit an easy extraction of the critical forward and backward phase fields.

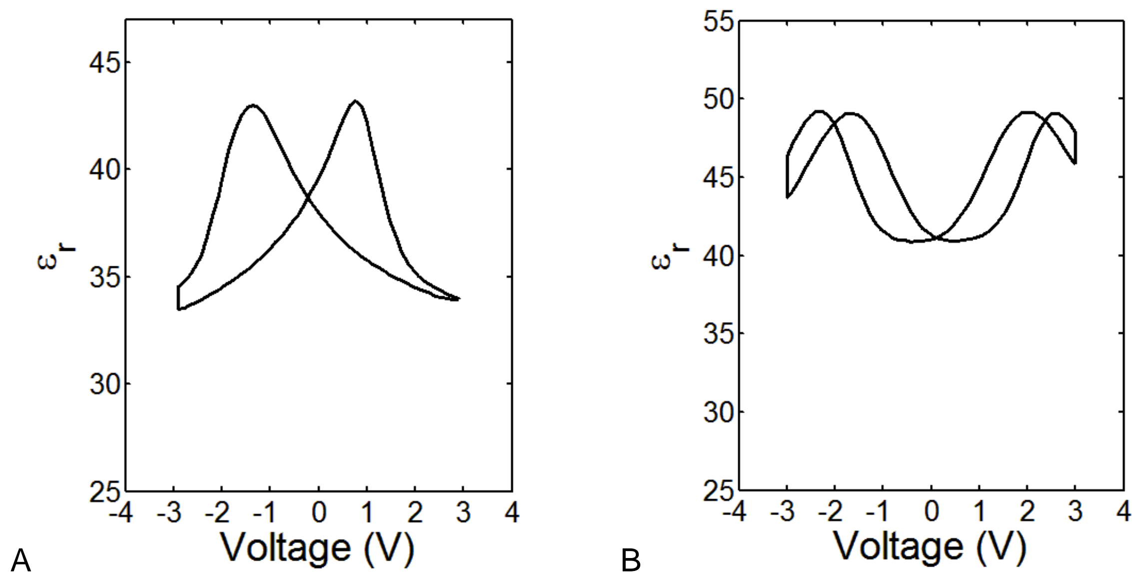

Figure 3-8. C-V characteristics of ferroelectric thin films. A) The classic butterfly curve is characteristic of ferroelectric materials. B) The double butterfly loop is a signature of an antiferroelectric.

The electrodes can play a significant role in the CV behavior of a ferroelectric thin film due to the generation of space charge regions within the ferroelectric at the electrode interfaces.[78,79] An asymmetry in the space charge regions at the two opposing electrode interfaces can create a depolarization field.[78] The switching characteristics present in a CV plot may be modeled by the method developed by Brennan.[78] Brennan's model is largely empirical and enables the extraction of the metal Schottky barrier heights and ionized charge concentrations at the interface, this information can be useful in estimating defect concentrations in ferroelectric thin films.[77]

3.2.5 Endurance Cycling

Nonvolatile memory elements are typically expected to store data up to 10 years in commercial products under certain operating conditions. However, most nonvolatile memory devices lose their ability to store data when they have been cycled beyond a certain point. As an example, NAND FLASH memory has a cycling endurance between 10,000 – 100,000 cycles before it loses its ability to store data.[80] Cycling refers to the exposure of a memory device to a number of write cycles. Device characteristics may be interrogated after cycling to evaluate the device's reliability as a memory element.

Endurance cycling measures how a memory element performs with increasing number of write cycles until device failure occurs. PZT-based FRAM capacitors have an impressive cycling endurance of > 10^{12} cycles.[52] A high cycling endurance is a requirement for FRAM applications because of the destructive read operation. Moreover, excellent cycling endurance is valuable for all types of nonvolatile memories and is an extremely important reliability metric. Cycling endurance tests are needed to evaluate the potential of new materials for nonvolatile memories and may highlight where improvements need to be made for viable technologies.

Ferroelectric capacitors can be cycled with a series resistor as shown in the circuit in Figure 3-9. Bipolar cycles should always be used when evaluating a ferroelectric for nonvolatile memory applications because it most closely resembles memory circuit operation. A basic procedure for evaluating the cycling characteristics of a ferroelectric capacitor consists of exposing the capacitor to a set number of bipolar square waves and then implementing measurements of interest such as hysteresis, PUND, or CV for example. It should be noted that when low-frequency measurements are being alternated with endurance cycling, such as the slow sweeping DC voltage of a

CV scan or a leakage current measurement, the ferroelectric's behavior may be influenced by the relatively long exposure time to an appreciable voltage. In this case, a new capacitor should be used for every cycling measurement.

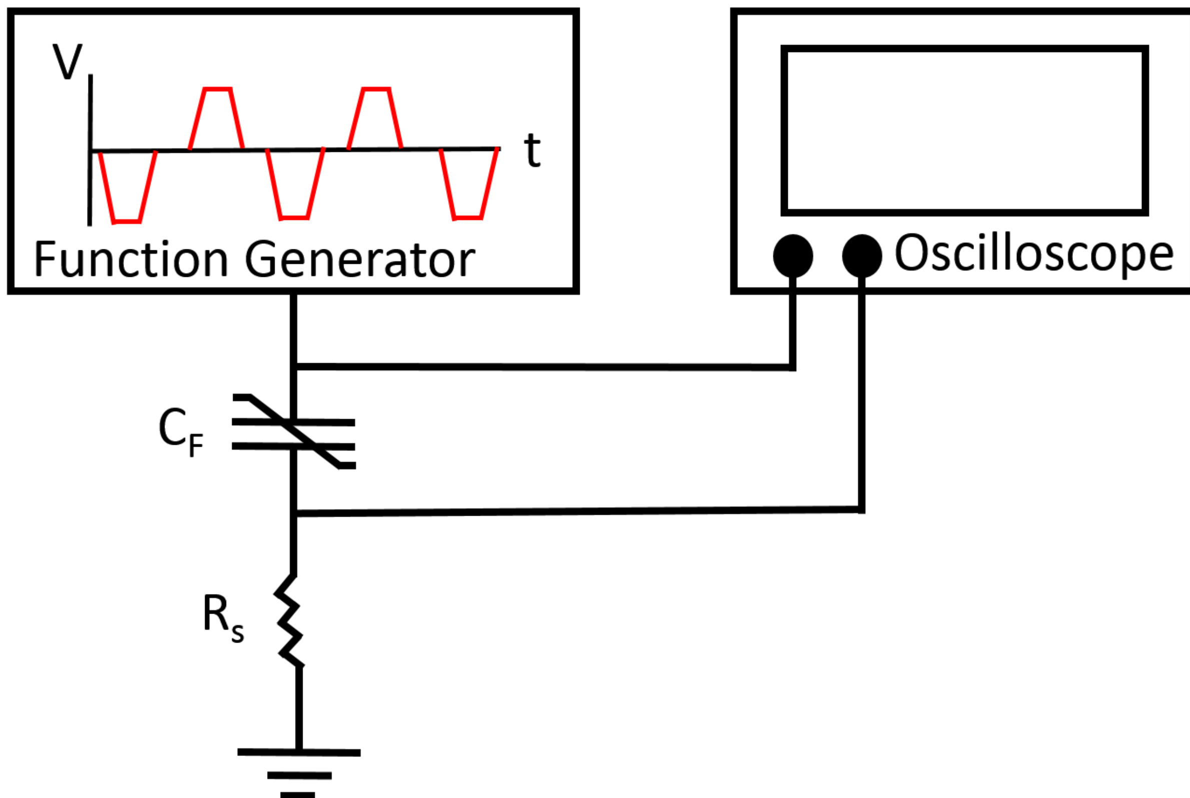

Figure 3-9. Bipolar square waves are used to cycle ferroelectric capacitors.

The behavior of a ferroelectric can be impacted by cycling in a variety of ways. A virgin ferroelectric capacitor may show signs of imprint whereby the hysteresis loop is shifted along the electric field axis due to a built-in electric field. Cycling may reduce the asymmetry in the hysteresis loop and improve the switching characteristics. Improvements in the switching properties of a ferroelectric with cycling is called wake-up.[8,52,81] Changes in the symmetry of a ferroelectric capacitor with the wake-up effect is generally ascribed to defect redistribution or charge trapping at the interfacial space charge layer.[77,81,82] Figure 3-10 illustrates how wake-up cycling can improve the

remanent polarization while making the hysteresis loop more vertical, thus bringing the ferroelectric thin film switching characteristics closer to the ideal square hysteresis behavior found in single crystals. Chapter 6 studies the effect of cycling on imprint in detail.

Cycling tends to improve the ferroelectric characteristics of thin films initially through the wake-up effect, but extensive cycling often leads to reliability concerns. The chief reliability concern for conventional ferroelectric capacitors with cycling is fatigue. Fatigue is the gradual reduction of the remanent polarization with cycling.[1] Because the amount of switched charge of a ferroelectric capacitor is the basis for data storage in nonvolatile memories such as FRAM, a reduction in the switching polarization can lead to memory failure.

While the underlying causes for fatigue have not been conclusively proven, it is understood that fatigue is the result of domain wall pinning which inhibits polarization reversal.[1] The origins of fatigue are believed to stem from either oxygen vacancy migration[1,83–86] or charge injection.[87] Scott *et al.*[1] have propounded the oxygen vacancy theory as the origin of fatigue based on a variety of experimental evidence including the absence of fatigue in PZT when using metal oxide electrodes such as IrO_2. Tagantsev *et al.*[87] have strongly advocated the charge injection model by asserting that faster charge relaxation occurs in the metal oxide electrodes and points out that the use of such electrodes is associated with a large increase in conduction. The works of both authors in the literature represent the two schools of thought on fatigue in conventional perovskite ferroelectrics. Wake-up and fatigue also seem to be related, although no

clear link between the two has been established to date.[88] Figure 3-10 illustrates fatigue in Al and Si co-doped ferroelectric HfO_2 thin films.

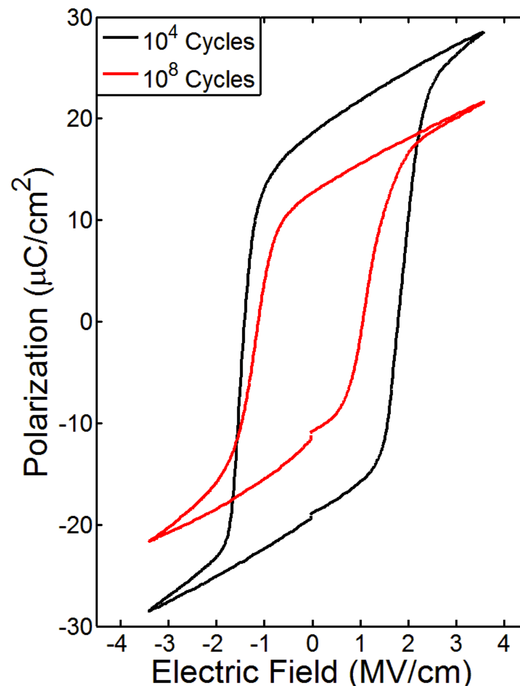

Figure 3-10. Fatigue occurs in these ferroelectric Al/Si-doped HfO_2 thin films from 10^4 to 10^8 cycles.

In addition to fatigue, cycling may also cause ferroelectric capacitors to undergo a hard breakdown event. Breakdown is rarely seen in ferroelectric perovskite capacitors because of the relatively low coercive fields that these materials exhibit. However, HfO_2-based ferroelectrics are vulnerable to breakdown events because of the large ~ 1 MV/cm coercive fields they exhibit and the typical 3 – 3.5 MV/cm applied fields necessary to achieve saturation.[89,90] Higher anneal temperatures lead to earlier breakdown with cycling for ferroelectric HfO_2 thin films, possibly due to the increased number of defects such as oxygen vacancies within the thin films.[89] While breakdown can be delayed by applying lower electric fields, this comes at the cost of a lower initial P_r and accelerated fatigue.[89,91] Depending on the annealing conditions and applied electric field, HfO_2-based capacitors typically breakdown between 10^4 – 10^9

cycles.[77,89,91,92] Although breakdown for ferroelectric HfO_2 has been reported beyond 10^9 cycles in some cases,[50,55,93] the electric field is reduced to an extent that leads to unsaturated hysteresis loops and significantly lower remanent polarizations. Intensive study and further development of ferroelectric HfO_2 thin films are required to improve the breakdown and fatigue behavior for nonvolatile memory applications.

3.2.6 Retention Tests

The ability of a ferroelectric to hold its polarization state allows it to behave as a memory element. Since electronic data must be stored up to 10 years under specific operating conditions, the stability of a ferroelectric’s polarization states are usually evaluated with respect to time and temperature. The two primary data retention reliability concerns are thermal depolarization and imprint.[52] Rapid polarization relaxation (i.e. transient polarization) also occurs at room temperature after switching due to initial back-switching of domains from the depolarization field, but appreciable polarization decay does not occur after 1 second.[52,76] Thermal depolarization is a reduction in the remanent polarization as the temperature is increased toward the phase transition temperature or Curie temperature of the ferroelectric material.[52] Thermal depolarization may be attributable to temperature dependent phase transitions, defect charge migration, and back-switching of domains in the presence of a depolarization field.[1,52,94,95] Imprint occurs when one polarization state is energetically preferable to the opposite polarization state and an internal electric field is established. When a ferroelectric is switched into a polarization state and exposed to high temperatures, imprint readily occurs.[52,89] The accumulation of charged defects at the electrode/ferroelectric interface and charge injection are possible causes for imprint.[52,96]

Retention tests are executed by using electrical pulses in the same electrical circuit as Figure 3-6. Each pulse can be accurately described by the use of the PUND acronyms and the relevant physics for each PUND term is the same as discussed in section 3.2.3. Four capacitors are needed to evaluate the positive and negative retention states. As shown in Figure 3-11, capacitors being compared are baked in opposite polarization states and then have their respective PUND terms interrogated to determine the data retention characteristics. Retention test protocols are well established for FRAM capacitors.[52,89]

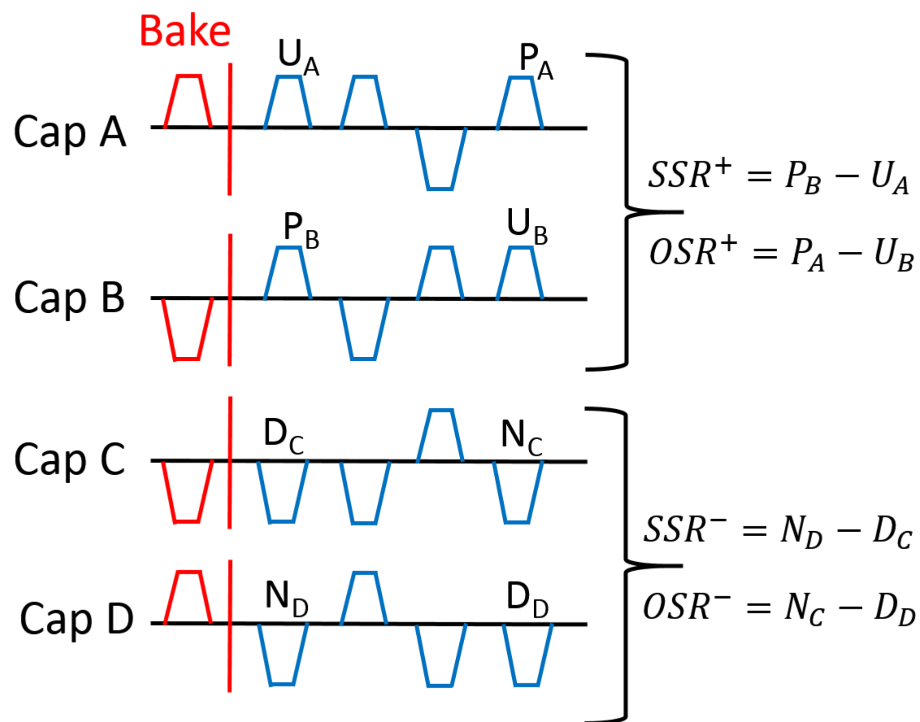

Figure 3-11. Retention tests are performed by baking ferroelectric capacitors in a polarization state and delivering pulse trains to measure data retention.

To evaluate the positive same state retention (SSR^+) and opposite state retention (OSR^+), one capacitor must be baked in a positive (P) state and another capacitor must be baked in a negative (N) state. To interpret the meaning of the retention tests, it is useful to understand each of the pulse terms in Figure 3-11. The U_A pulse consists of

the polarization loss that occurred during the P-state bake as well as the dielectric contribution. The P_B term represents the amount of polarization switching that occurs from an N→P transition after an N-state bake. Thus, the SSR^+ evaluates the resiliency of the P-state to thermal depolarization effects and imprint. The P_A pulse measures the switching polarization of an N→P transition after a P-bake and a read/write/restore sequence. The U_B term measures the transient polarization (or polarization loss) of the P state as well as the dielectric response after an N-bake and a read/write/restore pulse train. Since P_A and U_B terms are measured after a bake *and* a read/write/restore sequence of pulses at room temperature, the OSR^+ is primarily a measure of the imprint of the positive state. Simply translating the P and U terms as described above to N and D terms allows parallel arguments to be made for the negative same state retention (SSR^-) and opposite state retention (OSR^-) margins. Because data retention is the primary goal of any nonvolatile memory, an evaluation of imprint and thermal depolarization is critical to the assessment of ferroelectric materials for microelectronic memory technologies.

3.2.7 Impedance Spectroscopy

Impedance spectroscopy is a powerful technique that can be used to study the impedance characteristics of a material. The conduction properties and dielectric characteristics of materials as a function of frequency are readily probed using this technique. As will be shown, capacitance-voltage measurements discussed in section 3.1.4 are extracted using impedance spectroscopy. Impedance spectroscopy interrogates a device under test by applying a small AC waveform and measuring the current response.

The measured electrical impedance (Z) of a material is[97]

$$Z(\varpi) = \frac{V(\varpi)}{I(\varpi)} = Z_R + jZ_I = |Z|e^{j\theta} \tag{3-18}$$

where ω is the angular frequency in radians, Z_R is the real part of the impedance, Z_I is the imaginary part of the impedance, $|Z|$ is the magnitude of the impedance, V is the applied voltage, I is the measured current, and θ is the phase. The electrical impedance in its simplest forms can readily be understood by its association with common circuit elements and determined by the phase. When the phase is zero, the impedance is strictly a real number and a resistor is the result,

$$Z = |Z|e^{j0} = Z_R = R \tag{3-19}$$

where R is the resistance. Note that a purely resistive element does not have any frequency dependence.[97] When the phase is -90 °, the impedance is an imaginary number and a capacitor is the result,

$$Z(\varpi) = |Z|e^{-j\pi/2} = -jZ_I = \frac{1}{j\varpi C} \tag{3-20}$$

where C is the capacitance. An inductor has a 90 ° phase and the impedance relationship is

$$Z(\varpi) = |Z|e^{j\pi/2} = jZ_I = j\varpi L \tag{3-21}$$

where L is the inductance. When capacitors are measured experimentally, electrical losses cause the phase to be greater than -90 ° and the real component of the impedance is nonzero. In this case, it can be helpful to translate the real and imaginary impedance to the real and imaginary admittance variables through the following relationships,

$$Y_R(\varpi) = \frac{Z_R}{Z_R^2 + Z_I^2} \tag{3-22}$$

$$Y_{IM}(\varpi) = -\frac{Z_{IM}}{Z_R^2 + Z_I^2} \tag{3-23}$$

$$Y(\varpi) = Y_R + jY_I \tag{3-24}$$

where Y is the admittance, Y_R is the real admittance and Y_{IM} is the imaginary admittance. The capacitance can easily be extracted from Eq. 3-24,

$$C = \frac{Y}{2\pi f} = \frac{Y_R}{2\pi f} + j\frac{Y_I}{2\pi f} = C_R + jC_I \tag{3-25}$$

where C_R is the real capacitance and C_I is the imaginary capacitance. The real capacitance is the most familiar term seen in circuit analysis and signifies the electrical energy that is stored in the capacitor. The imaginary capacitance is associated with the electrical losses in the capacitor. The permittivity can now be extracted from Eq. 3-25,

$$\varepsilon = \frac{Cd}{A\varepsilon_0} = \frac{C_R d}{A\varepsilon_0} + j\frac{C_I d}{A\varepsilon_0} = \varepsilon_R + j\varepsilon_I \tag{3-26}$$

where ε_R is the real permittivity and ε_I is the imaginary permittivity. The real permittivity is the relative permittivity of the material whereas the imaginary permittivity is the dielectric loss. By using a single frequency AC signal and a sweeping DC voltage, the real portions of Eq. 3-25 and Eq. 3-26 are used to generate the familiar CV and $\varepsilon_r(V)$ plots for ferroelectrics. Finally, the loss tangent is simply the ratio of the real and imaginary permittivity from Eq. 3-26,

$$\tan\delta = \frac{\varepsilon_I}{\varepsilon_R}. \tag{3-27}$$

The loss tangent is an important metric that can be used to evaluate if the electrical losses of a capacitor are suitable for certain applications.

Impedance spectroscopy has been used on ferroelectrics to understand a variety of phenomena including fatigue,[98] dead layers,[99] defects,[100] and conduction characteristics.[101] Circuit models based on the impedance can also be applied to ferroelectric capacitors to elucidate additional physics and extraction of parameters for inline reliability measurements.[102] A circuit model employing a constant phase element (CPE), a resistor, and an inductor in series has been shown to accurately reproduce the frequency response of PZT ferroelectric capacitors.[102] A CPE can be described by[102]

$$Y_{CPE} = A_0\left(j\varpi\right)^n \tag{3-28}$$

where Y_{CPE} is the admittance of the constant phase element, A_0 is a constant, and n is the exponential constant. Like the name suggests, the constant phase element exhibits a phase that does not vary with frequency. An ideal capacitor can be represented as a CPE when n is 1. As n decreases from 1, the capacitor becomes increasingly lossy. The extraction of A_0 and n can be used to determine the static capacitance and the device reproducibility respectively.[102] Impedance spectroscopy is a powerful tool and future work on new ferroelectric materials will benefit from the further development of the physical interpretations of the technique.

3.3 Materials Characterization Techniques

3.3.1 X-ray Photoelectron Spectroscopy (XPS)

X-ray photoelectron spectroscopy (XPS) is a technique whereby high energy photons impinge upon a material and eject core electrons from the material's

constituent atoms.[103] The kinetic energy of the ejected core electrons is then sensed at a detector and the binding energy (*BE*) is calculated from[103]

$$BE = h\nu - KE \quad (3\text{-}29)$$

where *h* is the Planck constant (6.63 x 10^{-34} J*s), *v* is the photon frequency, and *KE* is the kinetic energy of the ejected electron. Every element in the periodic table has a unique set of binding energies for the core electrons which allows XPS to be used to quantitavely determine the composition of a material within 0.1 atomic % under the best case scenarios.[103] The binding energy of an atom can shift depending on how it is bonded with neighboring atoms. Thus, the chemical bonding information of a material can be investigated with XPS. Figure 3-12 illustrates the chemical bonding information that can be obtained about the surface of ALD grown TiN by analyzing the Ti 2p binding energy spectra.

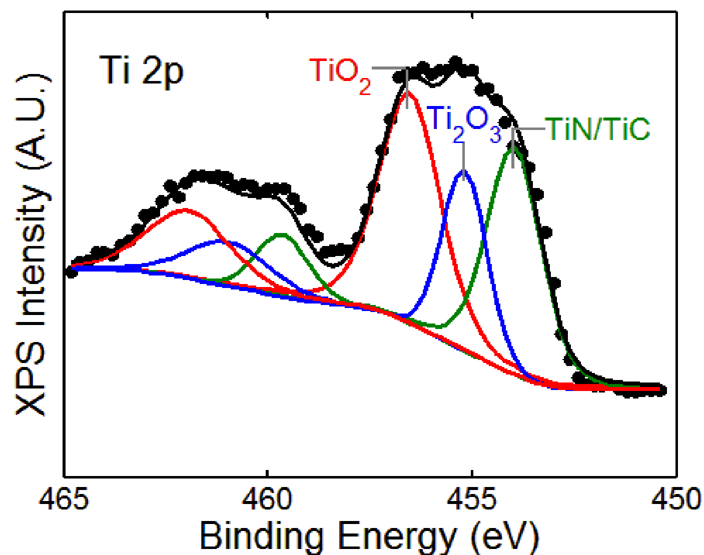

Figure 3-12. The Ti 2p binding energy spectra show that Ti is chemically bonded in the forms of TiO_2, Ti_2O_3, TiN, and TiC on the surface of an ALD TiN film.

XPS is a very surface sensitive technique due to the limited escape depth of ejected electrons. While surface sensitivity is often beneficial, in some cases it is useful to measure the composition as a function of sample depth. For instance, while the surface of a metal may be oxidized due to exposure to air, the bulk composition may contain much less oxygen. This is true for the case shown in Figure 3-13 where the bulk of the ALD grown TiN film contains much less oxygen than the surface. XPS instruments are usually designed with sputtering capability to achieve depth profile measurements. As will be shown in Chapter 6, XPS can help elucidate the chemical behavior of electrode interfaces and their influence on the ferroelectric characteristics of HfO_2 thin films.

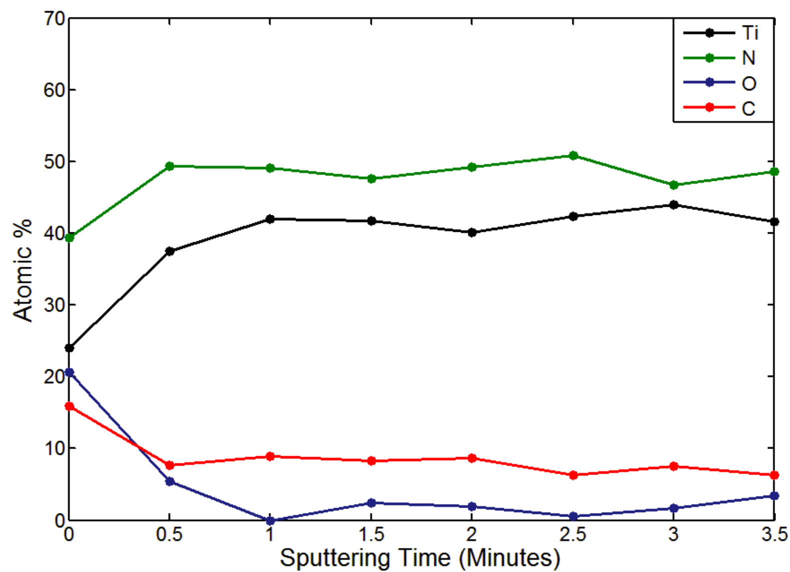

Figure 3-13. Depth profile obtained with XPS of ALD grown TiN electrodes.

3.3.2 Time-of-Flight Secondary Ion Mass Spectrometry (TOF-SIMS)

Secondary ion mass spectrometry (SIMS) techniques have the ability to detect elements down to 10^{12}-10^{16} /cm^3 and are frequently used to measure the depth profiles of dopants.[103] The elemental detection capabilities of SIMS is much higher than XPS

which allows better depth profiles to be made of trace impurities that are less than 0.1 atomic % of the sample. The best achievable depth resolution of dynamic SIMS is from about 2 nm and is determined by the mass, energy, and incident angle of the primary ion beam.[103]

The basic principles of how SIMS operates are easy to understand. Primary ions are accelerated into a beam directed onto a sample surface. When the primary ions reach the surface of the sample, a series of collisions occur whereby some of the atoms on the surface of the sample become ionized and are ejected. The ions which are ejected from the surface of the sample are called secondary ions. The secondary ions are then measured in a mass spectrometer. By continuously ejecting secondary ions from the sample and measuring them in a mass spectrometer, a depth profile of the sample is obtained as a result of the sputtering process. A time-of-flight (TOF) mass spectrometer operates by using short pulses of the primary ion beam which generates secondary ions. The pulsed secondary ions are then accelerated through a tube where the precise time they reach the detector is used to determine the mass.[103]

TOF-SIMS is a versatile technique because it can measure a broad mass range and has a high mass resolution. TOF-SIMS can be used qualitatively to understand changes in impurity profiles after certain processes without any sample calibrations. However, in order to provide a quantitative analysis of the elements in a SIMS depth profile, a representative sample must be made with a known impurity concentration and depth distribution.[103] Calibration samples can be made through the ion implantation of the desired impurities which need to be quantified in the host material. An example TOF-SIMS profile using this method is shown in Figure 3-14. In this plot the Si

concentration has been quantified using a calibration sample while the other elements are plotted as a relative value of their secondary ion count yield. Three monolayers of SiO_2 were deposited within the HfO_2 thin film which is shown in the TOF-SIMS profile as three Gaussian shaped bumps due to the spatial resolution of the instrument.

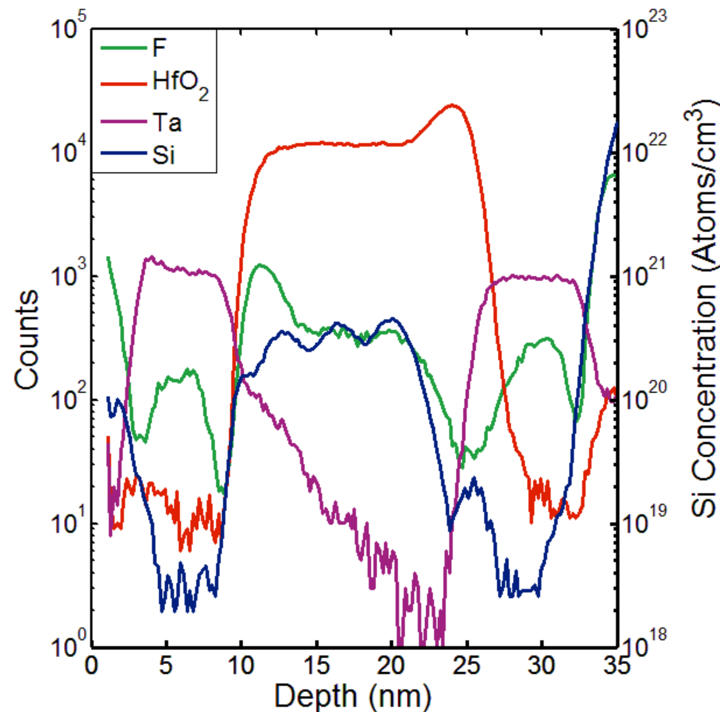

Figure 3-14. TOF-SIMS profile of a TaN/Si-doped HfO_2/TaN capacitor where the Si concentration has been quantified and relative count yields for the other elements are given.

3.3.3 Grazing Incidence X-ray Diffraction (GI-XRD)

X-ray diffraction (XRD) is a technique that can be used to determine the crystal structure of a material. Incident x-rays interfere with one another when they have traveled through the atomic planes of a crystalline material.[103] Grazing incidence x-ray diffraction (GI-XRD) is appropriate when determining the crystal structure of a polycrystalline thin film. GI-XRD utilizes a smaller incident angle than powder diffraction XRD to maximize the amount of interaction volume and provide a stronger diffraction signal from the x-rays. GI-XRD is very useful for studying the crystalline structure of

ferroelectric materials and can give insights about how the crystal structure changes under a variety of conditions.

3.3.4 Transmission Electron Microscopy (TEM)

To obtain high resolution images of nanoscale structures, optical microscopes cannot be used due to the large wavelength of the visible light spectrum. Instead, electron microscopes can be used where the wavelength can be adjusted by increasing or decreasing the energy of the incident electrons. Transmission electron microscopy (TEM) is particularly suited for taking high resolution cross-sectional images of nanometer scale capacitors and device structures. In TEM, a thin sample usually less than 200 nm thick is bombarded with electrons and the scattered and un-scattered electrons are then detected to create an image.[103] High resolution TEM images can be used to confirm the crystallinity of thin films, to measure nanometer-scale film thicknesses, and to determine the growth of interfacial layers which can help in characterizing ferroelectric capacitors as shown in Figure 3-15.

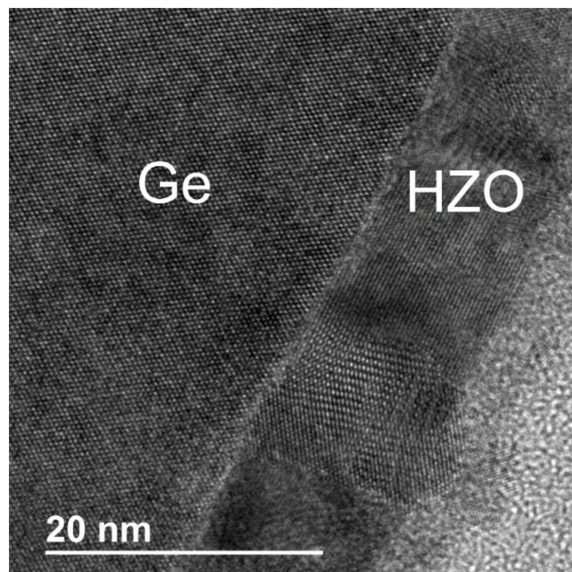

Figure 3-15. TEM is used to confirm the thickness and crystallinity of $Hf_{0.5}Zr_{0.5}O_2$ after ALD growth at 400 °C.

CHAPTER 4

FERROELECTRIC PHENOMENA IN Si-DOPED HfO_2 THIN FILMS WITH TiN AND Ir ELECTRODES

4.1 Background

Ferroelectric random access memory (FRAM) is one of the most promising embedded alternative memory technologies due to its high speed, low power, and nonvolatility.[104] The ability of doped hafnium oxide to serve as a ferroelectric opens up new potential for the next generation of FRAM devices.[105] Commonly used perovskite ferroelectrics such as lead zirconate titanate (PZT) suffer from an increase in coercive fields as thickness is scaled down.[56] Ferroelectric HfO_2 can exhibit a significant remanent polarization at thicknesses on the order of 10 nm, making it a potential candidate to replace PZT as the semiconductor industry's preferred FRAM material.[90] Ferroelectric thin film $Hf_{0.5}Zr_{0.5}O_2$ has also been shown to be more resistant to hydrogen degradation from forming gas anneals compared to PZT.[59] However, improvements in ferroelectric HfO2's coercive field and its reliability properties still need to be demonstrated before it can replace PZT.

Under normal bulk conditions, crystalline HfO_2 is monoclinic. However, high temperatures and pressures lead to bulk phase transformations from the monoclinic to the tetragonal (m → t) phase (1600 °C) and then from the tetragonal to the cubic (t → c) phase (2600 °C).[12] Böscke[36] and Müller[35] have shown that surface energy and decreasing film thickness effects lower the phase transformation temperatures of HfO_2 thin films when compared to bulk HfO_2. Incorporating dopants such as Si,[20] Al,[45] Y,[44]

Reprinted with permission from P.D. Lomenzo, P. Zhao, Q. Takmeel, S. Moghaddam, T. Nishida, M. Nelson, C.M. Fancher, E.D. Grimley, X. Sang, J.M. LeBeau, and J.L. Jones, J. Vac. Sci. Technol. B Microelectron. Nanom. Struct. 32, 03D123 (2014). DOI: 10.1116/1.4873323. Copyright 2014, American Institute of Physics.

and Gd[106] into thin film HfO_2 leads to a reduction in the monoclinic phase and aids in the tetragonal to orthorhombic (t → o) phase transformation that is thought to be responsible for the observed ferroelectricity in HfO_2 thin films.

A polar orthorhombic phase (space group $Pbc2_1$) has been observed in Mg-doped ZrO_2,[24] which shares many structural and chemical similarities with HfO_2.[12] Internal thermal mismatch stresses from competing neighboring crystal phases in partially stabilized zirconia (PSZ) are hypothesized to assist the tetragonal to orthorhombic phase transformation when cooling to cryogenic temperatures.[24] Work by Kisi also demonstrated that the competing phase transformations in Mg-PSZ, t→m and t→o, are influenced by hydrostatic pressure.[24] The orthorhombic phase transformation in HfO_2 benefits from the incorporation of Si into the crystal lattice since subsequent crystallization leads to the formation of the tetragonal phase.[17] In addition to phase changes caused by the incorporation of dopants, a TiN capping layer during the crystallization anneal of HfO_2 has been demonstrated to lower the fraction of the monoclinic phase while preventing void formation.[37] Rapid thermal annealing (RTA) of HfO_2 thin films, when used in conjunction with dopants and a confining electrode, will likely result in both internal thermal mismatch stresses from competing phase transformations, as seen in zirconia,[24] and external stresses arising from differences in the thermal expansion coefficients of the electrode materials, substrate, and the HfO_2 thin film.

The role of the TiN capping layer is thought to impede the volume expansion of the t→m phase transformation during high temperature crystallization.[37] The inhibition of the t→m phase transformation is desirable since a higher probability of the t→o phase

transformation will ensue. Previous work[20] has demonstrated that a predominantly tetragonal HfO_2 film with high SiO_2 doping concentrations (>5 mol. %) will exhibit antiferroelectric-like characteristics. However, HfO_2 thin films with SiO_2 doping concentrations that do not fully stabilize the tetragonal phase will stimulate the t→o phase transformation in mechanically constrained films through the suppression of the t→m phase transformation.

Research on PZT has underscored the importance of electrode materials on the performance and reliability properties of ferroelectric devices. Extensive work on PZT with Pt,[85,107,108] Ir,[85,109] IrO_x,[85,109] and $LaNiO_3$[108] electrodes has shown that the remanent polarization, coercive fields, and fatigue properties can be dramatically affected by the choice of electrode materials. The influence of the electrode capping material on the ferroelectric properties of HfO_2 and the resulting stresses from high temperature anneals remains unclear. However, if stresses generated from the thermal expansion mismatches of the electrode materials influence the ferroelectric properties of HfO_2, differences in the thermal expansion coefficients should be able to predict changes in the ferroelectric behavior. TiN[110] ($\alpha_{TiN} = 9.35 \times 10^{-6}$/K) and Ir[111] ($\alpha_{Ir} = 6.4 \times 10^{-6}$/K) top electrodes with similar thicknesses may influence the ferroelectric behavior of HfO_2 thin films if film stresses generated during high temperature annealing affects HfO_2's phase transformations. HfO_2 capacitors with TiN and Ir electrodes are fabricated and electrically characterized with varying SiO_2 doping concentrations under different annealing conditions. Ferroelectric characteristics of thin film HfO_2 in metal–ferroelectric–insulator–semiconductor (MFIS) capacitors are then contrasted with the metal–ferroelectric–metal (MFM) device structure. As shown in this work, other effects,

such as changes in the SiO_2 interface during annealing, the scavenging effect of TiN, and the polycrystalline bottom electrode, may form a more critical role in the observed ferroelectric behavior of Si-doped HfO_2 thin films than stresses generated from the differences in the thermal expansion coefficients.

4.2 Experiment

Ferroelectric HfO_2 capacitors were fabricated on highly doped (0.001–0.005 Ω-cm) (100) Si p-substrates to minimize the series resistance from the back substrate contact. The ~2 nm native SiO_2 was retained at the substrate interface to reduce the leakage current in MFIS capacitors unless mentioned otherwise. An approximately 1 nm Cr adhesion layer followed by 10 nm of Ir was sputtered at room temperature in a KJL CMS-18 multi-target sputtering system to form the bottom electrodes for the MFM capacitors followed by plasma enhanced atomic layer deposition (Ultratech/Cambridge Nano Fiji 200) of 10 nm layered HfO_2:SiO_2 at 200 °C. Tetrakis(dimethylamido)hafnium and tris(dimethylamino)silane were used as the HfO_2 and SiO_2 precursors, respectively. The ALD cycle ratio of HfO_2 and SiO_2 was altered to achieve SiO_2 doping concentrations in the range of 2.08–5.65 mol. %. The thickness of the HfO_2 film was confirmed using ellipsometry. 10 nm Ir and TiN top electrodes were sputtered at room temperature. After the top electrode deposition, post-metallization anneals (PMAs) were conducted with rapid thermal anneals in a STEAG 100CS and SSI Solaris 150. Post-deposition annealed (PDA) films were annealed after HfO_2 deposition and did not have a top electrode during annealing. The RTA temperatures explored in this work range from 700 °C to 1000 °C with a peak temperature duration of 1–20 s in nitrogen ambient. After annealing, 100 nm of Pt or Ir was deposited and subsequently lifted off to form the top contact. The Pt and Ir contacts were used as hard masks to define the device area.

Capacitors with a top TiN electrode were etched using a H_2O_2 solution at 65 °C. Iridium is not easily etched by wet processes; therefore, capacitors with a top Ir electrode were dry etched using a RIE/ICP Uniaxis SLR. The capacitor area was 10,000 μm^2.

An Agilent 4294A impedance analyzer was used to extract the capacitance–voltage (CV) and permittivity characteristics with an AC signal amplitude of 50mV at 50 kHz. Hysteresis measurements were made using a modified Sawyer–Tower circuit[72] with the ferroelectric capacitor in series with a 22 nF linear capacitor using an Agilent 33120A waveform generator and a Tektronix TDS5104B oscilloscope. The switched polarization measurements were obtained using the Positive-Up-Negative-Down (PUND) method[76] with a 37.5 kHz waveform frequency, a pulse width of 3 μs, and a 1 μs rise/fall time. The linear 22 nF capacitor was replaced with a 50 Ω load resistor in a modified Sawyer–Tower circuit. A Keithley 4200 was used to measure the current–voltage (I-V) characteristics of the capacitors.

Cross-sectional samples for high resolution transmission electron microscopy were prepared using a focused ion beam and conducted on a JEOL 2010F TEM (Fig. 1). Cross-sectional samples for scanning transmission electron microscopy (STEM) were prepared by wedge polishing with an Allied Multiprep before ion-milling with a Fischione Model 1050. High angle annular dark-field (HAADF) STEM [Fig. 2A)–D)] was conducted using a probe-corrected FEI Titan G2 60–300 kV S/TEM operated at 200 kV and with a probe semi-convergence angle of 21 mrad. The collection inner semi-angle was approximately 77 mrad.

Grazing incidence x-ray diffraction (GIXRD) measurements were performed on a Rigaku XRD (medium resolution parallel beam/parallel slit analyzer) with a 0.5 ° angle

of incidence, an incidence slit of 0.1 mm, a receiving slit of 20 mm, and a scan time of 1h and 25 min in a continuous scan mode with a 0.05 ° step size at a rate of 1 ° per min over a 10–95 ° scan range.

4.3 Results and Discussion

The annealing conditions of HfO_2 thin films strongly influence the ferroelectric device characteristics because crystallization during this period will give expression to the prevailing crystal phases. While a high degree of crystallinity is desired, grain boundaries and diffusion of the electrode materials can lead to high leakage currents, negating benefits higher temperature anneals with longer durations may provide. HfO_2 thin films doped with 5.65 mol. % Si exhibited partial crystallinity after undergoing a 600 °C anneal for 20 s, but regions of non-crystalline HfO_2 were still observed. Annealing at 800 °C for 20 s revealed a highly crystalline film as shown in Figure 4-1.

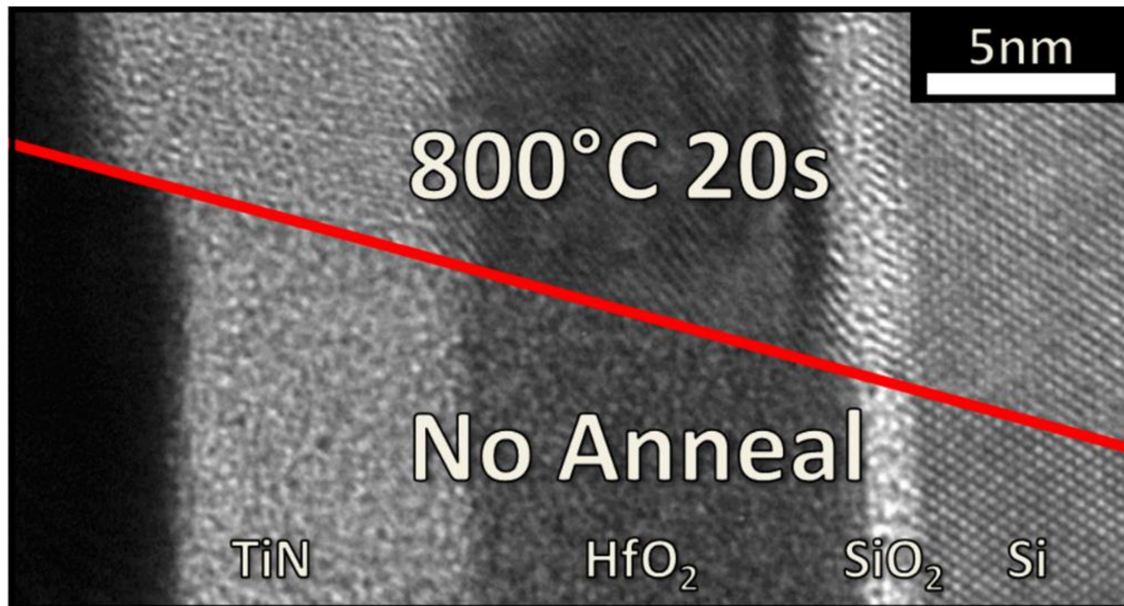

Figure 4-1. Growth of the HfO_2/SiO_2 interfacial layer and the expansion of the TiN electrode can be seen when compared to the as-deposited film. The red line denotes the boundary between the two TEM images of the 800 °C 20 s annealed film and the as-deposited film. Both images were taken with the same magnification.

The HfO_2/SiO_2 interfacial layer grew by approximately 0.5–1 nm and the TiN electrode expanded by 1–2 nm after the 800 °C anneal compared to the as-deposited film in the regions observed with TEM. The growth of the sputtered TiN electrode may possibly be due to the formation of TiON during annealing. Higher annealing temperatures have been observed to increase the HfO_2/SiO_2 interfacial layer through the formation of hafnium silicate, but anneals at 1000 °C can lead to decreases of silicate due to the formation of hafnium silicide at the substrate interface.[112]

MFIS capacitors with a TiN electrode and a 10 nm HfO_2 film doped with 5.65 mol. % Si underwent three different anneals to evaluate their electrical and ferroelectric characteristics, as seen in Figures 4-2 A)–C). TiN capped capacitors annealed at 800 °C for 20 s had the highest leakage currents, rounded hysteresis loops, and large coercive voltages. Decreasing the duration of the 800 °C anneal to 5 s improved the leakage current and the shape of the hysteresis loop, but the greatest improvement was found when annealing the capacitors at 700 °C for 20 s. The lower temperature anneal lowered the leakage current by more than one order of magnitude and decreased the coercive voltage. A remanent polarization (P_r) of 17.3 $\mu C/cm^2$ and a 3V coercive voltage was observed in the TiN capped MFIS capacitors annealed at 700 °C. Due to the pulsed operation of ferroelectric materials incorporated within FRAM, PUND measurements allow an evaluation of the switching polarization as it would be utilized within a memory circuit. As can be seen in Figures 4-2 C) and 4-3 C), the highest anneal temperatures created the largest peak load signals in the PUND circuit.

In comparison with TiN gate MFIS capacitors, MFIS capacitors with an Ir top electrode and a 10 nm HfO_2 film doped with 5.65 mol. % Si underwent similar anneals

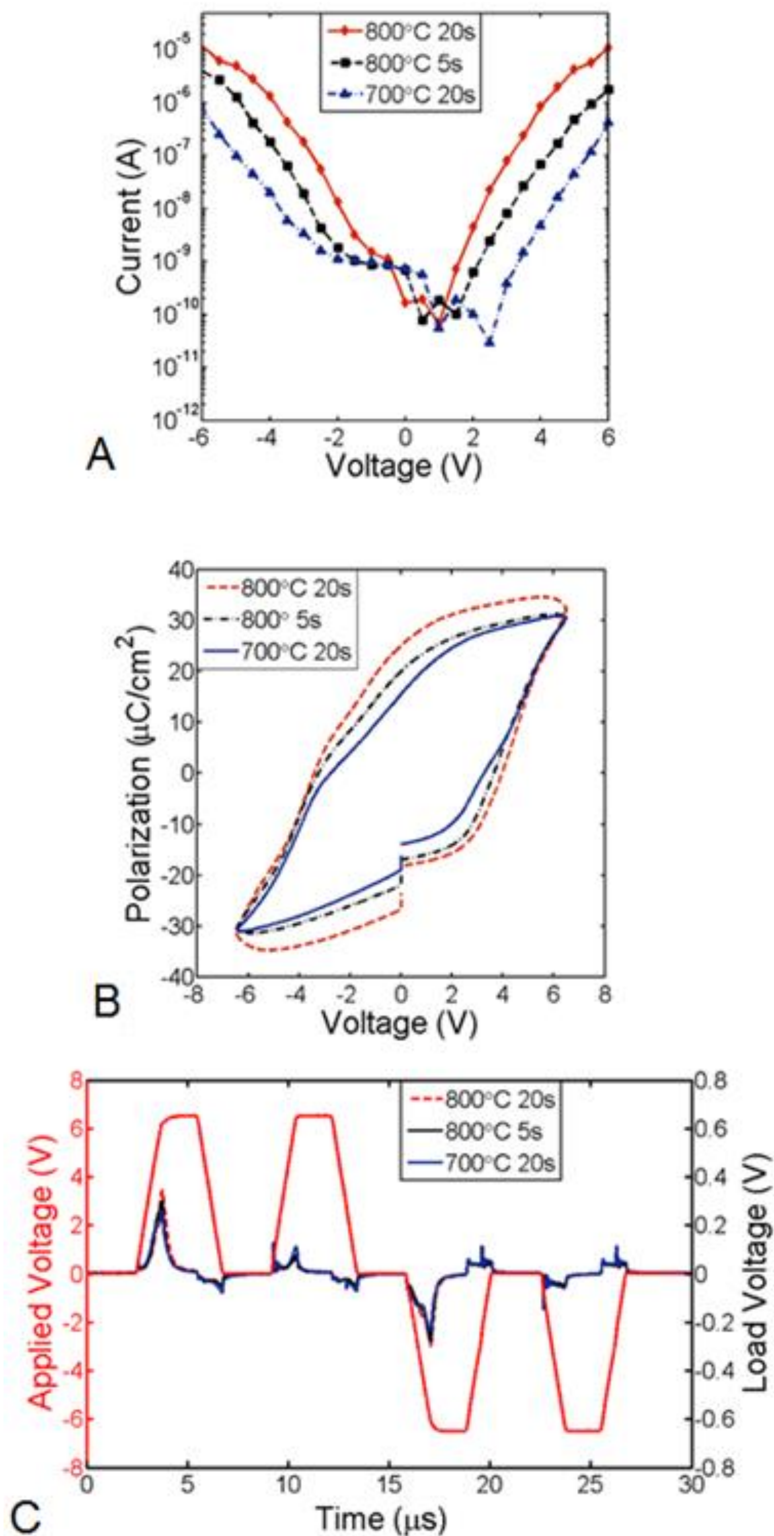

Figure 4-2. Electrical and ferroelectric characterization of TiN MFIS devices after different annealing conditions: A) leakage current, B) polarization vs voltage hysteresis, and C) PUND.

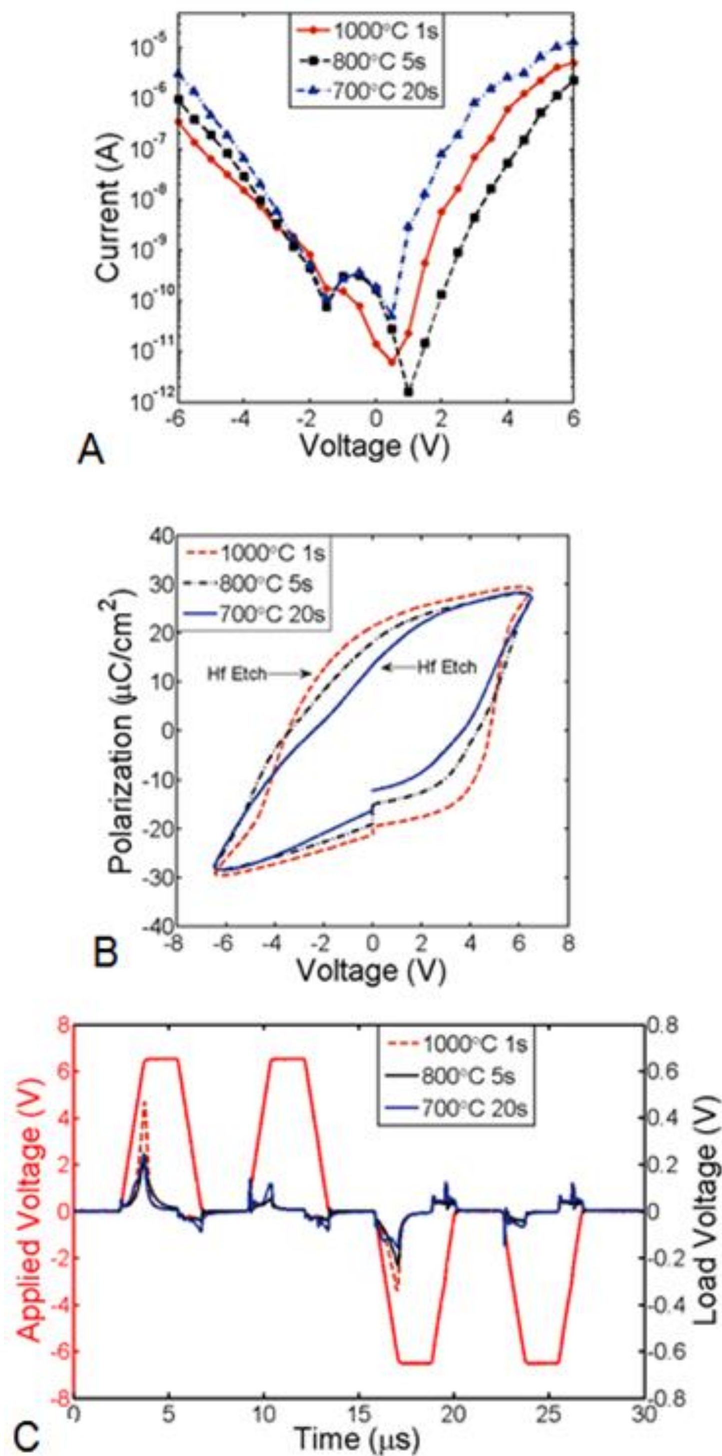

Figure 4-3. Electrical and ferroelectric characterization of Ir MFIS devices after different annealing conditions: A) leakage current, B) polarization vs voltage hysteresis, and C) PUND. The native SiO_2 was etched for devices annealed at 700 °C and 1000 °C, both of which have higher leakage currents than the 800 °C anneal where the native SiO_2 was incorporated within the MFIS stack.

to evaluate their electrical and ferroelectric characteristics, as seen in Figures 4-3 A)-C). Ir MFIS capacitors annealed at 700 °C demonstrated a high leakage current [Figure 4-3A)] because the native SiO_2 was removed with a hydrofluoric acid (HF) etch, but the 700 °C PMA capacitor still exhibited the lowest coercive voltage, 3 V, among the annealed Ir MFIS devices and a remanent polarization of 15.3 μC/cm^2.

The Ir MFIS capacitors annealed at 1000 °C also had their native SiO_2 removed by the HF etch, but exhibited the largest coercive voltage, 4 V, with a remanent polarization of 22 μC/cm^2. These results suggest the coercive voltages for the ferroelectric HfO_2 MFIS devices are a strong function of the annealing conditions with larger coercive voltages occurring for higher anneal temperatures. Similarly,[40] larger coercive voltages were observed with higher anneal temperatures in ferroelectric $Hf_{0.5}Zr_{0.5}O_2$ films, which were discussed in the context of a changing fractional percentage of the monoclinic, tetragonal, and orthorhombic phases for different anneal temperatures. The larger coercive voltages seen in MFIS devices with higher temperature anneals may also be due to the growth of nonferroelectric interfacial layers, i.e., dead layers.[99] Figures 4-4 A)-B) illustrate how the removal of the native SiO_2 layer etched using HF leads to a substantial increase in the leakage current and a small 2 μC/cm^2 gain in P_r, but no change in the coercive voltage occurs for otherwise identically processed devices. The lack of a significant change in the coercive voltage with the removal of the native SiO_2 for the 700 °C 20 s annealed TiN MFIS devices indicate that SiO_2 regrowth during ALD or high temperature annealing may have occurred.

The displacement current generated from switched charge gives rise to the characteristic P-V hysteresis loops found in ferroelectric materials; however, both

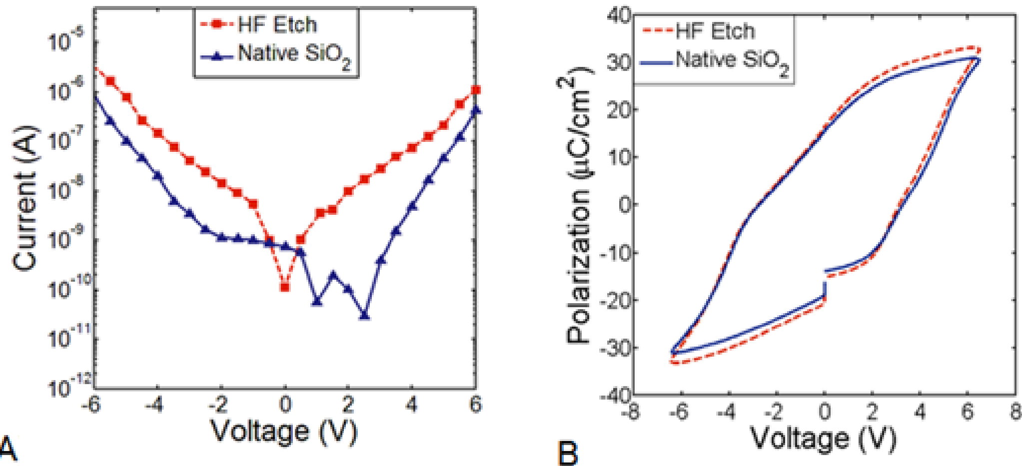

Figure 4-4. Comparison of HF surface treatment vs. native SiO2. A) Native SiO_2 improves the leakage current of the 5.65 mol. % Si-doped ferroelectric HfO_2 MFIS devices with a top TiN electrode annealed at 700 °C for 20 s. B) Etching the native oxide creates a modest increase in Pr, but does not change the coercive voltage. The absence of change in the coercive field may be due to regrowth of the SiO_2 layer after high temperature annealing.

leakage current and charge trapping contributions at the ferroelectric–insulator–semiconductor interfaces may be superimposed on the displacement current in MFIS devices, leading to an increase in the observed remanent polarization values. Coercive voltages observed in ferroelectric HfO_2 MFIS devices are influenced by the nonferroelectric SiO_2 layer, which expands after annealing at high temperatures and reduces the effective voltage seen by HfO_2. Hence, coercive voltages quoted for MFIS capacitors are apparent and not an intrinsic property of ferroelectric HfO_2.

A side by side STEM comparison of the Ir MFIS device annealed at 1000 °C for 1 s and the TiN MFIS annealed at 800 °C for 20 s is shown in Figure 4-5. The Ir/HfO_2 interface appears to be nearly atomically abrupt because of the rapid 1 s flash anneal, whereas the TiN/HfO_2 interface exhibits significant roughness due to a longer anneal. Moreover, the intensity decrease at the TiN/HfO_2 interface indicates density reduction, possibly from diffusion or an interfacial reaction. The Ir MFIS device in Figure 4-5 A) had

received a HF etch prior to the deposition of HfO_2, yet the amorphous SiO_2 layer is 0.6 nm thicker than the TiN MFIS device which did not receive the HF substrate treatment.

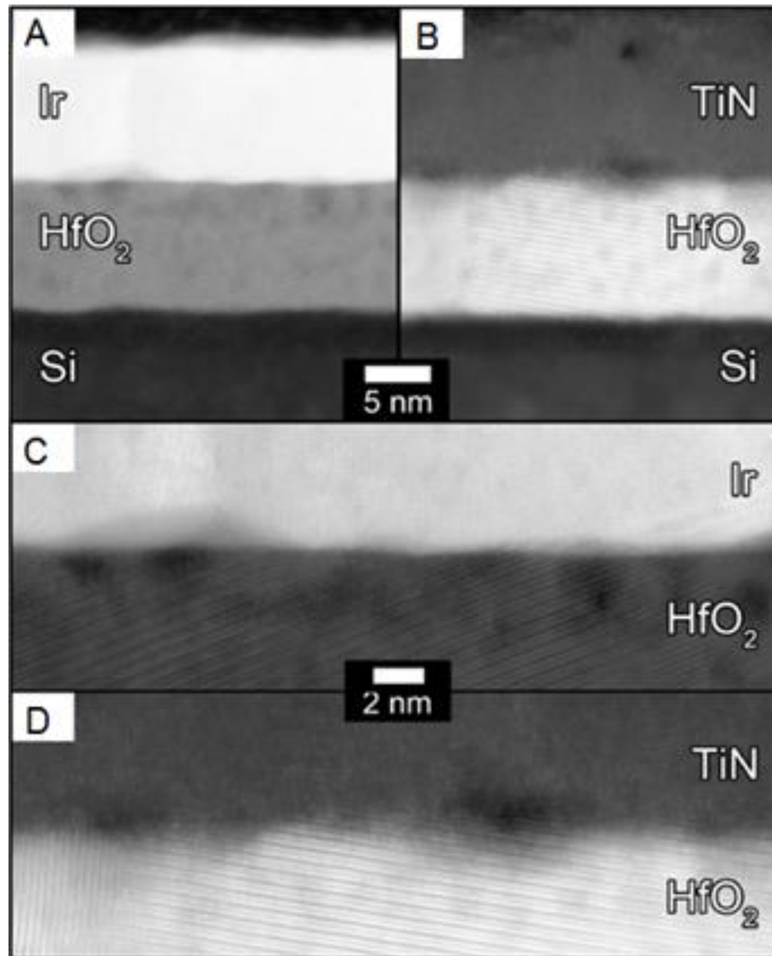

Figure 4-5. HAADF STEM images of Ir and TiN MFIS stacks. A) Ir/HfO_2/Si interfaces after a 1000 °C 1 s PMA. B) TiN/HfO_2/Si interfaces after an 800 °C 20 s PMA. C) and D) are enlargements of the interface between HfO_2 and the capping layers from A) and B), respectively. The Ir and TiN electrodes exhibit reversed contrast relative to HfO_2 due to the large difference in average atomic number compared to HfO_2. Image contrast and brightness were adjusted to enhance visibility of interfacial features and structural details.

While the expansion of the native SiO_2 layer from as-deposited films occurs at 800 °C (Figure 4-1), SiO_2 regrowth after the HF etch, possibly during ALD of HfO_2, leads to a thicker SiO_2 interfacial layer after the 1000 °C anneal as observed in Figure 4-5 A).

Ir capped HfO_2 MFIS capacitors doped with 5.65 mol. % Si exhibited similar hysteresis behavior as the TiN devices for the same annealing conditions (700 °C 20 s and 800 °C 5 s) (Figure 4-6); however, for equivalent annealing conditions, MFIS devices with an Ir electrode had a 13–14% lower P_r. The difference in P_r between the Ir and TiN MFIS capacitors may result from both film stresses arising from the thermal expansion coefficients and differences in the growth of the SiO_2 interfacial layer due to the scavenging effect of TiN.[30]

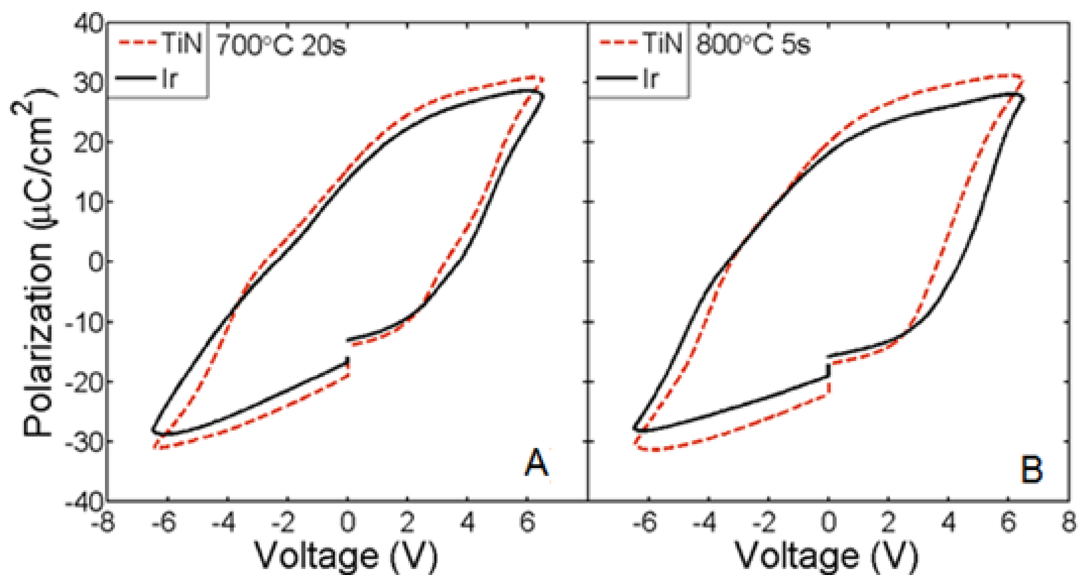

Figure 4-6. Hysteresis of TiN and Ir capped MFIS devices with a 700 °C 20 s anneal A) and a 800 °C 5 s anneal B). The HfO_2 films were doped with 5.65 mol. % Si. The devices annealed at 700 °C have a different shape and smaller coercive voltage than devices annealed at 800 °C. The 700 °C post-metallization annealed HfO_2 films have a shape that could indicate the presence of an antiferroelectric-like phase.

The lower positive coercive voltages seen in TiN MFIS devices in particular are attributed to the ability of the TiN top electrode to inhibit further growth of the SiO_2 layer during annealing. A more detailed study, beyond the scope of this work, is required to assess how mechanical stresses generated by the electrode materials after a post metallization anneal influence ferroelectric HfO_2.

Silicon's role in establishing ferroelectric behavior for thin film HfO_2 was confirmed by varying the SiO_2 concentration in both Ir and TiN capped MFIS devices, as shown in Figure 4-7. The highest Si-doping concentration explored in this work, 5.65 mol. %, produced the largest remanent polarization for HfO_2 thin films capped with Ir and TiN electrodes.

The remanent polarization of the Ir MFIS capacitors annealed at 1000 °C for 1 s underwent a steady increase as the doping levels rose from 3.00 to 5.65 mol. % Si, indicating an increase in the presence of the orthorhombic phase within the film without a ferroelectric-antiferroelectric phase transition. At a Si doping concentration of 2.08 mol. %, the Ir MFIS devices lost their ferroelectric characteristics, as illustrated by the closed hysteresis loop.

GIXRD of the Ir capped HfO_2 films with different doping concentrations are shown in Figure 4-8. While identification of all reflections is not possible because the precise polymorph of the HfO_2 phase cannot be unambiguously determined from the GIXRD data alone, a stronger monoclinic presence is detected in the post-deposition annealed 5.65 mol. % Si and the PMA 2.08 mol. % Si MFIS devices compared to the 5.65 mol. % Si MFM PMA devices. Capped HfO_2 films with a lower Si doping concentration contain a higher fraction of the monoclinic phase compared to capped HfO_2 films doped with 5.65 mol. % Si. Post-deposition annealed HfO_2 films with 5.65 mol. % Si did not produce ferroelectric characteristics and showed a highly monoclinic structure.

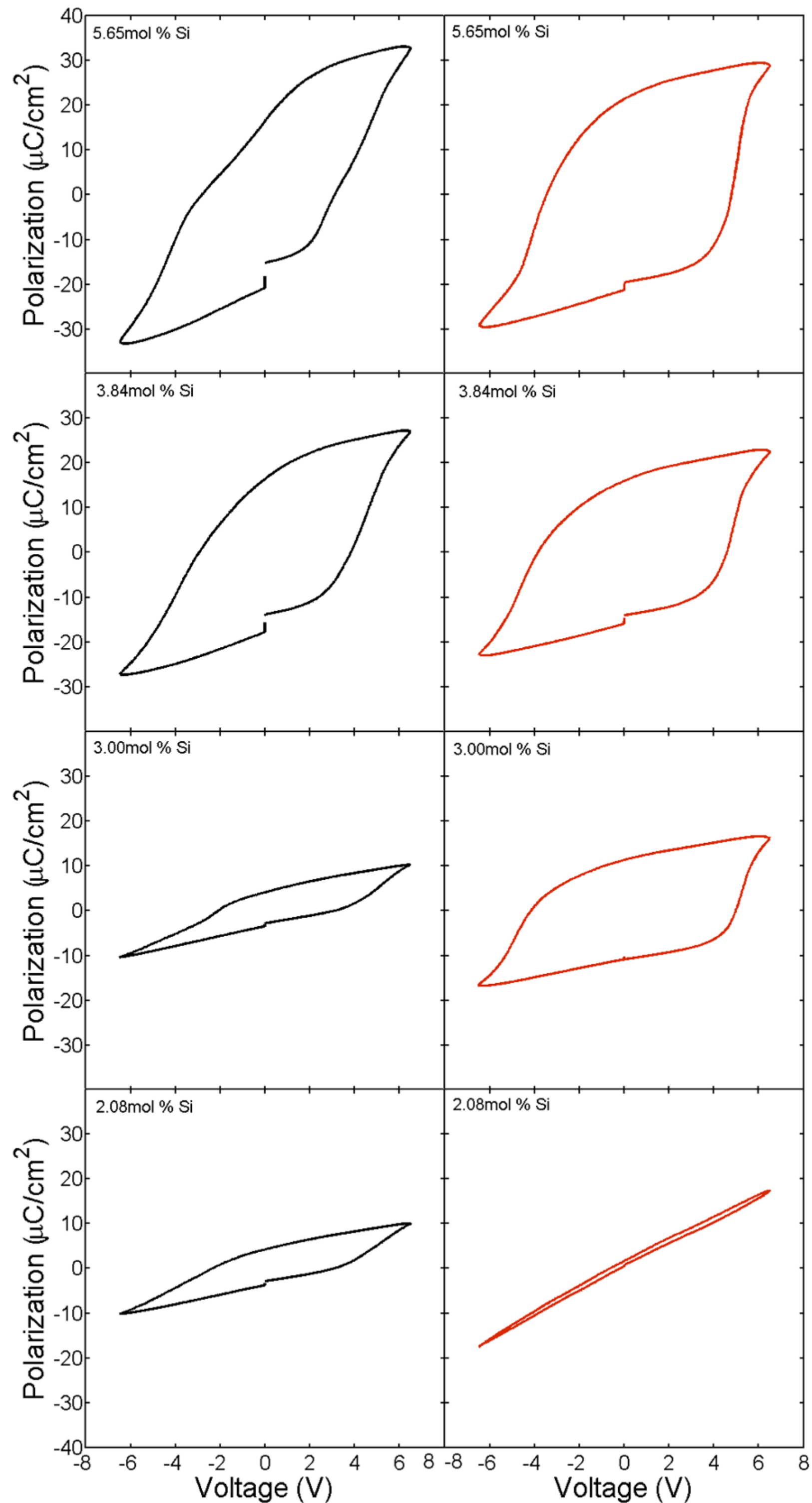

Figure 4-7. Hysteresis of MFIS HfO_2 capacitors with varying Si-doping concentrations. TiN capped devices annealed at 700 °C for 20 s (black) and Ir capped devices annealed at 1000 °C for 1 s (red) exhibited the largest remanent polarization at 5.65 mol. % Si-doping.

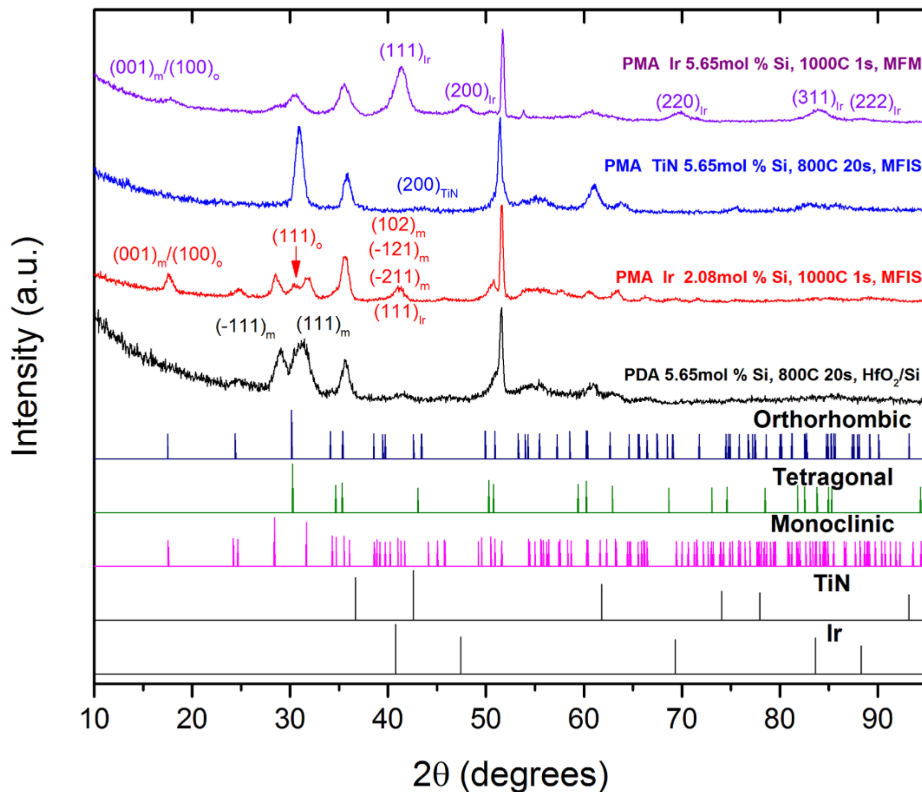

Figure 4-8. GIXRD of the Ir and TiN capped HfO_2 films with different doping concentrations are shown with the theoretical peak positions of the orthorhombic, tetragonal, and monoclinic phases of HfO_2. TiN and Ir theoretical peak positions are also shown. A stronger monoclinic presence is detected in the PDA films with 5.65 mol. % Si and the PMA 2.08 mol. % MFIS HfO_2 compared to the 5.65 mol. % Si MFM and MFIS PMA devices. All theoretical intensities were scaled to the range of 50–100% to enhance readability.

Stresses from Si substitution, the substrate, and the capping electrodes may be slightly shifting the expected tetragonal and orthorhombic peaks from their theoretical 2θ values in the PMA devices with 5.65 mol. % Si.

HfO_2 thin films annealed with a TiN top electrode at 700 °C for 20 s showed a similar decrease in the remanent polarization from 5.65 mol. % Si to 3.84mol. % Si doping concentrations (Figure 4-7) as Ir capped MFIS devices. However, at 3.00 mol. %, the TiN MFIS devices have hysteresis loops which are thoroughly contracted but not entirely closed. The cause of the rapid contraction of the hysteresis loop at the Si

doping level of 3.00 mol. % for the TiN capped MFIS devices is not clear. A slight reduction in the polarization is observed in the TiN MFIS capacitors when the Si-doping is reduced from 3.00 mol. % to 2.08 mol. %, but the TiN 2.08 mol. % Si-doped devices still exhibit open loops unlike the Ir capacitors with the same doping concentration. This may be attributable to the greater promotion of the m→t phase transformation induced by the TiN capping electrode compared to the Ir capping electrode, although the higher anneal temperature for the devices with an Ir electrode may also contribute to the closed hysteresis loop at a Si-doping concentration of 2.08mol. %. GIXRD (Figure 4-8) was used to confirm that a TiN capping electrode promotes the m→t phase transformation. The GIXRD pattern of the Ir MFM and TiN MFIS capacitor contains diffraction signals from multiple HfO_2 phases (tetragonal and monoclinic) and a single tetragonal HfO_2, respectively. There is evidence of a possible weak (111) orientation of the Ir electrodes in the MFM capacitor.

To investigate the role of the asymmetry in the top and bottom electrodes, Ir MFM HfO_2 capacitors were investigated. Ir MFM HfO_2 capacitors doped with 5.65mol. % Si annealed at 1000 °C for 1 s demonstrated a 1.2V coercive voltage and a remanent polarization of 8.6 μC/cm^2 [Figure 4-9 A)]. The dual capacitance peaks near the coercive voltages are a characteristic sign of ferroelectric materials [Figure 4-9 B)].[5] Unlike the MFIS devices, Ir capped MFM capacitors had to undergo 10^3 cycles to obtain repeatable hysteresis loops. The Ir MFM device structure exhibited a coercive voltage nearly 3V lower than the equivalent Ir MFIS devices. The large difference in the coercive voltages between the MFIS and MFM capacitors is caused by the interfacial SiO_2 layer in the MFIS structure, which can reduce the voltage seen by the ferroelectric

by approximately half. The SiO_2 interfacial layer and charge trapping are important factors which can influence the MFIS device characteristics in ferroelectric Si-doped HfO_2 films.[113] Improvements in the semiconductor interface quality and a reduction in charge trapping may aid in lowering the high coercive voltages observed in MFIS devices with Si-doped HfO_2 thin films.

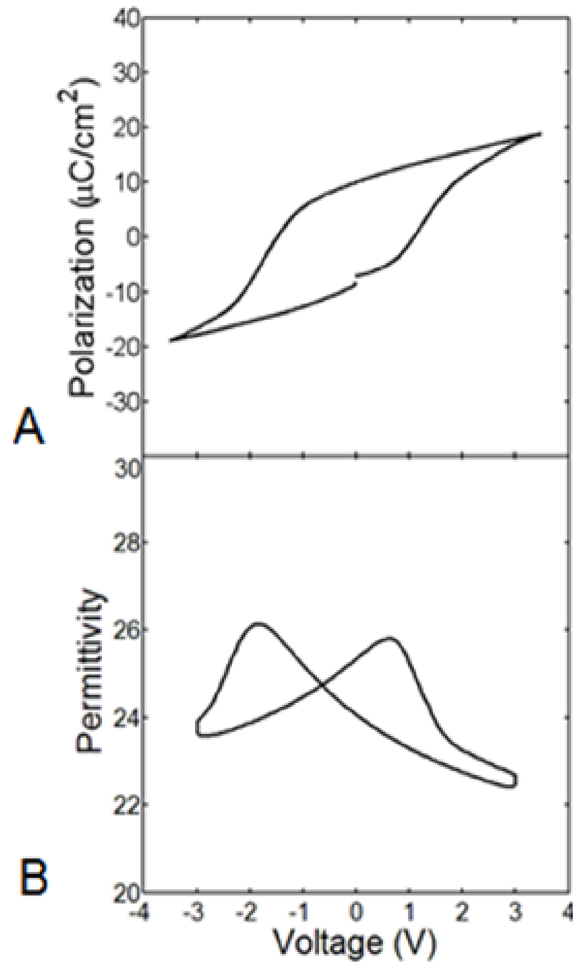

Figure 4-9. Ferroelectric and capacitance characteristics of MFM device with Ir electrodes annealed at 1000 °C for 1 s: A) polarization vs voltage hysteresis and B) permittivity vs voltage reveals the signature dual CV peak of ferroelectric materials.

The smaller P_r observed in Ir MFM compared to Ir MFIS devices may be due to the weak (111) orientation of the Ir bottom electrode while charge trapping may be a

smaller contributing factor. Notably, Park et al. found that highly (111)-textured bottom Pt electrodes completely inhibited the t→o phase transformation in $Hf_{0.5}Zr_{0.5}O_2$ which was attributed to the nearly equal tensile strain on the a-, b-, and c-axis of the tetragonal phase of the film.[114] The weak (111) orientation in the polycrystalline Ir bottom electrode may have suppressed the formation of the orthorhombic phase to some degree and lowered the observed remanent polarization when compared to HfO_2 thin films, which were deposited on the amorphous SiO_2/Si (100) substrate. Although Si-doped ferroelectric HfO_2 thin films in the MFM structure have lower operating voltages than the MFIS devices, future work should look at improving the coercive voltage and remanent polarization of the MFM structure to make Si-doped HfO_2 ferroelectric thin films more competitive with PZT for FRAM applications.

4.4 Conclusion

Si-doped thin film HfO_2 MFIS capacitors annealed with 10 nm thick TiN and Ir capping electrodes showed similar electrical and ferroelectric characteristics. However, for the same annealing conditions, capacitors annealed with an Ir electrode showed a 13–14% lower remanent polarization than TiN capped devices. Thermal stresses generated from differences in the thermal expansion coefficients between the capping electrode materials, HfO_2, and the Si substrate and the potential scavenging effect of TiN, which inhibits the growth of the interfacial SiO_2 layer, is attributed to the observed higher P_r in TiN capped MFIS capacitors. Higher temperature anneals tended to produce MFIS capacitors with higher remanent polarizations and larger coercive voltages. Incorporating the native SiO_2 layer into the MFIS device structure was shown to substantially reduce the leakage current and enable higher temperature anneals without producing significant changes in the coercive voltage compared to HF etched Si

substrates. Si-doped HfO_2 thin film Ir capped MFM devices demonstrated a significantly lower coercive voltage than the MFIS devices due to the absence of the HfO_2/SiO_2 interfacial layer. The lower Pr observed in Ir MFM devices compared to Ir MFIS may be attributable to the weak (111) orientation of the bottom Ir electrode.

CHAPTER 5
THE EFFECTS OF LAYERING IN FERROELECTRIC Si-DOPED HfO_2 THIN FILMS

5.1 Background

Doped ferroelectric HfO_2 thin films are a very promising candidate for the further development of ferroelectric random access memory (FRAM) and ferroelectric field-effect transistor (FeFET) technologies. The various dopants,[90] annealing conditions,[40,115] electrode materials,[92,114,115] and the capabilities of atomic layer deposition (ALD) provide a broad range of conditions to better understand and more carefully modify the properties of doped ferroelectric HfO_2 thin films. HfO_2-based films exhibit resistance to hydrogen annealing,[59] are CMOS compatible,[61] and have been accepted as a gate dielectric in advanced logic technologies which make them an attractive alternative for semiconductor fabrication facilities compared to typical perovskites, such as lead zirconate titanate (PZT), that require a sidewall diffusion barrier.[58] In addition to doped HfO_2 films for use in ferroelectric memory applications, antiferroelectric $Hf_xZr_{1-x}O_2$ capacitors have demonstrated an energy storage density with greater than 50% efficiency at 175°C which may be of great utility in energy storage applications.[69] For doped HfO_2 ferroelectrics to emerge in a competitive technology, fatigue and hard breakdown events, exacerbated by a large ~1MV/cm coercive field,[89,90,92] must be improved, particularly for metal-ferroelectric-metal (MFM) HfO_2 stacks to have comparable reliability properties as PZT for FRAM applications.

Reprinted with permission from P.D. Lomenzo, Q. Takmeel, C. Zhou, Y. Liu, C.M. Fancher, J.L. Jones, S. Moghaddam, and T. Nishida, Appl. Phys. Lett. 105, 072906 (2014). DOI: 10.1063/1.4893738. Copyright 2014, American Institute of Physics.

The monoclinic crystal phase typically forms in crystalline HfO_2 when it is broughtto room temperature, but the incorporation of Si[17] and a capping electrode[37] promotes the monoclinic to tetragonal (m→t) phase transformation in thin films following a rapid thermal anneal (RTA). The polar phase attributed to ferroelectricity in doped HfO_2, space group $Pbc2_1$, is hypothesized[20] to result from a tetragonal to orthorhombic (t→o) phase transition, though recently other HfO_2 ferroelectric crystal phases have been postulated.[116] The orthorhombic space group $Pbc2_1$ was originally identified by neutron diffraction measurements in partially stabilized Mg-doped ZrO_2.[24] The capping electrode is understood to impede the volume expansion associated with the t→m transformation,[37] thereby potentially promoting the t→o phase transformation in doped ferroelectric HfO_2 thin films.

The Si-doping concentration has a fundamental role in the paraelectric-ferroelectric phase transition at low concentrations (~3 mol %) and the ferroelectric-antiferroelectric phase transition at higher concentrations (~5-6 mol %) in TiN MFM capacitors;[20] however, there may be a difference of the phase transition behavior of HfO_2 thin films when incorporated into the MFM and the metal-ferroelectric-insulator-semiconductor (MFIS) device structures. For instance, Si-doped HfO_2 MFIS capacitors with an Ir capping electrode yielded a smooth paraelectric to ferroelectric transition[115] from 2.08 – 5.65 mol. % Si accompanied by a gradual increase of the remanent polarization (P_r). It is plausible that the Si substrate surface treatment, diffusion of Si into HfO_2 and growth of interfacial hafnium silicate and silicide during high temperature annealing,[112] alterations in phase stabilization at different anneal temperatures, and the choice of the capping electrode, which can lead to additional Si incorporation into the

HfO_2 film through the scavenging effect,[30] may be responsible for a wide range of Si-doping concentrations that stabilize the ferroelectric phase in Si-doped HfO_2 MFIS capacitors. This is in contrast to the relatively narrow 2.6-3.8 mol. % Si doping range previously reported as the compositional window in which ferroelectric behavior was observed in Si-doped HfO_2 MFM films with TiN electrodes.[61]

While the role of the Si-doping concentration in HfO_2 films can be understood to increase the crystallization temperature and tetragonality for both MFM and MFIS devices structures, it is demonstrated that the spatial distribution of the Si dopants within the film stack can be manipulated to adjust the remanent polarization for greater control over the ferroelectric device properties. The precision of atomic layering control permits a detailed doping profile to be tailored in doped HfO_2 ferroelectric thin films and facilitates a large process window for tuning the ferroelectric properties for FRAM and FeFET applications. By utilizing ALD's atomic control for positioning the dopants within the film stack, silicon doping profiles are changed by altering the ratio of the HfO_2 and SiO_2 cycles while keeping the total number of SiO_2 cycles for each film constant, thus enabling the fabrication of HfO_2 thin films with a constant Si concentration and distinct Si-dopant spatial distributions. This work explores the effects of Si layering and the role of Si concentration on the ferroelectric properties in thin film Si-doped HfO_2 MFIS capacitors.

5.2 Experiment

HfO_2 thin films were deposited on a highly doped Si (100) p+ substrate to reduce the series resistance from the back substrate contact. All substrates underwent a hydrofluoric acid (HF) etch to remove the native SiO_2 layer prior to the deposition of the Si-doped HfO_2 thin films. Approximately 10 nm thick Si-doped HfO_2 films with different

layering ratios of HfO_2 and SiO_2 were deposited by plasma enhanced atomic layer deposition (Ultratech/Cambridge Nano Fiji 200) at 200 °C. Tetrakis(dimethylamido)hafnium and Tris(dimethylamino)silane were used as the HfO_2 and SiO_2 precursors respectively. 10 nm thick top Ir electrodes were sputtered at room temperature using a KJL CMS-18 multi-target sputtering system. After the deposition of the Ir top electrodes, the samples underwent a post-metallization anneal (PMA) at 1000 °C for 1 s in N_2 with a SSI Solaris 150 RTA. Following the post-metallization anneal, 100 nm of Ir was deposited and subsequently lifted off to form the top contacts. The patterned Ir contacts were then used as a hard mask for etching the blanket 10 nm thick Ir to shape the capacitor geometry. Dry etching was performed using an Ar/O_2 plasma chemistry in a RIE/ICP Unaxis SLR. The resulting MFIS capacitor area was 10,000 μm^2.

The ALD cycle ratio was altered to achieve HfO_2 thin films with approximately the same doping concentration and distinct Si-doping profiles, expressed as {N*16:N, N = 1, 2, 3} for HfO_2:SiO_2 cycles. The effects of increasing Si-concentration were studied by depositing films with {16:N, N = 1, 2, 3} HfO_2:SiO_2 cycle ratios. To separate the role of layering from higher Si-doping concentrations, an 8:1 HfO_2:SiO_2 film was deposited to compare with a 16:2 HfO_2:SiO_2 film, both HfO_2 films have approximately the same Si mol. % but different Si layering distributions. The thicknesses of the films were confirmed with TEM and ellipsometry. Cross-sections of the Ir/HfO_2:SiO_2/Si-stacked samples (16:1 and 48:3 films) were prepared by focused ion beam (FIB) and characterized in a FEI Titan scanning transmission electron microscope (STEM). The Si mol. % and the Si-doping profiles were measured using time-of-flight secondary ion

mass spectroscopy (TOF-SIMS). The TOF-SIMS depth resolution obtained using the experiment setting is approximately 5 nm.

Electrical characterization was carried out using a modified Sawyer-Tower circuit[72] with a 22nF linear capacitor in series with the MFIS capacitors. An Agilent 33120A was used to deliver triangle waves at 1 kHz to the MFIS capacitors while a Tektronix TDS5104B oscilloscope recorded the waveforms during hysteresis, often referred to as polarization-voltage (P-V) loops. The endurance cycling was performed with bipolar square waves of varying frequencies to examine the cycling characteristics over several decades. The first 10 cycles in the endurance plots were obtained during normal hysteresis measurements. From 10^2 - 10^6 cycles, the cycling procedure consisted of delivering bipolar pulses for 10 second durations at frequencies of 10^1 - 10^5 Hz respectively. 10^7 cycles were obtained with a 10^5 Hz frequency and a cycling duration of 100 seconds.

5.3 Results

During the rapid thermal anneal, the as-deposited amorphous HfO_2 is crystallized, yielding a polycrystalline film where the monoclinic, tetragonal, and orthorhombic phases are stabilized in various fractional percentages.[40] Due to the increase in the crystallization temperature of HfO_2 with the incorporation of Si, common RTA temperatures used for ion implantation damage removal can be utilized in the standard high-k metal gate-first process for FeFET devices employing Si-doped HfO_2 to simultaneously crystallize the ferroelectric. In the Ir MFIS capacitors with HfO_2 films using {N*16:N, N = 1, 2, 3} HfO_2:SiO_2 cycle ratios, three distinct Si-doping profiles as obtained by TOF-SIMS are retained after the rapid 1000 °C 1s anneal (Figure 5-1 C)). TOF-SIMS is used to identify the distribution of Si-dopants and interfacial effects, such

as diffusion and evidence of chemical reactions, within the Ir MFIS stack. The TOF-SIMS profiles of the Ir MFIS stack before and after the RTA show that diffusion of the Si-dopants within the HfO_2 thin films is low. Diffusion of Si from the substrate into HfO_2 is present prior to the RTA and occurs during the atomic layer deposition of HfO_2 on the HF etched Si substrate. The Ir tail into the HfO_2 film occurred during sputtering. An approximately 2 – 3 nm IrO_x layer formed at the Ir/HfO_2 interface, as seen by the large peak in Figure 5-1 C). All of the {N*16:N, N = 1, 2, 3} HfO_2:SiO_2 films had a Si mol. % in the range of 5.56 - 5.82 mol. %, hence, differences in the ferroelectric behavior of the films are ascribed to differences in the layering of the Si-dopants, not the overall Si-doping concentrations of the films. As can be seen in Figure 5-1 A), an increasingly inhomogeneous Si-doping profile lowers the remanent polarization as N increases in the N*16:N films. The greater inhomogeneity of the Si-doping in the 32:2 and 48:3 HfO_2:SiO_2 films leads to both Si-rich and Si-deficient regions within the HfO_2 film without the formation of a distinct SiO_2 layer. Grazing incidence X-ray diffraction (GIXRD) patterns indicate a fluorite structure consistent with HfO_2 (not shown) and no noticeable changes between the different layered samples. It is evident that lowering the remanent polarization through alterations in the Si-dopant distribution in the MFIS gate stack, rather than an increase in the thickness of the HfO_2 film,[117] can be used to reduce the depolarization field[65] and maintain sharp sub-threshold slopes in FeFET devices.

The effects of increasing the Si-doping concentrations were observed by depositing HfO_2:SiO_2 thin films with a cycling ratio of 16:N for N = 1, 2, 3 (Figure 5-2 B)). The 16:2 film shows a distinct change in its shape, most noticeably an asymmetric pinching of the P-V loop. The thinning of the central region of the hysteresis loop can be

understood to arise from either the existence of an antiferroelectric phase within the HfO_2 film or from the generation of defects leading to domain wall pinning.[118]

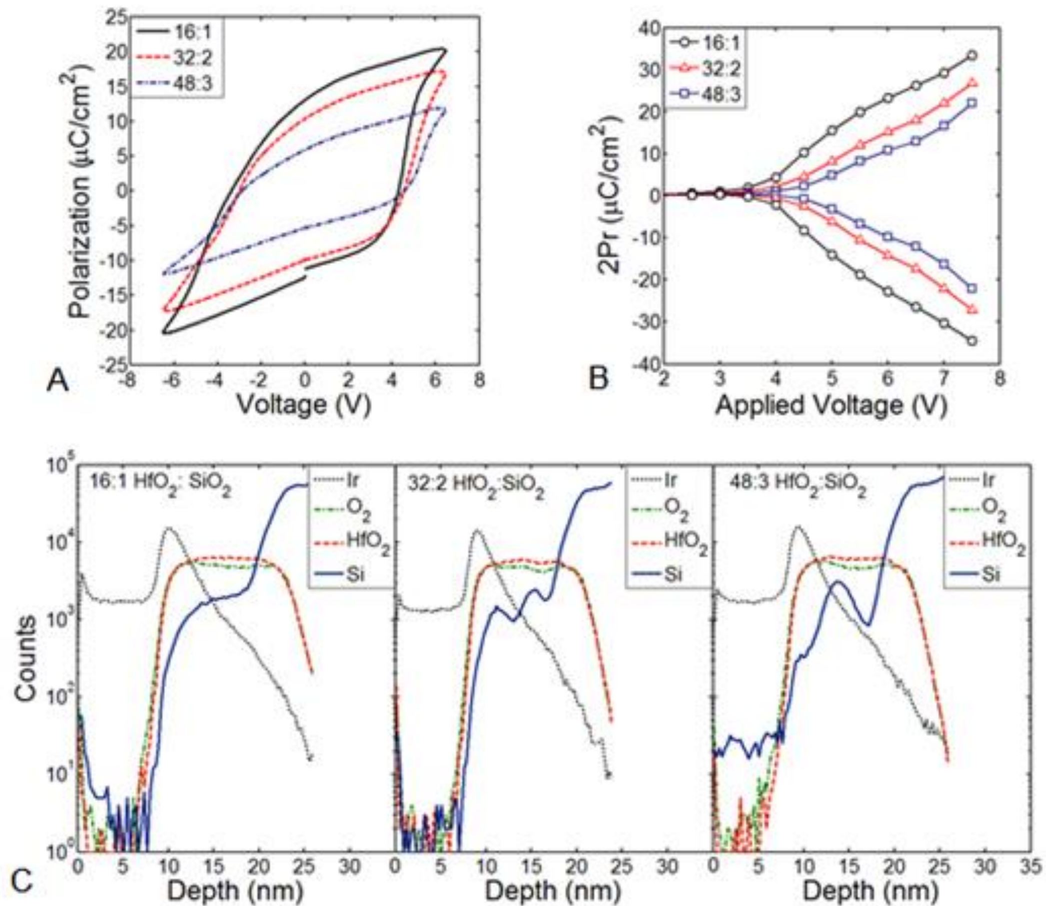

Figure 5-1. Hysteresis dependence on Si layering. A) The remanent polarization is reduced as the layering of the Si-dopants becomes more inhomogeneous with increasing N in N*16:N HfO_2:SiO_2 films, B) the differences in the remanent polarization of the N*16:N films are similar across a wide range of applied voltages, C) TOF-SIMS profiles for the 16:1, 32:2, and 48:3 HfO_2:SiO_2 films.

The 16:3 film shows a decline in polarization compared to the 16:1 and 16:2 HfO_2:SiO_2 films and yields a similar pinched P-V loop as the 16:2 film. The reduction in polarization of the 16:3 HfO_2:SiO_2 film may be attributable to the creation of a greater number of defects and the increase in crystallization temperature arising from the large Si-doping concentration (12.8 mol. % Si) which can degrade the crystal properties of the HfO_2 film. The 16:2 and 8:1 HfO_2:SiO_2 thin films have similar overall Si-doping concentrations of

9.55 and 9.42 mol. % Si respectively, yet the 8:1 film does not exhibit a pinched P-V loop (Figure 5-2 A)). The effects of inhomogeneous layering in the 16:2 are thought to have brought about a larger number of defects, though the formation of an antiferroelectric phase cannot be excluded. The 16:1 and 8:1 films show similar ferroelectric properties and have an apparent continuous distribution of Si-dopants with little local variation as observed within the spatial resolution of the TOF-SIMS. The high-resolution high angle annular dark field (HAADF) STEM images shown in Figure 5-3 confirm the crystallization of the as-deposited amorphous HfO_2:SiO_2 films during the RTA. It is worth noticing that the 16:1 film (Figure 5-3 A)) exhibits a larger grain size and smoother interfaces with the Ir top electrode and Si substrate, in comparison with the 48:3 film (Figure 5-3 B)), which can be attributed to the less homogeneous layering in the 48:3 film.

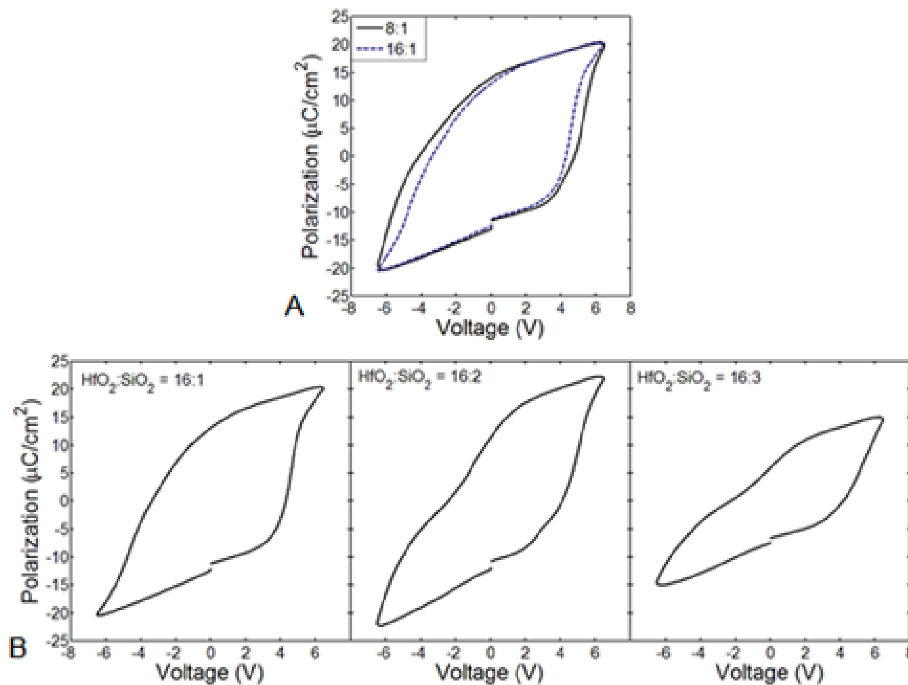

Figure 5-2. Changing the Si concentration and the ALD cycle ratio both show changes in the hysteresis characteristics. A) The 16:1 and 8:1 films exhibit similar ferroelectric properties, B) increasing N in the 16:N films leads to a pinching of the P-V loop and a diminution of the remanent polarization when N = 3.

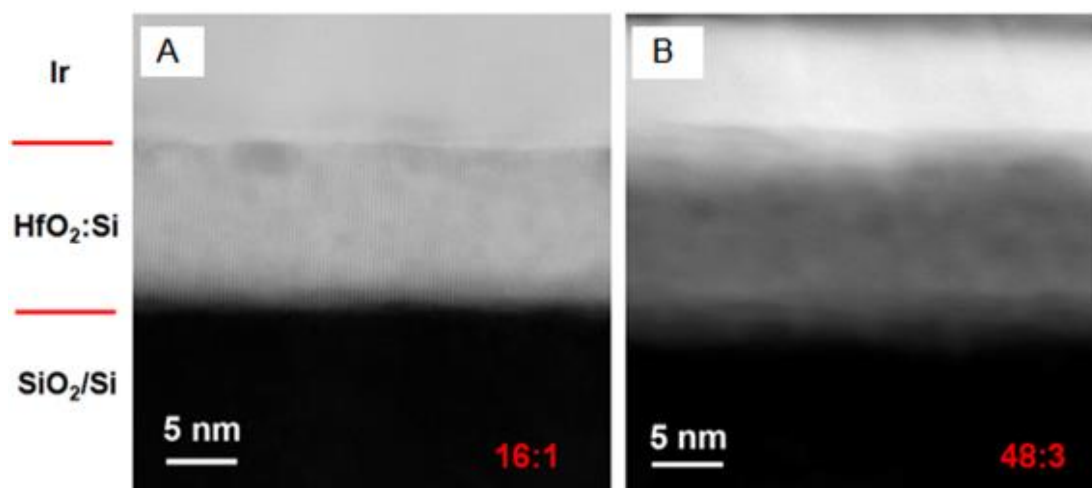

Figure 5-3. Cross-sectional HAADF STEM images of the Ir/HfO_2:SiO_2/Si-stacked samples for A) 16:1 film and B) 48:3 film. The 16:1 film shows larger grain size and smoother interfaces with the Ir top electrode and Si substrate than the 48:3 film.

The cycling characteristics of the ferroelectric Si-doped HfO_2 thin films are an important reliability metric for the consideration of the Ir MFIS capacitor's incorporation into a ferroelectric field effect transistor. FeFETs are a prospective alternative nonvolatile memory technology that could address the shortcomings of NAND FLASH as aggressive scaling continues.[80] Although a linear extrapolation from 17 days to 10 years has been reported to yield a stable memory window for Si-doped HfO_2 FeFETs,[119] a more rigorous demonstration of Si-doped HfO_2 FeFET's retention, yield, and reliability properties need to be performed on current technology platforms to evaluate its competitiveness with FLASH. The cycling characteristics of the 16:1 HfO_2:SiO_2 films show that the onset of fatigue occurs after 10^4 cycles for 5.5V and 6V endurance pulses, likely due to charge trapping at the semiconductor interface (Figure 5-4 A)). The Ir MFIS capacitors became leaky after 10^4 cycles with 6.5V bipolar pulses. All of the N*16:N HfO_2:SiO_2 Ir MFIS capacitors show similar cycling characteristics with fatigue beginning after 10^4 cycles and identical P_r values after 10^7 cycles (Figure 5-4 B)). In

contrast, the 16:2 and 16:3 HfO_2:SiO_2 Ir MFIS films show improved resistance to fatigue and little variation of P_r over 10^7 cycles (Figure 5-4 C)), although the maximum P_r of the films are ~ 5μC/cm^2 or less at an applied voltage of 5.5V. The pinching of the P-V loop in the 16:2 and 16:3 films may be influencing the cycling characteristics.

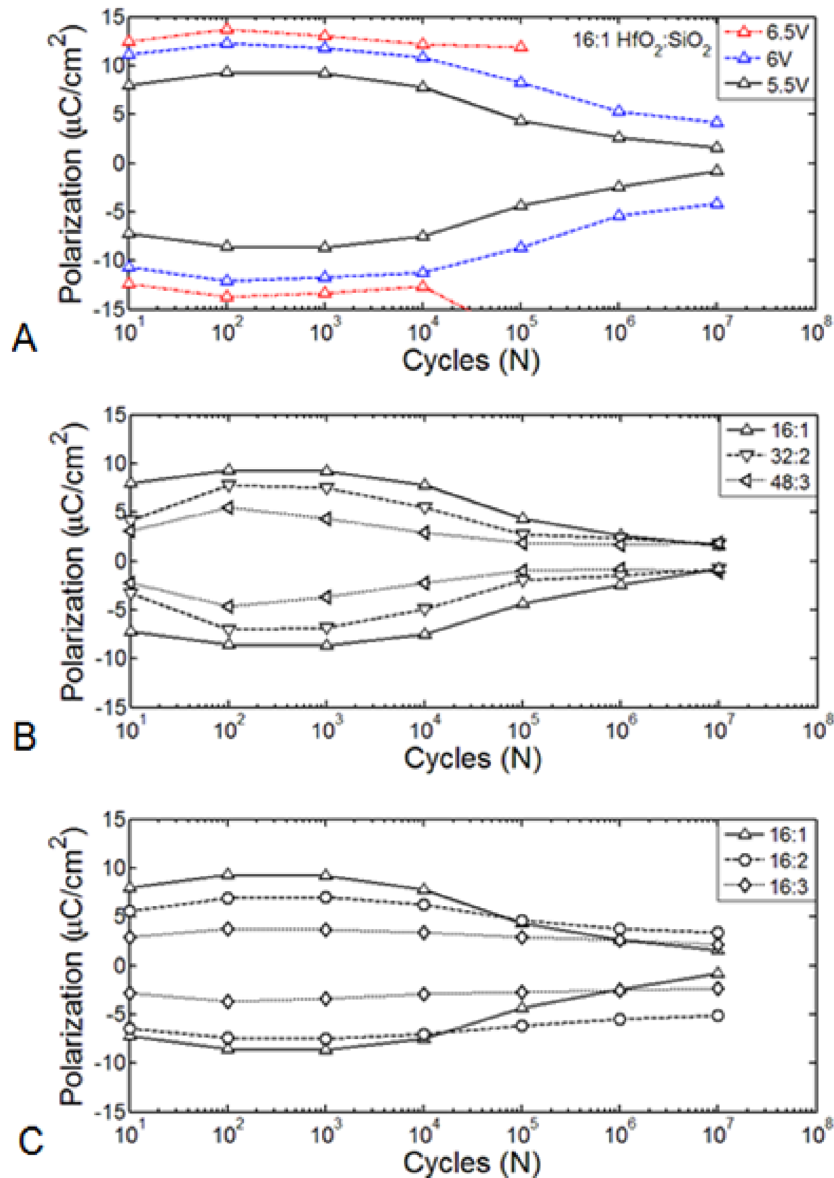

Figure 5-4. Cycling characteristics of layered Si-doped HfO_2 thin films. A) The cycling characteristics of the 16:1 HfO_2:SiO_2 Ir MFIS capacitor for various applied voltages, B) for the N*16:N, N = 1, 2, 3 capacitors at 5.5V, C) and for the 16:N, N = 1, 2, 3 at 5.5V which show less reduction in P_r with cycling for N = 2 and 3.

It should be noted that a HfO_2 thin film doped with 2.08 mol. % Si incorporated into the Ir MFIS structure yielded no discernible ferroelectric response and a P_r value less than 1μC/cm^2; hence, it is thought that the observed P_r values measured across the devices are primarily due to intrinsic effects such as switched charge originating from a ferroelectric phase within the HfO_2 thin film, though the influence of defect dipoles cannot be excluded. The cycling results for the layered Si-doped HfO_2 MFIS capacitors suggest a lifetime of approximately 10,000 - 100,000 cycles, similar to NAND FLASH[22], if the layered stacks are incorporated into operational FeFET devices. Moreover, the metal-oxide interface provided by IrO_x may act as a sink for oxygen vacancies and improve the cycling characteristics in FeFET. Mueller *et al.*[120] demonstrated that FeFET devices with a Si-doped HfO_2 ferroelectric film and TiN electrodes had robust endurance characteristics up to 10^4 cycles, after which charge trapping closed the memory window. Cycling dependent breakdown events, often reported for ferroelectric HfO_2-based MFM devices,[89,90,92] were not observed for applied voltages up to 6V after 10^7 cycles in the Si-doped HfO_2 thin films integrated into the Ir MFIS device structures.

5.4 Conclusion

Adjusting the Si-dopant distribution within the HfO_2 thin films at a ~5.5 – 5.7 Si mol. % resulted in alterations in the remanent polarization, with increasing inhomogeneity of the Si-dopants leading to a reduction in P_r. Higher doping concentrations lead to pinched P-V loops in the Ir MFIS capacitor, formed from either defect domain pinning or the formation of an antiferroelectric phase. A pinching of the P-V loop was found to be dependent on both the layering of the Si-dopants within the film stack and the overall Si doping concentration. Endurance cycling suggests the onset of

fatigue at about 10^4 cycles for the 16:1, 32:2, and 48:3 HfO_2:SiO_2 layered thin films in the Ir MFIS device structure. MFIS capacitors with pinched P-V loops were more resistant to decreases in P_r with voltage cycling. All of the MFIS devices exhibited no cycling dependent breakdown up to a voltage of 6V and 10^7 cycles. The Si-dopant distributions reported here may be used to reduce the depolarization field in FeFET devices for nonvolatile memory applications.

CHAPTER 6
TaN INTERFACE PROPERTIES AND ELECTRIC FIELD CYCLING EFFECTS IN Si-DOPED HfO_2 THIN FILMS[3]

6.1 Background

Growing reports on HfO_2-based ferroelectric thin films[20,39,40,44,45,50,106,121] are striking renewed interest in ferroelectrics for memory applications[63,66,120] and energy storage.[69] Si-doped HfO_2 thin films were the first ferroelectric HfO_2-based thin films reported with Böscke *et al.* showing that the crystallization of the Si:HfO_2 thin films in the presence of a capping TiN electrode can lead to the emergence of ferroelectric and antiferroelectric properties.[20] Robust retention characteristics of Si-doped HfO_2 ferroelectrics are promising for ferroelectric random access memory (FRAM) applications.[89] Further investigations into ferroelectric Si-doped HfO_2 thin films have illustrated the wide variety of process conditions which can influence the ferroelectric and electrical properties of Si-doped HfO_2, such as the choice of capping electrode,[115] the influence of the HfO_2 film thickness,[122] and the effects of Si-dopant layering.[123] In addition, the recent observation of ferroelectric domains through piezoresponse force microscopy in Si-doped HfO_2 thin films distinguishes its behavior from electrets and electrochemical responses.[124]

Due to the very small thicknesses (sub - 10 nm) in which ferroelectricity can be achieved in Si-doped HfO_2, the role of the electrodes and the electrode-ferroelectric interfaces on the ferroelectric behavior in the thin films cannot be overstated. Si-doped HfO_2 thin films with TiN electrodes have been shown to exhibit the so-called 'wake-up'

Reprinted with permission from P.D. Lomenzo, Q. Takmeel, C. Zhou, C.M. Fancher, E. Lambers, N.G. Rudawski, J.L. Jones, S. Moghaddam, and T. Nishida, J. Appl. Phys. 117, 134105 (2015). DOI: 10.1063/1.4916715. Copyright 2015, American Institute of Physics.

effect in which the remanent polarization increases and the internal electric field decreases with electric field cycling.[82] Zhou et al.[82] ascribed this effect to the difference in charge carrier concentrations between the bottom and top TiN electrodes whereby the removal or redistribution of mobile charge during bipolar cycling was believed to subsequently decrease the internal electric field and de-pin ferroelectric domains, although direct evidence of the chemical nature of the bottom and top TiN electrodes was not presented. The stability of the two ferroelectric polarization states, a prerequisite for nonvolatile memory applications, deteriorates with the existence of an internal or depolarization electric field. The term depolarizing field is used to signify the specific case when an internal electric field destabilizes a given polarization state. The term internal electric field (or internal bias) is employed more generally to describe the shifted ferroelectric characteristics along the electric field axis, often referred to as imprint, which stabilizes one polarization state at the expense of the other. Since doped ferroelectric HfO_2 thin films are being pursued to increase the memory density of FRAM[55] and to establish the scalability of ferroelectric field effect transistors (FeFETs),[63] the presence of a depolarizing field is highly undesirable. In addition, antiferroelectic-like characteristics observed in HfO_2-based films could be related to internal bias fields,[74] but no direct evidence has been established yet. Understanding the origin of the internal electric field and the effects of electric field cycling in doped ferroelectric HfO_2 thin films thus remains an important task from a scientific and technological perspective.

It is known that large surface electric fields originating from the spontaneous polarization of ferroelectrics cause band bending and ionization of trap states at the ferroelectric-electrode interface.[78,79,94] Brennan[78] points out several important factors

which influence the space charge distribution and the depolarization field in ferroelectric thin films. First, ionization of trap states at the ferroelectric-electrode interface will continue to increase until the surface space charge can effectively screen the internal polarization of the ferroelectric; it is through the unequal distribution of space charge between the top and bottom electrode interfaces which then gives rise to a depolarizing field. Secondly, the metal electrodes form Schottky contacts which provide a sheet of electrons at the electrode interface to maintain charge neutrality with the positive space charge region established on the ferroelectric side of the junction. Lastly, the space charge profile at the ferroelectric/electrode interfaces is influenced by the ferroelectric polarization, Schottky potential, and the applied electric field.

From the above arguments, it is clear that any investigation into the origin of an internal electric field observed in ferroelectric thin films should begin at the electrode/ferroelectric interfaces. To this end, x-ray photoelectron spectroscopy (XPS) is used to characterize the chemical properties of the top and bottom electrode interfaces of TaN metal-ferroelectric-metal capacitors which exhibit a large internal bias. The as-grown ferroelectric domains present in the film are shown to be oriented upward away from the bottom TaN electrode. Electric field cycling reduces the internal bias, increases the remanent polarization (P_r), and decreases the relative permittivity, but is not sufficient to obtain symmetric ferroelectric properties. Since this ‘wake-up’ effect has been proposed to originate from the asymmetry in the bottom and top electrodes[82] and such a large internal bias has not been seen in HfO_2-based devices with symmetric electrode materials, direct evidence of the chemical behavior of the electrode interfaces

between TaN and Si-doped HfO_2 provides timely insight into the growing body of knowledge for thin film HfO_2-based ferroelectrics.

6.2 Experiment

TaN bottom electrodes (BE) approximately 8.5 nm thick were RF sputtered on a highly doped (.001 - .005 Ω-cm) (100) p-Si substrate which had undergone a buffered oxide etch (BOE, 6:1, 40% NH_4F:49% HF in H_2O). The BOE was used to etch the native SiO_2 layer from the Si-substrate to reduce the bottom contact resistance before the TaN BE deposition. After TaN BE deposition, a 10 nm thick HfO_2:SiO_2 layered film was grown using plasma enhanced atomic layer deposition (PEALD) with a substrate temperature of 200°C. Tetrakis(dimethylamido)hafnium and Tris(dimethylamino)silane were used as the HfO_2 and SiO_2 precursors respectively. Time of flight - secondary ion mass spectrometry (TOF-SIMS) and XPS were used to determine the Si mol. % of the HfO_2 thin films corresponding to 24:1 and 16:1 ALD cycling ratios of HfO_2 and SiO_2. The Si content was determined to be 1.2 and 1.6 Si mol. % respectively. XPS and TOF-SIMS was found to be within 0.1 mol. % agreement. TOF-SIMS quantification of Si was achieved using standards which were created through ion implantation of Si into HfO_2. TOF-SIMS analyses were conducted using a TOF-SIMS V instrument equipped with a Bi_n^{m+} (n = 1 - 5, *m* = 1, 2) liquid metal ion gun. Approximately 8.5 nm thick TaN top electrodes (TE) were RF sputtered on the Si-doped HfO_2 thin films. Unless specified otherwise, the 1.2 and 1.6 mol. % Si-doped HfO_2 thin films were annealed at 700 °C and 800 °C for 20 s respectively in nitrogen to crystallize the Si-doped HfO_2 thin films. 100 nm thick Ir contacts were then sputtered and subsequently lifted off to serve as a hard mask. Wet etching was carried out with a 6:1.1:1 (H_2O:H_2O_2:NH_4OH) SC1 solution

at 65°C, a similar recipe has been reported to yield a greater than 100:1 selectivity between TaN:HfO_2.[125] The patterned capacitors are 10,000μm^2.

In previous work,[115,123] the Si concentration was measured in metal/HfO_2:Si/SiO_2/Si capacitors where it was witnessed that Si diffusion into the HfO_2 film from the substrate which led to a larger incorporated Si concentration. Furthermore, the lack of a clear boundary between the likely formation of a hafnium silicate layer at the HfO_2/SiO_2 interface in metal/HfO_2:Si/SiO_2/Si structures, the inhomogeneous nature of the Si-doping profile, and the weak sensitivity factor of Si relative to Hf and O in XPS makes quantification of small concentrations of Si in thin film HfO_2 nontrivial. Hence, it is believed to be helpful to provide the ALD cycling ratio which was used to fabricate the HfO_2:Si thin films since the ferroelectric characteristics can also be tuned through the Si-dopant layering profile.[123] It should be pointed out that Mueller *et al.*[105] used a 16:1 HfO_2:SiO_2 ALD cycling ratio which achieved 3.8 mol. % Si where in this work only 1.6 mol. % Si is observed in the films; however, variations in the actual Si concentration for a given ALD cycle ratio can be expected due to different deposition tools, deposition temperatures, and oxidizers to name just a few factors.

Hysteresis measurements were carried out on the metal-ferroelectric-metal (MFM) capacitors with a Sawyer-Tower circuit at 1 kHz to obtain the polarization – electric field (P-E) plots. An Agilent 4294A was used to take capacitance-voltage (C-V) measurements with an AC signal amplitude of 50mV at 50 kHz to extract the relative permittivity characteristics of the Si-doped HfO_2 thin films. Voltage cycling was performed with bipolar square waves at 1 kHz and the terms ‘unpoled’ and ‘pulse poled’ will be used to describe ferroelectric films before and after cycling respectively. Unless

specified otherwise, all bipolar cycling was performed with an electric field magnitude of 3.5 MV/cm. Pulsed transient current measurements were carried out with an Agilent 33511B waveform generator with a 50 Ω resistor in series with the ferroelectric capacitor. Electrical pulses during the extracted switching current transients had a 100 ms delay time. All electrical measurements were performed with the bottom electrode grounded.

XPS was carried out through a Phi 5000 Versaprobe II with a monochromated Al-Kα source (1486.6 eV), an exit angle of 45°, a pass energy of 23.5 eV, and the spectrum was aligned by putting the C1s binding energy at 284.8 eV. The XPS analysis beam spot size was 200 μm in diameter. *In-situ* depth profiling during XPS was achieved using an Ar^+ gun with an accelerating voltage ranging from 0.5 keV to 3.0 keV. Grazing incidence X-ray diffraction (GIXRD) patterns were measured using a Rigaku Smartlab diffractometer with a 0.5° angle of incidence. GIXRD patterns were measured from 10 to 95° 2θ with a step size of 0.05° and a 2 s/step counting time. High-resolution cross-sectional transmission electron microscopy (HR-XTEM) was used to investigate the structure of the capacitors and measure the thicknesses of the different layers using a JEOL 2010F transmission electron microscope operated at 200 kV and equipped with a Gatan Orius SC200B digital camera. HR-XTEM specimens were prepared using an FEI DB235 scanning electron microscope/Ga^+ focused ion beam system using methods described elsewhere;[126–129] care was taken to minimize sidewall damage to the specimens by performing the final milling steps using a 5 kV Ga^+ beam.[130,131] The specimens were prepared such that the thin dimension (foil normal) corresponded to an

in-plane <110> direction; during HR-XTEM imaging, the specimen was oriented such that the incident beam was aligned to this direction.

6.3 Results and Discussion

The hysteresis loop of the Si-doped HfO_2 thin films with TaN electrodes is shifted in the positive direction along the electric field axis as can be seen in Figure 6-1. The coercive field is usually determined by the electric field values for which the polarization becomes zero in the P-E curve. For as-fabricated devices, a coercive field of .85 MV/cm was extracted from the P-E curve while an approximately 1.2 MV/cm coercive field was obtained for both Si-doped HfO_2 thin films after electric field cycling. The cycled film's coercive field is higher than the coercive field value of ~ 1 MV/cm first reported for Si-doped HfO_2 ferroelectric thin films with TiN electrodes.[20] Alternatively, the coercive field can be determined by the peaks in the switching current which in our case results in a larger coercive field of 1.4 MV/cm for the pulse poled ferroelectric films. Since the switching current peaks in the unpoled ferroelectric capacitors have coercive values of 1.3 MV/cm and are in much closer agreement with the pulse poled device, the current transient method yields a more consistent determination of the coercive field value which is not expected to change in magnitude with electric field cycling. Schenk *et al.* has provided a review on the usefulness of the transient current analysis during hysteresis measurements.[74] The negative coercive field in the as-fabricated ferroelectric capacitors is ~ 0 MV/cm as seen clearly in the negative switching current peaks in Figure 6-1 A) and C). An internal electric field, E_I, (2) is produced from the significant asymmetry in the negative and positive coercive fields.

$$E_I = \frac{|E_c^+| - |E_c^-|}{2} \tag{6-1}$$

The unpoled Si-doped HfO_2 thin films with TaN electrodes exhibit a 1.3 MV/cm internal electric field. Furthermore, the positive P_r value is ~ 0 μC/cm^2 which indicates that the as-grown ferroelectric domains are aligned in one direction pointing toward the top electrode. The situation can be illustrated by looking more closely at the current transients in Figure 6-1 A) and C). As the ferroelectric is being excited by the clockwise triangle wave during hysteresis, the switching current peak occurs at about 2.6 MV/cm during the ramp upward. However, on the return to 0 MV/cm, the ferroelectric Si-doped HfO_2 thin film already begins switching back to its original state. Hence, there is only one stable polarization state in the as-fabricated ferroelectric Si-doped HfO_2 thin film because of the overwhelming depolarization field domains encounter when they point downward toward the bottom electrode. Electric field cycling reduces the internal electric field to ~ 0.6 MV/cm in the Si-doped HfO2 thin films after 10,000 bipolar cycles and increases both positive and negative remanent polarization values.

Similar to the observations made by Zhou *et al.,*[82] a logarithmic increase in the remanent polarization during electric field cycling is observed, Figure 6-2 A)-B), given by

$$P_r = P_{r0} + A\log(N) \tag{6-2}$$

where P_{r0} is the initial remanent polarization, A is the acceleration factor, and N is the number of bipolar cycles. The acceleration factor is larger for the positive remanent polarization and increases for stronger applied electric fields. The negative acceleration factor remains constant regardless of the magnitude of the electric field. The acceleration factors extracted from the logarithmic fits are given in Table I. The simultaneous decrease in the internal electric field and increase in remanent

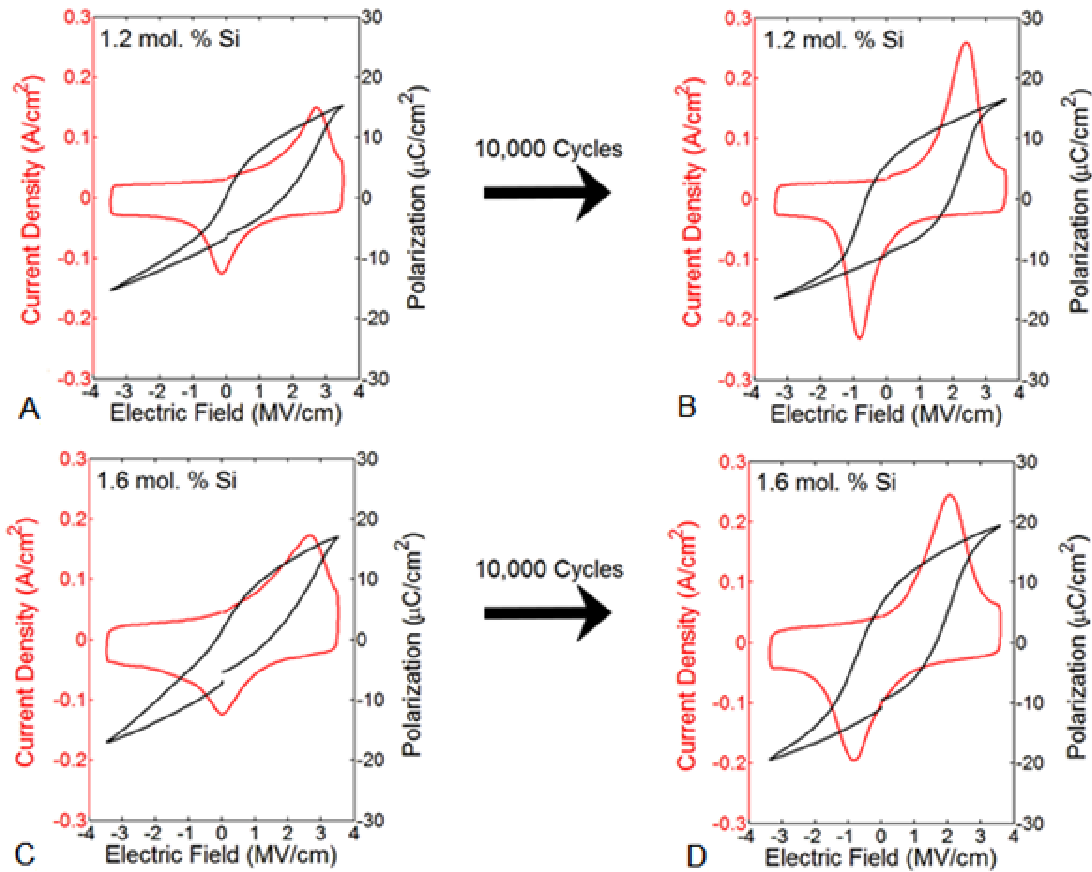

Figure 6-1. Hysteresis of the 1.2 mol. % Si films before A) and after B) 10,000 bipolar cycles illustrates the large increase in Pr and reduction of the internal bias. The 1.6 mol. % Si doped-HfO_2 thin films exhibit the same characteristics before C) and after D) cycling, but has a slightly larger background leakage current relative to the current switching peaks due to the higher anneal temperature. Both as-fabricated films have a negative coercive field ~ 0 MV/cm and a positive remanent polarization of ~ 0 μC/cm^2, indicating that the as-grown ferroelectric domains are pointing upward away from the TaN bottom electrode.

polarization lends support to the hypothesis that the redistribution or compensation of electrically charged defects is occurring with bipolar cycling. Moreover, the strong dependency of the positive acceleration factor on the magnitude of the electric field suggests that the redistribution of charged defects or defect dipoles is occurring more strongly at one electrode interface in the ferroelectric Si-doped HfO_2 thin film with electric field cycling.

Table 6-1. Acceleration factors for the Si-doped HfO_2 thin films.

	1.2 mol. % Si		1.6 mol. % Si	
Electric Field (MV/cm)	A^+ (μC/cm²)	A^- (μC/cm²)	A^+ (μC/cm²)	A^- (μC/cm²)
3.0	.334	-.234	.431	-.309
3.5	.521	-.251	.712	-.317
4.0	.676	-.236	.890	-.310

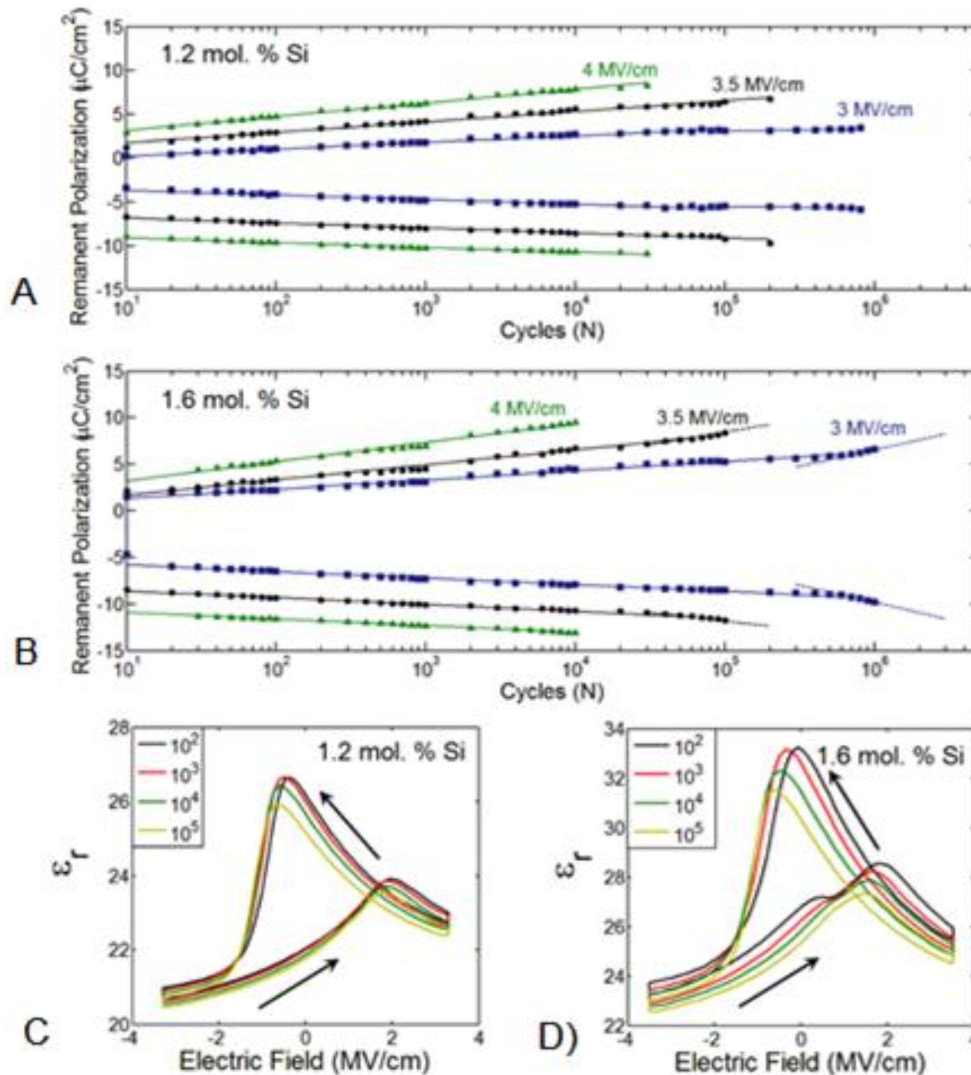

Figure 6-2. The change in the remanent polarization for the A) 1.2 mol. % Si-doped and the B) 1.6 mol. % Si-doped HfO_2 thin films exhibit a logarithmic dependence with electric field cycling, experimental data is given by the symbols and the logarithmic fits are given by the solid line. A change in the slope before breakdown indicated an increase in the leakage current contribution toward P_r and is given by a dashed line. Changes in ε_r for both Si compositions C)-D) show the switching peaks shifting left and on overall decrease in relative permittivity with electric field cycling.

The crystal structure of the Si-doped HfO_2 thin films is consistent with the tetragonal or *Pca*2_1 orthorhombic phase[116] as confirmed by GIXRD (Figure 6-3). The polar orthorhombic *Pca*2_1 space group was originally invoked to explain the emergence of ferroelectric behavior in Si-doped HfO_2 thin films.[20] Theoretical work has shown that two polar orthorhombic space groups, *Pca*2_1 and *Pmn*2_1, have very close free energies and can be formed through a distortion of the nonpolar tetragonal *P*4_2/*nmc* phase along the [001] and [100] directions respectively.[116] The concurrent increase in P_r and decrease in ε_r during electric field cycling is supportable by such a phase transformation, whereas the growth of an interfacial layer during pulsed poling would fail to explain the increase in P_r.

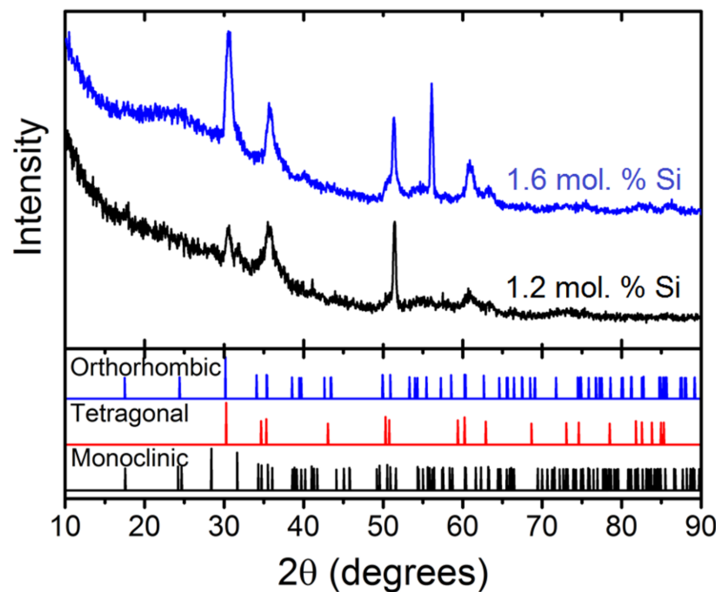

Figure 6-3. GIXRD of the Si-doped HfO2 thin films shows the crystal structure to be consistent with the tetragonal or orthorhombic phase for both compositions.

Up to this point the asymmetry in the ferroelectric characteristics still remains unexplained. As was noted in the introduction, the existence of an internal electric field is due to the unequal space charge densities at the top and bottom

electrode/ferroelectric interfaces. Motivated by this understanding, XPS was used to evaluate the chemical behavior of the TaN TE and BE interfaces on the Si-doped HfO_2 thin films. Due to the very high selectivity (100:1) of the SC1 wet chemistry with respect to TaN and HfO_2,[125] the wet-etched surface provides an excellent snapshot of the TaN/HfO_2 top electrode (TE) interface composition. Henceforth, the SC1 wet etched surface will be referred to as the TE interface. Interestingly, a significant presence of Hf-N bonds is present at the TE interface as seen by the low energy shoulder in the Hf 4*f* binding energy Figure 6-4 A). A low intensity tantalum and nitrogen signal was also picked up at the TE interface during XPS. High resolution XPS scans show that the residual tantalum on the surface is primarily metallic (Ta^0) with only a small fraction of Ta-N bonds contributing to the Ta 4*f* binding energy at the TE interface, Figure 6-4 B). Both Ta 4*f* and Hf 4*f* consist of a 4*f* 7/2 and 4*f* 5/2 spin doublet which gives rise to two peaks for each chemical species. The N 1*s* binding energy shows contributions from both N-Hf and N-Ta bonds, Figure 6-4 C). There are more N-Hf bonds than N-Ta bonds on the wet-etched TE interface, as seen by the greater contribution of N-Hf to the N 1*s* binding energy. The atomic concentration of tantalum at the TE interface is less than 4%, its detected presence after the SC1 wet etch is likely due to diffusion during the RTA and decomposition of interfacial TaN into Ta^0 and HfN. It should be noted that metallic Ta^0 has a lower etch rate than TaN for the SC1 chemistry, and since both Ta and TaN SC1 etch rates are larger than HfO_2, the TaN/HfO_2 interfacial surface composition is preserved without any contribution from the bulk of the TaN top electrode.

Using an Ar^+ ion beam during XPS, the Si-doped HfO_2 thin films were etched down to the bottom electrode (BE) interface to determine the chemical heterogeneity of the BE and TE interfaces. The Hf 4*f* binding energy at the BE interface confirms that Hf-N bonds are again present, Figure 6-4 D). Significantly, the Ta 4*f* binding energy at the bottom electrode interface shows the presence Ta-O bonds, Figure 6-4 E), thus verifying that the bottom electrode TaN interface is oxidized. The exact oxidation state of Ta cannot be resolved, but TOF-SIMS yielded the most ionized molecular fragments for TaO_2 and Ta_2O_5 respectively.

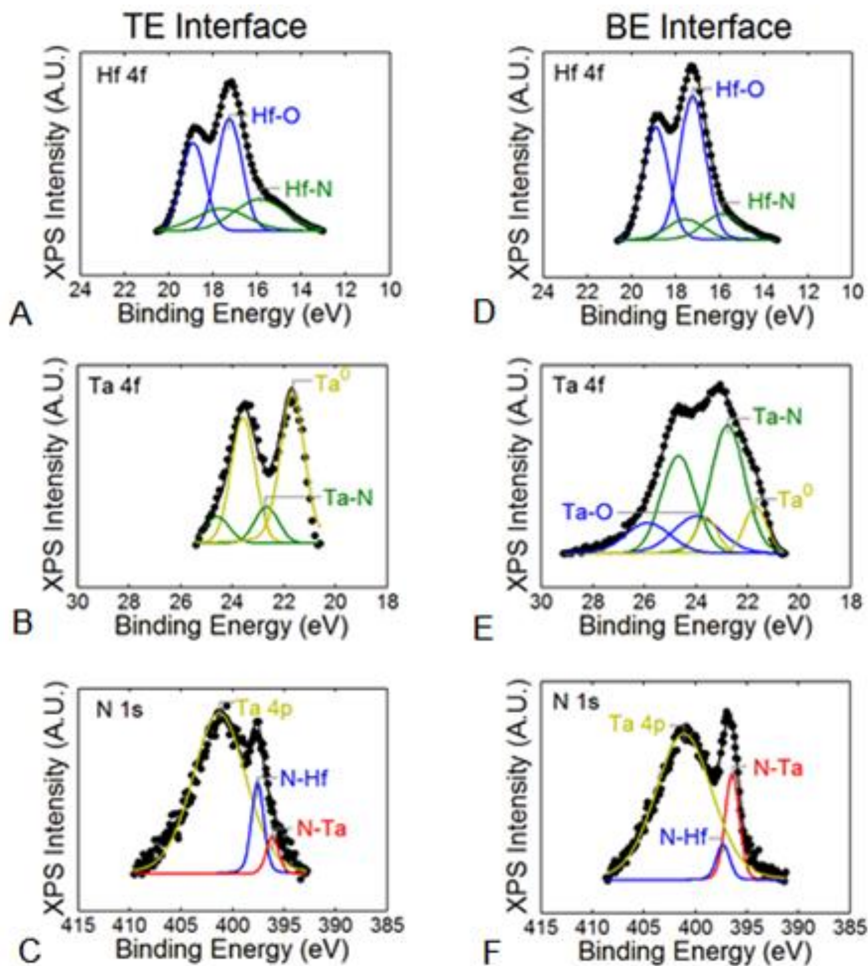

Figure 6-4. XPS analysis of the TE interface shows A) Hf-N bonds in Hf 4f, B) residual metallic Ta0 in Ta 4f, and C) both N-Hf and Ta-N bonds in N 1s. The BE interface shows D) Hf-N bonds in Hf 4f, E) Ta-O bonds in Ta 4f, and F) N-Hf and and N-Ta bonds in the N 1s binding energy.

The presence of metallic Ta^0 and Hf-N bonds suggest decomposition of TaN at the BE interface during ALD or the rapid thermal anneal. The N 1*s* binding energy of the BE interface shows a greater degree of N-Ta bonds than N-Hf bonds, Figure 6-4 F).

The observed N-Hf bonds at both electrode interfaces, in which the nitrogen atom substitutes for oxygen in the lattice, will effectively neutralize the gap states caused by oxygen vacancies and raise the valence band maximum by 0.2 eV.[132,133] Umezawa *et al.* found that when two nitrogen atoms occupy the nearest neighbor oxygen sites next to a neutral oxygen vacancy (V_O), each nitrogen atom extracts an electron and produces a positively charged oxygen vacancy (V_O^{2+}).[132] The addition of an electron to the two neighboring nitrogen atoms and the resulting production of a positively charge oxygen vacancy thus forms an electric dipole.[132] Since both electrode interfaces contain substitutional nitrogen atoms at concentrations greater than 10 atomic %, positively charged oxygen vacancies and the resulting N-V_0^{2+}-N dipole complexes are expected to be present in the films. Moreover, the redistribution of the positively charged oxygen vacancies and subsequent reorientation or randomization of the N-V_0^{2+}-N dipole complexes can explain the electric field cycling behavior in the Si-doped HfO_2 thin films. Since the bottom TaN interface is oxidized, the aggregation of V_O^{2+} at the BE interface will not be adequately screened by the sheet of electrons in the metal due to the physical separation interposed by the Ta_xO_y layer.

The situation can be visualized in Figure 6-5. The internal bias present in the Si-doped HfO_2 thin films is caused by the accumulation of positively charged oxygen vacancies at the BE. Since the positively charged oxygen vacancies are not adequately screened at the oxidized TaN BE interface, the as-grown ferroelectric domains are

polarized upward toward the TE. Thus, it is through the redistribution of V_O^{2+} accumulated at the BE interface which causes a decrease in the internal bias with electric field cycling. Oxidation of the bottom TiN electrode in ferroelectric $Hf_{0.5}Zr_{0.5}O_2$ films was also associated with a positive bias shift[92] and can be explained by this model.

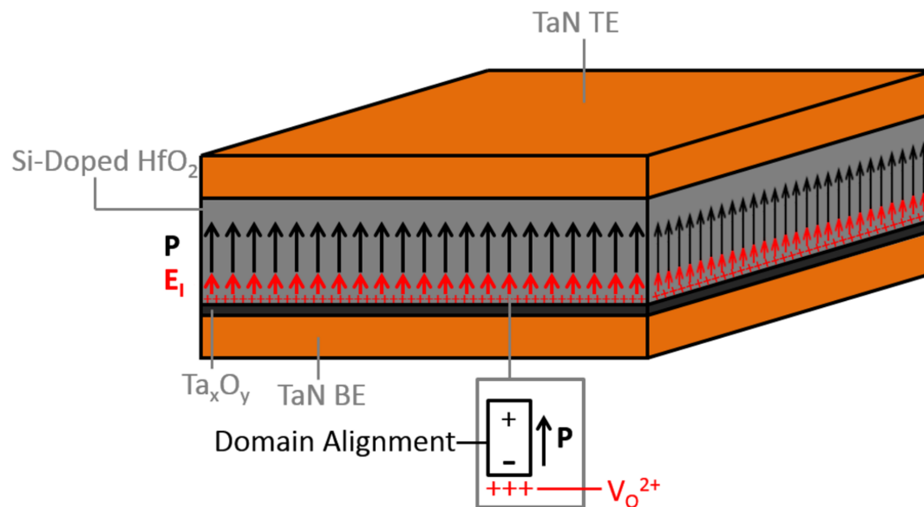

Figure 6-5. As-grown ferroelectric domains are preferentially polarized upward toward the top electrode in the Si-doped HfO_2 thin films. The accumulation of positively charged oxygen vacancies at the oxidized TaN BE interface leads to the internal bias observed in the Si-doped HfO_2 thin films.

Further confirmation of the oxidation of the TaN/HfO_2 BE interface can be seen in Figure 6-6. TEM shows a 1-2 nm thick Ta_xO_y layer present at the bottom electrode interface. The large 1.3-1.4 MV/cm coercive field observed earlier can be explained by the voltage drop across the Ta_xO_y layer which will increase the measured value of E_c. Oxidation of the TaN BE interface occurred after exposure to air during the wafer transfer to the ALD chamber and subsequent exposure to oxygen plasma during the deposition of the Si:HfO_2 thin films. Since ferroelectric HfO_2-based thin films exhibit coercive fields 1-2 orders of magnitude larger than conventional perovskite ferroelectrics, shifts in the P-E loop are necessarily accompanied by larger space

charge densities. Modeling the C-V characteristics after Brennan,[78] ionized charge densities on the order of $10^{19} – 10^{20}$ cm^{-3} are extracted which are 1-2 orders of magnitude larger than values extracted from lead zirconate titanate thin films[78,79] and supports the magnitude of the electric field shift observed in the hysteresis loop. It was found that in Sr-doped HfO_2 thin films, the activation energy for 'wake-up' cycling and subsequent fatigue was found to be one order of magnitude lower than perovskites.[88] Schenk *et al.* suggested that the redistribution of oxygen vacancies and defects along domain or grain boundaries were likely candidates for 'wake-up' and fatigue; the lower activation energies for these phenomena were attributed to the larger applied electric fields in HfO_2-based films compared to perovskite ferroelectrics.[88]

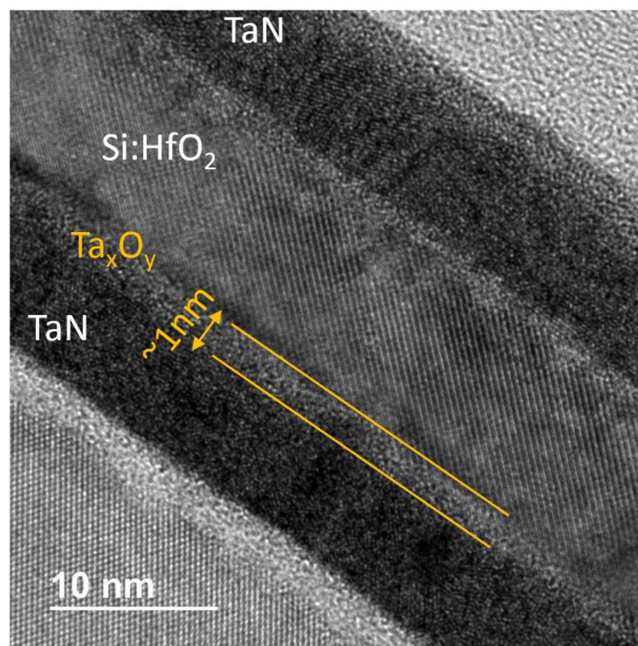

Figure 6-6. TEM confirms the presence of a ~ 1 nm Ta_xO_y layer at the TaN BE interface.

To determine if the switching kinetics were influenced by the internal electric field and the unequal space charge distribution, a variation of the Positive-Up-Negative-

Down (PUND) pulse methodology[76] utilizing repeating NPU and PND pulse trains were used to calculate P_{sw}^+ and P_{sw}^-, (Eq. 6-3) as a function of pulse width.

$$\begin{cases} P_{sw}^+ = \int J_{sw}^+(t)dt \\ P_{sw}^- = \int J_{sw}^-(t)dt \end{cases} \tag{6-3}$$

The switching current densities are extracted from the PU and ND pulse sequences given by

$$\begin{cases} J_{sw}^+(t) = J_P(t) - J_U(t) \\ J_{sw}^-(t) = J_N(t) - J_D(t) \end{cases} \tag{6-4}$$

Integrating the switching current density profile yields the switched charge resulting from the P and N pulses while the transient polarization in the U and D terms is also taken into account. Since the dielectric response and leakage current are nominally the same in the PU and ND pulses, these contributions are effectively negated in Eq. 6-4. Thus, the pulsed transient current method has the advantage of being able to account for the leakage current, dielectric relaxation, and the charging/discharging currents so that a precise extraction of the polarization switching current can be made.

Similar to previous observations in ferroelectric Si-doped HfO_2 thin films,[105] a logarithmic dependence of switched charge can be seen with pulse width in cycled films (Figure 6-7 A)), indicating that the thin films obey the nucleation limited switching model[134] whereby reverse nucleation of domains occurs through an ensemble of independently switching regions with a distribution of switching times. The as-fabricated films show power-law behavior with pulse-width and have steeper slopes than the poled devices. The power-law behavior can be attributed to the gradual redistribution of charged defects in the film during the measurement and is not believed to be an intrinsic

property of the switching kinetics within the film. Electric field cycling produces a substantial increase in the switched polarization. The switching current vs. electric field profiles for a 50 μs pulse width with a 1 μs rise time can be seen in Figure 6-7 B)-E).

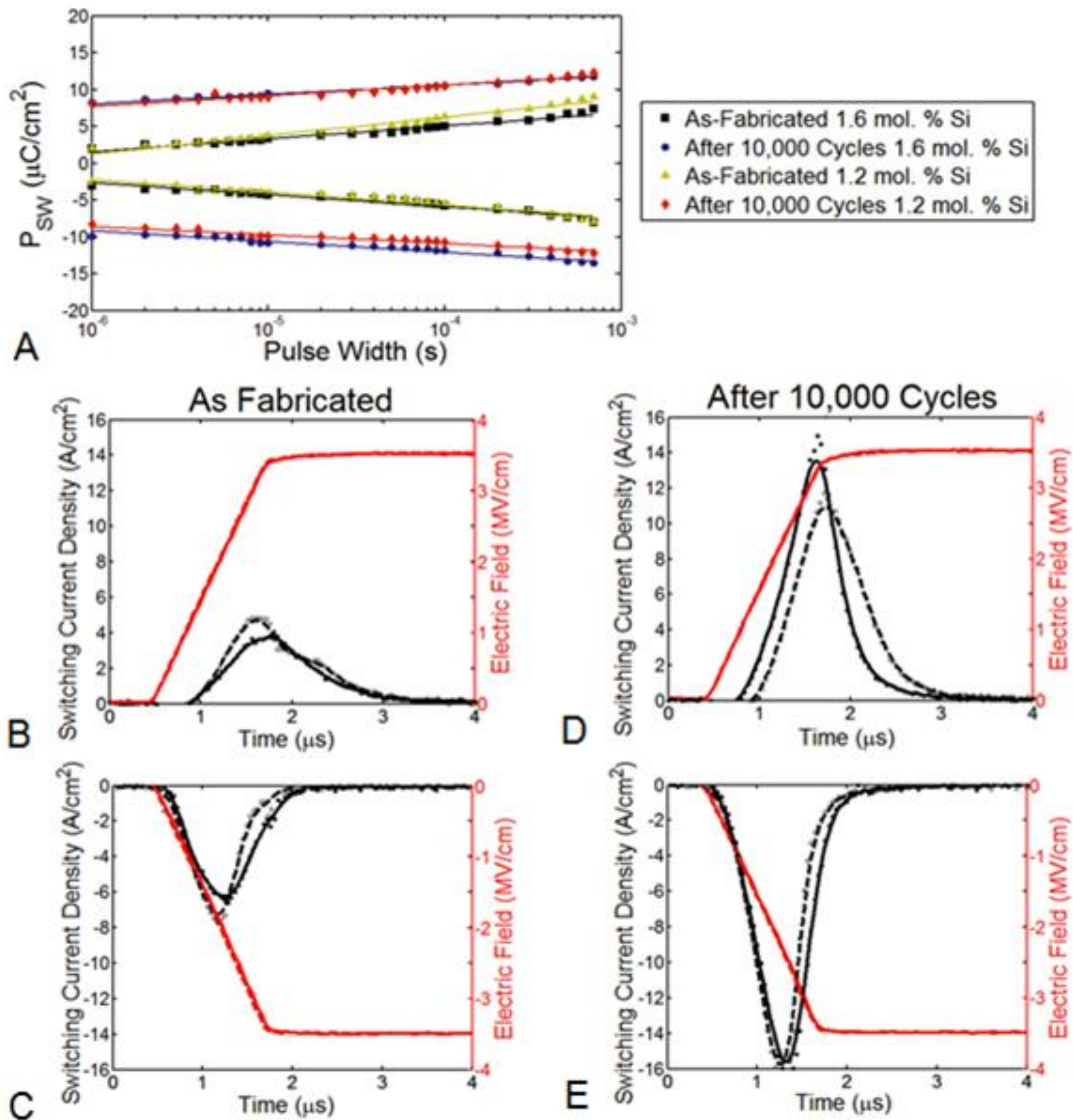

Figure 6-7. Switching properties of the Si-doped HfO_2 thin films with TaN electrodes. A) The switching kinetics of the Si-doped HfO_2 thin films follow a logarithmic dependence in accordance with the nucleation limited switching model, experimental data is given by the symbols and the logarithmic fits are given by the solid lines. B)-E) The switching current before and after electric field cycling with the 1.2 mol. % and 1.6 mol. % Si-doped HfO_2 thin films are given by the dashed and solid lines respectively as discussed in the text. The pulse width is 50 μs with a 1μs rise and fall time.

Importantly, a small second switching current transient peak is observed in the as-fabricated 1.2 mol. % Si-doped HfO_2 thin film Figure 6-7 B), dashed line, indicating that an ensemble of domains have longer switching times when attempting to reverse nucleate against the internal electric field. This would suggest that the broad tail at the end of the positive switching current accounts for the switching of domains localized near the accumulation of positively charged oxygen vacancies and defect dipole complexes at the bottom TaN electrode. Switching occurs later when reverse nucleation must overcome the internal electric field, but cycling the capacitor decreases the mean switching time for domains nucleating under a positive electric field while the switching time remains unchanged for applied negative electric fields before and after cycling. It can therefore be concluded that electric field cycling redistributes the defect charge or defect dipoles away from the TaN BE and permits faster reverse nucleation of domains at that interface.

Previous reports[20,61,122,124] on Si-doped HfO_2 thin films have shown antiferroelectric-like characteristics where the P-E loops were pinched. Pinched hysteresis loops are observed in the Si-doped HfO_2 thin films which were doped with 1.6 mol. % Si and annealed at 700 °C for 20 s, Figure 6-8 A). The current transient during hysteresis shows that the pinched P-E loop is accompanied by four broad and relatively low intensity current switching peaks in the four quadrants. This is expected for an antiferroelectric material[74] where two sub-lattices produce oppositely oriented polarization vectors and result in a net zero spontaneous polarization.[135] After electric field cycling, the hysteresis loop becomes narrow and de-pinched with only one clearly distinguishable switching peak because the merging of the negative current switching

peaks cannot be resolved above the background leakage current, Figure 6-8 B). The P-E loops in Figure 6-8 are not symmetric because $P_r \approx P_r^-$ and $P_r^+ \approx 0$ μC/cm^2, indicating that the defect charge at the bottom electrode is still influencing the antiferroelectric-like thin film's behavior. The ε_r vs. electric field profiles exhibit the double butterfly loop which is well-known to occur in PZT-based antiferroelectrics.[75] Electric field cycling subsequently suppresses two out of the four ε_r peaks with an overall decrease in relative permittivity, Figure 6-8 D). The resulting relative permittivity response to the electric field after cycling closely resembles the asymmetric switching peaks found in the ferroelectric Si:HfO_2 thin films in Figure 6-2, corroborating evidence that defect charge is influencing the switching properties of the antiferroelectric-like film. Furthermore, the two permanent ε_r switching peaks shift leftward indicating a reduction in the internal electric field. As noted earlier, the decrease in relative permittivity and the reduction in the internal bias with electric field cycling could be due to a tetragonal → orthorhombic phase transition as a result of oxygen vacancy electromigration and reorientation or elimination of defect dipoles which stabilize the ferroelectric phase. Higher Si-doping concentrations can be used to stabilize antiferroelectric behavior in thin film Si:HfO_2 with little dependence on electric field cycling.[124]

To overcome the lack of detail in the current transient during hysteresis before and after electric field cycling, pulsed transient current analysis was used to obtain a closer look at the switching current vs. electric field profile. As can be seen in Figure 6-8 E), the as-fabricated films exhibit back-switching when a positive electric field is applied. Back-switching is shown by the minima in the switching current profile and is due to the transient charge that is switched in the U pulse in the NPU pulse train. The inversion of

the polarity of the switching current density in Figure 6-8 E) possibly indicates a change in the switching kinetics of the transient polarization from the N→P and P→U pulse transitions. For this case the switched charge in the U pulse exceeded the switched charge in the P pulse for a duration of time, although the total switched charged in the P pulse is larger overall indicating the presence of some ferroelectric domains within the antiferroelectric-like film. Back-switching current transients have also been observed in antiferroelectric $PbZrO_3$ thin films.[136] Cycling the film resulted in an overall increase in the forward switching current and the magnitude of the back-switched charge was reduced.

When negative electric fields are applied to the as-fabricated thin films, back-switching still occurs which is consistent for an antiferroelectric material since a ferroelectric→antiferroelectric transition will proceed when the applied electric field is removed. In this case, back-switching is found in the D pulse in the PND pulse train, where the transient polarization decay after the N pulse leads to domain switching in the D term. Cycling the film results in the merging of the two distinct negative switching current peaks and the switched charge increases in magnitude. Furthermore, back-switching is no longer appreciable in the pulsed current transient for negative electric fields after electric field cycling. Back-switching is exacerbated when domains have to reverse nucleate against the internal electric field as seen for applied positive electric fields in the antiferroelectric-like Si:HfO_2 thin films.

Overall, electric field cycling increases the switched charge in the antiferroelectric-like Si-doped HfO_2 films regardless of the polarity of the applied electric field and results in de-pinching of the hysteresis loop. The redistribution of positively

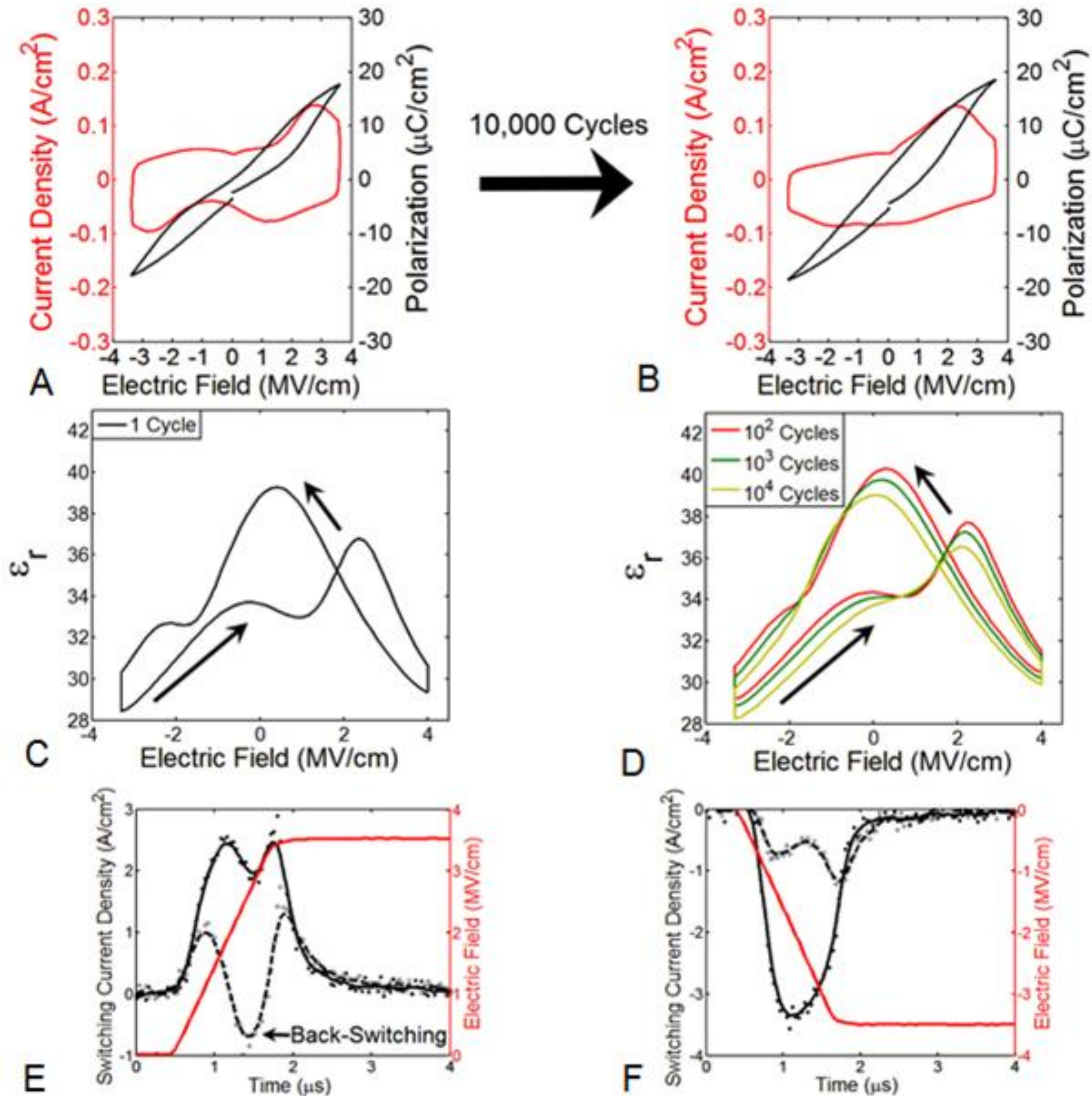

Figure 6-8. With a lower temperature anneal, the 1.6 mol. % Si-doped HfO_2 thin films exhibit a pinched hysteresis loop A) which opens up after electric field cycling B). C) Four ε_r peaks are observed as expected for an antiferroelectric material. D) Cycling the Si:HfO_2 film results in the disappearance of two of the ε_r switching peaks. The switching current density vs. electric field profile shows E) back-switching occurring for the as-fabricated films (dashed line) when nucleation must overcome the internal electric field. After 10,000 bipolar cycles (solid line), back-switching still occurs due to the depolarization field as seen by the minima in the switching current peak. F) Switching currents in the direction of the internal electric field are still subject to back-switching (dashed line), but back-switching is suppressed after 10,000 bipolar cycles (solid line).

charged oxygen vacancies and the reorientation or elimination of N-V_O^{2+}-N dipole complexes at the oxidized TaN BE is the most probable cause for the stabilization of the ferroelectric phase with electric field cycling in the pinched Si-doped HfO_2 thin films. It can be concluded that the prevention of oxidation of the electrode interface, which can be achieved through *in-situ* ALD deposition or careful selection of the electrode materials, is a prerequisite to avoid the development of internal electric fields in doped ferroelectric HfO_2 thin films.

6.4 Conclusion

Ferroelectric Si-doped HfO_2 thin films with sputtered TaN electrodes were observed to have highly asymmetric ferroelectric characteristics due to the existence of a large internal electric field. Electric field cycling increased the remanent polarization and reduced the magnitude of the internal bias as a result of the redistribution of charged defects and defect dipoles. The chemical behavior of the TaN bottom and top electrode interfaces were analyzed using XPS and it was observed that both interfaces showed nitrogen incorporation into HfO_2 while only the bottom electrode interface was oxidized. It was deduced that the most likely candidate for the internal electric field was the aggregation of positively charged oxygen vacancies (V_O^{2+}) and N-V_O^{2+}-N dipoles at the oxidized BE interface. The physical separation between the accumulated positive charge at the BE interface was inadequately screened by the sheet of electrons in the TaN electrode because of the Ta_xO_y layer. The inadequate charge screening at the electrode interface caused the as-grown ferroelectric domains to preferentially polarize upward away from the bottom electrode.

The larger, field-dependent positive acceleration factor indicated that the redistribution of positively charged oxygen vacancies and the reorientation or

elimination of defect dipole complexes at the BE occurred during electric field cycling. The simultaneous increase in P_r and decrease in relative permittivity was hypothesized to indicate structural changes in the Si-doped HfO_2 thin film as a result of the redistribution of the charged defects, notably a distortion of the higher ε_r tetragonal $P4_2/nmc$ phase to the lower ε_r $Pca2_1$ or $Pmn2_1$ polar orthorhombic phases. The switching kinetics showed the films to be governed by nucleation limited switching with longer nucleation times for domains reverse nucleating against the internal electric field. Electric field cycling improved the switching times and magnitude of the switched charge as a result of the redistribution of defect charge and defect dipoles at the BE interface. Si-doped HfO_2 thin films with pinched P-E loops exhibited four permittivity peaks and were observed to back-switch when having to reverse nucleate against the internal electric field. Subsequent cycling de-pinched the Si-doped HfO_2 thin films, reduced ε_r, caused the disappearance of two out of the four relative permittivity peaks, and increased the amount of switched charge due to the stabilization of the ferroelectric phase. The stabilization of the ferroelectric phase in ferroelectric capacitors with initially pinched P-E loops was concomitant with the reduction of the internal electric field due to the redistribution of charged defects and defect dipoles.

The emergence of internal electric fields arising from the unequal distribution of space charge at the electrodes can be detrimental to ferroelectric-based nonvolatile memory technologies because of the resulting instability of one of the polarization states. From this work it can be concluded that *in-situ* ALD electrode deposition may be beneficial to avoid oxidation of the electrode surface or that chemically inert electrode materials should be chosen to avoid the development of a depolarization field. This

work established that the antiferroelectric-like characteristics of Si-doped HfO_2 can be influenced by an internal electric field, but the relationship between internal electric fields and antiferroelectric-like behavior in HfO_2-based films requires further investigation.

CHAPTER 7
FERROELECTRIC Si-DOPED HfO_2 DEVICE PROPERTIES ON HIGHLY DOPED GERMANIUM

7.1 Background

Ferroelectric HfO_2-based thin films are compelling candidates for the realization of CMOS-compatible ferroelectric field effect transistors (FeFETs) due to the highly conformal atomic layer deposition (ALD) process and its potential for scaling.[63,137] FeFETs remain one of the most intriguing emerging memory technologies due to its small 1-transistor (1T) memory cell when compared to ferroelectric random access memory (FRAM) architectures with 1 transistor – 1 capacitor (1T/1C) and 2T/2C cells.[1] However, FeFETs have remained an elusive memory technology due to the poor compatibility of conventional perovskite ferroelectrics on Si and the emergence of strong depolarizing fields arising from the growth of interfacial layers.[62]

Recent efforts have demonstrated the feasibility of using Si-doped HfO_2 as the ferroelectric gate in FeFETs.[63,120,137] In each of those studies, a SiON interfacial layer was grown in between the Si substrate and the ferroelectric Si-doped HfO_2 thin film to form a metal-ferroelectric-insulator-semiconductor (MFIS) stack. The SiON interfacial layer (IL) ultimately leads to control of IL growth during annealing, but this comes at the cost of increasing the operating voltage.[137] Thus, despite the excellent CMOS compatibility of HfO_2-based ferroelectrics on Si, the interfacial layer between the ferroelectric Si-doped HfO_2 thin films and the Si channel still remains a reliability concern.[64]

Reprinted with permission from © 2015 IEEE. Reprinted, with permission, from P.D. Lomenzo, Q. Takmeel, C.M. Fancher, C. Zhou, N.G. Rudawski, S. Moghaddam, J.L. Jones, and T. Nishida, Ferroelectric Si-doped HfO_2 Device Properties on Highly Doped Germanium, IEEE Electron Device Lett. 3106, 1 (2015). DOI: 10.1109/LED.2015.2445352. Copyright 2015, IEEE.

One alternative is to use a different semiconductor material as the template for the ferroelectric field effect transistor such as Ge which is a candidate for future p-type FETs due to its high hole mobility.[138] High temperature anneals of HfO_2 on Ge leads to less interfacial layer growth than HfO_2 on Si [139] and ferroelectric HfO_2-based gates should be able to leverage the improved thermal stability of the Ge interface toward more robust FeFETs in the metal-ferroelectric-semiconductor (MFS) stack structure. Aiming in this direction, ferroelectric Si-doped HfO_2 thin films on p+ Si and p+ Ge substrates are compared and demonstrate that ferroelectric HfO_2 on Ge exhibits lower voltage operation similar to TaN/HfO_2:Si/TaN metal-ferroelectric-metal (MFM) device performance. The enhanced device properties of ferroelectric Si-doped HfO_2 thin films on Ge are thus presented as a path forward for the realization of Ge-based ferroelectric field effect transistors with improved reliability characteristics and low voltage operation.

7.2 Experiment

Highly doped p+ (0.001-0.005 Ω-cm) Si (100) substrates underwent a buffered oxide etch (BOE) to remove the native SiO_2 layer, and (0.008-0.05 Ω-cm) Ge (100) 6° towards (111) p+ wafers were dipped in 49 wt. % HF. A self-limiting SiO_2 layer was grown in ultrapure ozonized water on the Si substrate. For the TaN metal-ferroelectric-metal (MFM) stack, 8.5 nm TaN top and bottom electrodes were deposited by RF sputtering. Si-doped HfO_2 thin films were deposited by plasma enhanced atomic layer deposition (PEALD) at 200 °C using Tetrakis(dimethylamido)hafnium and Tris(dimethylamino)silane with a 16:1 HfO_2:SiO_2 layering ratio. The Si content was measured to be 1.6 mol. % by time-of-flight secondary ion mass spectrometry. All stacks underwent an 800 °C 20 s post-metallization anneal in N_2 to crystallize the Si-doped HfO_2 thin films. 50 nm Pt contacts were sputtered on TaN and served as a hard

mask to define the capacitor geometry. High-resolution cross-sectional transmission electron microscopy (HR-XTEM) was performed to examine the structure of the stacks using a JEOL 2010F transmission electron microscope. Hysteresis measurements were carried out at 1 kHz using a Sawyer-Tower circuit with a 220 nF capacitor connected to the top contact. The switching kinetics were studied with a 50 Ω resistor in series with the ferroelectric capacitors to extract the switching current profiles and switched charge as a function of pulse width.

7.3 Results and Discussion

HR-XTEM cross-sectional images show the Ge MFS, TaN MFM, and Si MFIS stack structures in Figure 7-1. The interface between the crystalline Si-doped HfO_2 thin film and the Ge substrate is atomically abrupt as shown in Figure 7-1 A), with possible indications of local epitaxial growth as shown by the inset. Local epitaxial growth of ZrO_2, which shares many chemical and structural similarities to HfO_2, has been previously reported on Ge.[140] An approximately 1.5 nm thick SiO_2 interfacial layer is seen in the Si MFIS stack shown in Figure 7-1 C). Oxidation of the bottom TaN interface is also observed in Figure 7-1 B).

The hysteresis characteristics of the three stacks show significant differences in the properties of the ferroelectric Si-doped HfO_2 thin films, Figure 7-2 A). The TaN MFM exhibits a positive bias shift (imprint) which is due to positively charged oxygen vacancies at the oxidized TaN bottom electrode interface.[77] 3.5 V was insufficient to reverse nucleate domains within the Si MFIS capacitor which resulted in sub-loop behavior with a small P_r, but the Si MFIS devices reach a P_r of 10 μC/cm^2 with an applied bias of 5.5 V.

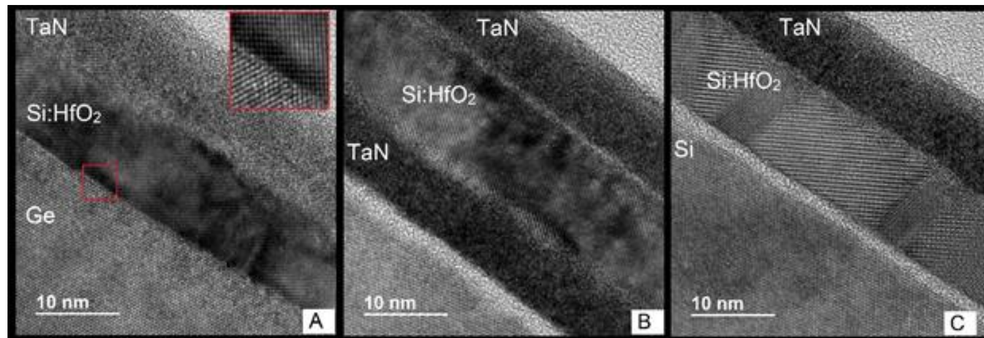

Figure 7-1. HRTEM cross-sectional images of different device stacks. A) TaN/Si:HfO_2/Ge, B) TaN/Si:HfO_2/TaN, and C) TaN/Si:HfO_2/SiO_2/Si stacks. The inset in A) shows that the crystallinity of the Si-doped HfO_2 thin film extends to the Ge substrate interface after the crystallization anneal.

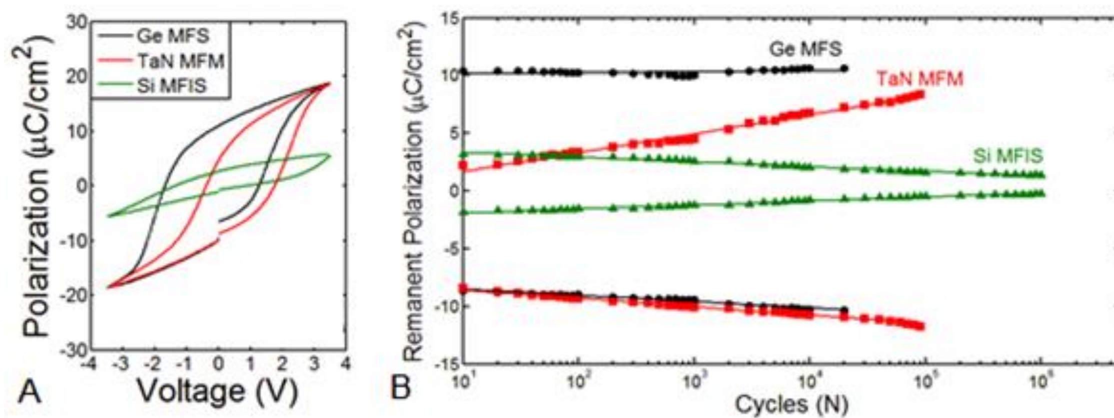

Figure 7-2. Ferroelectric characteristics of Si-doped HfO_2 on Ge. A) Hysteresis characteristics of the Ge MFS, TaN MFM, and Si MFIS at 3.5V. B) Cycling characteristics at +/- 3.5 V with 1 kHz bipolar square waves.

The Ge MFS ferroelectric characteristics are improved compared to the other two device stacks with a nearly symmetric hysteresis loop and a P_r of 10 μC/cm^2 at 3.5 V. Cycling characteristics confirm that the Ge MFS devices have stable ferroelectric characteristics whereas the TaN MFM shows the 'wake-up' effect with an increase in P_r with voltage cycling, Figure 7-2 B). The increase in P_r during wake-up is attributable to the migration of defect charges from the electrode interfaces and has been hypothesized to originate from structural changes in the Si-doped HfO_2 thin films during cycling [77]. The Si MFIS sub-loop operation during cycling is hindered by fatigue. The

maximum number of cycles was limited by breakdown in the Ge MFS and TaN MFM capacitor stacks.

The ferroelectric behavior in HfO_2-based films has been attributed to a polar orthorhombic (*Pca*2_1) phase.[20] Grazing incidence x-ray diffraction (GIXRD) of HfO_2-based films has been used to confirm the possible existence of the *Pca*2_1 phase in Si doped HfO_2 films, Figure 7-3. The sharp reflections at ~50 and ~55 2θ in MFIS and MFM films are attributed to the signal from the single crystal quartz sample holder.

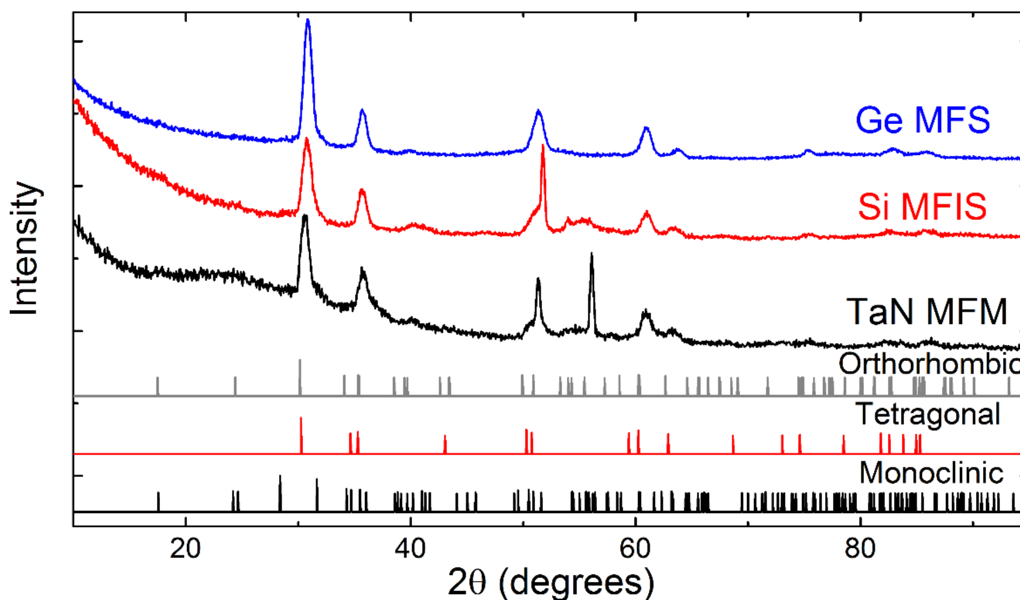

Figure 7-3. Grazing incidence x-ray diffraction shows that the Si-doped HfO2 thin films are consistent with the tetragonal or Pca2_1 orthorhombic phase.

The switching kinetics of the Si-doped HfO_2 thin films in the Ge MFS device follow a logarithmic dependence on pulse width, Figure 7-4 A). Extrapolating to a 100 ns pulse width at 4 V predicts the switched charge (P_{sw}) to be > 15 μC/cm^2 which is promising for high-speed operation of Ge-based FeFET devices. Furthermore, the lower voltage needed to reverse nucleate domains in the Ge MFS compared to the Si MFIS will ultimately lead to lower power operation for Ge based FeFETs incorporating

ferroelectric Si-doped HfO_2. Improved same state data margins have been observed in the Ge MFS compared to the Si MFIS for bakes in ambient atmosphere up to 175 °C for 300 s, likely due to improvements in the interfacial layer. Reducing the thickness of the interfacial layer or preventing it altogether can reduce the depolarization field in FeFETs. [62] The intrinsically high mobility of p-type Ge FETs may enable HfO_2-based MFS FeFET devices for the next generation of high-density, high performance nonvolatile memory devices.

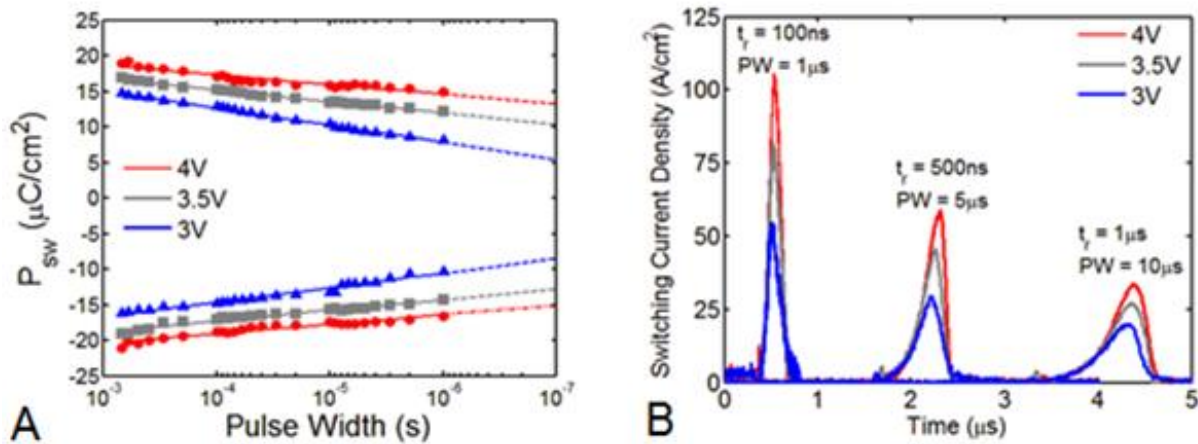

Figure 7-4. Switching characteristics of ferroelectric SI-doped HfO_2 on Ge. A) The switched charge (P_{sw}) in the Ge MFS capacitor follows a logarithmic trend with pulse width. B) Switching currents in the Ge MFS as a function of rise time (t_r) and pulse width (PW) with a 1:10 ratio. Switching current profiles were offset in the time axis from one another.

7.4 Conclusion

Three different device stacks consisting of a Si p+ MFIS, a Ge p+ MFS, and a TaN MFM were characterized to understand their influence on the ferroelectric behavior of Si-doped HfO_2 thin films. HR-XTEM showed that the Si-doped HfO_2 thin films incorporated into the Ge p+ MFS device showed abrupt interfaces with little interfacial layer growth. The lack of an interfacial oxide layer in the Ge p+ MFS devices favored a lower operating voltage when compared to the Si p+ MFIS stack. The ferroelectric Si-

doped HfO_2 thin films showed promising characteristics on the Ge substrate with nearly symmetric hysteresis loops, voltage cycling stability, and a P_r of 10 μC/cm^2. It is predicted that Ge FeFETs based on the MFS device characteristics observed in this study can provide the framework for low-power, high-speed devices with improved retention characteristics for future nonvolatile memory technologies.

CHAPTER 8
MIXED Al AND Si DOPING IN FERROELECTRIC HfO_2 THIN FILMS[5]

8.1 Background

The emergence of ferroelectricity in HfO_2-based thin films is remarkable due to the advancements it may enable for developing and emerging memory technologies such as ferroelectric random access memory (FRAM) and ferroelectric field effect transistors (FeFETs).[141] Ferroelectric behavior in HfO_2-based thin films can be generated through a suitable combination of doping and annealing conditions.[20] Various dopants have promoted ferroelectricity in HfO_2 thin films including Si, Al, Y, Gd, Sr, La, and Zr.[20,38,44,45,49,50,106,115] Atomic layer deposition (ALD) is most frequently used to deposit HfO_2 thin films because of its ability to tailor precise doping profiles[123] and its highly conformal growth process which can enable high aspect ratio device structures.[55] Ferroelectric HfO_2-based thin films are typically grown in an amorphous state and then crystallized during a rapid thermal anneal (RTA) with a capping electrode. A capping electrode during rapid thermal annealing enhances and often facilitates ferroelectric behavior in HfO_2-based thin films.[44,45,115]

The combination of chemical doping and a mechanically constraining top electrode is postulated to encourage a tetragonal to orthorhombic (t→o) phase transformation during the crystallization anneal.[20] A noncentrosymmetric, polar $Pca2_1$ orthorhombic phase is the candidate source for ferroelectricity in HfO_2 thin films. Atomic imaging has provided some structural evidence for the existence of this crystal phase,[51]

Reprinted with permission from P.D. Lomenzo, Q. Takmeel, C. Zhou, C. Chung, S. Moghaddam, J.L. Jones, and T. Nishida, Appl. Phys. Lett. 107, 242903 (2015). DOI: 10.1063/1.4937588. Copyright 2015, American Institute of Physics.

although a mixture of phases may be present in polycrystalline HfO_2 thin films after rapid thermal annealing.[40] The coexistence of the monoclinic, tetragonal, orthorhombic, and cubic phases may thus become manifest in doped polycrystalline HfO_2 thin films. In order to maximize the remanent polarization (P_r) of ferroelectric HfO_2, the fraction of the polar orthorhombic crystal phase should be increased within the thin films to enlarge the magnitude of switched charge.

While ferroelectric $Hf_{0.5}Zr_{0.5}O_2$ is attractive due its simple binary composition and low thermal budget,[40] more flexibility in engineering the properties of HfO_2-based ferroelectrics may be achieved with other dopants. For instance, adjusting the Si-dopant layering distribution in HfO_2 thin films integrated into the metal-ferroelectric-insulator-semiconductor (MFIS) structure illustrated how the P_r could be lowered by increasing the distance between the Si layers.[123] FeFETs may benefit from the engineering of the ferroelectric for lower P_r's because of the consequent reduction in the depolarization field.[62] Furthermore, the small quantity of Al and Si dopants required to induce ferroelectricity in HfO_2 thin films opens up the possibility of placing the dopants within the HfO_2 stack simultaneously. It is shown that mixed Al and Si-doped HfO_2 thin films exhibit a wide range of ferroelectric properties through the placement of the dopant layers within the HfO_2 film.

8.2 Experiment

ALD TiN bottom electrodes 10 nm thick were deposited at 200 °C on highly doped (0.001–0.005 Ω-cm) (100) p+ Si wafers. Tetrakis(dimethylamido)titanium was used as the Ti precursor and exposed to N_2 plasma during TiN growth. HfO_2 thin films doped with both Al and Si were grown by thermal ALD at 200 °C. The Hf, Al, and Si precursors used were tetrakis(dimethylamido)hafnium, trimethylaluminum (TMA), and

tris(dimethylamino)silane respectively. A 24:1 Hf:(Al, Si) pulse ratio was maintained where a total of 4 dopant layers were incorporated into the 10 nm thick HfO_2 thin films. Three different distributions of the Al and Si dopant layers within the film stack were fabricated. The three different dopant distributions may be denoted as Si-Al-Al-Si (0.87 mol. % Al, 0.49 mol. % Si), Al-Si-Si-Al (1.08 mol. % Al, 0.75 mol. % Si), and Al-Si-Al-Si (1.12 mol. % Al, 0.68 mol. % Si) which represents the placement of the dopant layers from the bottom-up within the HfO_2 film. Time of flight secondary ion mass spectrometry (TOF-SIMS) was employed to quantify the Al and Si content within the HfO_2 thin films. Approximately 2.4 nm of HfO_2 are in between each dopant layer in the as-grown films. ALD TiN top electrodes 10 nm thick were deposited at 200 °C. In previous work, we had observed ferroelectric behavior in Si-doped HfO_2 with a 24:1 HfO_2:SiO_2 ALD cycle ratio.[77] Thus, the 24:1 ALD cycle ratio was chosen to investigate mixed Al and Si doping in HfO_2 thin films. The entire TiN metal-ferroelectric-metal (MFM) stack was grown within the ALD chamber at 200 °C to prevent oxidation of the HfO_2/electrode interface.[77] The MFM stacks were annealed at 700 °C - 900 °C for 20 s in N_2. 50 nm thick Pt contacts were deposited in a liftoff process and used as a hard mask in an SC1 wet etch for capacitor geometry formation. The capacitor area was 3,600 μm^2.

The hysteresis characteristics, also referred to as polarization vs. electric field (P-E) plots, of the mixed Al and Si doped HfO_2 thin films were extracted from a Sawyer-Tower circuit with a 220nF linear capacitor and a 1 kHz triangle wave. Virgin device characteristics were extracted from the average of the first 50 hysteresis measurements. Endurance cycling was performed at 1 MHz with bipolar square waves and a 50 Ω resistor in series with the ferroelectric capacitor during cycling. Grazing

incidence x-ray diffraction (GIXRD) was performed with a Rigaku SmartLab X-Ray Diffractometer with a grazing incidence angle of 0.5 °, a .05 ° step size, and a 4 s count time per step.

8.3 Results and Discussion

Simultaneously doping HfO_2 thin films with spatially segregated Al and Si dopant layers may influence the internal strain of the ferroelectric. The strain in ferroelectric HfO_2 impacts the formation of the ferroelectric o-phase[114] and could alter the magnitude of the coercive field.[142] Internal strain within HfO_2 can be expected to arise from the mixed doping in view of the experimentally extracted differences in the HfO_2 lattice volume between pure Al (127.88 $Å^3$) and Si (129.57 $Å^3$) doped HfO_2 thin films.[142] In-plane tensile stress is thought to promote the favorable t→o phase transformation[114] and enhance the P_r for ferroelectric HfO_2 thin films.

The hysteresis characteristics of the mixed Al and Si doped HfO_2 thin films reveal significant differences in the P_r and overall shape of the P-E loop before and after electric field cycling at anneal temperatures of 800 °C and 900 °C, Figure 8-1(A)-(D). The virgin characteristics of the Si-Al-Al-Si doped HfO_2 thin films exhibit a P_r of 19 $\mu C/cm^2$ which increases by ~ 1 $\mu C/cm^2$ after cycling. The P-E loops of both the Al-Si-Si-Al and the Al-Si-Al-Si doped HfO_2 thin films look distorted horizontally in their virgin state with a P_r of 13 $\mu C/cm^2$ and 7 $\mu C/cm^2$ respectively. Cycling subsequently increases the P_r in the two films by 2 $\mu C/cm^2$ and 5 $\mu C/cm^2$ respectively. Electric field cycling, sometimes referred to as the “wake-up” effect, has been postulated to increase P_r and decrease the asymmetry in ferroelectric Si-doped HfO_2 through the redistribution of mobile defect charge (i.e. oxygen vacancies) originating from the electrode interfaces.[77,82] Since the mixed Al and Si doped HfO_2 thin films show unequal

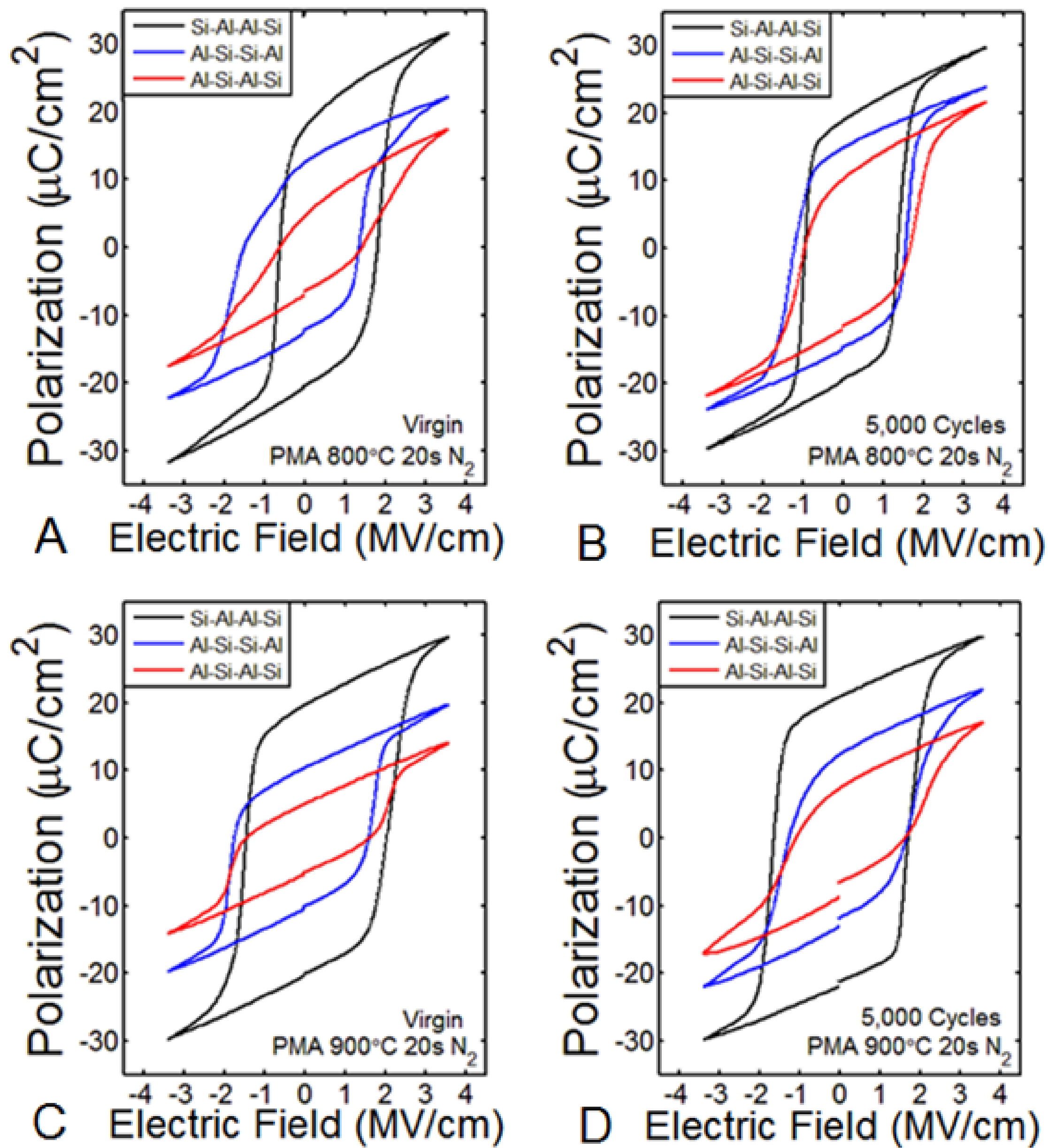

Figure 8-1. Hysteresis characteristics of the mixed Al and Si doped HfO_2 thin films annealed at 800 °C A) before and B) after 5,000 cycles. Annealing the films at 900 °C for 20 s led to increases in the coercive field in the P-E of C) the virgin and D) cycled capacitors. Cycling was performed with +/- 3.5 MV/cm bipolar square waves at 1 kHz.

enhancements of P_r with electric field cycling, lattice relaxations associated with the promotion of the o-phase may occur at different rates within the differently doped films. At 900 °C, the P_r trends amongst the three doping layering distributions remain similar,

although a significant increase in the coercive field occurs for all of the films. The remanent polarization value of ~ 20 μC/cm^2 found in these mixed Al and Si doped HfO_2 thin films are in good agreement with theoretical simulations of the spontaneous polarization predicted for the *Pca*2_1 phase of 52 ~ μC/cm^2, which is expected to be double the P_r found experimentally.[116,142] The mixed Al and Si doped HfO_2 thin films exhibit remanent polarization values comparable to Si-, Al-, and Y-doped HfO_2, although higher P_r values have been reported for Gd and La-doped HfO_2 thin films.[49]

GIXRD was used to confirm that all of the mixed Al and Si doped HfO_2 thin films show the possible existence of the *Pca*2_1 orthorhombic phase, Figure 8-2. GIXRD indicates the coexistence of multiple phases within the doped HfO_2 thin films. The full width at half maximum (FWHM) of the t(111)/o(211) diffraction peak around 30 ° is largest in the Si-Al-Al-Si and smallest in the Al-Si-Al-Si doped HfO_2 thin films. Peak width broadening of the mixed doped HfO_2 thin films supports the hypothesis that the doping distribution of the Al and Si layers may be influencing the strain of the HfO_2 thin film, although changes in grain size cannot be ruled out. Since the largest peak width broadening was found in the Si-Al-Al-Si doped HfO_2 thin films, these films may have the greatest amount of microstrain. The sharp reflections in the GIXRD plots at ~ 52 ° are attributed to the signal from the single crystal quartz sample holder.

The way in which the different dopants are layered within the HfO_2 thin films affect the formation of the orthorhombic phase through the induced strain and competing phase transformations. Since the Si-Al-Al-Si doped HfO_2 thin films exhibit the highest remanent polarization and the most significant peak broadening, it is likely that strain is aiding in the stabilization of the orthorhombic phase.

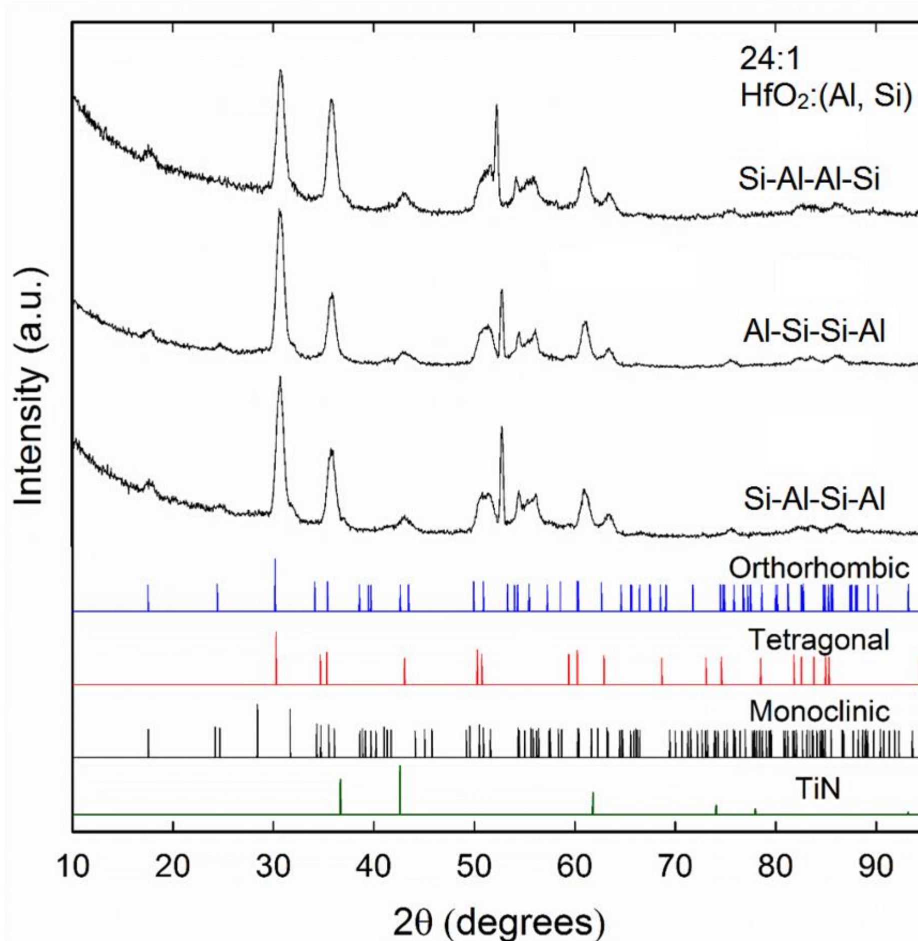

Figure 8-2. GIXRD confirms the possible existence of the orthorhombic $Pca2_1$ phase in all three of the Al and Si doped HfO_2 thin films annealed at 800 °C.

Simulations have shown that the tetragonal $P4_2/nmc$ phase may transition into the polar orthorhombic $Pca2_1$ through a suitable combination of stress and/or electric field.[116] In particular, the preferential formation of the o-phase in the Si-Al-Al-Si distribution may be generated through a large in-plane tensile strain due to the smaller Al-doped HfO_2 lattice volume compared to the larger Si-doped HfO_2 lattice volume.[114,142] The doping distribution of Al and Si in the annealed HfO_2 thin films was confirmed with TOF-SIMS, Figure 8-3. The Gaussian shape of the Si and Al distributions are caused by the limited depth resolution of TOF-SIMS. The dopant layers are consistent with a monolayer or sub-monolayer of Al or Si.

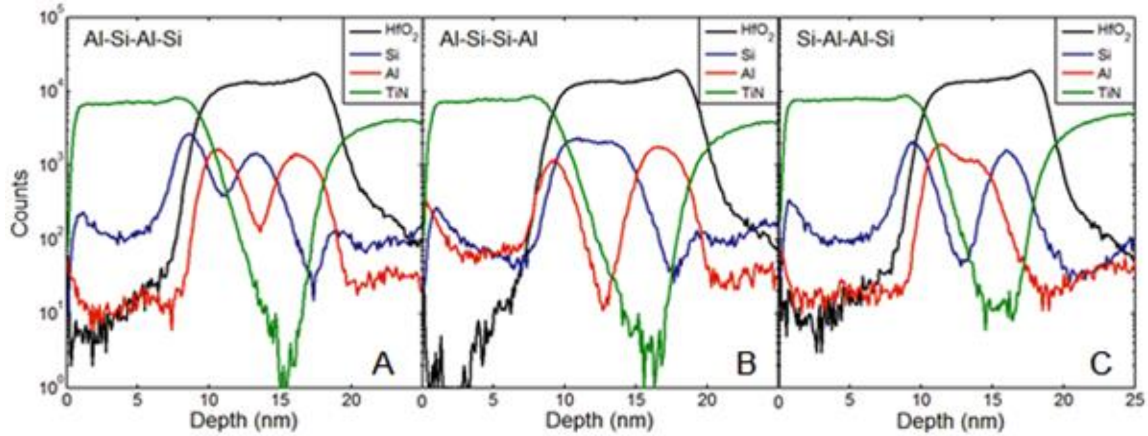

Figure 8-3. TOF-SIMS depth profiles of the A) Al-Si-Al-Si, B) Al-Si-Si-Al, and C) Si-Al-Al-Si doped HfO_2 thin films annealed at 800 °C.

High resolution cross-sectional transmission electron microscopy (HR-TEM) confirmed that the Al and Si doped HfO_2 thin films were crystallized after annealing, Figure 8-4.

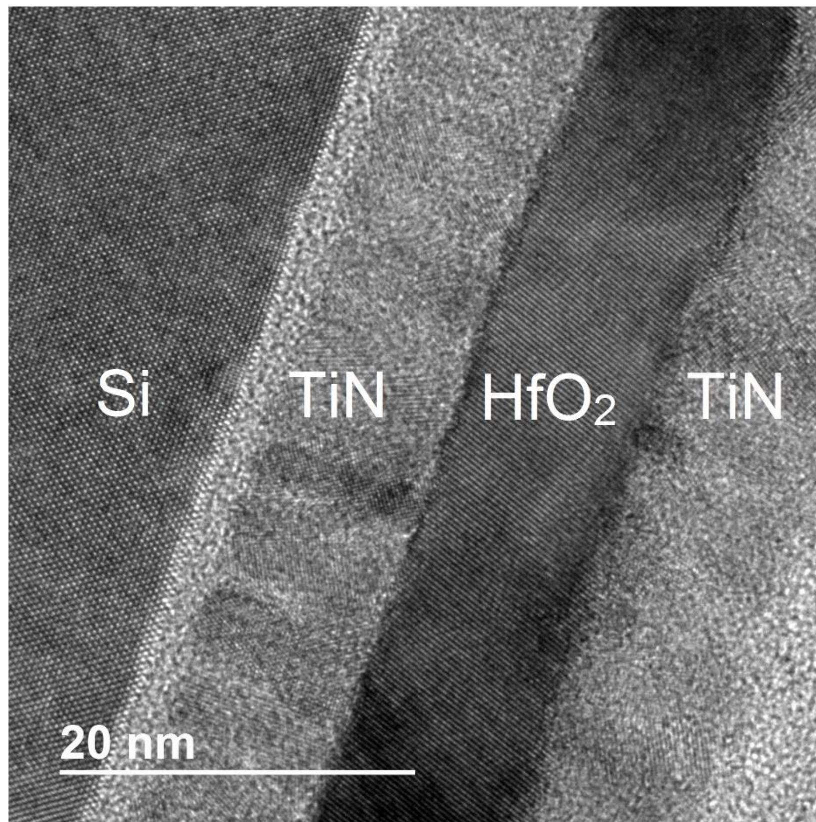

Figure 8-4. HR-TEM image of the Si-Al-Al-Si doped HfO_2 thin film after annealing at 850 °C. Lattice fringes can be seen in the polycrystalline TiN electrodes.

The P_r dependence on annealing temperature and electric field cycling are shown for the mixed Al and Si-doped HfO_2 thin films in Figure 8-5 A)-D). The Al-Si-Al-Si doped HfO_2 thin films favor a lower anneal temperature and reach a maximum virgin P_r of ~ 9 μC/cm^2 at 700 °C. The Al-Si-Si-Al doped HfO_2 thin films reach a maximum virgin P_r of ~ 14 μC/cm^2 at 850 °C. An anneal temperature range from 800 °C – 900 °C yields the highest P_r values on the order of ~ 20 μC/cm^2 in the Si-Al-Al-Si doped HfO_2 thin films with the "wake-up" effect being noticeably absent for the 800 °C and 900 °C anneals. These trends indicate that the proper selection of annealing conditions to maximize P_r are highly dependent on the doping distributions employed in HfO_2-based thin films. Endurance cycling characteristics of the Si-Al-Al-Si doped HfO_2 thin films annealed at 800 °C for 20 s are shown in Figure 8-5 D). At 3.5 MV/cm, a P_r greater than 15 μC/cm^2 is observed up to 10^8 until breakdown.

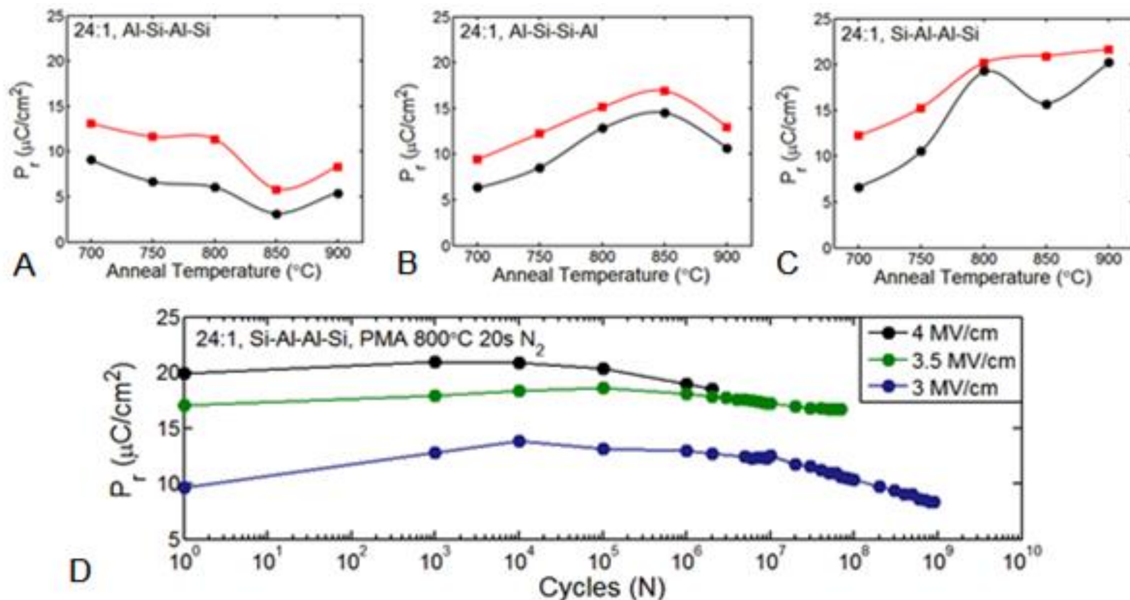

Figure 8-5. Anneal temperature dependence of the A) Al-Si-Al-Si, B) Al-Si-Si-Al, and C) Si-Al-Al-Si doped HfO_2 thin films. The black dots denote the virgin P_r and the red squares represent the Pr after 5,000 cycles at 1 kHz, 3.5 MV/cm. D) Endurance cycling of the Si-Al-Al-Si doped HfO2 thin films annealed at 800 °C for different applied electric fields.

Breakdown is accelerated at 4 MV/cm and occurs after 10^6 cycles. Cycling the mixed Al and Si doped HfO_2 thin film at 3 MV/cm delays breakdown until 10^9 cycles at the cost of a lower P_r and the acceleration of fatigue. The cycling characteristics are promising for memory applications such as FRAM which require a very high number of read and write cycles. Further optimization of the processing conditions, including the doping and annealing conditions, are likely to provide greater improvements in the maximum number of cycles HfO_2-based ferroelectrics can withstand before breakdown.

8.4 Conclusion

In summary, HfO_2 thin films 10 nm thick were simultaneously doped with Al and Si with different dopant layering distributions. The resulting ferroelectric properties in the mixed Al and Si doped HfO_2 thin films were dependent on the layering distribution and the anneal temperature. The influence of strain on the formation of the ferroelectric o-phase may be supported by differences in peak broadening measured from GIXRD which was found to be dependent on the Al and Si doping distribution. The Al and Si doped HfO2 thin films were cycled up to 10^8 times with an applied electric field strength of 3.5 MV/cm before breakdown occurred. The ability to engineer the ferroelectric properties of HfO_2 thin films by simultaneously doping HfO_2 thin films with multiple dopant species are thus presented as an accessible route for enhancing HfO_2-based ferroelectrics for a variety of applications.

CHAPTER 9
ANNEALING BEHAVIOR OF FERROELECTRIC Si-DOPED HfO_2 THIN FILMS

9.1 Background

HfO_2-based thin films exhibit ferroelectric and antiferroelectric properties under various doping and annealing conditions.[49,90] Ferroelectricity in HfO_2 thin films is intriguing since it could improve and enable nonvolatile memory technologies such as ferroelectric random access memory (FRAM) and ferroelectric field effect transistors (FeFETs). Industry adoption of ferroelectric-based memory technologies has been relegated to niche applications due to the CMOS incompatibility and poor scaling ability of conventional perovskite ferroelectric materials despite their low-power operation, fast read/write speeds, and excellent cycling characteristics (> 10^{12}).[52] HfO_2-based ferroelectric thin films may overcome these integration barriers due to its conformal atomic layer deposition (ALD) process for 3-dimensional capacitor structures,[55] sub-10 nm scaling ability, and CMOS compatibility.

Si-doped HfO_2 ferroelectric thin films crystallize at relatively high temperatures from around 650 °C – 1000 °C.[89,122] The high anneal temperature may be particularly suitable for FeFETs since the source/drain junction implantation rapid thermal anneals (RTAs) may be used to simultaneously crystallize Si-doped HfO_2.[120] Previous reports have implemented anneals in this temperature range using coarse increments of temperature (>100 °C) in a mostly isochronal manner,[20,77,89,115,120,122] but a systematic evaluation of the annealing temperature and duration on the electrical properties of Si-doped HfO_2 thin films has not been reported. The remanent polarization (P_r) of Si-doped ferroelectric HfO_2 thin films is generally enhanced at higher annealing temperatures.[89,122] A more comprehensive study on the annealing dependence of the

leakage current and breakdown field of ferroelectric Si-doped HfO_2 thin film capacitors may lead to additional insights.

Electric field cycling effects, such as wake-up and an antiferroelectric-like to ferroelectric transition, are frequently observed in doped HfO_2 ferroelectrics.[77,82,88,143] Oxygen vacancies at the electrode interfaces and within the HfO_2 thin film are one candidate for the effects of cycling,[77,88,144] although charge compensation and trapping/detrapping of charge carriers may also influence nucleation at the interfaces.[143] The cycling endurance of HfO_2-based ferroelectric thin films has tended to be limited by hard breakdown events[55,89,105,144–146] and oxygen vacancies are the prime candidate for the breakdown behavior. Oxygen vacancy conduction and vacancy filament formation are well-known phenomena in HfO_2-based resistive random access memory (RRAM) devices.[147,148] Cycling stability is a very important metric for ferroelectric memories and traditional lead zirconate titanate ferroelectrics do not exhibit breakdown despite being cycled for more than 10^{12} times.[52] Breakdown behavior in HfO_2 thin films needs to be studied in order to improve the cycling properties for memory applications. Since oxygen vacancy formation will be influenced by the annealing conditions, the breakdown behavior of ferroelectric Si-doped HfO_2 thin films will be affected by the anneal temperature and duration.

Thus, the electrical and ferroelectric properties of Si-doped HfO_2 thin films is presented as a function of anneal temperature and anneal time. Three different Si layering ratios are used to probe the influence of the annealing conditions on the differently layered Si-doped HfO_2 thin films. The RTA dependence of the electrical characteristics of Si-doped HfO_2 thin films incorporated into ALD TiN metal-ferroelectric-

metal (MFM) capacitors are discussed in detail, readers are referred to related works for structural details on Si-doped ferroelectric HfO_2 thin films.[20,77,115,122]

9.2 Experiment

10 nm thick ALD TiN electrodes were deposited at 200 °C on highly doped (0.001–0.005 Ω-cm) (100) p+ Si wafers. N_2 plasma was used with tetrakis(dimethylamido)titanium to grow the TiN electrodes. HfO_2:SiO_2 ALD thin films 10 nm thick were deposited at 200 °C with O_2 plasma using tetrakis(dimethylamido)hafnium and tris(dimethylamino)silane as the Hf and Si precursors respectively. HfO_2:SiO_2 layering ratios of 24:1, 16:1, and 12:1 were used to produce ferroelectric and antiferroelectric properties in the 10 nm thick HfO_2 thin films which contained 4, 6, and 8 layers of Si respectively. Fabrication of the TiN MFM capacitors was realized through *in situ* ALD growth at 200 °C to maintain pristine HfO_2/electrode interfaces.[77] Rapid thermal anneals were performed at 700 °C – 900 °C with durations between 5 s – 60 s in N_2. 50 nm thick Pt contacts were patterned in a liftoff process, then used as a hard mask with an SC1 wet etch to form the capacitors. Electrical measurements were performed on capacitors with areas of 3,600 μm^2 and 14,400 μm^2.

A Sawyer-Tower circuit was used with a linear 220 nF capacitor connected to the grounded conducting substrate during hysteresis measurements. A 1 kHz triangle wave was delivered to the top contact to extract the hysteresis characteristics of the Si-doped HfO_2 thin films. Hysteresis loops for the virgin or as-fabricated films are extracted from the average of the first 50 hysteresis measurements. Capacitance – voltage (C – V) measurements to extract the relative permittivity vs. voltage (ε_r – V) curves were undertaken on an Agilent 4294A with an amplitude of 50 mV and a 50 kHz frequency.

Cycling was performed with bipolar square waves at 1 kHz with a 50 Ω resistor in series with the ferroelectric capacitor. Dynamic hysteresis current measurements were also carried out with a 50 Ω series resistor which replaced the 220 nF sense capacitor. Leakage current densities and breakdown fields were extracted with a Keithley 4200. Breakdown field measurements were performed with a 1 V/s sweep rate. A current density of 250 mA/cm^2 was used to define the hard breakdown event.

9.3 Results and Discussion

The ferroelectric properties of Si-doped HfO_2 thin films can be highly dependent on the annealing conditions used and the Si doping.[122] Higher anneal temperatures tend to lead to a larger remanent polarization in Si-doped HfO_2 thin films[89,115,122] and we observe a similar trend in the hysteresis characteristics of the Si-doped HfO_2 thin films in Figure 9-1. Pinching of the virgin hysteresis loops occur at 700 °C for both the 24:1 and 16:1 layered thin films. This antiferroelectric-like behavior can be modified with electric field cycling to increase the remanent polarization and open up the hysteresis loops. 700 °C was insufficient to crystallize the 12:1 HfO_2:SiO_2 layered films, as shown by its paraelectric behavior, but the films become antiferroelectric at anneal temperatures ≥ 750 °C. The antiferroelectric behavior is relatively stable with cycling in the 12:1 layered films. Martin *et al.* also demonstrated the cycling stability of antiferroelectric Si-doped HfO_2 thin films with the highest Si content (~ 8.5 mol. %) reported in that work.[124] The antiferroelectric-like behavior that is present at 700 °C in the 24:1 and 16:1 layered films transitions to a ferroelectric response at 900 °C, indicating that an antiferroelectric-like → ferroelectric transition occurs with increasing anneal temperature. Figure 9-2 demonstrates the antiferroelectric-like → ferroelectric

transition with increasing anneal temperature as seen in the ε_r switching peaks in the 24:1 HfO_2:SiO_2 layered thin films.

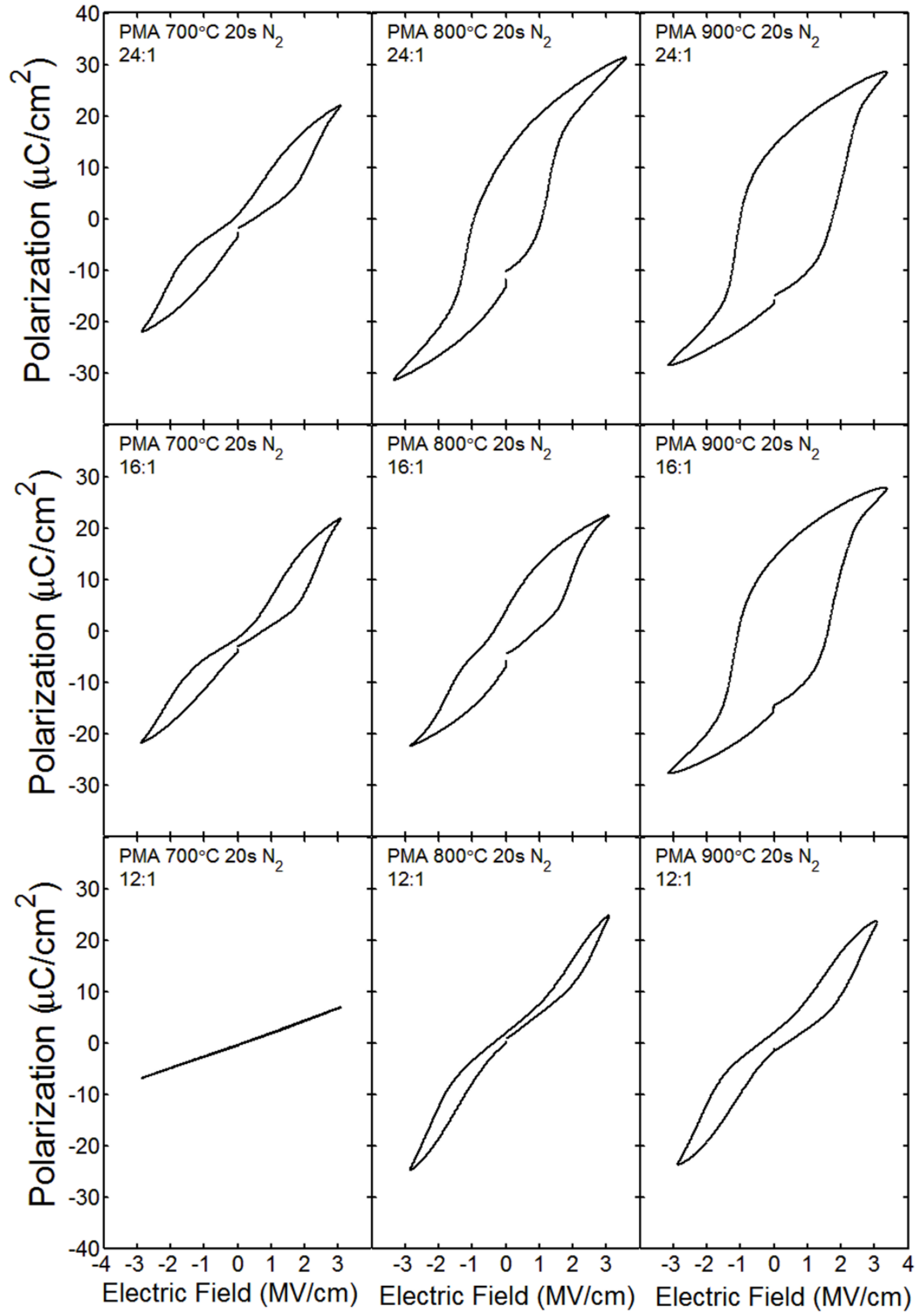

Figure 9-1. The virgin hysteresis characteristics of the 24:1 and 16:1 HfO_2:SiO_2 thin films show an antiferroelectric-like to ferroelectric transition for increasing anneal temperature. The paraelectric behavior of the 12:1 HfO_2:SiO_2 thin films annealed at 700 °C indicates the films are amorphous, while higher temperatures lead to antiferroelectric properties.

A merging of the four switching peaks of the double butterfly loop converges into two switching peaks characteristic of ferroelectrics as the anneal temperature is increased. In contrast to the more lightly doped HfO_2 thin films, the 12:1 films retain antiferroelectric behavior at 900 °C, although they exhibit greater loss as seen by the increase in the internal area of the hysteresis loop in Figure 9-1.

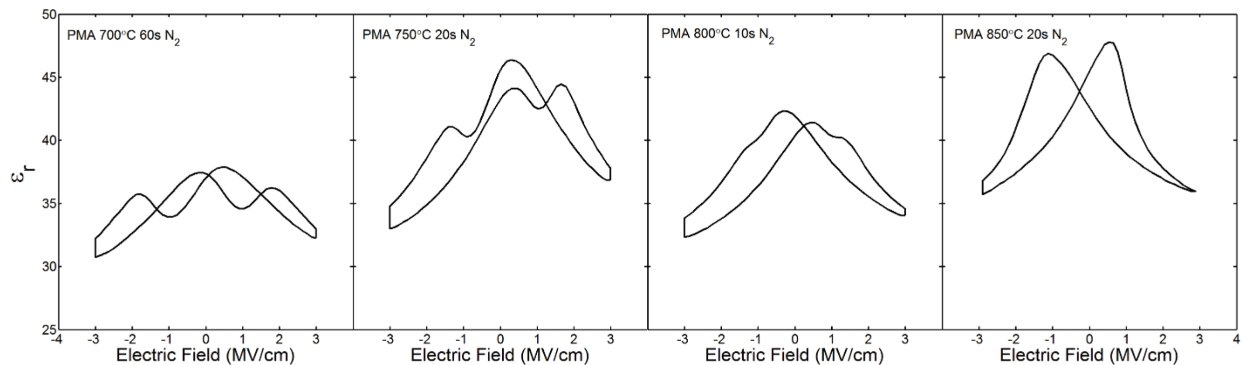

Figure 9-2. The relative permittivity of the virgin 24:1 HfO_2:SiO_2 captures the antiferroelectric-like to ferroelectric transition which occurs with increasing anneal temperature. The four switching peaks in the double butterfly loop merge into two switching peaks from left to right as the anneal temperature is increased.

The P_r of the layered HfO_2:SiO_2 thin films after wake-up cycling is plotted as a function of anneal temperature with a 20 s anneal duration in Figure 9-3 A). The 24:1 films have the highest P_r across the entire anneal temperature range compared to the other film compositions, peaking at approximately 15 μC/cm^2 around 850 °C and 900 °C. Since antiferroelectric behavior is more stable in the 12:1 HfO_2:SiO_2 thin films, the P_r values are on the order of 1 μC/cm^2 except at 900 °C, where the effects of cycling begin to de-pinch the hysteresis loop. Thus, even Si-doped HfO_2 thin films with relatively large amounts of Si incorporation can begin to exhibit field cycling effects when the anneal temperature is large enough. Intermediate P_r values are extracted from the 16:1 layered films and they start to converge with the 24:1 films at 900 °C. The remanent polarization

of the Si-doped HfO_2 thin films becomes larger with increasing anneal temperature, and the greater Si content within the HfO_2 thin films requires higher anneal temperatures to avoid antiferroelectric-like characteristics.

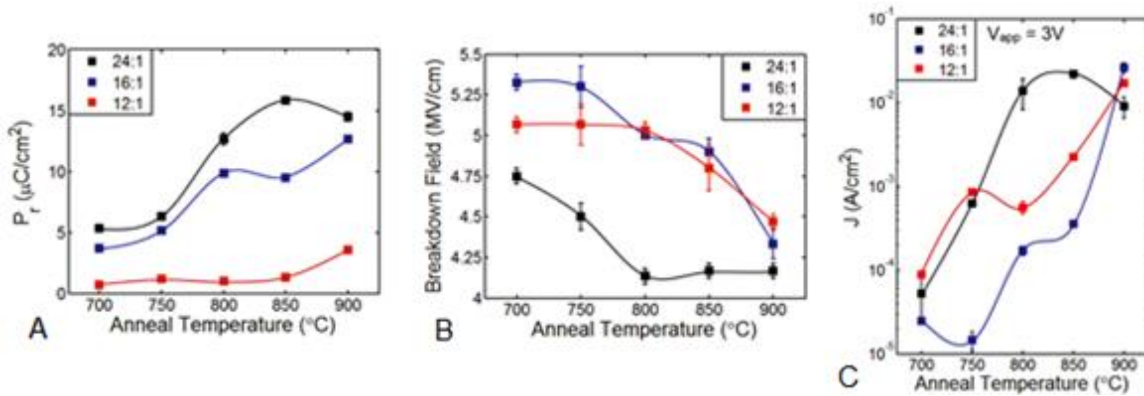

Figure 9-3. Electrical and ferroelectric parameters of Si-doped HfO_2 with anneal temperature. The A) remanent polarization (P_r), B) breakdown field, and C) leakage current density at 3V for the three layered Si-doped HfO_2 thin films as a function of anneal temperature with a 20 s anneal time. The P_r was extracted after 1,000 cycles, whereas the breakdown field and leakage current density were measured on as-fabricated capacitors. Symbols in some cases are larger than the error bars.

The breakdown fields in the Si-doped HfO_2 thin films decrease with increasing anneal temperatures, Figure 9-3 B). The most lightly doped HfO_2 thin films exhibit the lowest breakdown fields across the temperature range with a 4.75 MV/cm maximum at 700 °C and a 4.2 MV/cm minimum at 800 °C. Both the 16:1 and 12:1 layered films exhibit breakdown fields ≥ 5 MV/cm at anneal temperatures less than or equal to 800 °C, indicating that a greater amount of Si incorporation can improve the breakdown characteristics of HfO_2 thin films for low to moderate anneal temperatures. At 900 °C, the breakdown fields in all of the Si-doped HfO_2 thin films begin to converge, indicating that increasing the Si-doping may not be a feasible route to enhance the breakdown characteristics of films annealed at the highest temperature where the P_r tends to maximized. Thus, the breakdown characteristics and the ferroelectric performance

(nominally determined by P_r) improve for low temperature and high temperature anneals respectively in Si-doped HfO_2 thin films.

Leakage current densities of the Si-doped HfO_2 thin films increase with anneal temperature in all of the layered HfO_2:SiO_2 thin films, Figure 9-3 C). At anneal temperatures of 700 °C and 750 °C, the leakage current densities of the 12:1 and 24:1 films are nearly the same whereas an improvement of almost 1 – 2 orders of magnitude is observed in the 16:1 HfO_2:SiO_2 thin films. At moderate anneal temperatures, the 24:1 films exhibit the highest leakage current densities while the 16:1 films have a leakage current density two orders of magnitude lower. While increasing the number of Si layers does not uniformly improve the leakage current densities across the entire anneal temperature range, greater Si incorporation does result in an overall improvement with moderate anneal temperatures compared to the most lightly doped Si-HfO_2 thin films. At 900 °C, the leakage current densities of all of the Si-doped HfO_2 thin films become very similar.

The lower breakdown field, higher leakage current density, and increased P_r with higher anneal temperatures in all of these Si-doped HfO_2 thin films suggests that the three parameters may be correlated in these capacitors, which may point to a single underlying mechanism. The trends suggest that the creation of defects, such as oxygen vacancies, is promoted with higher anneal temperatures and would certainly lead to a lower breakdown field and higher leakage current density. Similar trends in P_r and breakdown behavior were observed when TiN electrodes were replaced by TaN electrodes, with the latter being hypothesized to more efficiently scavenge oxygen from HfO_2 and thus lead to more oxygen vacancies in Gd-doped HfO_2.[144] In that work, *ab*

initio simulations were used to confirm that oxygen vacancies may encourage the stabilization of the ferroelectric phase compared to the paraelectric monoclinic phase. Therefore, the oxygen vacancy model could very well be applicable to the annealing temperature trends that we observe in the Si-doped HfO_2 thin films whereby an increase in P_r, due to the greater stabilization of the ferroelectric phase, is attended with a decrease in breakdown field and larger leakage current densities.

The anneal time dependence of the P_r for the 24:1 HfO_2:SiO_2 thin films is shown in Figure 9-4 A). The P_r does not change much from 5 s – 40 s at 700 °C, but the 60 s anneal doubled the P_r to 10 μC/cm^2. Therefore, there may be some benefit to extending the relatively low 700 °C anneal temperature to 60 s durations and beyond for enhanced ferroelectric characteristics with a lower thermal budget for the Si-doped HfO_2 thin film system. At 800 °C, the remanent polarization increases from about 10 μC/cm^2 to 13 μC/cm^2 from 5 s to 40 s anneal durations. P_r peaks at 18 μC/cm^2 for a 40 s anneal time at 900 °C. Overall, the remanent polarization can undergo a 30 % – 50 % change by varying the anneal time at a given temperature in the 5 s – 60 s range. Longer anneal times tend to promote a larger P_r in the Si-doped HfO_2 thin films.

The breakdown field shows a clear anneal time dependence at 700 °C, but at higher temperatures no dominant trend with anneal time is present, Figure 9-4 B). The breakdown field undergoes a small decrease from 5 s – 40 s at 700 °C, but then drops from approximately 4.7 MV/cm to almost 4.4 MV/cm at 60 s. The breakdown field generally decreases with anneal time at 900 °C, but at 800 °C the anneal time is a poor indicator of the breakdown characteristics. Since the anneal temperature is a strong indicator of the expected breakdown field range, it may serve as a more reliable metric

than the anneal times explored in this work. Trends in the leakage current density versus anneal time, as shown Figure 9-4 C), follow opposing lines as the breakdown field time dependence. At 700 °C the leakage current density generally increases with anneal time, whereas no consistent anneal time dependence is observed at higher anneal temperatures. Therefore, the anneal temperature is a better predictor of the leakage current density than the duration of the anneal.

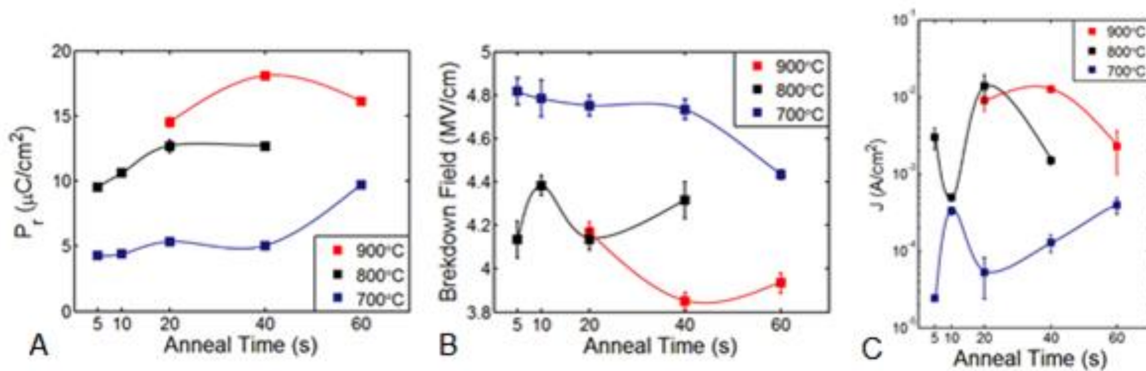

Figure 9-4. Electrical and ferroelectric parameters of Si-doped HfO_2 with anneal time. The anneal time dependence of the A) P_r, B) breakdown field, and C) leakage current density for 24:1 HfO_2:SiO_2 thin films at 700 °C, 800 °C, and 900 °C. The P_r was extracted after 1,000 cycles, whereas the breakdown field and leakage current density were measured on as-fabricated capacitors. Symbols in some cases are larger than the error bars.

The anneal time, while not as strongly influential as the anneal temperature, can substantially affect the remanent polarization, but the leakage current and breakdown field are largely determined by the anneal temperature in the 800 °C – 900 °C range. The strongest temporal dependence is found in the relatively low anneal temperature at 700 °C where the increase in P_r, and simultaneous decrease in breakdown field and higher leakage current density attends the longer anneal durations. Hence, the anneal time trends, when present, reflect the same overall correlation of the P_r, breakdown field, and the leakage current density as the trends reflected with anneal temperature.

The creation of oxygen vacancies can certainly be expected to be dependent on both the anneal time and temperature, though the clearer, more consistent trends in anneal temperature seem to indicate that the RTA temperature plays the dominant role in determining the ferroelectric and electrical properties in the TiN MFM thin film capacitors.

Electric field cycling and the ferroelectric properties of Si-doped HfO_2 thin films are affected by the annealing conditions and the Si-dopant layering ratio, as shown in Figure 9-5. Three unique cases of electric field cycling are identified in the ferroelectric and antiferroelectric-like capacitors. The pinching of the polarization – electric field (P – E) loop in as-fabricated 24:1 films annealed at 750 °C open up with electric field cycling, Figure 9-5 A). Dynamic hysteresis currents confirms that the virgin 24:1 films have four switching current peaks near or within all four quadrants, indicating that the behavior is consistent with an antiferroelectric material.[74] The four switching current peaks begin to merge into two dominant switching current peaks with electric field cycling and become stable at about 1 MV/cm, the coercive field of ferroelectric Si-doped HfO_2. Thus, standard hysteresis measurements and dynamic switching currents indicate that antiferroelectric characteristics are present in the as-fabricated HfO_2 thin films but undergo a transition to ferroelectric behavior with electric field cycling.

In contrast to the 24:1 HfO_2:SiO_2 thin films, the 12:1 thin films annealed under the same conditions exhibit relatively stable antiferroelectric properties with electric field cycling, Figure 9-5 C)-D). The hysteresis loops of the antiferroelectric thin films undergo some reduction in pinching and an increase in spontaneous polarization with cycling.

Interestingly, the positive and negative switching current peaks move inward towards lower electric fields with cycling.

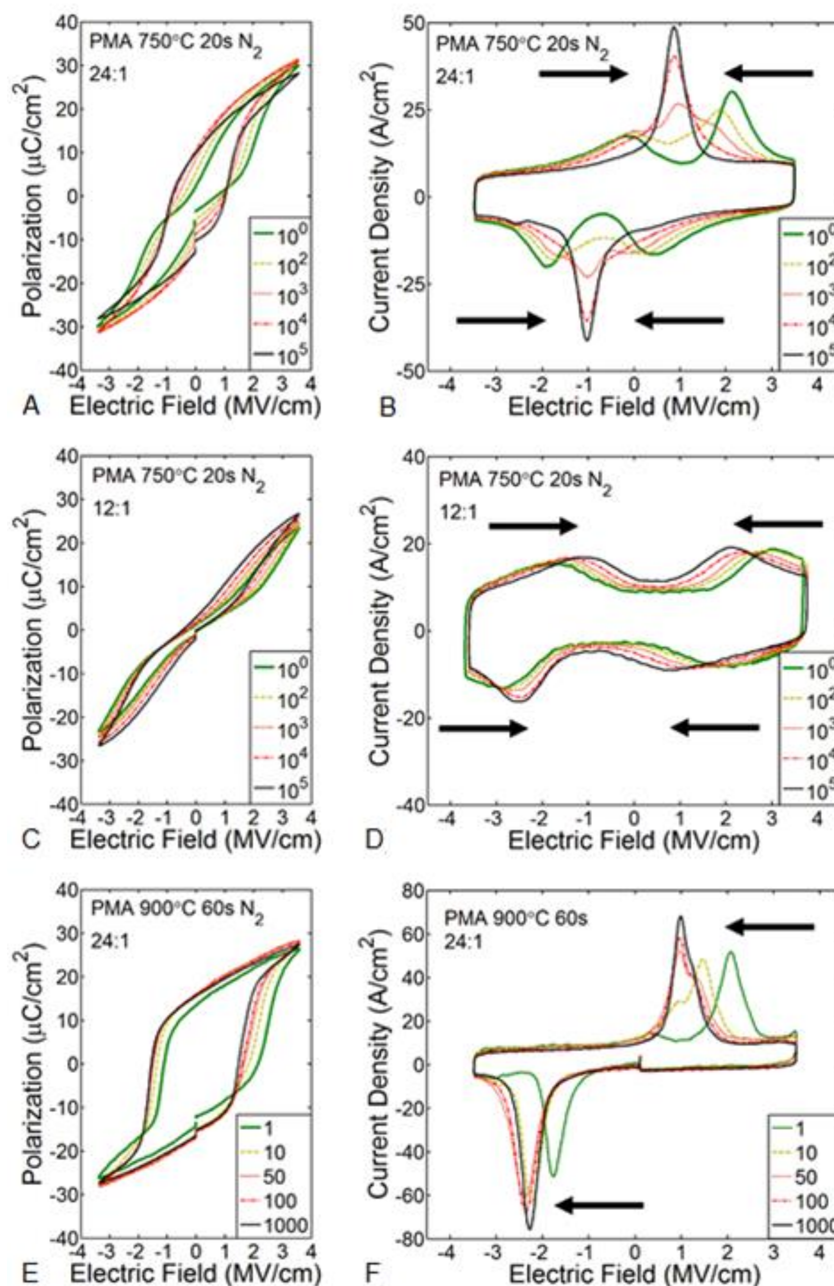

Figure 9-5. Three unique cases demonstrating the effects of electric field cycling in the Si-doped HfO_2 thin films are shown with the hysteresis and dynamic hysteresis current plots side by side for A) - B) the antiferroelectric-like to ferroelectric transition, C) – D) stable antiferroelectric characteristics, and E) – F) the reduction of imprint in 900 °C 60 s annealed 24:1 layered HfO_2:SiO_2 thin films.

The observed stability in antiferroelectric behavior in the thin films seems to be related to the higher electric fields needed to cause an antiferroelectric → ferroelectric field transition, where the switching current peaks are further away from the origin and more distinctly located within the four quadrants of the hysteresis plot. The ferroelectric 24:1 HfO_2:SiO_2 thin films annealed at 900 °C for 60 s show a small positive bias imprint in the as-fabricated MFM TiN capacitors, Figure 9-5 E)-F). After just 5 cycles, both switching current peaks shift leftward by approximately 0.5 MV/cm. Increasing the number of cycles leads to a split-up in the positive switching current peak to two peaks whereby the small switching peak at 1 MV/cm becomes dominant and absorbs the higher field induced positive switching current with increasing cycles. After the initial 5 cycles, the negative switching current peak increases in height but does not change its location.

Imprint has been hypothesized to originate from the aggregation of positively charged oxygen vacancies at the oxidized bottom electrode interface in TaN MFM capacitors,[77] and the possibly greater tendency towards oxidation by TaN compared to TiN electrodes has been linked to larger coercive fields.[144] Since two different time-scales of change in the switching current peaks with electric field cycling occurs, two separate mechanisms are likely occurring in the TiN MFM capacitors which influence the ferroelectric switching characteristics. The rapid leftward shift field within the first 5 cycles is unlikely to be generated by the redistribution of oxygen vacancies, but points to the possibility of trapping and/or detrapping of charge carriers at one or both of the electrode interfaces. The split-up into two positive switching current peaks and their gradual merging together over 1,000 cycles may instead be attributable to the

redistribution of charged defects such as oxygen vacancies which could depin ferroelectric domains and assist in reducing the energy required for reverse nucleation at the interface. The larger 2.2 MV/cm negative coercive field suggests that strong oxidation occurs at one of the TiN electrodes. The high 900 °C anneal temperature with a 60 s anneal time may lead to chemical changes in the TiN electrodes and a worsening of the quality of the interface since TiN has been known to exhibit a strong oxidation dependence on anneal temperature.[149,150]

9.4 Conclusion

The anneal temperature and anneal time dependence of Si-doped HfO_2 thin films incorporated into TiN metal-ferroelectric-metal capacitors was investigated with different Si dopant layerings. A strong temperature dependence of the P_r, breakdown field, and leakage current densities was observed in the HfO_2:SiO_2 thin films. An antiferroelectric-like to ferroelectric transition with increasing anneal temperature was identified from 700 °C – 900 °C. While moderate to high anneal temperatures did not lead to clear trends with anneal time, increasing the anneal duration at lower anneal temperatures showed similar effects on P_r and the breakdown field as raising the anneal temperature. The anneal time dependence of P_r lead to variations of 20 % - 50 %, with longer anneals generally producing higher remanent polarizations.

A correlation of increasing P_r and larger leakage current densities was observed with a reduction in the breakdown field at higher anneal temperatures. The creation of defects, such as oxygen vacancies, was proposed as a likely candidate in facilitating the influence of the RTA conditions on the electrical and ferroelectric properties of Si-doped HfO_2 thin films. Electric field cycling effects for three distinct film behaviors demonstrated the importance of the annealing conditions on the properties of Si-doped

HfO_2 thin films. This study adds growing evidence to the link between the RTA conditions and the ferroelectric properties of Si-doped HfO_2 whereby the creation of oxygen vacancies and the interaction between the TiN electrodes with the HfO_2 thin film may play a dominant role in the overall behavior of the ferroelectric HfO_2 thin films.

CHAPTER 10
STUDIES ON FERROELECTRIC AND ANTIFERROELECTRIC HAFNIUM-ZIRCONIUM OXIDE-BASED THIN FILMS

10.1 Background

The ferroelectric and antiferroelectric characteristics of $Hf_xZr_{1-x}O_2$ thin films are interesting because of the complete miscibility of the hafnia-zirconia material system.[12,21,39] Moreover, ferroelectric $Hf_xZr_{1-x}O_2$ thin films may be particularly suited for integrated microelectronic applications because of their relatively low crystallization temperature (400 – 800 °C) and resistance to hydrogen annealing.[40,59] It has been demonstrated that optimal ferroelectric properties tend to occur at the binary $Hf_{0.5}Zr_{0.5}O_2$ composition, whereas increasing the Hf content leads to an increasing presence of the monoclinic phase and a reduction in the remanent polarization.[39] Zr-rich $Hf_xZr_{1-x}O_2$ thin films exhibit antiferroelectric behavior and may be used as energy storage capacitors.[39,69]

The antiferroelectric properties of $Hf_{0.3}Zr_{0.7}O_2$ showed a promising energy storage density (ESD) of 30 J/cm^3 with a 50 % efficiency over a wide temperature range.[69] A reversible tetragonal → orthorhombic field-induced phase transition is believed to be responsible for generating antiferroelectricity.[41] Since it has been found that Si and Al can encourage the formation of the tetragonal phase,[49] doping $Hf_xZr_{1-x}O_2$ with Al or Si could be a viable route towards improving the antiferroelectric properties of the thin films. It was shown that antiferroelectric Si-doped HfO_2 thin films exhibited up to a 40 J/cm^3 energy storage density with an efficiency of 80 %.[71] The potential for using antiferroelectric Si-doped HfO_2 thin films for supercapacitors or infrared sensors was adequately demonstrated in that work, although the large 1000 °C anneal temperature will likely prove prohibitive for integrated applications.[71] As will be shown in this work,

doping $Hf_xZr_{1-x}O_2$ with Al or Si can enhance the energy storage density and efficiency without increasing the thermal budget.

The thickness and anneal dependence of ferroelectric $Hf_{0.5}Zr_{0.5}O_2$ has been previously studied in the context of the remanent polarization and the manifested crystal phases.[40] However, several unresolved points about $Hf_{0.5}Zr_{0.5}O_2$ and its thickness dependence remain. For instance, the data retention characteristics of $Hf_{0.5}Zr_{0.5}O_2$ thin films have not been studied. Data retention is the most important reliability metric for a ferroelectric to be used in a nonvolatile memory technology such as FRAM, thus, an assessment of any ferroelectric material's potential for memory applications requires retention tests. Furthermore, a thickness dependence study on the data retention may yield additional insight about ultrathin $Hf_{0.5}Zr_{0.5}O_2$ films which may be subject to an appreciable depolarization field with decreasing film thicknesses.[151]

While the thickness dependence of $Hf_{0.5}Zr_{0.5}O_2$ is well understood, it is not known how different compositions of the $Hf_xZr_{1-x}O_2$ system will be affected by the film thickness. It is also unclear what effect a spatial gradient in the distribution of Hf and Zr within $Hf_xZr_{1-x}O_2$ thin films would have on the ferroelectric properties. Since the critical grain size for the formation of the tetragonal phase is larger in ZrO_2 (~ 30 nm) than HfO_2 (~ 7 – 10 nm), a compositional gradient which includes a Hf-rich region in $Hf_{0.5}Zr_{0.5}O_2$ may inhibit the tetragonal phase in ultrathin films. Thus, a study on the size effect and compositional dependence of $Hf_xZr_{1-x}O_2$ may help in distinguishing whether the changes in ferroelectric behavior in ultrathin $Hf_xZr_{1-x}O_2$ originates from a depolarization field or in the favorability of the formation of the tetragonal phase.

Chapter 10 studies the ferroelectric and antiferroelectric properties of $Hf_xZr_{1-x}O_2$ and is split into three major sections. The first section will explore the effect of Si or Al doping of $Hf_{0.5}Zr_{0.5}O_2$ thin films. The second section will investigate the thickness dependence of $Hf_{0.5}Zr_{0.5}O_2$. The last section will study the thickness dependence of compositionally graded in $Hf_xZr_{1-x}O_2$ thin films. Overall, each section yields experimental results which have important implications for future applications of $Hf_xZr_{1-x}O_2$ thin films.

10.2 Experiment

Thin film capacitors were fabricated on a highly doped (0.001–0.005 Ω-cm) (100) p+ Si substrate. The conducting Si substrate was grounded and served as the bottom contact. Plasma enhanced atomic layer deposition was used to deposit 10 nm thick TiN bottom electrodes where tetrakis(dimethylamido)titanium was used as the titanium precursor and exposed to N_2 plasma at 200 °C. $Hf_{0.5}Zr_{0.5}O_2$ thin films were grown by thermal ALD at 200 °C by alternating tetrakis(dimethylamino)zirconium and tetrakis(dimethylamido)hafnium precursors. $Hf_xZr_{1-x}O_2$ film thicknesses were calibrated from the approximately 1 Å/cycle growth rate for each precursor and were confirmed with TEM. For Al or Si doped $Hf_{0.5}Zr_{0.5}O_2$ thin films, trimethylaluminum (TMA) and tris(dimethylamino)silane were sued as the precursors respectively. The ALD cycle ratio of $Hf_{0.5}Zr_{0.5}O_2$:Si was 48:1 and 24:1 which led to the incorporation of 2 and 4 layers of Si within 10 nm thick $Hf_{0.5}Zr_{0.5}O_2$ films. Al-doped $Hf_{0.5}Zr_{0.5}O_2$ thin films were fabricated with a 24:1 ALD cycle ratio. Unless stated otherwise, all $Hf_{0.5}Zr_{0.5}O_2$-based thin films fabricated were 10 nm thick. Compositionally graded $Hf_xZr_{1-x}O_2$ films were fabricated in two ways. The first film is binary $Hf_{0.5}Zr_{0.5}O_2$ with a Hf-rich center. The stack structure can be denoted by $Hf_{0.5}Zr_{0.5}O_2/Hf_{0.75}Zr_{0.25}O_2/Hf_{0.5}Zr_{0.5}O_2$. The other compositionally graded stack structure is $Hf_{0.25}Zr_{0.75}O_2/Hf_{0.75}Zr_{0.25}O_2/Hf_{0.25}Zr_{0.75}O_2$, where the center of

the film is Hf-rich and the ends of the film are Zr-rich. Each $Hf_xZr_{1-x}O_2$ layers is one third of the total film thickness. For all of the $Hf_xZr_{1-x}O_2$ thin films, top TiN electrodes were deposited by plasma enhanced ALD at 200 °C. Post-metallization anneals were performed after the top electrode deposition in N_2 for 20 s. The capacitor geometries were then formed by a lift-off process where 50 nm thick Pt contacts were used as a hard mask in an SC1 wet etch. Capacitor areas were 3,600 μm^2 and 14,400 μm^2.

A Saywer-Tower circuit was used to take hysteresis measurements where a 220 nF linear capacitor was placed in series with the ferroelectric capacitors. Endurance cycling was performed at 1 MHz with bipolar square waves unless otherwise mentioned. Dynamic hysteresis current measurements and retention tests were performed where the linear capacitor in the Sawyer-Tower circuit was replaced by a 50 Ω resistor. Retention bakes were carried out in ambient atmosphere for 1,000 s. Retention waveforms were implemented with a 1 μs rise and fall time, a 10 μs pulse width, and a 100 ms pulse delay. An Agilent 4294A was used to measure the impedance and C-V characteristics of the $Hf_{0.5}Zr_{0.5}O_2$ thin films. Capacitance and permittivity plots were extracted with a 50 mV AC signal at 50 kHz.

10.3 Influence of Doping $Hf_{0.5}Zr_{0.5}O_2$ with Al or Si

The binary $Hf_{0.5}Zr_{0.5}O_2$ thin film composition has been found to be optimal for ferroelectric behavior while more Zr-rich compositions lead to antiferroelectric-like characteristics.[39] As shown in Figure 10-1 A), 10 nm thick $Hf_{0.5}Zr_{0.5}O_2$ capacitors exhibit good ferroelectric properties with a remanent polarization of ~ 24 μC/cm^2 after cycling. The slight pinching of the virgin $Hf_{0.5}Zr_{0.5}O_2$ hysteresis loop may be due to a tetragonal → orthorhombic phase transition or a redistribution of charged defects with cycling.[77,152] Dynamic hysteresis currents shows four switching current peaks in the virgin

$Hf_{0.5}Zr_{0.5}O_2$ films which merge into two homogeneous switching peaks after cycling. Incorporating two monolayers of Si into $Hf_{0.5}Zr_{0.5}O_2$ leads to a pronounced pinching of the virgin P-E loop in the 48:1 $Hf_{0.5}Zr_{0.5}O_2$:Si when compared to the binary composition Figure 10-1 B). Moreover, the four switching current peaks in the 48:1 Si-doped $Hf_{0.5}Zr_{0.5}O_2$ thin films move to higher electric fields. While cycling leads to an opening of the hysteresis loop, the resulting two switching current peaks are inhomogeneous and broad, indicating that there is a wide variation in the nucleation times for polarization reversal in the 48:1 Si-doped $Hf_{0.5}Zr_{0.5}O_2$ thin films.

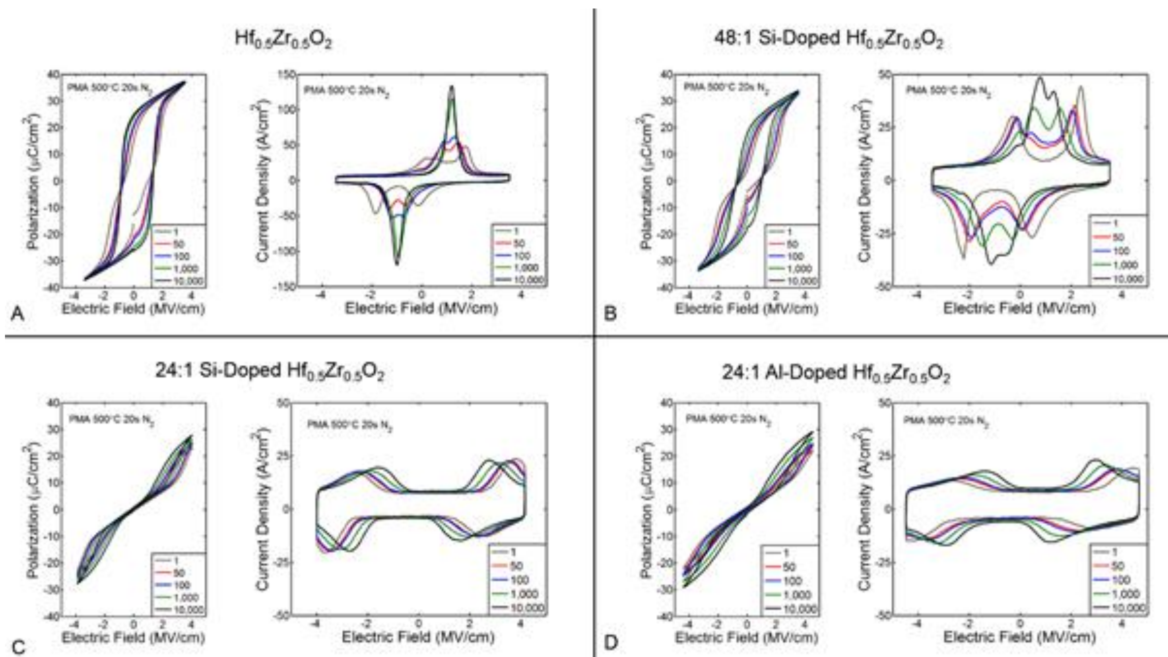

Figure 10-1. Hysteresis and dynamic hysteresis currents with cycling for HZO films. A) $Hf_{0.5}Zr_{0.5}O_2$ thin films are slightly pinched initially while cycling leads to an increase in P_r and more uniform switching current peaks, B) 48:1 Si-doped $Hf_{0.5}Zr_{0.5}O_2$ thin films exhibit more severe pinching whereas cycling leads to inhomogeneous switching current peaks, C) 24:1 Si-doped $Hf_{0.5}Zr_{0.5}O_2$ thin films are strongly antiferroelectric and the four switching current peaks migrate to lower electric fields with cycling, and D) Al-doped $Hf_{0.5}Zr_{0.5}O_2$ thin films exhibit antiferroelectric behavior with a larger electric field required to induce a field-induced phase transition. All cycling was done with bipolar square waves at 1 kHz.

Surprisingly, adding only two more monolayers of Si into $Hf_{0.5}Zr_{0.5}O_2$ thin films produces strongly antiferroelectric-like capacitors, Figure 10-1 C). The antiferroelectric behavior of the 24:1 Si-doped $Hf_{0.5}Zr_{0.5}O_2$ thin films remains stable with cycling while the field induced phase transitions shift to lower electric fields. Doping $Hf_{0.5}Zr_{0.5}O_2$ thin films with Al has a similar effect on $Hf_{0.5}Zr_{0.5}O_2$ thin films, Figure 10-1 D), although the field induced phase transitions occur at higher electric fields than the Si-doped $Hf_{0.5}Zr_{0.5}O_2$ thin films. In all of the capacitors, cycling has the tendency to reduce the distance between the two pairs of positive and negative switching current peaks. These trends indicate that the predicted field-induced reversible t→o transition, which is believed to be the origin of antiferroelectric behavior in $Hf_{0.5}Zr_{0.5}O_2$ thin films,[41] requires less energy as the capacitors are cycled. Local conversion of the tetragonal phase to the orthorhombic phase, possibly as a result of a change in the charge distribution and local coercive fields within the thin films,[143] could be responsible for the cycling behavior shown in Figure 10-1 A)-B). It is clear that the polar orthorhombic phase, however, is not stabilized with cycling in Figure 10-1 C)-D), although the field induced t→o phase transition requires lower electric fields to occur after cycling. For this case, it seems highly likely that charged defects are being redistributed within the thin films which changes the local electric field in such a way as to make the t→o phase transition more favorable with cycling. Local charged defects could act as pinning centers which inhibit the t→o phase transition and the nucleation characteristics of the polar orthorhombic phase. Theoretically it is possible that enough local charged defects could lead to oppositely biased regions within a ferroelectric thin film whereby the ferroelectric switching characteristics would mimic antiferroelectric behavior without an actual field-

induced phase transition taking place.[74] However, charged defects alone cannot adequately describe why trace doping has such a large impact on antiferroelectric behavior whereas it has been well-established that trace dopants can aid in stabilizing the tetragonal phase.[18,33] Thus, there seems to be an interplay between the crystal phases, dopants, and charged defects which coexist within the polycrystalline $Hf_{0.5}Zr_{0.5}O_2$ thin films that give rise to the observed cycling phenomena.

Due to the smaller inner area of the hysteresis loops in the 24:1 Al and Si-doped $Hf_{0.5}Zr_{0.5}O_2$ thin films, they may be well-suited for high efficiency energy storage capacitors. Figure 10-2 shows the energy storage density and efficiency of the 24:1 Si and Al-doped $Hf_{0.5}Zr_{0.5}O_2$ thin films. Antiferroelectric behavior is exhibited in the doped $Hf_{0.5}Zr_{0.5}O_2$ thin films in the anneal temperature range from 500 °C – 700 °C. Anneal temperatures greater than 700 °C led to capacitors which exhibited ferroelectric characteristics, as shown by the decrease in the efficiency which is due to the large internal area of a ferroelectric hysteresis loop. The Si-doped $Hf_{0.5}Zr_{0.5}O_2$ thin films have a large energy storage density from ~ 40 – 50 J/cm^3 with an efficiency from 85 – 80 % in the 500 °C – 700 °C anneal temperature range. The energy storage characteristics surpass antiferroelectric Si-doped HfO_2 thin films while utilizing an anneal temperature that is ~ 500 °C lower,[71] making Si-doped $Hf_{0.5}Zr_{0.5}O_2$ thin films a more viable candidate for integrated supercapacitor applications. Al-doped $Hf_{0.5}Zr_{0.5}O_2$ thin films exhibit a lower energy storage density of ~ 22 – 32 J/cm^3 with a slightly higher efficiency of 93 – 87 %. The switching current peaks of Al-doped films require higher electric fields which causes a lower energy storage density when equivalent electric fields are applied to the two differently doped $Hf_{0.5}Zr_{0.5}O_2$ films.

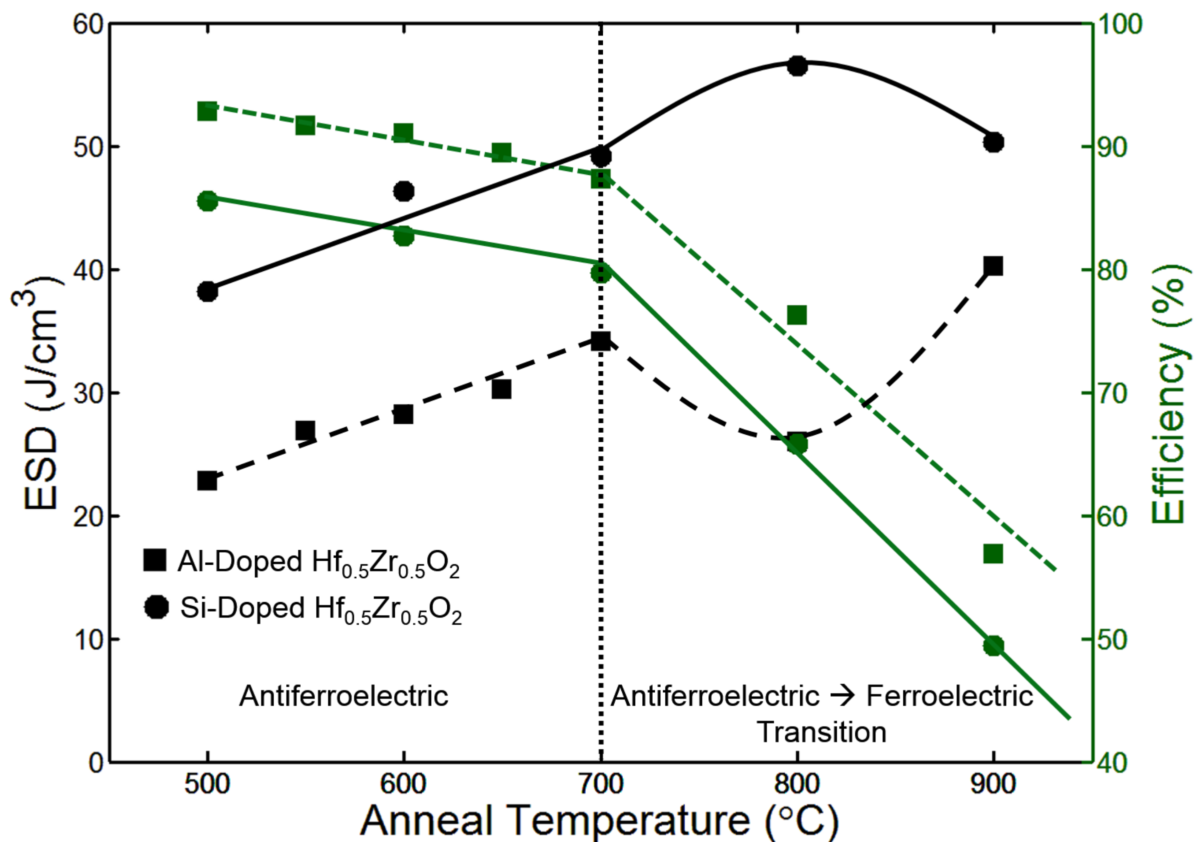

Figure 10-2. Energy storage density and efficiency of Al or Si-doped $Hf_{0.5}Zr_{0.5}O_2$ thin films with anneal temperature. Anneal temperatures greater than 700 °C led to an antiferroelectric → ferroelectric transition, as seen by the large decrease in efficiency and nonlinear behavior in energy storage density.

For practical applications, the doped $Hf_{0.5}Zr_{0.5}O_2$ thin film capacitors will have to operate at elevated temperatures and exhibit resistance to degradation with repeated cycling. The energy storage density and efficiency is shown as a function of electric field and number of cycles at room temperature for Si and Al-doped $Hf_{0.5}Zr_{0.5}O_2$ thin films in Figure 10-3. The ESD of the Si-doped $Hf_{0.5}Zr_{0.5}O_2$ thin films increases from ~ 38 J/cm^3 to ~ 53 J/cm^3 when the voltage is increased from 4 V to 4.5 V, Figure 10-3 A). In contrast, the Al-doped $Hf_{0.5}Zr_{0.5}O_2$ thin films can only achieve comparable ESD values at voltages from 4.5 V to 5 V which would likely prove to be a reliability concern.

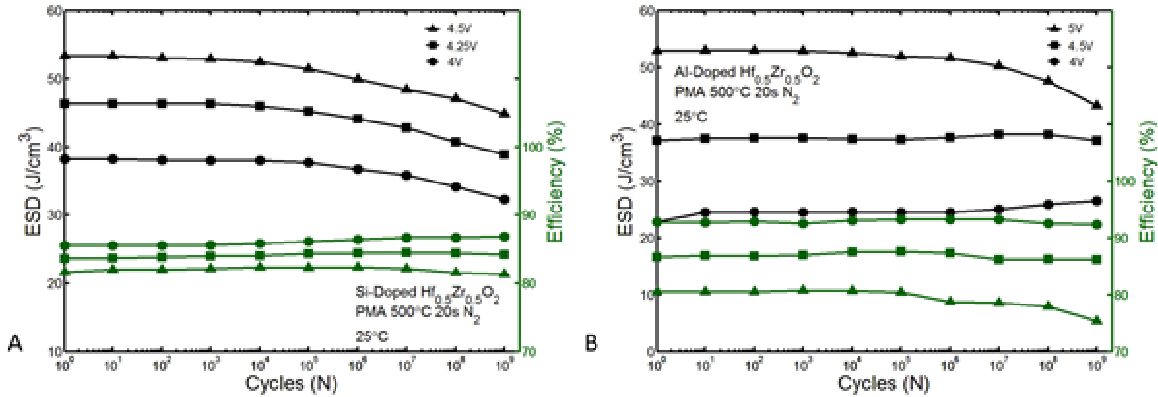

Figure 10-3. Energy storage density and efficiency of A) Si-doped $Hf_{0.5}Zr_{0.5}O_2$ thin films annealed at 500 °C with different electric fields with cycling and B) Al-doped $Hf_{0.5}Zr_{0.5}O_2$ thin films annealed at 500 °C with different electric fields with cycling.

The cycling characteristics of the Si-doped $Hf_{0.5}Zr_{0.5}O_2$ thin films at elevated temperatures is shown in Figure 10-4. At an applied voltage of 4 V, the antiferroelectric Si-doped $Hf_{0.5}Zr_{0.5}O_2$ capacitors exhibit an ESD of larger than 30 J/cm^3 with an efficiency of greater than 80 % up to 125 °C and 10^9 cycles. The higher 600 °C anneal temperature yields larger energy storage densities with a slight sacrifice in efficiency, but has similar reliability characteristics as the Si-doped $Hf_{0.5}Zr_{0.5}O_2$ thin films annealed at 500 °C. The excellent cycling characteristics of the antiferroelectric Si-doped $Hf_{0.5}Zr_{0.5}O_2$ thin films make them excellent candidates for supercapacitors and possibly dynamic random access memory applications where charge storage is of paramount importance. The cycling characteristics of the ESD and efficiency at elevated temperatures for the Al-doped $Hf_{0.5}Zr_{0.5}O_2$ thin film capacitors is shown in Figure 10-5. The energy storage density is significantly smaller for the Al-doped $Hf_{0.5}Zr_{0.5}O_2$ thin films and voltages greater than 4 V led to high leakage currents at elevated temperatures. Therefore, Si-doped $Hf_{0.5}Zr_{0.5}O_2$ thin films exhibit overall better energy storage characteristics for supercapacitor applications than Al-doped $Hf_{0.5}Zr_{0.5}O_2$ capacitors.

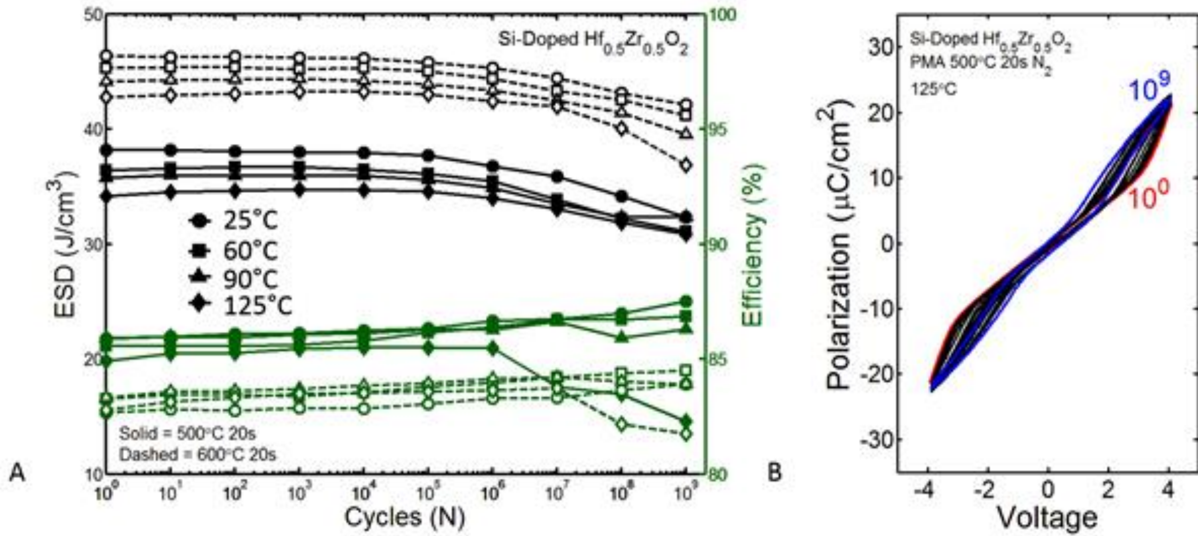

Figure 10-4. Reliability of Si-doped $Hf_{0.5}Zr_{0.5}O_2$ with cycling at elevated temperature. A) The energy storage density and efficiency of Si-doped $Hf_{0.5}Zr_{0.5}O_2$ thin films with cycling at elevated temperatures with an applied voltage of 4 V. B) Hysteresis characteristics at 125 °C with cycling.

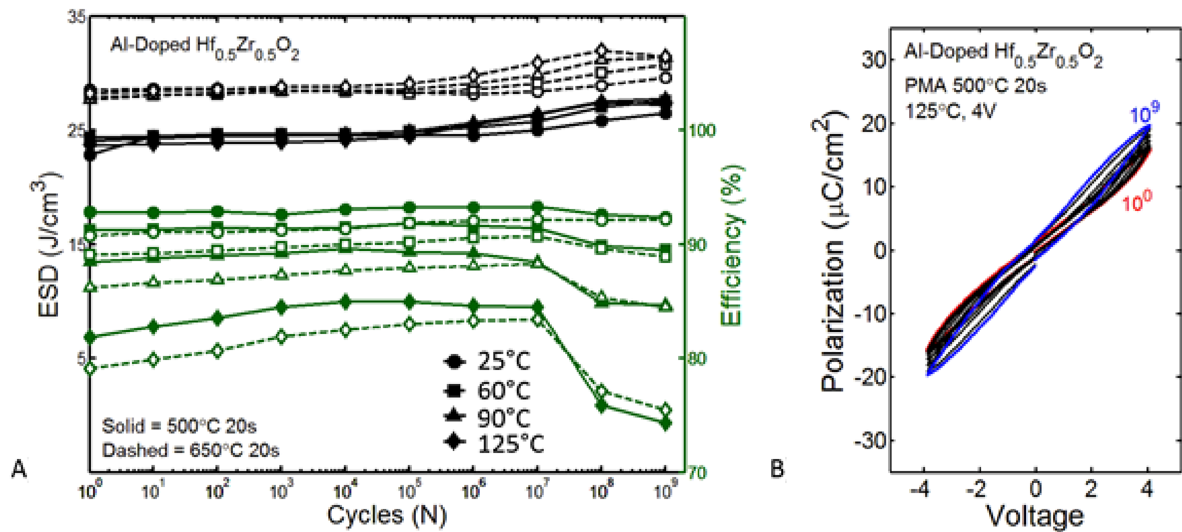

Figure 10-5. Reliability of Al-doped $Hf_{0.5}Zr_{0.5}O_2$ with cycling at elevated temperature. A A) The energy storage density and efficiency of Al-doped $Hf_{0.5}Zr_{0.5}O_2$ thin films with cycling at elevated temperatures with an applied voltage of 4 V. B) Hysteresis characteristics at 125 °C with cycling.

10.4 Thickness Dependence of Ferroelectric $Hf_{0.5}Zr_{0.5}O_2$

The ferroelectric properties of $Hf_{0.5}Zr_{0.5}O_2$ thin films can be influenced by both the anneal temperature and the film thickness.[40] The preference for the formation of the

monoclinic, tetragonal, and orthorhombic crystal phases can vary with film thickness where thicker films have a tendency to form the monoclinic phase.[40,122] Thinner $Hf_{0.5}Zr_{0.5}O_2$ films (< 10 nm) tend to exhibit more severe pinching of the hysteresis loop which suggests either a predominantly tetragonal film or a large depolarization field.[151] Figure 10-6 shows the hysteresis loops of $Hf_{0.5}Zr_{0.5}O_2$ thin films from 15 nm – 6 nm with different anneal temperatures. All of the films show some degree of pinching of the P-E loop in the as-fabricated state, although this diminishes as the anneal temperature approaches 700 °C. The overall decrease in relative permittivity (taken from the slope of the P-E loop) and the increase in the coercive field with anneal temperature is indicative of an increase in the monoclinic phase, possibly grown on top of the o-phase or t-phase as postulated by Park *et al.*[40] Cycling the films results in opening up the hysteresis loops, although the 6 nm $Hf_{0.5}Zr_{0.5}O_2$ thin films remain slightly pinched.

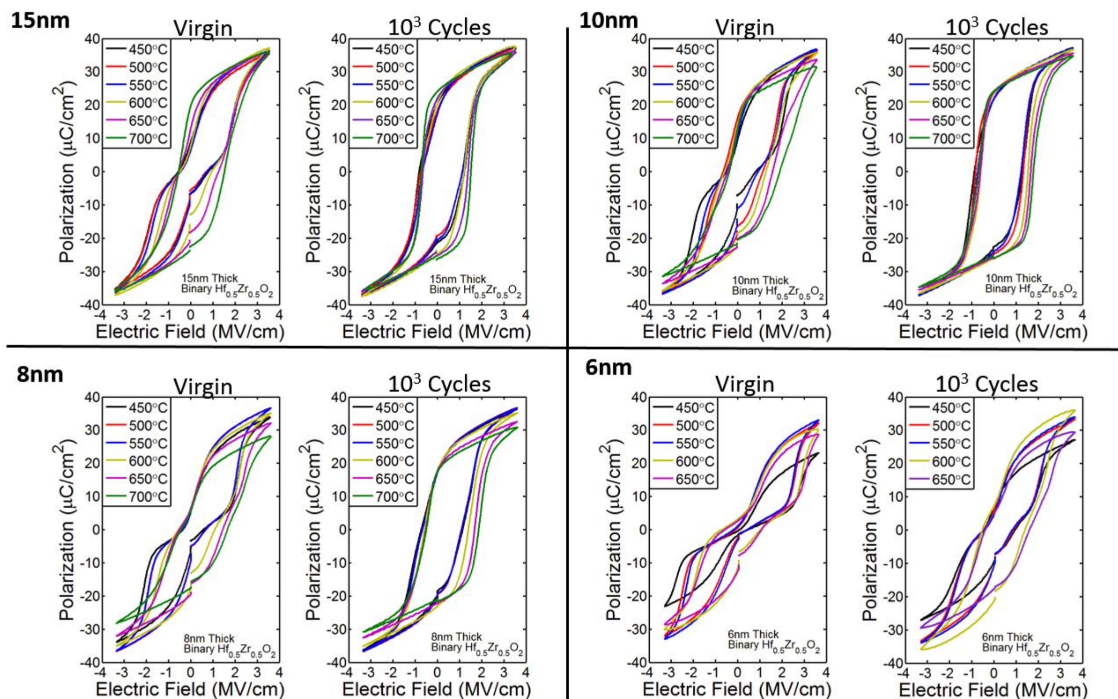

Figure 10-6. Hysteresis characteristics of $Hf_{0.5}Zr_{0.5}O_2$ thin films from 15 nm – 6 nm in thickness with different anneal temperatures. Cycling was carried out at 1kHz.

The much stronger pinching of the hysteresis loops in the 6 nm thick $Hf_{0.5}Zr_{0.5}O_2$ films corroborates the supposition of a depolarization field or a predisposition for the formation of the tetragonal phase.[151] The remanent polarization is largest in the 10 nm thick $Hf_{0.5}Zr_{0.5}O_2$ films and reach ~ 25 μC/cm^2 after cycling. The 6 nm $Hf_{0.5}Zr_{0.5}O_2$ films have the smallest P_r due to their antiferroelectric-like characteristics. Cycling the films results in a 5 – 10 μC/cm^2 increase in the remanent polarization for all of the films which may be attributable to a t→o phase conversion or depinning of ferroelectric domains.[77,82] The relative permittivity (Figure 10-8) is similar across film thicknesses, and cycling leads to an overall reduction in ε_r. The high field shoulders in the ε_r-E plots are similar to the double butterfly loops found in antiferroelectric films,[75] but cycling reduces these smaller peaks and the resultant curve takes the shape of a ferroelectric butterfly loop. The 6 nm thick $Hf_{0.5}Zr_{0.5}O_2$ films, however, have greater separation between the high-field and low-field ε_r peaks and cycling does not completely lead to the emergence of the classical ferroelectric butterfly loop.

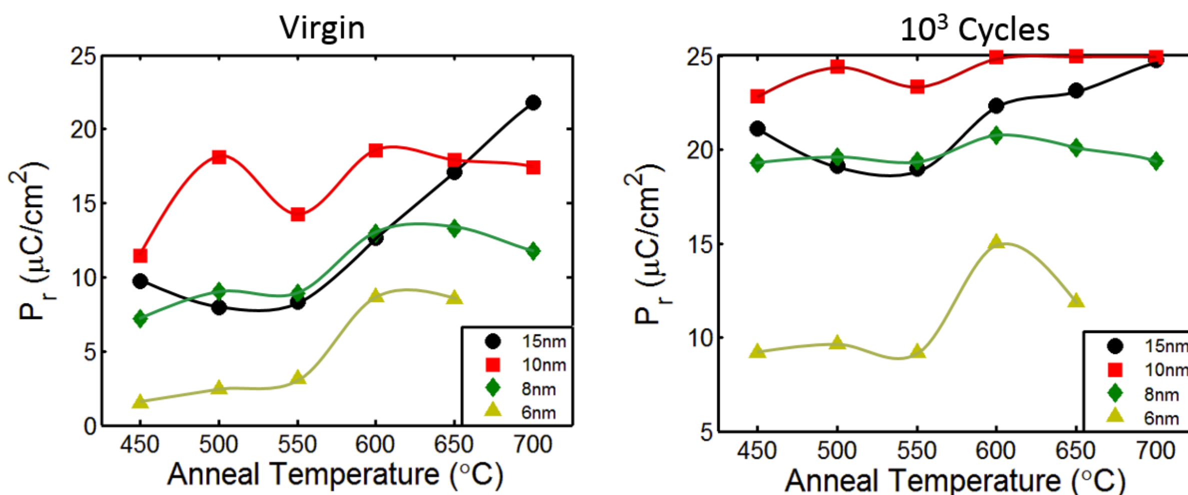

Figure 10-7. The remanent polarization of the $Hf_{0.5}Zr_{0.5}O_2$ films with thickness and anneal temperature, before and after cycling at 1 kHz.

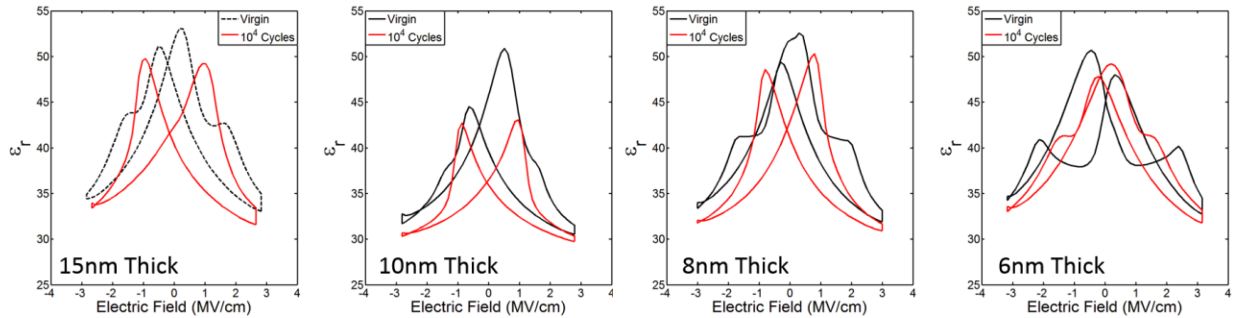

Figure 10-8. The relative permittivity vs. electric field curves show that most of the films have secondary high-field shoulders which disappear after cycling, except in the case of the 6 nm thick $Hf_{0.5}Zr_{0.5}O_2$ films. Cycling was carried out at 1 kHz and the $Hf_{0.5}Zr_{0.5}O_2$ films in this figure were annealed at 500 °C.

Given the increase in the remanent polarization and the depinching of the hysteresis loops with cycling, the retention characteristics of the $Hf_{0.5}Zr_{0.5}O_2$ thin films should be affected as well. Figure 10-9 shows the retention characteristics of 10 nm thick $Hf_{0.5}Zr_{0.5}O_2$ films from room temperature to 120 °C before and after cycling. Cycling causes a significant increase in the polarization margin and an overall improvement in the data retention compared to the as-fabricated films. The opposite state retention for positive and negative states decreases the most after a 120 °C bake which is indicative of imprint as being a reliability concern.

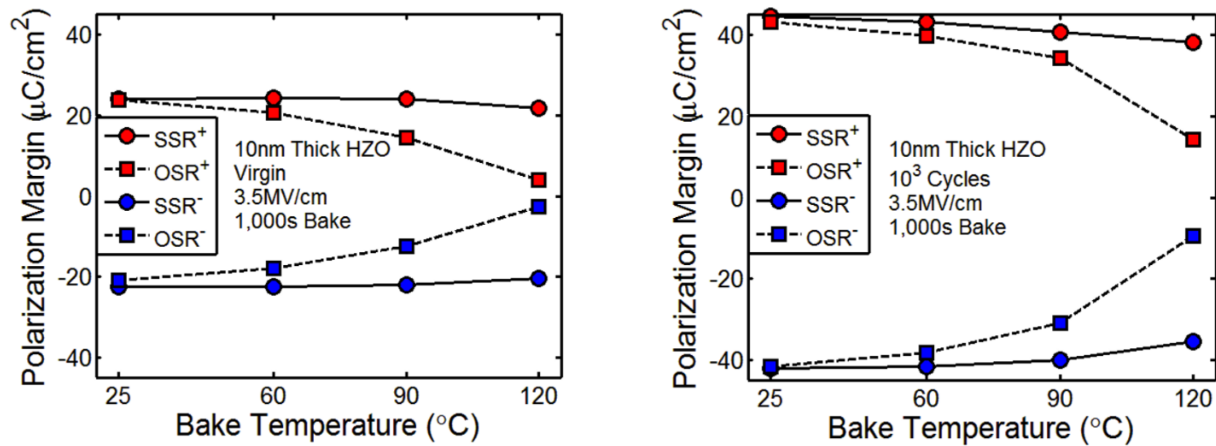

Figure 10-9. Retention characteristics of 10 nm $Hf_{0.5}Zr_{0.5}O_2$ films before and after cycling at 1 kHz.

The thickness dependence of the retention characteristics was carried out on 15 nm, 10 nm, and 6 nm thick $Hf_{0.5}Zr_{0.5}O_2$ films after cycling, Figure 10-10. Since the 6 nm thick $Hf_{0.5}Zr_{0.5}O_2$ films exhibited the most severe pinching of the P-E loop, the retention characteristics may be unsuitable for nonvolatile memory applications. The data retention was found to be the worst in the 6 nm thick $Hf_{0.5}Zr_{0.5}O_2$ films, confirming strong thickness dependence for the detrimental effect of a depolarization field or the predominantly tetragonal film. The 15 nm thick $Hf_{0.5}Zr_{0.5}O_2$ films did not have as large of a polarization margin as the 10 nm thick films, possibly due to a smaller fraction of the polar orthorhombic phase in the thicker film. Thus, the 10 nm thick films exhibit the best retention characteristics of the $Hf_{0.5}Zr_{0.5}O_2$ films.

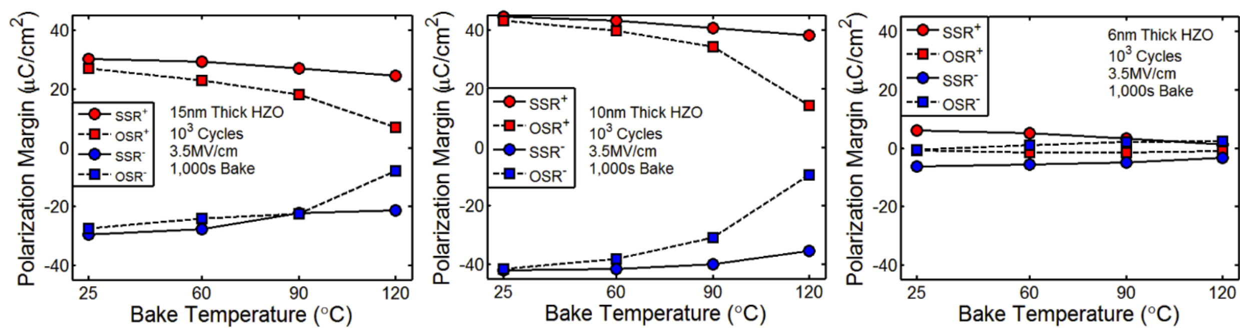

Figure 10-10. Retention tests carried out on 15, 10, and 6 nm thick $Hf_{0.5}Zr_{0.5}O_2$ films after cycling at 1 kHz.

The greater instability of the opposite state retention in the $Hf_{0.5}Zr_{0.5}O_2$ thin films is indicative of imprint. As shown in Figure 10-11, when $Hf_{0.5}Zr_{0.5}O_2$ capacitors are baked in a positive state, the hysteresis loops shift leftward and a negative state bake leads to a shift to the right. Thus, the polarity of the internal electric field which forms after baking the ferroelectric capacitors is dependent on the polarization state. Pinning of ferroelectric domains due to charged defects such as oxygen vacancies or interfacial trap states may be responsible for the observed imprint shifts with bakes.

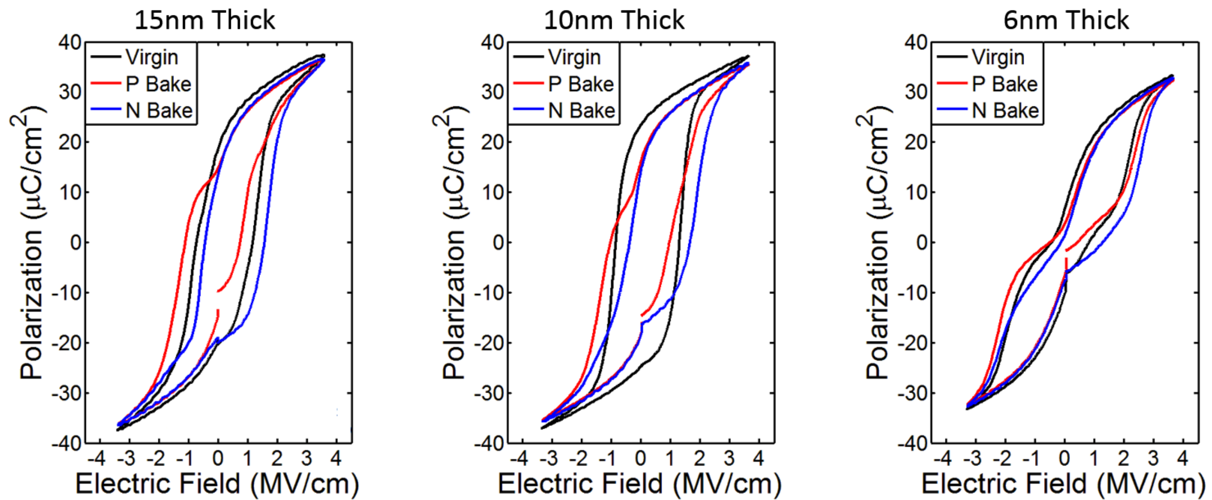

Figure 10-11. Imprint shifts are shown in red and blue for positive and negative state bakes respectively.

10.5 Compositionally Graded $Hf_xZr_{1-x}O_2$ Thin Films

Pinching of the P-E loops in $Hf_{0.5}Zr_{0.5}O_2$ thin films could pose a serious obstacle for producing thin ferroelectric films for nonvolatile memory applications. To determine if changing the composition of the films could be used to avoid such antiferroelectric-like behavior, two different compositionally graded $Hf_xZr_{1-x}O_2$ thin films were fabricated. One film is composed of a $Hf_{0.5}Zr_{0.5}O_2$/$Hf_{0.75}Zr_{0.25}O_2$/$Hf_{0.5}Zr_{0.5}O_2$ stack structure which will be referred to as the Hf-rich center (HRC) films. The other stack structure is composed of $Hf_{0.25}Zr_{0.75}O_2$/$Hf_{0.75}Zr_{0.25}O_2$/$Hf_{0.25}Zr_{0.75}O_2$ which will be referred to as the Zr-rich end (ZRE) films. The hysteresis characteristics of the HRC films are shown in Figure 10-12. As can be seen, virtually no pinching of the P-E loop occurs down to HRC films 6 nm thick. At higher anneal temperatures than 600 °C, some distortion of the hysteresis loops occur but it is attended by a decrease in the relative permittivity, indicating that the growth of an interfacial layer or the separation of phases within the compositionally graded films might be occurring. Cycling the HRC films results in a net increase in the remanent polarization, but the P_r is lower than the binary $Hf_{0.5}Zr_{0.5}O_2$ thin films. Since

the films have become more Hf-rich, it is very probable that the stability of the monoclinic phase has been encouraged instead of tetragonal phase.[39] The concomitant disappearance of pinched hysteresis behavior and the reduced likelihood of the formation of the tetragonal phase adds evidence that the tetragonal phase is indeed responsible for the antiferroelectric-like behavior observed in binary $Hf_{0.5}Zr_{0.5}O_2$ thin films.

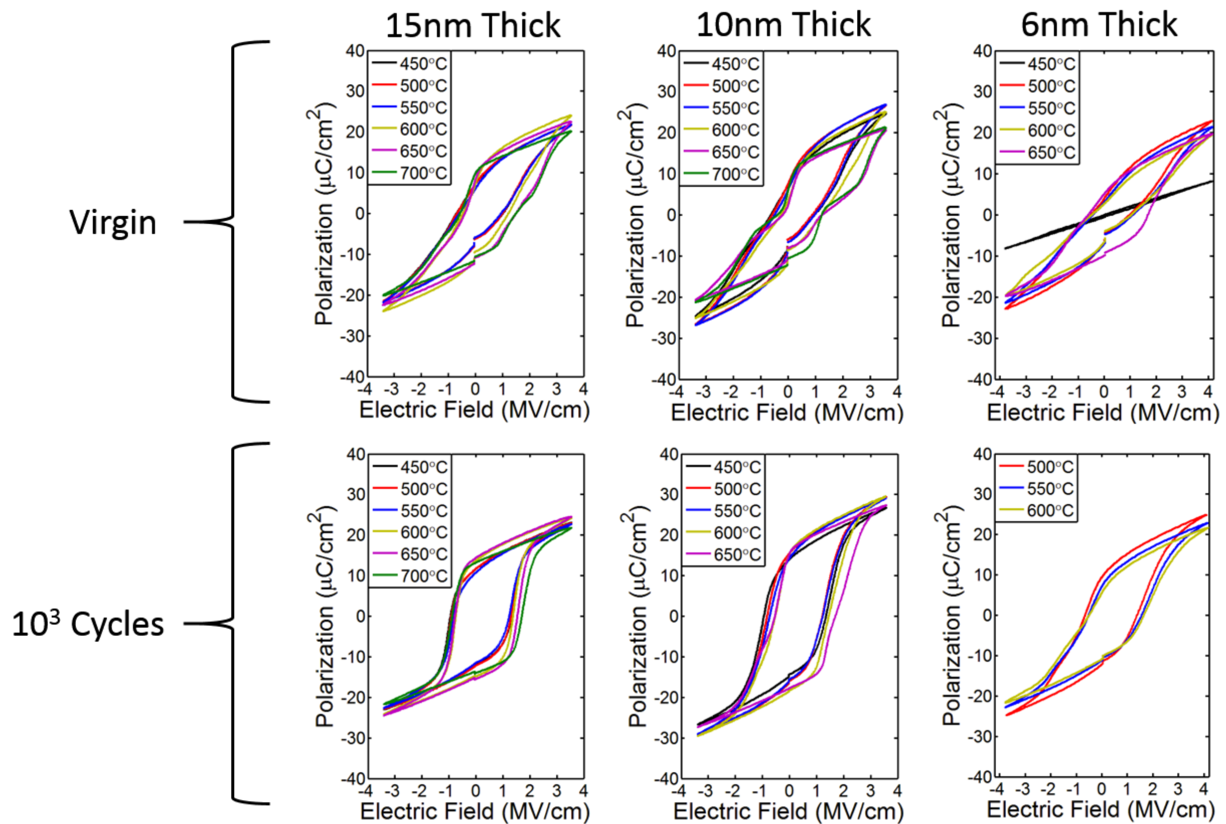

Figure 10-12. Hysteresis characteristics of $Hf_{0.5}Zr_{0.5}O_2$ thin films with a Hf-rich center at different thicknesses and anneal temperatures. Cycling was performed at 1 kHz.

In contrast to the HRC films, the ZRE films show more pronounced pinched P-E behavior for 10 nm and 6 nm thick films, as shown in Figure 10-13. Cycling is able to open up the hysteresis loops, but they remain more or less antiferroelectric-like for the 6 nm thick films. Thus, the pinched P-E loop resulting from adding more Zr content to the

$Hf_xZr_{1-x}O_2$ can be attributed to increasing the tetragonal phase in 6 nm thick films which accounts for the stronger antiferroelectric-like characteristics. The thicker 15 nm ZRE films did not exhibit an antiferroelectric-like virgin hysteresis loop because the change in surface energy and the Hf-rich central region likely made the tetragonal phase less favorable.

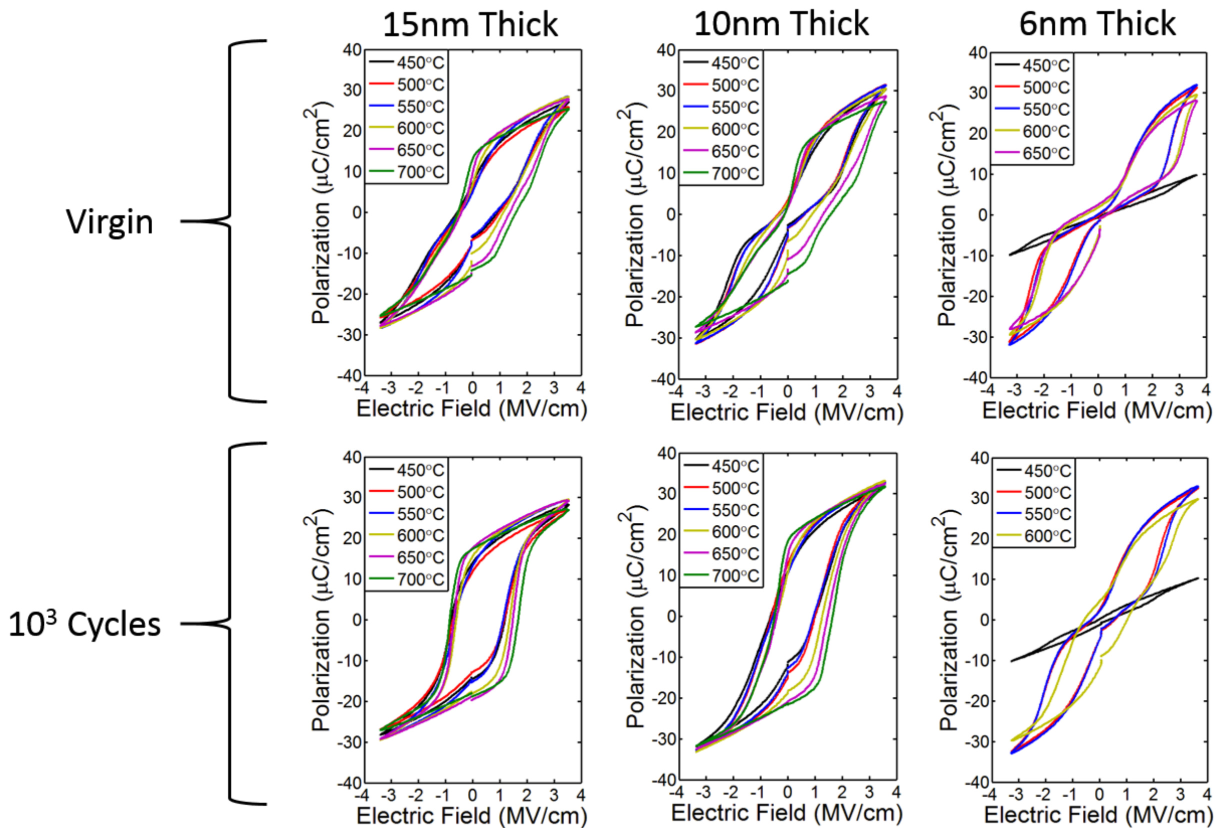

Figure 10-13. Hysteresis characteristics of $Hf_xZr_{1-x}O_2$ thin films with a Hf-rich center and Zr-rich ends at different thicknesses and anneal temperatures. Cycling was performed at 1 kHz.

The retention of 6 nm thick HRC films were evaluated to determine if the lack of antiferroelectric-like behavior in the as-fabricated capacitors would be associated with an improvement in the retention properties. The HRC films were cycled at different electric fields and underwent bakes up to 120 °C, as shown in Figure 10-14. While the polarization margins are similar to binary $Hf_{0.5}Zr_{0.5}O_2$ thin films at 3.5 MV/cm, higher

electric fields yield improvements in the data margins. The HRC films are notably more stable at higher electric fields than binary $Hf_{0.5}Zr_{0.5}O_2$ thin films with reduced leakage currents and improved cycling endurance, therefore, higher electric field operation may be feasible. While polarization margins in the 6 nm thick HRC films might be acceptable up to 60 °C, higher temperatures lead to a deterioration in opposite state retention due to an imprint shift caused by baking the capacitors in the positive or negative polarization state.

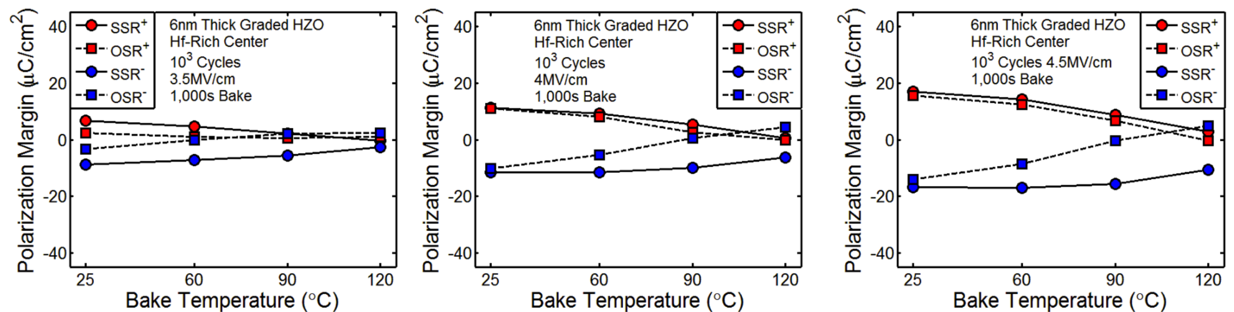

Figure 10-14. The retention characteristics of the HRC films at 6 nm shows an increase in the polarization margin with higher electric fields.

One possible explanation for the changes in ferroelectric behavior with decreasing film thicknesses in the $Hf_xZr_{1-x}O_2$ thin films is the increasingly prominent role an interfacial layer may play as the bulk ferroelectric region is reduced. In order to determine the possible presence of an interfacial layer in ferroelectric thin films, a plot of 1/C vs film thickness can be used such that a linear extrapolation to zero film thickness would uncover the interfacial capacitance at the y-intercept.[108,153] Figure 10-15 shows that extrapolating the inverse capacitance for the binary $Hf_{0.5}Zr_{0.5}O_2$, HRC, and ZRE films does in fact indicate that there may be an interfacial layer in at least two of the films. Both the binary $Hf_{0.5}Zr_{0.5}O_2$ and the ZRE films exhibit a positive intercept which is evidence that these films have interfacial capacitance in series with the bulk ferroelectric

capacitance. Moreover, these two film types both exhibit pinched hysteresis characteristics at 6 nm and the smaller interfacial capacitance term for the ZRE films in comparison to the binary $Hf_{0.5}Zr_{0.5}O_2$ films is correlated with stronger antiferroelectric-like behavior.

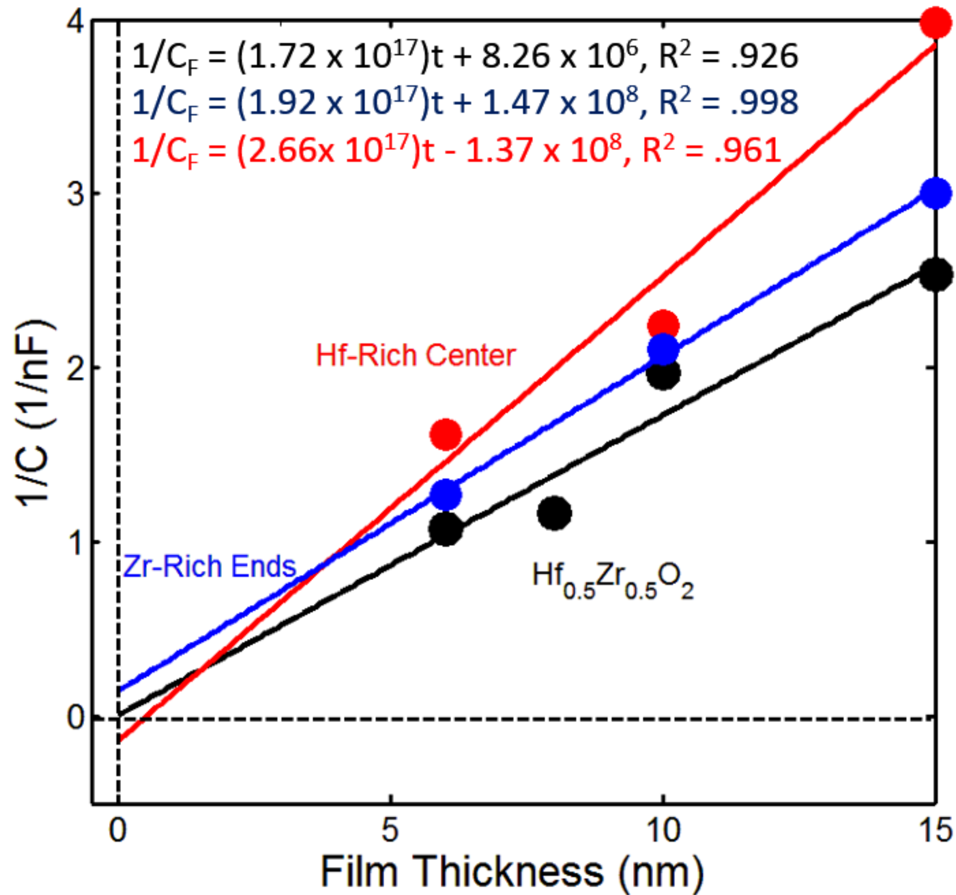

Figure 10-15. Inverse capacitance with film thickness for binary $Hf_{0.5}Zr_{0.5}O_2$, HRC, and ZRE films.

The slope of the linear lines in Figure 10-15 is the bulk ferroelectric capacitance and can be used to extract the bulk relative permittivity of the different films. Using this method, the bulk permittivity was found to be 45.6, 29.5, and 40.9 for the binary $Hf_{0.5}Zr_{0.5}O_2$, HRC, and ZRE films respectively. The significantly lower relative permittivity of the HRC films indicate the presence of the monoclinic phase in the bulk. The inverse of the

(positive) intercepts can be used to extract the interface capacitance. Assuming the interfacial layer is composed of the tetragonal phase (k ~ 70)[13], the thickness of the interfacial layer for the binary $Hf_{0.5}Zr_{0.5}O_2$ would be less than an Å thick while the ZRE films have an extracted interfacial layer thickness of 1.3 nm. The unrealistic interfacial layer thickness for the binary $Hf_{0.5}Zr_{0.5}O_2$ films is likely due to the greater uncertainty in the linear extrapolation. However, a 1.3 nm interfacial layer in the ZRE films is plausible due to the excellent linear fit to the measured data and the increased likelihood that the tetragonal phase would be promoted in the Zr-rich end regions instead of the Hf-rich bulk. In contrast to the binary $Hf_{0.5}Zr_{0.5}O_2$ and the ZRE films, the HRC films exhibit a negative intercept value which is incompatible with the presence of an interfacial layer. The simultaneous absence of pinching and lack of an interfacial capacitance term in the HRC films supports the hypothesis that an interfacial layer may be promoting pinching of the hysteresis loops in ultrathin ferroelectric $Hf_{0.5}Zr_{0.5}O_2$ thin films. Due to the correlation between the preference for the tetragonal phase and the interfacial capacitance term, it is likely that the tetragonal phase may predominantly form at the electrode interfaces where it acts as both a parasitic capacitance layer and adds a field dependent secondary switching current as a result of a t→o transition during nucleation switching with the application of an electric field.

10.6 Conclusion

$Hf_{0.5}Zr_{0.5}O_2$ thin films 10 nm thick were doped with Al or Si which produced antiferroelectric behavior. The Si-doped $Hf_{0.5}Zr_{0.5}O_2$ thin films exhibited a large 40 J/cm^3 energy storage density with a 85% efficiency. The cycling characteristics of the Si-doped $Hf_{0.5}Zr_{0.5}O_2$ antiferroelectric thin were promising due to the robust performance after undergoing 10^9 cycles up to 125 °C. The Al-doped $Hf_{0.5}Zr_{0.5}O_2$ thin films were not

as robust due to the larger electric fields needed to generate a t$\rightarrow$o field induced phase transition.

$Hf_{0.5}Zr_{0.5}O_2$ thin films of different thicknesses were fabricated and characterized. Pronounced pinching of the P-E loops were observed in 6 nm thick $Hf_{0.5}Zr_{0.5}O_2$ thin films. Retention tests carried out on the films indicated the benefits of cycling compared to as-fabricated ferroelectric $Hf_{0.5}Zr_{0.5}O_2$ thin films. The retention characteristics were best in the 10 nm thick $Hf_{0.5}Zr_{0.5}O_2$ thin films and the 10 nm thick films also had the largest remanent polarization. 6 nm thick $Hf_{0.5}Zr_{0.5}O_2$ thin films exhibited very poor retention characteristics in part due to the strongly pinched P-E loops seen in the as-fabricated films.

Compositionally graded $Hf_xZr_{x-}O_2$ thin films showed that increasing the Hf content within the center of the film could eliminate antiferroelectric-like behavior in the virgin films down to 6 nm thick. In contrast, when the Zr content was increased in the graded $Hf_xZr_{1-x}O_2$ thin films, antiferroelectric-like behavior became more pronounced in the 10 nm and 6 nm thick films. Films which favored a tetragonal structure as the thickness was reduced, indicated by their antiferroelectric-like behavior, were also to found have an interfacial capacitance term. It was postulated that the formation of the tetragonal phase at the electrode interfaces could explain both the observation of a small signal interfacial capacitance term and the antiferroelectric-like switching behavior where a t$\rightarrow$o phase transition occurs when large electric fields are applied to accomplish nucleation and polarization reversal of existing ferroelectric domains.

CHAPTER 11
SUMMARY AND FUTURE WORK

Ferroelectric HfO_2 thin films have the potential to be incorporated into nonvolatile memory technologies such as FRAM and FeFETs. The ferroelectric characteristics of nanometer-scale HfO_2 films are highly dependent on a variety of factors including the substrate, electrode interfaces, and the distribution of incorporated dopants as shown in this dissertation. TiN and Ir electrodes were both found to promote ferroelectric behavior in Si-doped HfO_2 after post-metallization anneals. Chemical asymmetries in the electrode/ferroelectric interfaces in Si-doped HfO_2 thin films with sputtered TaN electrodes led to imprint and the development of an internal electric field. When ferroelectric HfO_2 was grown on a Si substrate and annealed, the growth of an interfacial SiO_2 layer caused an increase in the switching voltage. Si-doped HfO_2 thin films grown on a Ge substrate did not have an observable interfacial layer and exhibited a lower operating voltage compared to the Si MFIS device stack, highlighting the potential for low-power Ge-based FeFETs in the MFS device structure.

Co-doping HfO_2 with Al and Si produced ferroelectric behavior that was dependent on how the dopants were layered. The remanent polarization was influenced by the annealing conditions and the Al and Si dopant distribution. Si-layering in HfO_2 thin films was also found to lead to alterations in the remanent polarization. Modifying the ferroelectric characteristics of HfO_2-based thin films through dopant layering is a viable route to improve the performance of ferroelectric HfO_2 for FRAM and FeFET applications. Compositionally graded $Hf_xZr_{1-x}O_2$ thin films may enable tuning of the thin film properties for specific applications while adding Al or Si dopants into $Hf_xZr_{1-x}O_2$ is promising for energy storage capacitors and potentially infrared sensors. Moving

forward, a wide variety of fundamental scientific studies need to be conducted on the ferroelectric HfO_2 material system to better understand the mechanisms which stabilize the polar orthorhombic phase. Future work on ferroelectric HfO_2 can look at making the films thinner than 5 nm for FTJ applications, implementing a Ge FeFET, and finding ways to increase the robustness of the retention characteristics for other nonvolatile memory technologies.

APPENDIX A
PROCESS FLOW FOR FERROELECTRIC HfO_2 CAPACITORS

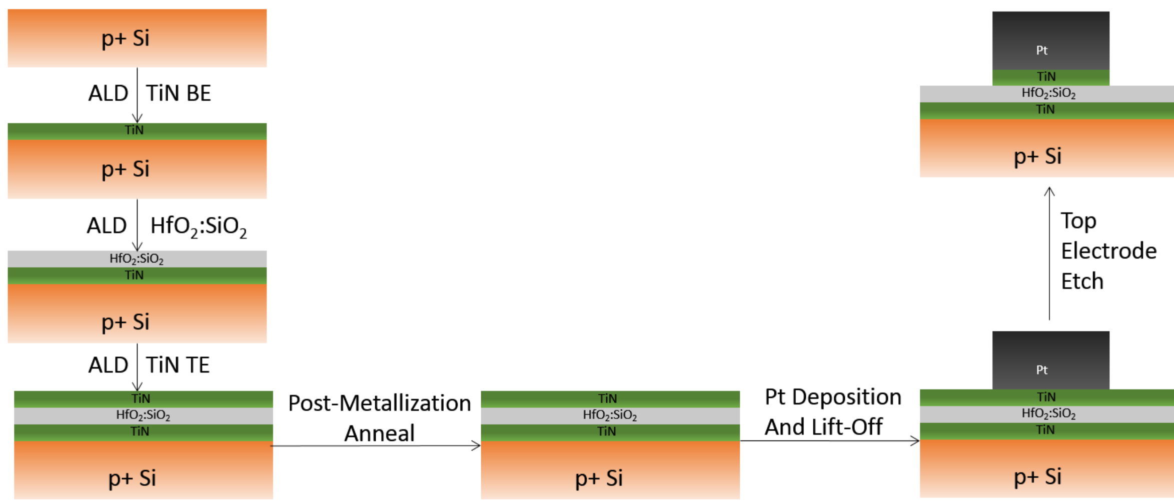

APPENDIX B
DESCRIPTION OF ATOMIC LAYER DEPOSITION PROCESS

Atomic layer deposition (ALD) is a thin film deposition technique whereby individual atomic layers of a material are grown on a substrate. The growth of atomic monolayers in ALD is a result of a self-limiting surface reaction as precursor molecules adsorb onto the substrate. Once the substrate surface has been covered in adsorbed precursor molecules, excess precursor molecules and byproducts are evacuated from the ALD chamber. Next, a reactant such as a plasma or H_2O is delivered to the substrate surface which is blanketed with adsorbed precursor molecules. Once the ALD precursor is exposed to a reactant, a surface reaction takes place in which a monolayer of material has been grown on the substrate. After the precursor has been reacted, the byproducts are then removed from the ALD chamber and another layer can be grown.

The process of growing one atomic layer is usually referred to as one ALD cycle. By varying the number of ALD cycles and measuring the thickness of the grown layers, it is possible to determine the growth rate of the precursor. Growth rates can be affected by a variety of factors such as substrate temperature, surface chemistry, and choice of reactant. The method of precursor reaction can divide ALD growth into two types, thermal and plasma. Thermal ALD employs H_2O as the reactant and is usually used in growing oxides. Plasma ALD employs plasmas, such as O_2, N_2, and H_2, to react with the adsorbed precursor molecules. A combination of plasma and thermal ALD can be used to great advantage in fabricating capacitors which require a high quality gate oxide (thermal ALD of HfO_2) and conducting electrodes (plasma ALD of TiN). ALD recipes can be modified to grow structures in any sequence or combination of layers which makes it a very flexible tool. The ability to tailor doping profiles and composition as a function of

position makes ALD the most suited deposition technique in which to explore ferroelectric behavior in HfO_2. Table B-1 lists the ALD precursors and the materials grown from them in this dissertation. Figure B-1 shows the flow diagram of a basic ALD program and Table B-2 lists the recipe specifications.

Table B-1. List of ALD precursors and the materials grown.

ALD Precursors	Chemical Formula	Material Grown
Tetrakis(dimethylamido)hafnium	$[(CH_3)_2N]_4Hf$	HfO_2
Tris(dimethylamino)silane	$[(CH_3)_2N]_3SiH$	SiO_2
Trimethylaluminum	$(CH_3)_3Al$	Al_xO_y
Tetrakis(dimethylamido)titanium	$[(CH_3)_2N]_4Ti$	TiN
Tetrakis(dimethylamino)zirconium	$[(CH_3)_2N]_4Zr$	ZrO_2

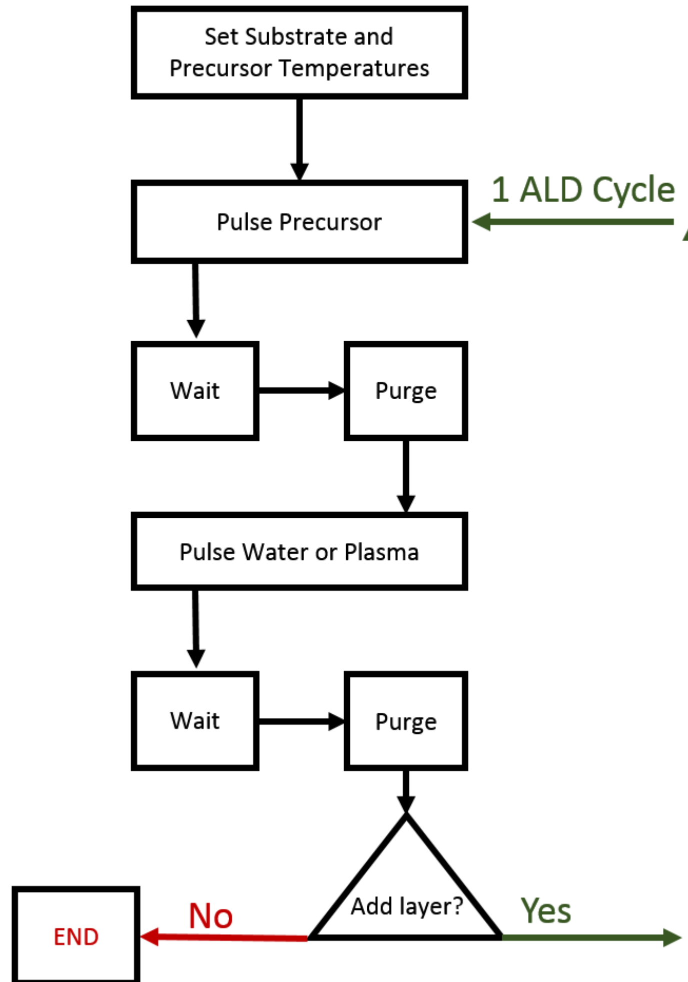

Figure B-1. Flow diagram of an ALD recipe.

Table B-2. ALD recipe specifications.

Material Grown	Substrate Temperature	Precursor Pulse	Precursor Purge	Reactant Pulse	Reactant Purge	Reactant Type
HfO_2	200°C	.25s	15s	.06s	15s	H_2O
SiO_2	200°C	.4s	10s	20s	5s	Plasma
Al_xO_y	200°C	.06s	20s	.06s	10s	H_2O
ZrO_2	200°C	.25s	20s	.1s	10s	H_2O
TiN	200°C	.2s	6s	20s	5s	Plasma

LIST OF REFERENCES

[1] M. Dawber, K.M. Rabe, and J.F. Scott, Rev. Mod. Phys. **77**, 1083 (2005).

[2] C. Kittel, *Introduction to Solid State Physics*, Sixth (John Wiley & Sons, Inc., New York, 1986).

[3] F.T. Ulaby, E. Michielssen, and U. Ravaioli, *Fundamentals of Applied Electromagnetics*, 6/E ed. (Prentive Hall, Upper Saddle River, 2010).

[4] D. Damjanovic, Reports Prog. Phys. **61**, 1267 (1998).

[5] S. Hong, editor , *Nanoscale Phenomena in Ferroelectric Thin Films* (Kluwer Academic Publishers, Boston, 2004).

[6] Y.L. Tang, Y.L. Zhu, Y.J. Wang, W.Y. Wang, Y.B. Xu, W.J. Ren, Z.D. Zhang, and X.L. Ma, Sci. Rep. **4**, 4115 (2014).

[7] E. Fatuzzo and W.J. Merz, *Ferroelectricity* (North-Holland Publishing Co., Amsterdam, 1967).

[8] M. Kohli, P. Muralt, and N. Setter, Appl. Phys. Lett. **72**, 3217 (1998).

[9] H. Zhu, D.P. Chu, N.A. Fleck, S.E. Rowley, and S.S. Saxena, **105**, 061609 (2010).

[10] J. Rodel, A.B. Kounga, E. Aulbach, T. Granzow, and T. Leist, in *Sixt. IEEE Int. Symp. Appl. Ferroelectr.* (IEEE, Nara, 2007), pp. 638–640.

[11] M.H. Lente and J.A. Eiras, J. Appl. Phys. **89**, 5093 (2001).

[12] J. Wang, H.P. Li, and R. Stevens, J. Mater. Sci. **27**, 5397 (1992).

[13] X. Zhao and D. Vanderbilt, Phys. Rev. B **65**, 233106 (2002).

[14] C.E. Curtis, L.M. Doney, and J.R. Johnson, J. Am. Ceram. Soc. **37**, 458 (1954).

[15] G.D. Wilk, R.M. Wallace, and J.M. Anthony, **89**, 5243 (2001).

[16] B.H. Lee, L. Kang, W. Qi, R. Nieh, Y. Jeon, K. Onishi, and J.C. Lee, in *Int. Electron Devices Meet.* (IEEE, Washington DC, 1999), pp. 133–136.

[17] K. Tomida, K. Kita, and A. Toriumi, Appl. Phys. Lett. **89**, 142902 (2006).

[18] A. Toriumi, K. Kita, K. Tomida, and Y. Yamamoto, ECS Trans. **1**, 185 (2006).

[19] S. V Ushakov, C.E. Brown, and A. Navrotsky, Mater. Res. **19**, 693 (2004).

[20] T.S. Böscke, J. Müller, D. Bräuhaus, U. Schröder, and U. Böttger, Appl. Phys. Lett. **99**, 102903 (2011).

[21] R. Ruh, H.J. Garrett, R.F. Domagala, and N.M. Tallan, J. Am. Ceram. Soc. **51**, 23 (1968).

[22] O. Ohtaka, H. Fukui, T. Kunisada, T. Fujisawa, K. Funakoshi, W. Utsumi, T. Irifune, K. Kuroda, and T. Kikegawa, J. Am. Ceram. Soc. **84**, 1369 (2001).

[23] J.E. Lowther, J.K. Dewhurst, J.M. Leger, and J. Haines, Phys. Rev. B **60**, 485 (1999).

[24] E.H. Kisi, J. Am. Ceram. Soc. **81**, 741 (1998).

[25] M.H. Park, Y.H. Lee, H.J. Kim, Y.J. Kim, T. Moon, K. Do Kim, J. Müller, A. Kersch, U. Schroeder, T. Mikolajick, and C.S. Hwang, Adv. Mater. **27**, 1811 (2015).

[26] E.P. Gusev, D.A. Buchanan, E. Cartier, A. Kumar, D. DiMaria, S. Guha, A. Callegari, S. Zafar, P.C. Jamison, D.A. Neumayer, M. Copel, M.A. Gribelyuk, H. Okorn-Schmidt, C. D'Emic, P. Kozlowski, K. Chan, N. Bojarczuk, L.-A. Ragnarsson, P. Ronsheim, K. Rim, R.J. Fleming, A. Mocuta, and A. Ajmera, in *Int. Electron Devices Meet.* (IEEE, Washington, DC, 2001), pp. 20.1.1–20.1.4.

[27] B.H. Lee, L. Kang, R. Nieh, W.-J. Qi, and J.C. Lee, Appl. Phys. Lett. **76**, 1926 (2000).

[28] J.H. Choi, Y. Mao, and J.P. Chang, Mater. Sci. Eng. R Reports **72**, 97 (2011).

[29] R.D. Clark, Materials (Basel). **7**, 2913 (2014).

[30] T. Ando, Materials (Basel). **5**, 478 (2012).

[31] H. Kim, P.C. Mcintyre, C.O. Chui, K.C. Saraswat, and S. Stemmer, J. Appl. Phys. **96**, 3467 (2004).

[32] L.A. Ragnarsson, T. Chiarella, M. Togo, T. Schram, P. Absil, and T. Hoffmann, Microelectron. Eng. **88**, 1317 (2011).

[33] D. Fischer and A. Kersch, Microelectron. Eng. **84**, 2039 (2007).

[34] T. Roessler, J. Gluch, M. Albert, and J.W. Bartha, Thin Solid Films **518**, 4680 (2010).

[35] J. Müller, T.S. Böscke, U. Schröder, M. Reinicke, L. Oberbeck, D. Zhou, W. Weinreich, P. Kücher, M. Lemberger, and L. Frey, Microelectron. Eng. **86**, 1818 (2009).

[36] T.S. Böscke, P.Y. Hung, P.D. Kirsch, M.A. Quevedo-Lopez, and R. Ramírez-Bon, Appl. Phys. Lett. **95**, 052904 (2009).

[37] D.H. Triyoso, P.J. Tobin, B.E. White, R. Gregory, and X.D. Wang, Appl. Phys. Lett. **89**, 132903 (2006).

[38] J. Müller, T.S. Böscke, D. Bräuhaus, U. Schröder, U. Böttger, J. Sundqvist, P. Kücher, T. Mikolajick, and L. Frey, Appl. Phys. Lett. **99**, 112901 (2011).

[39] J. Müller, T.S. Böscke, U. Schröder, S. Mueller, D. Bräuhaus, U. Böttger, L. Frey, and T. Mikolajick, Nano Lett. **12**, 4318 (2012).

[40] M. Hyuk Park, H. Joon Kim, Y. Jin Kim, W. Lee, T. Moon, and C.S. Hwang, Appl. Phys. Lett. **102**, 242905 (2013).

[41] S.E. Reyes-Lillo, K.F. Garrity, and K.M. Rabe, Phys. Rev. B **90**, 140103 (2014).

[42] R. Materlik, C. Künneth, and A. Kersch, J. Appl. Phys. **117**, 134109 (2015).

[43] H.J. Kim, M.H. Park, Y.J. Kim, Y.H. Lee, W. Jeon, T. Gwon, T. Moon, K.D. Kim, and C.S. Hwang, Appl. Phys. Lett. **105**, 192903 (2014).

[44] J. Müller, U. Schröder, T.S. Böscke, I. Müller, U. Böttger, L. Wilde, J. Sundqvist, M. Lemberger, P. Kücher, T. Mikolajick, and L. Frey, J. Appl. Phys. **110**, 114113 (2011).

[45] S. Mueller, J. Mueller, A. Singh, S. Riedel, J. Sundqvist, U. Schroeder, and T. Mikolajick, Adv. Funct. Mater. **22**, 2412 (2012).

[46] A. Chernikova, M. Kozodaev, A. Markeev, Y. Matveev, D. Negrov, and O. Orlov, Microelectron. Eng. **147**, 15 (2015).

[47] T. Olsen, U. Schröder, S. Müller, A. Krause, D. Martin, A. Singh, J. Müller, M. Geidel, and T. Mikolajick, Appl. Phys. Lett. **101**, 082905 (2012).

[48] S. Starschich, D. Griesche, T. Schneller, R. Waser, and U. Böttger, Appl. Phys. Lett. **104**, 202903 (2014).

[49] U. Schroeder, E. Yurchuk, J. Müller, D. Martin, T. Schenk, P. Polakowski, C. Adelmann, M.I. Popovici, S. V Kalinin, and T. Mikolajick, Jpn. J. Appl. Phys. **53**, 08LE02 (2014).

[50] T. Schenk, S. Mueller, U. Schroeder, R. Materlik, A. Kersch, M. Popovici, C. Adelmann, S. Van Elshocht, and T. Mikolajick, in *2013 Proc. Eur. Solid-State Device Res. Conf.* (IEEE, Bucharest, 2013), pp. 260–263.

[51] X. Sang, E.D. Grimley, T. Schenk, U. Schroeder, and J.M. LeBeau, Appl. Phys. Lett. **106**, 162905 (2015).

[52] J.A. Rodriguez, K. Remack, K. Boku, K.R. Udayakumar, S. Aggarwal, S.R. Summerfelt, F.G. Celii, S. Martin, L. Hall, K. Taylor, T. Moise, H. McAdams, J. McPherson, R. Bailey, G. Fox, and M. Depner, IEEE Trans. Device Mater. Reliab. **4**, 436 (2004).

[53] T. Eshita, W. Wang, K. Nakamura, S. Ozawa, Y. Okita, S. Mihara, Y. Hikosaka, H. Saito, J. Watanabe, K. Inoue, H. Yamaguchi, and K. Nomura, J. Phys. Sci. Appl. **5**, 29 (2015).

[54] J. Müller, P. Polakowski, S. Muller, and T. Mikolajick, ECS Trans. **64**, 159 (2014).

[55] P. Polakowski, S. Riedel, W. Weinreich, M. Rudolf, J. Sundqvist, K. Seidel, and J. Müller, in *2014 IEEE 6th Int. Mem. Work.* (IEEE, Taipei, 2014), pp. 1–4.

[56] N.A. Pertsev, J. Rodriguez Contreras, V.G. Kukhar, B. Hermanns, H. Kohlstedt, and R. Waser, Appl. Phys. Lett. **83**, 3356 (2003).

[57] Y. Sakashita, H. Segawa, K. Tominaga, and M. Okada, J. Appl. Phys. **73**, 7857 (1993).

[58] T. Sakoda, T.S. Moise, S.R. Summerfelt, L. Colombo, G. Xing, S.R. Gilbert, A.L.S. Loke, S. Ma, R. Kavari, L.A. Wills, and J. Amano, Jpn. J. Appl. Phys. **40**, 2911 (2001).

[59] M.H. Park, H.J. Kim, Y.J. Kim, W. Lee, H.K. Kim, and C.S. Hwang, Appl. Phys. Lett. **102**, 112914 (2013).

[60] J. Meena, S. Sze, U. Chand, and T.-Y. Tseng, Nanoscale Res. Lett. **9**, 526 (2014).

[61] T.S. Böscke, J. Müller, D. Bräuhaus, U. Schröder, and U. Böttger, in *2011 Int. Electron Devices Meet.* (IEEE, Washington, DC, 2011), pp. 24.5.1–24.5.4.

[62] T.P. Ma and J.-P. Han, IEEE Electron Device Lett. **23**, 386 (2002).

[63] E. Yurchuk, J. Müller, J. Paul, T. Schlösser, D. Martin, R. Hoffmann, S. Müeller, S. Slesazeck, U. Schröeder, R. Boschke, R. van Bentum, and T. Mikolajick, IEEE Trans. Electron Devices **61**, 3699 (2014).

[64] E. Yurchuk, S. Mueller, D. Martin, S. Slesazeck, U. Schroeder, T. Mikolajick, J. Müller, J. Paul, R. Hoffmann, J. Sundqvist, T. Schlösser, R. Boschke, R. van Bentum, and M. Trentzsch, in *2014 IEEE Int. Reliab. Phys. Symp.* (IEEE, Waikoloa, 2014), pp. 2E.5.1–2E.5.5.

[65] T.P. Ma, in *2014 IEEE 6th Int. Mem. Work.* (IEEE, Taipei, 2014), pp. 1–4.

[66] C.-H. Cheng and A. Chin, IEEE Electron Device Lett. **35**, 138 (2014).

[67] C.H. Cheng and A. Chin, IEEE Electron Device Lett. **35**, 274 (2014).

[68] M.H. Lee, Y.-T. Wei, C. Liu, J.-J. Huang, M. Tang, Y.-L. Chueh, K.-Y. Chu, M.-J. Chen, H.-Y. Lee, Y.-S. Chen, L.-H. Lee, and M.-J. Tsai, IEEE J. Electron Devices Soc. **3**, 377 (2015).

[69] M.H. Park, H.J. Kim, Y.J. Kim, T. Moon, K.D. Kim, and C.S. Hwang, Adv. Energy Mater. **4**, 1400610 (2014).

[70] M.H. Park, H.J. Kim, Y.J. Kim, T. Moon, K.D. Kim, and C.S. Hwang, Nano Energy **12**, 131 (2015).

[71] M. Hoffmann, U. Schroeder, C. Künneth, A. Kersch, S. Starschich, U. Böttger, and T. Mikolajick, Nano Energy **18**, 154 (2015).

[72] C.B. Sawyer and C.H. Tower, Phys. Rev. **35**, 269 (1930).

[73] J.T. Evans, *Introduction to the Ferroelectric Memory* (Radiant Technologies Inc., Albuquerque, 2013).

[74] T. Schenk, E. Yurchuk, S. Mueller, U. Schroeder, S. Starschich, U. Böttger, and T. Mikolajick, Appl. Phys. Rev. **1**, 041103 (2014).

[75] X. Hao, J. Zhai, L.B. Kong, and Z. Xu, Prog. Mater. Sci. **63**, 1 (2014).

[76] S. Bernacki, L. Jack, Y. Kisler, S. Collins, S.D. Bernstein, R. Hallock, B. Armstrong, J. Shaw, J. Evans, B. Tuttle, B. Hammetter, S. Rogers, B. Nasby, J. Henderson, J. Benedetto, R. Moore, C.R. Pugh, and A. Fennelly, Integr. Ferroelectr. **3**, 97 (1993).

[77] P.D. Lomenzo, Q. Takmeel, C. Zhou, C.M. Fancher, E. Lambers, N.G. Rudawski, J.L. Jones, S. Moghaddam, and T. Nishida, J. Appl. Phys. **117**, 134105 (2015).

[78] C.J. Brennan, Integr. Ferroelectr. **2**, 73 (1992).

[79] C.J. Brennan, MRS Proc. **243**, 141 (1991).

[80] L.M. Grupp, J.D. Davis, and S. Swanson, in *Proc. 10th USENIX Conf. File Storage Technol.* (USENIX Association, San Jose, CA, 2012).

[81] S. Okamura, M. Takaoka, T. Nishida, and T. Shiosaki, Jpn. J. Appl. Phys. **39**, 5481 (2000).

[82] D. Zhou, J. Xu, Q. Li, Y. Guan, F. Cao, X. Dong, J. Müller, T. Schenk, and U. Schröder, Appl. Phys. Lett. **103**, 192904 (2013).

[83] M. Dawber and J.F. Scott, Appl. Phys. Lett. **76**, 1060 (2000).

[84] J.F. Scott, C.A. Araujo, B.M. Melnick, L.D. McMillan, and R. Zuleeg, J. Appl. Phys. **70**, 382 (1991).

[85] T. Hase, T. Noguchi, K. Takemura, and Y. Miyasaka, in *Proc. Elev. IEEE Int. Symp. Appl. Ferroelectr.* (IEEE, Montreux, 1998), pp. 7–10.

[86] U. Robels and G. Arlt, J. Appl. Phys. **73**, 3454 (1993).

[87] A.K. Tagantsev, I. Stolichnov, E.L. Colla, and N. Setter, J. Appl. Phys. **90**, 1387 (2001).

[88] T. Schenk, U. Schroeder, M. Pešić, M. Popovici, Y. V Pershin, and T. Mikolajick, ACS Appl. Mater. Interfaces **6**, 19744 (2014).

[89] S. Mueller, J. Muller, U. Schroeder, and T. Mikolajick, IEEE Trans. Device Mater. Reliab. **13**, 93 (2013).

[90] U. Schroeder, S. Mueller, J. Mueller, E. Yurchuk, D. Martin, C. Adelmann, T. Schloesser, R. van Bentum, and T. Mikolajick, ECS J. Solid State Sci. Technol. **2**, N69 (2013).

[91] P.D. Lomenzo, Q. Takmeel, C. Zhou, C.-C. Chung, S. Moghaddam, J.L. Jones, and T. Nishida, Appl. Phys. Lett. **107**, 242903 (2015).

[92] M.H. Park, H.J. Kim, Y.J. Kim, W. Jeon, T. Moon, and C.S. Hwang, Phys. Status Solidi - Rapid Res. Lett. **8**, 532 (2014).

[93] D. Zhou, Y. Guan, M.M. Vopson, J. Xu, H. Liang, F. Cao, X. Dong, J. Mueller, T. Schenk, and U. Schroeder, Acta Mater. **99**, 240 (2015).

[94] R.R. Mehta, B.D. Silverman, and J.T. Jacobs, J. Appl. Phys. **44**, 3379 (1973).

[95] T.S. Böscke, S. Teichert, D. Bräuhaus, J. Müller, U. Schröder, U. Böttger, and T. Mikolajick, Appl. Phys. Lett. **99**, 112904 (2011).

[96] N. Setter, D. Damjanovic, L. Eng, G. Fox, S. Gevorgian, S. Hong, A. Kingon, H. Kohlstedt, N.Y. Park, G.B. Stephenson, I. Stolitchnov, A.K. Taganstev, D. V. Taylor, T. Yamada, and S. Streiffer, J. Appl. Phys. **100**, 051606 (2006).

[97] E. Barsoukov and J.R. Macdonald, editors , *Impedance Spectroscopy: Theory, Experiment, and Applications*, 2nd ed. (John Wiley & Sons, Inc., Hoboken, NJ, 2005).

[98] C. Verdier, F.D. Morrison, D.C. Lupascu, and J.F. Scott, J. Appl. Phys. **97**, 024107 (2005).

[99] L.-W. Chang, M. Alexe, J.F. Scott, and J.M. Gregg, Adv. Mater. **21**, 4911 (2009).

[100] N.J. Donnelly and C.A. Randall, IEEE Trans. Ultrason. Ferroelectr. Freq. Control **59**, 1883 (2012).

[101] A. Khodorov, S.A.S. Rodrigues, M. Pereira, and M.J.M. Gomes, J. Appl. Phys. **102**, 114109 (2007).

[102] F.D. Morrison, D.J. Jung, and J.F. Scott, J. Appl. Phys. **101**, 094112 (2007).

[103] C.R. Brundle, C.A.J. Evans, S. Wilson, and L.E. Fitzpatrick, editors , *Encyclopedia of Materials Characterization* (Manning Publicatins Co., Boston, MA, 1992).

[104] K.R. Udayakumar, K. Boku, K.A. Remack, J. Rodriguez, S.R. Summerfelt, F.G. Celii, S. Aggarwal, J.S. Martin, L. Hall, L. Matz, B. Rathsack, H. McAdams, and T.S. Moise, Jpn. J. Appl. Phys. **45**, 3202 (2006).

[105] S. Mueller, S.R. Summerfelt, J. Müller, U. Schroeder, and T. Mikolajick, IEEE

Electron Device Lett. **33**, 1300 (2012).

[106] S. Mueller, C. Adelmann, A. Singh, S. Van Elshocht, U. Schroeder, and T. Mikolajick, ECS J. Solid State Sci. Technol. **1**, N123 (2012).

[107] K. Niwa, Y. Kotaka, M. Tomotani, H. Ashida, Y. Goto, and S. Otani, Acta Mater. **48**, 4755 (2000).

[108] R. Bouregba, N. Sama, C. Soyer, G. Poullain, and D. Remiens, J. Appl. Phys. **107**, 104102 (2010).

[109] H. Fujisawa, S. Hyodo, K. Jitsui, M. Shimizu, H. Niu, H. Okino, and T. Shiosaki, Integr. Ferroelectr. **21**, 107 (1998).

[110] H.O. Pierson, *Handbook of Refractory Carbides & Nitrides: Properties, Characteristics, Processing and Applications* (Noyes Publications, NJ, 1996).

[111] J.W. Arblaster, Platin. Met. Rev. **33**, 14 (1989).

[112] A. Deshpande, R. Inman, G. Jursich, and C.G. Takoudis, J. Appl. Phys. **99**, 094102 (2006).

[113] J. Müller, E. Yurchuk, T.S. Böscke, R. Hoffmann, U. Schröder, T. Mikolajick, and L. Frey, in *Proc. 17th Work. Dielectr. Microelectron.* (2012), p. 1.

[114] M.H. Park, H.J. Kim, Y.J. Kim, T. Moon, and C.S. Hwang, Appl. Phys. Lett. **104**, 072901 (2014).

[115] P.D. Lomenzo, P. Zhao, Q. Takmeel, S. Moghaddam, T. Nishida, M. Nelson, C.M. Fancher, E.D. Grimley, X. Sang, J.M. LeBeau, and J.L. Jones, J. Vac. Sci. Technol. B Microelectron. Nanom. Struct. **32**, 03D123 (2014).

[116] T.D. Huan, V. Sharma, G.A. Rossetti, and R. Ramprasad, Phys. Rev. B **90**, 064111 (2014).

[117] S. Mueller, E. Yurchuk, S. Slesazeck, T. Mikolajick, J. Müller, T. Herrmann, and A. Zaka, in *2013 Jt. IEEE Int. Symp. Appl. Ferroelectr. Work. Piezoresponse Force Microsc.* (IEEE, Prague, 2013), pp. 248–251.

[118] T. Rojac, M. Kosec, B. Budic, N. Setter, and D. Damjanovic, J. Appl. Phys. **108**, 074107 (2010).

[119] J. Müller, T.S. Böscke, U. Schröder, R. Hoffmann, T. Mikolajick, and L. Frey, IEEE Electron Device Lett. **33**, 185 (2012).

[120] S. Mueller, J. Müller, R. Hoffmann, E. Yurchuk, T. Schlösser, R. Boschke, J. Paul, M. Goldbach, T. Herrmann, A. Zaka, U. Schroder, and T. Mikolajick, IEEE Trans. Electron Devices **60**, 4199 (2013).

[121] T. Shimizu, T. Yokouchi, T. Shiraishi, T. Oikawa, P.S.S.R. Krishnan, and H. Funakubo, Jpn. J. Appl. Phys. **53**, 09PA04 (2014).

[122] E. Yurchuk, J. Müller, S. Knebel, J. Sundqvist, A.P. Graham, T. Melde, U. Schröder, and T. Mikolajick, Thin Solid Films **533**, 88 (2013).

[123] P.D. Lomenzo, Q. Takmeel, C. Zhou, Y. Liu, C.M. Fancher, J.L. Jones, S. Moghaddam, and T. Nishida, Appl. Phys. Lett. **105**, 072906 (2014).

[124] D. Martin, J. Müller, T. Schenk, T.M. Arruda, A. Kumar, E. Strelcov, E. Yurchuk, S. Müller, D. Pohl, U. Schröder, S. V. Kalinin, and T. Mikolajick, Adv. Mater. **26**, 8198 (2014).

[125] M.M. Hussain, N. Moumen, J. Barnett, J. Saulters, D. Baker, and Z. Zhang, Electrochem. Solid-State Lett. **8**, G333 (2005).

[126] L.A. Giannuzzi and F.A. Stevie, Micron **30**, 197 (1999).

[127] M. Sugiyama and G. Sigesato, J. Electron Microsc. (Tokyo). **53**, 527 (2004).

[128] L.A. Giannuzzi, J.L. Drown, S.R. Brown, R.B. Irwin, and F.A. Stevie, Microsc. Res. Tech. **41**, 285 (1998).

[129] J. Mayer, L.A. Giannuzzi, T. Kamino, and J. Michael, MRS Bull. **32**, 400 (2007).

[130] S. Bals, W. Tirry, R. Geurts, Z. Yang, and D. Schryvers, Microsc. Microanal. **13**, 80 (2007).

[131] N.I. Kato, J. Electron Microsc. (Tokyo). **53**, 451 (2004).

[132] N. Umezawa, K. Shiraishi, T. Ohno, H. Watanabe, T. Chikyow, K. Torii, K. Yamabe, K. Yamada, H. Kitajima, and T. Arikado, Appl. Phys. Lett. **86**, 143507 (2005).

[133] V. Cuny and N. Richard, J. Appl. Phys. **104**, 033709 (2008).

[134] A.K. Tagantsev, I. Stolichnov, N. Setter, J. Cross, and M. Tsukada, Phys. Rev. B **66**, 214109 (2002).

[135] B. Jaffe, Proc. IRE **49**, 1264 (1961).

[136] S.S.N. Bharadwaja and S.B. Krupanidhi, J. Appl. Phys. **89**, 4541 (2001).

[137] D. Martin, E. Yurchuk, S. Müller, J. Müller, J. Paul, J. Sundquist, S. Slesazeck, T. Schlösser, R. Van Bentum, M. Trentzsch, U. Schröder, and T. Mikolajick, Solid. State. Electron. **88**, 65 (2013).

[138] R. Pillarisetty, Nature **479**, 324 (2011).

[139] S.V.J. Chandra, M.-I. Jeong, Y.-C. Park, J.-W. Yoon, and C.-J. Choi, Mater. Trans.

52, 118 (2011).

[140] H. Kim, C.O. Chui, K.C. Saraswat, and P.C. McIntyre, Appl. Phys. Lett. **83**, 2647 (2003).

[141] J. Müller, P. Polakowski, S. Riedel, S. Mueller, E. Yurchuk, and T. Mikolajick, in *2014 14th Annu. Non-Volatile Mem. Technol. Symp.* (IEEE, Jeju Island, 2014), pp. 1–7.

[142] S. Clima, D.J. Wouters, C. Adelmann, T. Schenk, U. Schroeder, M. Jurczak, and G. Pourtois, Appl. Phys. Lett. **104**, 092906 (2014).

[143] T. Schenk, M. Hoffmann, J. Ocker, M. Pešić, T. Mikolajick, and U. Schroeder, ACS Appl. Mater. Interfaces **7**, 20224 (2015).

[144] M. Hoffmann, U. Schroeder, T. Schenk, T. Shimizu, H. Funakubo, O. Sakata, D. Pohl, M. Drescher, C. Adelmann, R. Materlik, a. Kersch, and T. Mikolajick, J. Appl. Phys. **118**, 072006 (2015).

[145] P.D. Lomenzo, Q. Takmeel, C.M. Fancher, C. Zhou, N.G. Rudawski, S. Moghaddam, J.L. Jones, and T. Nishida, IEEE Electron Device Lett. **36**, 766 (2015).

[146] P. Polakowski and J. Müller, Appl. Phys. Lett. **106**, 232905 (2015).

[147] K.L. Lin, T.-H. Hou, J. Shieh, J.H. Lin, C.-T. Chou, and Y.-J. Lee, J. Appl. Phys. **109**, 084104 (2011).

[148] S.U. Sharath, T. Bertaud, J. Kurian, E. Hildebrandt, C. Walczyk, P. Calka, P. Zaumseil, M. Sowinska, D. Walczyk, A. Gloskovskii, T. Schroeder, and L. Alff, Appl. Phys. Lett. **104**, 063502 (2014).

[149] H.-Y. Chen and F.-H. Lu, J. Vac. Sci. Technol. A Vacuum, Surfaces, Film. **23**, 1006 (2005).

[150] H.C. Barshilia and K.S. Rajam, J. Mater. Res. **19**, 3196 (2004).

[151] M.H. Park, H.J. Kim, Y.J. Kim, Y.H. Lee, T. Moon, K.D. Kim, S.D. Hyun, and C.S. Hwang, Appl. Phys. Lett. **107**, 192907 (2015).

[152] H.J. Kim, M.H. Park, Y.J. Kim, Y.H. Lee, T. Moon, K.D. Kim, S.D. Hyun, and C.S. Hwang, Nanoscale **8**, 1383 (2016).

[153] P.K. Larsen, G.J.M. Dormans, D.J. Taylor, and P.J. van Veldhoven, J. Appl. Phys. **76**, 2405 (1994).

BIOGRAPHICAL SKETCH

Patrick Lomenzo was born and raised in New Jersey. After living for a few years in Morgantown, WV, Patrick moved to Florida and finished high school. Patrick earned his Associate of Arts degree at Indian River State College and then transferred into the Electrical and Computer Engineering Department at the University of Florida. While working as an undergraduate researcher at UF, Patrick was approached with an opportunity to work on an SRC project and was subsequently awarded an SRC Fellowship to complete his PhD. He interned at Texas Instruments as a process integration engineer for high voltage power technologies.